Large Scale Electronic Structure Studies on the Energetics of Dislocations in Al-Mg Materials System and Its Connection to Mesoscale Models

by

Sambit Das

A dissertation submitted in partial fulfillment
of the requirements for the degree of
Doctor of Philosophy
(Mechanical Engineering)
in The University of Michigan
2019

Doctoral Committee:

Associate Professor Vikram Gavini, Chair
Dr. Sylvie Aubry, Lawrence Livermore National Laboratory
Professor Krishnakumar Garikipati
Assistant Professor Liang Qi

Sambit Das

dsambit@umich.edu

ORCID iD: 0000-0002-6356-6015

© Sambit Das 2019

For my beloved wife and my parents.

TABLE OF CONTENTS

CHAPTER

LIST OF FIGURES

Figure

LIST OF TABLES

Table

LIST OF APPENDICES

Appendix

ABSTRACT

Computational modeling of dislocation behavior is vital for designing new lightweight metallic alloys. However, extraordinary challenges are posed by the multiscale physics ranging over a vast span of interacting length-scales from electronic-structure and atomic-scale effects at the dislocation core ($< 10^{-9}$m) to long-ranged elastic interactions at the continuum scale ($\sim 10\mu$). In particular, quantification of the energetics associated with electronic-structure effects inside the dislocation core and its interaction with the external macroscopic elastic fields have not been explored due to limitations of current electronic-structure methods based on the widely used plane-wave based discretization. This thesis seeks to address the above challenges by developing computational methodologies to conduct large-scale real-space electronic-structure studies of energetics of dislocations in Aluminum and Magnesium, and use these results to develop phenomenological connections to mesoscale models of plasticity like discrete dislocation dynamics (DDD), which study the collective behavior of the dislocations at longer length scales ($\sim$ 1–15 μ).

First, a local real-space formulation of orbital-free Density Functional Theory is developed based on prior work, and implemented using finite-element discretization. The local real-space formulation coupled with bulk Dirichlet boundary conditions enables a direct computation of the isolated dislocation core energy. Studies on dislocations in Aluminum and Magnesium suggest that the core-size—region with significant contribution of electronic effects to dislocation energetics—is around seven to eleven times the magnitude of the Burgers vector. This is in stark contrast to prior displacement field based core size estimates of one to three times the magnitude of

the Burgers vector. Interestingly, our study further indicates that the core-energy of the dislocations in both Aluminum and Magnesium is strongly dependent on external macroscopic strains with a non-zero slope at zero external strain.

Next, the computed dislocation core energetics is used to develop a continuum model for an arbitrary aggregate of dislocations in an infinite isotropic elastic continua. This model, which accounts for the core energy dependence on macroscopic deformation provides a phenomenological approach to incorporate the electronic structure effects into mesoscale DDD simulations. Application of this model to derive nodal forces in a discrete dislocation network, leads to additional configurational forces beyond those considered in existing DDD models. Using case studies, we show that even up to distances of $10-15$ nm between the dislocations, these additional configurational forces are non-trivial in relation to the elastic Peach-Koehler force. Furthermore, the core force model is incorporated into a DDD implementation, where significant influence of core force on elementary dislocation mechanisms in Aluminum such as critical stress of a Frank-Read source and structure of a dislocation binary junction are demonstrated.

To enable the above electronic-structure studies of dislocations in generic material systems, calculations using the more accurate and transferable Kohn-Sham Density Functional Theory (KS-DFT) are required. The final part of this thesis extends previous work on real-space adaptive spectral finite-element discretization of KS-DFT to develop numerical strategies and implementation innovations, which significantly reduce the computational pre-factor, while increasing the arithmetic intensity and lowering the data movement costs on both many-core and heterogeneous architectures. This has enabled systematically convergent and massively parallel (demonstrated up to 192,000 MPI tasks) KS-DFT calculations on material systems up to $\sim 100,000$ electrons. Using GPUs, an unprecedented sustained performance of 46 PFLOPS (27.8% of peak FP64 performance) is demonstrated on a large-scale benchmark dislocation system in Magnesium containing 105,080 electrons.

CHAPTER I

Introduction

Plasticity in crystalline materials is governed by defects and their collective behavior, which includes their nucleation, kinetics, evolution and interaction with other defects (cf. [5–7]). The primary defect type responsible for plasticity are dislocations, which are line defects. However, developing a predictive dislocation based model of plasticity poses extraordinary challenges due to the multiscale physics ranging over a vast span of interacting length-scales (cf. [8]) ranging from electronic-structure effects at the dislocation core to continuum elastic effects, with mesoscale physics of the dislocation microstructure (cf. [9]) playing an important role. While mesoscopic models like the discrete dislocation dynamics (DDD) [10–19], phase field methods [20–25], and continuum theories based on continuously distributed dislocations [26–31] correctly account for the elastic interactions outside the dislocation core using linear elastic theories of dislocations [5, 32–34] or non-linear elastic theories of dislocations [31, 35], the physics inside the dislocation core has been supplemented by atomistic calculations of dislocation core structure, dislocation core energetics, dislocation mobilities, and solute strengthening (cf. e.g. [15, 36–42]). However, these atomistic calculations are based on interatomic potentials, which may not adequately describe the significant electronic structure effects inside the dislocation core. In fact, recent investigations of dislocation core structure in Aluminum and Magnesium [43–47] using explicit electronic structure calculations based on plane-wave implementations of density functional theory (DFT) have demonstrated that atomistic predictions of the dislocation core structure properties are widely sensitive to the choice of the interatomic potential, and also show discrepancies in comparison to the more transferable and accurate electronic structure calculations. However, these electronic structure studies of dislocations have a major limitation that the periodic boundary conditions inherent in plane wave based methods are incompatible with the displacement fields of an isolated dislocation. Such studies are thus limited to either using dipole and quadrapole configurations of dislocations [48, 49], or introducing a vacuum region around the isolated dislocation [43, 44, 47]. While these approaches have been useful to predict the dislocation core structures [43, 44, 47, 49], and to compute Peierls stress [46, 48, 49] and interaction energetics such as dislocation-solute binding energies [50, 51], a direct calculation of dislocation core energy using plane-wave based DFT implementations has been beyond reach.

This thesis seeks to address the above challenges by developing computational methodologies to conduct large-scale, electronic-structure studies of core energetics of isolated dislocations in Aluminum and Magnesium, and use these results to develop phenomenological connections to mesoscale models of plasticity like discrete dislocation dynamics (DDD), which study the collective behavior of the dislocations at longer length scales ($\sim$ 1–15 μ). As a first step [52], we improved upon previous research [53, 54] to develop a local, real-space formulation of orbital-free DFT in conjunction with higher-order finite-element discretization, whose general basis set offers significant advantages over the previously mentioned plane wave discretization like allowing for arbitrary boundary conditions, ease of handling complex geometries, excellent scalability on parallel computing architectures, and tailoring the mesh-resolution to the system physics, all of which make the developed framework very well suited to study dislocations.

In the next step, we use the developed local real-space formulation of orbital-free DFT to study the core energetics and core structure of an isolated screw dislocation in Aluminum [55], and isolated basal edge and basal screw dislocations in Magnesium. We adopt the bulk Dirichlet boundary conditions approach proposed in [56], which allows for direct calculation of the dislocation core energy of an isolated dislocation embedded in the bulk. Using this direct energetics approach, we estimate the core size of a perfect screw dislocation in Aluminum to be $\approx 7\ |\mathbf{b}|$, and core sizes of perfect basal edge and screw dislocations in Magnesium to be be $\approx 8\ |\mathbf{b}|$ and $\approx 11\ |\mathbf{b}|$ respectively. These are considerably larger than previous atomistics based estimates of $1-3\ |\mathbf{b}|$. The perfect dislocations in both Aluminum and Magnesium dissociate into two Shockley partials with partial separation distances measured from differential displacement plots comparing well with previous DFT estimates. Similar to a previous electronic structure study on edge dislocation [56, 57], we find that the core energy of the screw dislocation in Aluminum and basal dislocations in Magnesium are not a constant, but strongly dependent on macroscopic deformations with a non-zero slope at zero external strain. Next, we use the above core energetics data with physically reasonable assumptions to develop a continuum energetics model for an aggregate of dislocations that accounts for the core energy dependence on macroscopic deformations. Further, we use this energetics model in a discrete dislocation network, and from the variations of the core energy with respect to the nodal positions of the network, we obtain the nodal core force which can directly be incorporated into discrete dislocation dynamics frameworks. We analyze and classify the nodal core force into three different contributions based on their decay behavior. Two of these contributions to the core force, both arising from the core energy dependence on macroscopic deformations, are not accounted for in currently used discrete dislocation dynamics models which assume the core energy to be a constant excepting for its dependence on the dislocation line orientation. Using case studies involving simple dislocation structures, we demonstrate that the contribution to the core force from the core energy dependence on macroscopic deformations can be significant in comparison to the elastic Peach-Koehler force even up to distances of $10 - 15$ nm between dislocation structures. Thus, these core effects, whose origins are in the electronic structure of the dislocation core, can play an important role in influencing dislocation-dislocation interactions to much larger distances than considered heretofore. Furthermore, we have incorporated the core force into a DDD implementation, and demonstrate the influence of core effects on elementary dislocation mechanisms in Aluminum such as structure of a dislocation binary junction and critical stress of a Frank-Read source.

Though orbital-free DFT is demonstrated to be accurate for Aluminum-Magnesium materials system in comparison to Kohn-Sham DFT, the kinetic energy functionals are not well developed or are not sufficiently accurate for generic material systems, such as transition metals and covalently bonded systems. For example, Kohn-Sham DFT is important in studying the electronic structure effects in dislocation-solute interactions [50, 58–60]. However, the cubic scaling computational complexity of Kohn-Sham DFT coupled with limited parallel scaling of widely used plane-wave basis implementations have so far been a significant bottleneck in accessing large system sizes reaching thousands of atoms as required for studying dislocations. Thus, in the final part of this thesis, we extend previous work on real-space adaptive spectral finite-element discretization of Kohn-Sham DFT [61, 62] to develop a capability (`DFT-FE`) to perform large scale and accurate Kohn-Sham DFT calculations. The present work [63][1] develops numerical strategies and implementation innovations, which significantly reduce the computational pre-factor and delay the onset of cubic scaling computational complexity. This has enabled systematically convergent and massively parallel (demonstrated up to 192,000 MPI tasks) Kohn-Sham DFT calculations on material systems up to $\sim 100,000$ electrons. Further, these devel-

---

[1] Phani Motamarri and Sambit Das are co-first authors.

opments have resulted in `DFT-FE` being more than 10× faster in time to solution and 5–10× more computationally efficient than the state-of-the-art plane-wave codes for large-scale metallic systems with more than 10,000 electrons at similar accuracy. The above approaches have also been extended to efficiently use Graphical Processing Units (GPUs) [64] through implementation innovations which increase arithmetic intensity and lower the data movement costs. Using GPUs on the Summit supercomputer, we demonstrated an unprecedented sustained performance of 46 PFLOPS (27.8% of peak FP64 performance) on a large-scale benchmark dislocation system in Magnesium containing 105,080 electrons.

The remainder of this thesis is organized as follows. Chapter II provides an overview of orbtial-free DFT and subsequently discusses the local real-space formulation of orbital-free DFT and its accuracy and transferability for the Aluminum-Magnesium materials system. Chapter III applies the developed real-space orbital-free DFT framework to study core energetics of isolated dislocations in Aluminum and Magnesium. Subsequently, the obtained isolated dislocation core energetics is used in Chapter IV to develop a continuum model for an aggregate of dislocations, which is then incorporated into a DDD framwork and importance of this model for dislocation-dislocation interactions is demonstrated using various case studies. Next, Chapter V discusses development of numerical and implementation strategies for large-scale Kohn-Sham DFT calculations, and demonstration on large-scale benchmark material systems. Finally we conclude in Chapter VI with a short discussion and consider the scope for future work.

CHAPTER II

Real-Space Formulation of Orbital-Free Density Functional Theory Using Finite-Element Discretization

2.1 Introduction

Electronic structure calculations have played an important role in understanding the properties of a wide range of materials systems [65]. In particular, the Kohn-Sham formalism of density functional theory [66, 67] has been the workhorse of ground-state electronic structure calculations. However, the Kohn-Sham approach requires the computation of single-electron wavefunctions to compute the kinetic energy of non-interacting electrons, whose computational complexity typically scales as $\mathcal{O}(N^3)$ for an N-electron system, thus, limiting standard calculations to materials systems containing few hundreds of atoms. While there has been progress in developing close to linear-scaling algorithms for the Kohn-Sham approach [68, 69], these are still limited to a few thousands of atoms, especially for metallic systems [70]. The orbital-free approach to DFT [71], on the other hand, models the kinetic energy of non-interacting electrons as an explicit functional of the electron density, thus circumventing the computationally intensive step of computing the single-electron wavefunctions. Further, the computational complexity of orbital-free DFT scales linearly with the system size as the ground-state DFT problem reduces to a minimization problem in a single field—the electron density. The past two decades has seen considerable progress in the development of accurate models for orbital-free kinetic energy functionals [2, 72–78], and, in particular, for systems whose electronic-structure is close to a free electron gas (for e.g. Al, Mg). Also, orbital-free DFT calculations are being increasingly used in the simulations of warm dense matter where the electronic structure is close to that of a free electron gas at very high temperatures [79–83]. As the reduced computational complexity of orbital-free DFT enables consideration of larger computational domains, recent studies have also focused on studying extended defects in Al and Mg, and have provided important insights into the energetics of these defects [44, 46, 53, 56, 84, 85].

The widely used numerical implementation of orbital-free DFT is based on a Fourier space formalism using a plane-wave discretization [1, 86]. A Fourier space formulation provides an efficient computation of the extended interactions arising in orbital-free DFT—electrostatics and kinetic energy functionals—through Fourier transforms. Further, the plane-wave basis is a complete basis and provides variational convergence in ground-state energy with exponential convergence rates. However, the Fourier space formulations are restricted to periodic geometries and boundary conditions that are suitable for perfect bulk materials, but not for materials systems containing extended defects. Also, the extended spatial nature of the plane-wave basis affects the parallel scalability of the numerical implementation and is also not suitable for multi-scale methods that rely on coarse-graining. In order to address the aforementioned limitations of Fourier space techniques, recent efforts have focused on developing real-space formulations for orbital-free DFT and numerical implementations based on finite-element [54, 87, 88] and finite difference discretizations [89–91].

In the present work [52], we build upon prior efforts [54, 87] to develop an efficient real-space formulation of orbital-free DFT employing the widely used non-local

Wang-Govind-Carter (WGC) [2] kinetic energy functional. We also propose an unified variational framework for computing the configurational forces associated with geometry optimization of both internal atomic positions as well as the cell geometry. We subsequently investigate the accuracy and transferability of the proposed real-space formulation of orbital-free DFT for Aluminum and Magnesium materials systems, where we obtain good agreement with Kohn-Sham DFT calculations on a wide range of properties and benchmark calculations. We finally investigate the cell-size effects in the electronic structure of a mono-vacancy in Aluminum using bulk Dirichlet boundary conditions, where the perturbations in the electronic structure arising due to the vacancy vanishes on the boundary of the computational domain. We note that the bulk Dirichlet boundary conditions are crucial to the study of energetics of isolated dislocations embedded in the bulk as will be discussed in Chapter III.

2.2 Orbital-free density functional theory

The ground-state energy of a charge neutral materials system containing M nuclei and N valence electrons in density functional theory is given by [65, 71]

$$E(\rho, \mathbf{R}) = T_s(\rho) + E_{xc}(\rho) + E_H(\rho) + E_{ext}(\rho, \mathbf{R}) + E_{zz}(\mathbf{R}) \,, \tag{2.1}$$

where ρ denotes the electron-density and $\mathbf{R} = \{\mathbf{R}_1, \mathbf{R}_2, \ldots, \mathbf{R}_M\}$ denotes the vector containing the positions of M nuclei. In the above, T_s denotes the kinetic energy of non-interacting electrons, E_{xc} is the exchange-correlation energy, E_H is the Hartree energy or classical electrostatic interaction energy between electrons, E_{ext} is the classical electrostatic interaction energy between electrons and nuclei, and E_{zz} denotes the electrostatic repulsion energy between nuclei. We now discuss the various contributions to the ground-state energy, beginning with the exchange-correlation energy.

The exchange-correlation energy, denoted by E_{xc}, incorporates all the quantum-mechanical interactions in the ground-state energy of a materials system. While the existence of a universal exchange-correlation energy as a functional of electron-density has been established by Hohenberg, Kohn and Sham [66, 67], its exact functional form has been elusive to date, and various models have been proposed over the past decades. For solid-state calculations, the local density approximation (LDA) [3, 92] and the generalized gradient approximation [93] have been widely adopted across a range of materials systems. In particular, the LDA exchange-correlation energy, which is adopted in the present work, has the following functional form:

$$E_{\mathrm{xc}}(\rho) = \int \varepsilon_{\mathrm{xc}}(\rho)\rho(\mathbf{x})\, d\mathbf{x} \ , \tag{2.2}$$

where $\varepsilon_{\mathrm{xc}}(\rho) = \varepsilon_x(\rho) + \varepsilon_c(\rho)$, and

$$\varepsilon_x(\rho) = -\frac{3}{4}\left(\frac{3}{\pi}\right)^{1/3} \rho^{1/3}(\mathbf{x}) \ , \tag{2.3}$$

$$\varepsilon_c(\rho) = \begin{cases} \frac{\gamma}{(1+\beta_1\sqrt{(r_s)}+\beta_2 r_s)} & r_s \geq 1, \\ A\,\log r_s + B + C\,r_s \log r_s + D\,r_s & r_s < 1, \end{cases} \tag{2.4}$$

and $r_s = (3/4\pi\rho)^{1/3}$. In the present work, we use the Ceperley and Alder constants [3] in equation (2.4).

The last three terms in equation (2.1) represent electrostatic interactions between electrons and nuclei. The Hartree energy, or the electrostatic interaction energy between electrons, is given by

$$E_H(\rho) = \frac{1}{2}\int\int \frac{\rho(\mathbf{x})\rho(\mathbf{x}')}{|\mathbf{x}-\mathbf{x}'|}\, d\mathbf{x}\, d\mathbf{x}' \, . \tag{2.5}$$

The interaction energy between electrons and nuclei, in the case of local pseudopotentials that are adopted in the present work, is given by

$$\begin{aligned} E_{ext}(\rho, \mathbf{R}) &= \int \rho(\mathbf{x}) V_{ext}(\mathbf{x}, \mathbf{R})\, d\mathbf{x} \\ &= \sum_J \int \rho(\mathbf{x}) V_{ps}^J(|\mathbf{x} - \mathbf{R}_J|) d\mathbf{x}\,, \end{aligned} \tag{2.6}$$

where V_{ps}^J denotes the pseudopotential corresponding to the J^{th} nucleus, which, beyond a core radius is the Coulomb potential corresponding to the effective nuclear charge on the J^{th} nucleus. The nuclear repulsive energy is given by

$$E_{zz}(\mathbf{R}) = \frac{1}{2} \sum_I \sum_{J, J \neq I} \frac{Z_I Z_J}{|\mathbf{R}_I - \mathbf{R}_J|}\,, \tag{2.7}$$

where Z_I denotes the effective nuclear charge on the I^{th} nucleus. The above expression assumes that the core radius of the pseudopotential is smaller than internuclear distances, which is often the case in most solid-state materials systems. We note that in a non-periodic setting, representing a finite atomic system, all the integrals in equations (2.5)-(2.6) are over $\mathbb{R}^3$ and the summations in equations (2.6)-(2.7) include all the atoms. In the case of an infinite periodic crystal, all the integrals over $\mathbf{x}$ in equations (2.5)-(2.6) are over the unit cell whereas the integrals over $\mathbf{x}'$ are over $\mathbb{R}^3$. Similarly, in equations (2.6)-(2.7), the summation over I is on the atoms in the unit cell, and the summation over J extends over all lattice sites. Henceforth, we will adopt these notions for the domain of integration and summation.

The remainder of the contribution to the ground-state energy is the kinetic energy of non-interacting electrons, denoted by T_s, which is computed exactly in the Kohn-Sham formalism by computing the single-electron wavefunctions (eigenfunctions) in the mean-field [65]. The conventional solution of the Kohn-Sham eigenvalue problem, which entails the computation of the lowest N eigenfunctions and eigenvalues of the Kohn-Sham Hamiltonian, scales as $O(N^3)$ that becomes prohibitively expensive for materials systems containing a few thousand atoms. While efforts have been focused towards reducing the computational complexity of the Kohn-Sham eigenvalue problem [68, 69], this remains a significant challenge especially in the case of metallic systems. In order to avoid the computational complexity of solving for the wavefunctions to compute T_s, the orbital-free approach to DFT models the kinetic energy of non-interacting electrons as an explicit functional of electron density [71]. These models are based on theoretically known properties of T_s for a uniform electron gas, perturbations of uniform electron gas, and the linear response of uniform electron gas [2, 71–74]. As the orbital-free models for the kinetic energy functional are based on properties of uniform electron gas, their validity is often limited to materials systems whose electronic structure is close to a free electron gas, in particular, the alkali and alkali earth metals. Further, as the orbital-free approach describes the ground-state energy as an explicit functional of electron-density, it limits the pseudopotentials calculations to local pseudopotentials. While these restrictions constrain the applicability of the orbital-free approach, numerical investigations [2, 94] indicate that recently developed orbital-free kinetic energy functionals and local pseudopotentials can provide good accuracy for Al and Mg, which comprise of technologically important materials systems. Further, there are ongoing efforts in developing orbital-free kinetic energy models for covalently bonded systems and transition metals [95, 96].

In the present work, we restrict our focus to the Wang-Goving-Carter (WGC) density-dependent orbital-free kinetic energy functional [2], which is a widely used kinetic energy functional for ground-state calculations of materials systems with an electronic structure close to a free electron gas. In particular, the functional form of the WGC orbital-free kinetic energy functional is given by

$$T_s(\rho) = C_F \int \rho^{5/3}(\mathbf{x})\, d\mathbf{x} + \frac{1}{2} \int |\nabla \sqrt{\rho(\mathbf{x})}|^2\, d\mathbf{x} + T_K(\rho) \tag{2.8}$$

where

$$\begin{aligned} T_K(\rho) &= C_F \int\!\!\int \rho^{\alpha}(\mathbf{x})\, K(\xi_\gamma(\mathbf{x},\mathbf{x}'), |\mathbf{x}-\mathbf{x}'|)\, \rho^{\beta}(\mathbf{x}')\, d\mathbf{x}\, d\mathbf{x}' \,, \\ \xi_\gamma(\mathbf{x},\mathbf{x}') &= \Big(\frac{k_F^{\gamma}(\mathbf{x}) + k_F^{\gamma}(\mathbf{x}')}{2}\Big)^{1/\gamma}, \quad k_F(\mathbf{x}) = \big(3\pi^2\rho(\mathbf{x})\big)^{1/3} . \end{aligned}$$

In equation (2.8), the first term denotes the Thomas-Fermi energy with $C_F = \frac{3}{10}(3\pi^2)^{2/3}$, and the second term denotes the von-Weizsäcker correction [71]. The last term denotes the density dependent kernel energy, T_K, where the kernel K is chosen such that the linear response of a uniform electron gas is given by the Lindhard response [97]. In the WGC functional [2], the parameters are chosen to be $\{\alpha, \beta\} = \{5/6+\sqrt{5}/6, 5/6-\sqrt{5}/6\}$ and $\gamma = 2.7$. For materials systems whose electronic structure is close to a free-electron gas, the Taylor expansion of the density dependent kernel about a reference electron density (ρ_0), often considered to be the average electron density of the bulk crystal, is employed and is given by

$$\begin{aligned} K(\xi_\gamma(\mathbf{x},\mathbf{x}'), |\mathbf{x}-\mathbf{x}'|) = &K_0(|\mathbf{x}-\mathbf{x}'|) + K_1(|\mathbf{x}-\mathbf{x}'|)\big(\Delta\rho(\mathbf{x}) + \Delta\rho(\mathbf{x}')\big) \\ &+ \frac{1}{2}K_{11}(|\mathbf{x}-\mathbf{x}'|)\big((\Delta\rho(\mathbf{x}))^2 + (\Delta\rho(\mathbf{x}'))^2\big) \\ &+ K_{12}(|\mathbf{x}-\mathbf{x}'|)\Delta\rho(\mathbf{x})\Delta\rho(\mathbf{x}') + \dots \, . \end{aligned} \tag{2.9}$$

In the above equation, $\Delta\rho(\mathbf{x}) = \rho(\mathbf{x}) - \rho_0$ and the density independent kernels resulting from the Taylor expansion are given by

$$
\begin{aligned}
K_0(|\mathbf{x}-\mathbf{x}'|) &= K(\xi_\gamma, |\mathbf{x}-\mathbf{x}'|)\Big|_{\rho=\rho_0} \\
K_1(|\mathbf{x}-\mathbf{x}'|) &= \frac{\partial K(\xi_\gamma, |\mathbf{x}-\mathbf{x}'|)}{\partial \rho(\mathbf{x})}\Big|_{\rho=\rho_0} \\
K_{11}(|\mathbf{x}-\mathbf{x}'|) &= \frac{\partial^2 K(\xi_\gamma, |\mathbf{x}-\mathbf{x}'|)}{\partial \rho^2(\mathbf{x})}\Big|_{\rho=\rho_0} \\
K_{12}(|\mathbf{x}-\mathbf{x}'|) &= \frac{\partial^2 K(\xi_\gamma, |\mathbf{x}-\mathbf{x}'|)}{\partial \rho(\mathbf{x})\partial \rho(\mathbf{x}')}\Big|_{\rho=\rho_0} \\
&\dots
\end{aligned}
\tag{2.10}
$$

Numerical investigations have suggested that the Taylor expansion to second order provides a good approximation of the density dependent kernel for materials systems with electronic structure close to a free electron gas [2, 98]. In particular, in the second order Taylor expansion, the contribution from K_{12} has been found to dominate contributions from K_{11}. Thus, in practical implementations, often, only contributions from K_{12} in the second order terms are retained for computational efficiency.

2.3 Real-space formulation of orbital-free DFT

In this section, we present the local variational real-space reformulation of orbital-free DFT, the configurational forces associated with internal ionic relaxations and cell relaxation, and the finite-element discretization of the formulation.

2.3.1 Local real-space formulation

We recall that the various components of the ground-state energy of a materials system (cf. section 2.2) are local in real-space, except the electrostatic interaction energy and the kernel energy component of the WGC orbital-free kinetic energy functional that are extended in real-space. Conventionally, these extended interactions are computed in Fourier space to take advantage of the efficient evaluation of convolution integrals using Fourier transforms. For this reason, Fourier space formulations have been the most popular and widely used in orbital-free DFT calculations [1, 86]. However, Fourier space formulations employing the plane-wave basis result in some significant limitations. Foremost of these is the severe restriction of periodic geometries and boundary conditions. While this is not a limitation in the study of bulk properties of materials, this is a significant limitation in the study of defects in materials. For instance, the geometry of a single isolated dislocation in bulk is not compatible with periodic geometries, and, thus, prior electronic structure studies have mostly been limited to artificial dipole and quadrapole arrangements of dislocations. Further, numerical implementations of Fourier-space formulations also suffer from limited scalability on parallel computing platforms. Moreover, the plane-wave discretization employed in a Fourier space formulation provides a uniform spatial resolution, which is not suitable for the development of coarse-graining techniques—such as the quasi-continuum method [99]—that rely on an adaptive spatial resolution of the basis.

We now propose a real-space formulation that is devoid of the aforementioned limitations of a Fourier space formulation. The proposed approach, in spirit, follows along similar lines as recent efforts [53, 54], but the proposed formulation differs importantly in the way the extended electrostatic interactions are treated. In particular, the proposed formulation provides a unified framework to compute the configurational forces associated with both internal ionic and cell relaxations discussed in 2.3.2.

We begin by considering the electrostatic interactions that are extended in the real-space. We denote by $\tilde{\delta}(\mathbf{x}-\mathbf{R}_I)$ a regularized Dirac distribution located at $\mathbf{R}_I$, and the I^{th} nuclear charge is given by the charge distribution $-Z_I\tilde{\delta}(\mathbf{x}-\mathbf{R}_I)$. Defining $\rho_{nu}(\mathbf{x}) = -\sum_I Z_I\tilde{\delta}(|\mathbf{x}-\mathbf{R}_I|)$ and $\rho_{nu}(\mathbf{x}') = -\sum_J Z_J\tilde{\delta}(|\mathbf{x}'-\mathbf{R}_J|)$, the repulsive energy

E_{zz} can subsequently be reformulated as

$$E_{zz} = \frac{1}{2}\int\int \frac{\rho_{nu}(\mathbf{x})\rho_{nu}(\mathbf{x}')}{|\mathbf{x}-\mathbf{x}'|}d\mathbf{x}d\mathbf{x}' - E_{self}\,, \tag{2.11}$$

where E_{self} denotes the self energy of the nuclear charges and is given by

$$E_{self} = \frac{1}{2}\sum_I \int\int \frac{Z_I\tilde{\delta}(|\mathbf{x}-\mathbf{R}_I|)Z_I\tilde{\delta}(|\mathbf{x}'-\mathbf{R}_I|)}{|\mathbf{x}-\mathbf{x}'|}d\mathbf{x}d\mathbf{x}'\,. \tag{2.12}$$

We denote the electrostatic potential corresponding to the I^{th} nuclear charge $(-Z_I\tilde{\delta}(|\mathbf{x}'-\mathbf{R}_I|))$ as $\bar{V}^I_{\tilde{\delta}}(\mathbf{x})$, and is given by

$$\bar{V}^I_{\tilde{\delta}}(\mathbf{x}) = -\int \frac{Z_I\tilde{\delta}(|\mathbf{x}'-\mathbf{R}_I|)}{|\mathbf{x}-\mathbf{x}'|}d\mathbf{x}'\,. \tag{2.13}$$

The self energy, thus, can be expressed as

$$E_{self} = -\frac{1}{2}\sum_I \int Z_I\tilde{\delta}(|\mathbf{x}-\mathbf{R}_I|)\bar{V}^I_{\tilde{\delta}}(\mathbf{x})d\mathbf{x}\,. \tag{2.14}$$

Noting that the kernel corresponding to the extended electrostatic interactions in equations (2.12)-(2.13) is the Green's function of the Laplace operator, the electrostatic potential and the electrostatic energy can be computed by taking recourse to the solution of a Poisson equation, or, equivalently, the following local variational problem:

$$E_{self} = -\sum_I \min_{V^I\in H^1(\mathbb{R}^3)}\left\{\frac{1}{8\pi}\int|\nabla V^I(\mathbf{x})|^2d\mathbf{x} + \int Z_I\tilde{\delta}(|\mathbf{x}-\mathbf{R}_I|)V^I(\mathbf{x})d\mathbf{x}\right\}, \tag{2.15a}$$

$$\bar{V}^I_{\tilde{\delta}}(\mathbf{x}) = arg \min_{V^I\in H^1(\mathbb{R}^3)}\left\{\frac{1}{8\pi}\int|\nabla V^I(\mathbf{x})|^2d\mathbf{x} + \int Z_I\tilde{\delta}(|\mathbf{x}-\mathbf{R}_I|)V^I(\mathbf{x})d\mathbf{x}\right\}. \tag{2.15b}$$

In the above, $H^1(\mathbb{R}^3)$ denotes the Hilbert space of functions such that the functions and their first-order derivatives are square integrable on $\mathbb{R}^3$.

We next consider the electrostatic interaction energy corresponding to both electron and nuclear charge distribution. We denote this by $J(\rho, \rho_{nu})$, which is given by

$$J(\rho, \rho_{nu}) = \frac{1}{2}\int\int \frac{\big(\rho(\mathbf{x}) + \rho_{nu}(\mathbf{x})\big)\big(\rho(\mathbf{x}') + \rho_{nu}(\mathbf{x}')\big)}{|\mathbf{x}-\mathbf{x}'|} d\mathbf{x}d\mathbf{x}' \,. \tag{2.16}$$

We denote the electrostatic potential corresponding to the total charge distribution (electron and nuclear charge distribution) as $\bar{\phi}$, which is given by

$$\bar{\phi}(\mathbf{x}) = \int \frac{\rho(\mathbf{x}') + \rho_{nu}(\mathbf{x}')}{|\mathbf{x}-\mathbf{x}'|} d\mathbf{x}' \,. \tag{2.17}$$

The electrostatic interaction energy of the total charge distribution, in terms of $\bar{\phi}$, is given by

$$J(\rho, \rho_{nu}) = \frac{1}{2}\int (\rho(\mathbf{x}) + \rho_{nu}(\mathbf{x}))\bar{\phi}(\mathbf{x}) d\mathbf{x} \,. \tag{2.18}$$

As before, the electrostatic interaction energy as well as the potential of the total charge distribution can be reformulated as the following local variational problem:

$$J(\rho, \rho_{nu}) = -\min_{\phi \in \mathcal{Y}} \left\{ \frac{1}{8\pi}\int |\nabla\phi(\mathbf{x})|^2 d\mathbf{x} - \int (\rho(\mathbf{x}) + \rho_{nu}(\mathbf{x}))\phi(\mathbf{x}) d\mathbf{x} \right\} , \tag{2.19a}$$

$$\bar{\phi}(\mathbf{x}) = arg \min_{\phi \in \mathcal{Y}} \left\{ \frac{1}{8\pi}\int |\nabla\phi(\mathbf{x})|^2 d\mathbf{x} - \int (\rho(\mathbf{x}) + \rho_{nu}(\mathbf{x}))\phi(\mathbf{x}) d\mathbf{x} \right\} . \tag{2.19b}$$

In the above, $\mathcal{Y}$ is a suitable function space corresponding to the boundary conditions of the problem. In particular, for non-periodic problems such as isolated cluster of atoms $\mathcal{Y} = H^1(\mathbb{R}^3)$. For periodic problems, $\mathcal{Y} = H^1_{per}(Q)$ where Q denotes the unit cell and $H^1_{per}(Q)$ denotes the space of periodic functions on Q such that the functions and their first-order derivatives are square integrable.

The electrostatic interaction energy in DFT, comprising of E_H, E_{ext} and E_{zz} (cf.

equations (2.5)-(2.7)), can be rewritten in terms of $J(\rho, \rho_{nu})$ and E_{self} as

$$\begin{aligned} E_H(\rho) + E_{ext}(\rho, \mathbf{R}) + E_{zz}(\mathbf{R}) = & J(\rho, \rho_{nu}) \\ & + \sum_J \int (V_{ps}^J(|\mathbf{x} - \mathbf{R}_J|) - \bar{V}_{\tilde{\delta}}^J(|\mathbf{x} - \mathbf{R}_J|))\rho(\mathbf{x}) d\mathbf{x} \\ & - E_{self} \, . \end{aligned} \tag{2.20}$$

For the sake of convenience of representation, we will denote by $\mathcal{V} = \{V^1, V^2, \ldots, V^M\}$ the vector containing the electrostatic potentials corresponding to all nuclear charges in the simulation domain. Using the local reformulation of $J(\rho, \rho_{nu})$ and E_{self} (cf. equations (2.15) and (2.19)), the electrostatic interaction energy in DFT can now be expressed as the following local variational problem:

$$E_H + E_{ext} + E_{zz} = \max_{\phi \in \mathcal{Y}} \min_{V^I \in H^1(\mathbb{R}^3)} \mathcal{L}_{el}(\phi, \mathcal{V}, \rho, \mathbf{R}) \tag{2.21a}$$

$$\begin{aligned} \mathcal{L}_{el}(\phi, \mathcal{V}, \rho, \mathbf{R}) = & -\frac{1}{8\pi} \int |\nabla \phi(\mathbf{x})|^2 d\mathbf{x} + \int (\rho(\mathbf{x}) + \rho_{nu}(\mathbf{x}))\phi(\mathbf{x}) d\mathbf{x} \\ & + \sum_J \int (V_{ps}^J(|\mathbf{x} - \mathbf{R}_J|) - \bar{V}_{\tilde{\delta}}^J(|\mathbf{x} - \mathbf{R}_J|))\rho(\mathbf{x}) d\mathbf{x} \\ & + \sum_I \left\{ \frac{1}{8\pi} \int |\nabla V^I(\mathbf{x})|^2 d\mathbf{x} + \int Z_I \tilde{\delta}(|\mathbf{x} - \mathbf{R}_I|) V^I(\mathbf{x}) d\mathbf{x} \right\} . \end{aligned} \tag{2.21b}$$

In the above, the minimization over V^I represents a simultaneous minimization over all electrostatic potentials corresponding to $I = 1, 2, \ldots, M$. We note that, while the above reformulation of electrostatic interactions has been developed for pseudopotential calculations, this can also be extended to all-electron calculations in a straightforward manner by using $V_{ps}^J = \bar{V}_{\tilde{\delta}}^J$ and Z_I to be the total nuclear charge in the above expressions. Thus, this local reformulation provides a unified framework for both pseudopotential as well as all-electron DFT calculations.

We now consider the local reformulation of the extended interactions in the kernel energy component of the WGC orbital-free kinetic energy functional (cf. (2.9)). Here we adopt the recently developed local real-space reformulation of the kernel energy [54, 88], and recall the key ideas and local reformulation for the sake of completeness. We present the local reformulation of K_0 and the local reformulations for other kernels (K_1, K_{11}, K_{12}) follows along similar lines. Consider the kernel energy corresponding to K_0 given by

$$T_{K_0}(\rho) = C_F \int\int \rho^{\alpha}(\mathbf{x})\, K_0(|\mathbf{x}-\mathbf{x}'|)\, \rho^{\beta}(\mathbf{x}')\, d\mathbf{x}\, d\mathbf{x}' \,. \tag{2.22}$$

We define potentials v^0_α and v^0_β given by

$$\begin{aligned} v^0_\alpha(\mathbf{x}) &= \int K_0(|\mathbf{x}-\mathbf{x}'|)\rho^{\alpha}(\mathbf{x}')d\mathbf{x}' \,, \\ v^0_\beta(\mathbf{x}) &= \int K_0(|\mathbf{x}-\mathbf{x}'|)\rho^{\beta}(\mathbf{x}')d\mathbf{x}' \,. \end{aligned} \tag{2.23}$$

Taking the Fourier transform of the above expressions we obtain

$$\begin{aligned} \widehat{v^0_\alpha}(\mathbf{k}) &= \widehat{K_0}(|\mathbf{k}|)\widehat{\rho^{\alpha}}(\mathbf{k}) \,, \\ \widehat{v^0_\beta}(\mathbf{k}) &= \widehat{K_0}(|\mathbf{k}|)\widehat{\rho^{\beta}}(\mathbf{k}) \,. \end{aligned} \tag{2.24}$$

Following the ideas developed by Choly & Kaxiras [98], $\widehat{K_0}$ can be approximated to very good accuracy by using a sum of partial fractions of the following form

$$\widehat{K_0}(|\mathbf{k}|) \approx \sum_{j=1}^{m} \frac{A_j|\mathbf{k}|^2}{|\mathbf{k}|^2 + B_j}, \tag{2.25}$$

where A_j, B_j, $j = 1 \ldots m$ are constants, possibly complex, that are determined using a best fit approximation. Using this approximation and taking the inverse Fourier transform of equation (2.24), the potentials in equation (2.23) reduce to

$$\begin{aligned} v^0_\alpha(\mathbf{x}) &= \sum_{j=1}^m \left[\omega^0_{\alpha_j}(\mathbf{x}) + A_j \rho^\alpha(\mathbf{x})\right], \\ v^0_\beta(\mathbf{x}) &= \sum_{j=1}^m \left[\omega^0_{\beta_j}(\mathbf{x}) + A_j \rho^\beta(\mathbf{x})\right]. \end{aligned} \tag{2.26}$$

where $\omega^0_{\alpha_j}(\mathbf{x})$ and $\omega^0_{\beta_j}(\mathbf{x})$ for $j = 1 \dots m$ are given by the following Helmholtz equations:

$$\begin{aligned} -\nabla^2 \omega^0_{\alpha_j} + B_j \omega^0_{\alpha_j} + A_j B_j \rho^\alpha = 0\,, \\ -\nabla^2 \omega^0_{\beta_j} + B_j \omega^0_{\beta_j} + A_j B_j \rho^\beta = 0\,. \end{aligned} \tag{2.27}$$

We refer to these auxiliary potentials, $\omega^0_\alpha = \{\omega^0_{\alpha_1} \dots \omega^0_{\alpha_m}\}$ and $\omega^0_\beta = \{\omega^0_{\beta_1} \dots \omega^0_{\beta_m}\}$ introduced in the local reformulation of the kernel energy as *kernel potentials*. Expressing the Helmholtz equations in a variational form, we reformulate T_{K_0} in (2.22) as the following local variational problem in kernel potentials:

$$T_{K_0}(\rho) = \min_{\omega^0_{\alpha_j} \in \mathcal{Y}} \max_{\omega^0_{\beta_j} \in \mathcal{Y}} \mathcal{L}_{K_0}(\omega^0_\alpha, \omega^0_\beta, \rho)\,, \tag{2.28a}$$

$$\begin{aligned} \mathcal{L}_{K_0}(\omega^0_\alpha, \omega^0_\beta, \rho) = \sum_{j=1}^m C_F \Big\{ \int \big[&\frac{1}{A_j B_j} \nabla \omega^0_{\alpha_j}(\mathbf{x}) \cdot \nabla \omega^0_{\beta_j}(\mathbf{x}) \\ &+ \frac{1}{A_j} \omega^0_{\alpha_j}(\mathbf{x}) \omega^0_{\beta_j}(\mathbf{x}) + \omega^0_{\beta_j}(\mathbf{x}) \rho^\alpha(\mathbf{x}) + \omega^0_{\alpha_j}(\mathbf{x}) \rho^\beta(\mathbf{x}) \\ &+ A_j \rho^{(\alpha+\beta)}(\mathbf{x}) \big] d\mathbf{x} \Big\}. \end{aligned} \tag{2.28b}$$

The variational problem in equation (2.28) represents a simultaneous saddle point problem on kernel potentials $\omega^0_{\alpha_j}$ and $\omega^0_{\beta_j}$ for $j = 1, \dots, m$. Following a similar procedure, we construct the local variational reformulations for the kernel energies T_{K_1}, $T_{K_{11}}$ and $T_{K_{12}}$ corresponding to kernels K_1, K_{11} and K_{12}, respectively. We denote by $\mathcal{L}_{K_1}(\omega^1_\alpha, \omega^1_\beta, \rho)$, $\mathcal{L}_{K_{11}}(\omega^{11}_\alpha, \omega^{11}_\beta, \rho)$ and $\mathcal{L}_{K_{12}}(\omega^{12}_\alpha, \omega^{12}_\beta, \rho)$ the Lagrangians with respective kernel potentials corresponding to kernel energies of K_1, K_{11} and K_{12}, respectively. We refer to the supplemental material for the numerical details of the approximations for each of the kernels used in the present work.

Finally, using the local variational reformulations of the extended electrostatic and kernel energies, the problem of computing the ground-state energy for a given positions of atoms is given by the following local variational problem in electron-density, electrostatic potentials, and kernel potentials:

$$\begin{aligned} E_0(\mathbf{R}) = \min_{\sqrt{\rho}\in\mathcal{X}} \max_{\phi\in\mathcal{Y}} \min_{\omega^s_{\alpha_j}\in\mathcal{Y}} \max_{\omega^s_{\beta_j}\in\mathcal{Y}} \Big\{ & C_F \int \rho(\mathbf{x})^{5/3}\, d\mathbf{x} \\ & + \frac{1}{2}\int |\nabla\sqrt{\rho(\mathbf{x})}|^2\, d\mathbf{x} + \int \varepsilon_{\text{xc}}(\rho)\rho(\mathbf{x})\, d\mathbf{x} \\ & + \sum_s \mathcal{L}_{K_s}(\omega^s_\alpha, \omega^s_\beta, \rho) + \min_{V^I\in H^1(\mathbb{R}^3)} \mathcal{L}_{el}(\phi, \mathcal{V}, \rho, \mathbf{R}) \Big\} . \end{aligned} \tag{2.29}$$

In the above, s denotes the index corresponding to a kernel, and $\mathcal{X}$ and $\mathcal{Y}$ are suitable function spaces corresponding to the boundary conditions of the problem. In particular, for periodic problems, $\mathcal{Y} = H^1_{per}(Q)$ and $\mathcal{X} = \{\sqrt{\rho} | \sqrt{\rho} \in H^1_{per}(Q), \int \rho = N\}$. It is convenient to use the substitution $u(\mathbf{x}) = \sqrt{\rho(\mathbf{x})}$, and enforce the integral constraint in $\mathcal{X}$ using a Lagrange multiplier. Also, for the sake of notational simplicity, we will denote by ω_α and ω_β the array of kernel potentials $\{\omega^0_\alpha, \omega^1_\alpha, \omega^{11}_\alpha, \omega^{12}_\alpha\}$ and $\{\omega^0_\beta, \omega^1_\beta, \omega^{11}_\beta, \omega^{12}_\beta\}$, respectively. Subsequently, the variational problem in equation (2.29) can be expressed as

$$
\begin{aligned}
E_0(\mathbf{R}) = \min_{u\in\mathcal{Y}} \max_{\phi\in\mathcal{Y}} \min_{\omega^s_{\alpha_j}\in\mathcal{Y}} \max_{\omega^s_{\beta_j}\in\mathcal{Y}} \ \mathcal{L}(u,\phi,\omega_\alpha,\omega_\beta;\mathbf{R}) \qquad & \text{subject to :} \int u^2(\mathbf{x})\,d\mathbf{x} = N \qquad (2.30)\\
\mathcal{L}(u,\phi,\omega_\alpha,\omega_\beta;\mathbf{R}) = \tilde{\mathcal{L}}(u) + \mathcal{L}_K(\omega_\alpha,\omega_\beta,u^2) + \mathcal{L}_c(u,\lambda) + & \min_{V^I\in H^1(\mathbb{R}^3)} \mathcal{L}_{el}(\phi,\mathcal{V},u^2,\mathbf{R})\,,\\
\tilde{\mathcal{L}}(u) = C_F \int u^{10/3}(\mathbf{x})\,d\mathbf{x} + \frac{1}{2}\int |\nabla u(\mathbf{x})|^2\,d\mathbf{x} + & \int \varepsilon_{\text{xc}}(u^2)u^2(\mathbf{x})\,d\mathbf{x}\,,\\
\mathcal{L}_K(\omega_\alpha,\omega_\beta,u^2) = & \sum_s \mathcal{L}_{K_s}(\omega^s_\alpha,\omega^s_\beta,u^2)\,,\\
\mathcal{L}_c(u,\lambda) = & \lambda\left(\int u^2(\mathbf{x})\,d\mathbf{x} - N\right)\,.
\end{aligned}
$$

2.3.2 Configurational forces

We now turn our attention to the configurational forces corresponding to geometry optimization. To this end, we employ the approach of inner variations, where we evaluate the generalized forces corresponding to perturbations of underlying space, which provides a unified expression for the generalized force corresponding to the geometry of the simulation cell—internal atomic positions, as well as, the external cell domain. We consider infinitesimal perturbations of the underlying space $\psi_\epsilon : \mathbb{R}^3 \to \mathbb{R}^3$ corresponding to a generator $\Gamma(\mathbf{x})$ given by $\Gamma = \frac{d\psi_\epsilon(\mathbf{x})}{d\epsilon}|_{\epsilon=0}$ such that $\psi_0 = I$. We constrain the generator Γ such that it only admits rigid body deformations in the compact support of the regularized nuclear charge distribution ρ_{nu} in order to preserve the integral constraint $\int \tilde{\delta}(\mathbf{x}-\mathbf{R}_I)d\mathbf{x} = 1$. Let $\mathbf{x}$ denote a point in Q, whose image in $Q' = \psi_\epsilon(Q)$ is $\mathbf{x}' = \psi_\epsilon(\mathbf{x})$. The ground-state energy on Q' is given by

$$E_0(\psi_\epsilon) = \mathcal{L}_\epsilon(u_\epsilon,\phi_\epsilon,\omega_{\alpha\epsilon},\omega_{\beta_\epsilon};\mathbf{R}_\epsilon) \tag{2.31}$$

where u_ϵ, ϕ_ϵ, $\omega_{\alpha\epsilon}$ and ω_{β_ϵ} are solutions of the saddle point variational problem given by equation (2.30) evaluated over the function space $\mathcal{Y}' = H^1_{per}(Q')$. The subscript ϵ on $\mathcal{L}$ is used to denote that the variational problem is solved on $Q' = \psi_\epsilon(Q)$. For the sake of convenience, we will represent the integrand of the Lagrangian $\mathcal{L}$ in equation (2.30) by $f(u, \nabla u, \phi, \nabla\phi, \omega_\alpha, \nabla\omega_\alpha, \omega_\beta, \nabla\omega_\beta; V_{ps}, \bar{V}_{\tilde{\delta}}, \mathbf{R})$ and $g(\bar{V}^I_{\tilde{\delta}}, \nabla\bar{V}^I_{\tilde{\delta}}; \mathbf{R})$, where f denotes the integrand whose integrals are over Q and g denotes the integrand whose integrals are over $\mathbb{R}^3$. The ground-state energy on Q' in terms of f and g can be expressed as

$$\begin{aligned}
&E_0(\psi_\epsilon) = \int_{Q'} f(u_\epsilon(\mathbf{x}'), \nabla_{\mathbf{x}'} u_\epsilon(\mathbf{x}'), \phi_\epsilon(\mathbf{x}'), \nabla_{\mathbf{x}'}\phi_\epsilon(\mathbf{x}'), \omega_{\alpha\epsilon}(\mathbf{x}'),\\
&\nabla_{\mathbf{x}'}\omega_{\alpha\epsilon}(\mathbf{x}'), \omega_{\beta_\epsilon}(\mathbf{x}'), \nabla_{\mathbf{x}'}\omega_{\beta_\epsilon}(\mathbf{x}'); V_{ps}(\mathbf{x}'), \bar{V}_{\tilde{\delta}}(\mathbf{x}'), \psi_\epsilon(\mathbf{R}))d\mathbf{x}'\\
&+\sum_I \int_{\mathbb{R}^3} g(\bar{V}^I_{\tilde{\delta}_\epsilon}(\mathbf{x}'), \nabla_{\mathbf{x}'}\bar{V}^I_{\tilde{\delta}_\epsilon}(\mathbf{x}'); \psi_\epsilon(\mathbf{R}))d\mathbf{x}' \,.
\end{aligned} \tag{2.32}$$

Transforming the above integral to domain Q, we obtain

$$\begin{aligned}
&E_0(\psi_\epsilon) = \int_{Q} f(u_\epsilon(\psi_\epsilon(\mathbf{x})), \nabla_{\mathbf{x}} u_\epsilon(\psi_\epsilon(\mathbf{x})).\frac{\partial\mathbf{x}}{\partial\mathbf{x}'}, \phi_\epsilon(\psi_\epsilon(\mathbf{x})),\\
&\nabla_{\mathbf{x}}\phi_\epsilon(\psi_\epsilon(\mathbf{x})).\frac{\partial\mathbf{x}}{\partial\mathbf{x}'}, \omega_{\alpha\epsilon}(\psi_\epsilon(\mathbf{x})), \nabla_{\mathbf{x}}\omega_{\alpha\epsilon}(\psi_\epsilon(\mathbf{x})).\frac{\partial\mathbf{x}}{\partial\mathbf{x}'}, \omega_{\beta_\epsilon}(\psi_\epsilon(\mathbf{x})),\\
&\nabla_{\mathbf{x}}\omega_{\beta_\epsilon}(\psi_\epsilon(\mathbf{x})).\frac{\partial\mathbf{x}}{\partial\mathbf{x}'}; V_{ps}(\psi_\epsilon(\mathbf{x})), \bar{V}_{\tilde{\delta}}(\psi_\epsilon(\mathbf{x})), \psi_\epsilon(\mathbf{R}))\det(\frac{\partial\mathbf{x}'}{\partial\mathbf{x}})\,d\mathbf{x}\\
&+\sum_I \int_{\mathbb{R}^3} g(\bar{V}^I_{\tilde{\delta}_\epsilon}(\psi_\epsilon(\mathbf{x})), \nabla_{\mathbf{x}}\bar{V}^I_{\tilde{\delta}_\epsilon}(\psi_\epsilon(\mathbf{x})).\frac{\partial\mathbf{x}}{\partial\mathbf{x}'}; \psi_\epsilon(\mathbf{R}))\det(\frac{\partial\mathbf{x}'}{\partial\mathbf{x}})\,d\mathbf{x}
\end{aligned} \tag{2.33}$$

We now evaluate the configurational force given by the Gâteaux derivative of $E_0(\psi_\epsilon)$:

$$
\begin{aligned}
&\frac{dE_0(\psi_\epsilon)}{d\epsilon}\Big|_{\epsilon=0} = \int_Q f(u_0(\mathbf{x}), \nabla u_0(\mathbf{x}), \phi_0(\mathbf{x}), \nabla\phi_0(\mathbf{x}), \omega_{\alpha 0}(\mathbf{x}), \\
&\nabla\omega_{\alpha 0}(\mathbf{x}), \omega_{\beta_0}(\mathbf{x}), \nabla\omega_{\beta_0}(\mathbf{x}); V_{ps}(\mathbf{x}), \bar{V}_{\tilde{\delta}}(\mathbf{x}), \mathbf{R}) \frac{d}{d\epsilon}(\det(\frac{\partial \mathbf{x}'}{\partial \mathbf{x}}))\Big|_{\epsilon=0} d\mathbf{x} \\
&+ \int_Q \Big(\frac{\partial f}{\partial \nabla u}(\nabla u_0) \otimes \nabla u_0 + \frac{\partial f}{\partial \nabla \phi}(\nabla \phi_0) \otimes \nabla \phi_0 \\
&+ \sum_s \Big(\frac{\partial f}{\partial \nabla \omega^s_\alpha}(\nabla \omega^s_{\alpha 0}) \otimes \nabla \omega^s_{\alpha 0} + \frac{\partial f}{\partial \nabla \omega^s_\beta}(\nabla \omega^s_{\beta_0}) \otimes \nabla \omega^s_{\beta_0} \Big) \Big) : \Big(\frac{d}{d\epsilon} \frac{\partial \mathbf{x}}{\partial \mathbf{x}'}\Big|_{\epsilon=0} \Big) d\mathbf{x} \\
&+ \sum_J \int_Q u_0^2(\mathbf{x}) \left(\nabla V^J_{ps}(|\mathbf{x} - \mathbf{R}_J|) - \nabla \bar{V}^J_{\tilde{\delta}}(|\mathbf{x} - \mathbf{R}_J|) \right) . \Big(\frac{d\psi_\epsilon(\mathbf{x})}{d\epsilon}\Big|_{\epsilon=0} - \frac{d\psi_\epsilon(\mathbf{R}_J)}{d\epsilon}\Big|_{\epsilon=0} \Big) d\mathbf{x} \\
&+ \sum_I \int_{\mathbb{R}^3} g(\bar{V}^I_{\tilde{\delta}_0}(\mathbf{x}), \nabla \bar{V}^I_{\tilde{\delta}_0}(\mathbf{x}); \mathbf{R}) \frac{d}{d\epsilon}(\det(\frac{\partial \mathbf{x}'}{\partial \mathbf{x}}))\Big|_{\epsilon=0} d\mathbf{x} \\
&+ \sum_I \int_{\mathbb{R}^3} \frac{\partial g}{\partial \nabla \bar{V}^I_{\tilde{\delta}}}(\nabla \bar{V}^I_{\tilde{\delta}_0}) \otimes \nabla \bar{V}^I_{\tilde{\delta}_0} : \Big(\frac{d}{d\epsilon} \frac{\partial \mathbf{x}}{\partial \mathbf{x}'}\Big|_{\epsilon=0} \Big) d\mathbf{x}\,.
\end{aligned}
\tag{2.34}
$$

In the above, we denote by '$\otimes$' the outer product between two vector, by '.' the dot product between two vectors and by ':' the dot product between two tensors. We note that in the above expression there are no terms involving the explicit derivatives of f and g with respect to $\mathbf{R}$ as $\tilde{\delta}(|\mathbf{x}' - \psi_\epsilon(\mathbf{R})|) = \tilde{\delta}(|\mathbf{x} - \mathbf{R}|)$, which follows from the restriction that ψ_ϵ corresponds to rigid body deformations in the compact support of ρ_{nu}. We further note that terms arising from the inner variations of $E_0(\psi_\epsilon)$ with respect to u_ϵ, ϕ_ϵ, $\omega_{\alpha\epsilon}$, ω_{β_ϵ} and $\bar{V}^I_{\tilde{\delta}_\epsilon}$ vanish as u_0 ϕ_0, $\omega_{\alpha 0}$, ω_{β_0} and $\bar{V}^I_{\tilde{\delta}_0}$ are the solutions of the saddle point variational problem corresponding to $E_0(\psi_0)$. We now note the following identities

$$
\begin{aligned}
\frac{d}{d\epsilon}\left\{ \frac{\partial x_i}{\partial x'_j} \right\}\Big|_{\epsilon=0} &= - \frac{\partial x_i}{\partial x'_k} \Big(\frac{d}{d\epsilon} \left\{ \frac{\partial \psi_{\epsilon k}}{\partial x_l} \right\} \Big) \frac{\partial x_l}{\partial x'_j}\Big|_{\epsilon=0} \\
&= - \frac{\partial \Gamma_i}{\partial x_j}\,,
\end{aligned}
\tag{2.35}
$$

$$\begin{aligned}\frac{d}{d\epsilon}\left\{\det\big(\frac{\partial x'_l}{\partial x_m}\big)\right\}\Big|_{\epsilon=0} &= \det\big(\frac{\partial x'_l}{\partial x_m}\big)\frac{\partial x_j}{\partial x'_i}\Big(\frac{d}{d\epsilon}\left\{\frac{\partial \psi_{\epsilon i}}{\partial x_j}\right\}\Big)\Big|_{\epsilon=0} \\ &= \frac{\partial \Gamma_j}{\partial x_j}.\end{aligned} \tag{2.36}$$

Using these identities in equation (2.34), and rearranging terms, we arrive at

$$\begin{aligned}\frac{dE_0(\psi_\epsilon)}{d\epsilon}\Big|_{\epsilon=0} = &\int_Q \mathbf{E} : \nabla\Gamma(\mathbf{x})\,d\mathbf{x} + \sum_I \int_{\mathbb{R}^3} \mathbf{E}'_I : \nabla\Gamma(\mathbf{x})\,d\mathbf{x} \\ &+ \sum_J \int_Q u_0^2(\mathbf{x})\left(\nabla\left(V^J_{ps} - \bar{V}^J_{\tilde{\delta}}\right)\right).\left(\Gamma(\mathbf{x}) - \Gamma(\mathbf{R}_J)\right)d\mathbf{x}\end{aligned} \tag{2.37}$$

where $\mathbf{E}$ and $\mathbf{E}'$ denote Eshelby tensors corresponding to f and g, respectively. The expressions for the Eshelby tensors $\mathbf{E}$ and $\mathbf{E}'_I$ explicitly in terms of u, ϕ, ω_α, ω_β, V_{ps} and $\bar{V}_{\tilde{\delta}}$ are given by

$$\begin{aligned}\mathbf{E} = &\Bigg(C_F u^{10/3} + \frac{1}{2}|\nabla u|^2 + \varepsilon_{xc}(u^2)u^2 + \lambda u^2 - \frac{1}{8\pi}|\nabla\phi|^2 + u^2\phi \\ &+ \sum_J \left(V^J_{ps} - \bar{V}^J_{\tilde{\delta}}\right)u^2 + \sum_s f_{K_s}(\omega^s_\alpha, \nabla\omega^s_\alpha, \omega^s_\beta, \nabla\omega^s_\beta, u^2)\Bigg)\mathbf{I} \\ &- \nabla u \otimes \nabla u + \frac{1}{4\pi}\nabla\phi\otimes\nabla\phi - \sum_s\left(\frac{\partial f_{K_s}}{\partial\nabla\omega^s_\alpha}\otimes\nabla\omega^s_\alpha + \frac{\partial f_{K_s}}{\partial\nabla\omega^s_\beta}\otimes\nabla\omega^s_\beta\right)\end{aligned} \tag{2.38}$$

$$\mathbf{E}'_I = \frac{1}{8\pi}|\nabla\bar{V}^I_{\tilde{\delta}}|^2\mathbf{I} - \frac{1}{4\pi}\nabla\bar{V}^I_{\tilde{\delta}}\otimes\nabla\bar{V}^I_{\tilde{\delta}} \tag{2.39}$$

In the above, for the sake of brevity, we represented by f_{K_s} the integrand corresponding to $\mathcal{L}_{K_s}$. We also note that the terms $\phi\rho_{nu}$ and $V^I_{\tilde{\delta}}\tilde{\delta}(\mathbf{x} - \mathbf{R}_I)$ do not appear in the expressions for $\mathbf{E}$ and $\mathbf{E}'_I$, respectively, as $\nabla.\Gamma = 0$ on the compact support of ρ_{nu} owing to the restriction that Γ corresponds to rigid body deformations in these regions. It may appear that evaluation of the second term in equation (2.37) is not tractable as it involves an integral over $\mathbb{R}^3$. To this end, we split this integral on a bounded domain Ω containing the compact support of $\tilde{\delta}(\mathbf{x}-\mathbf{R}_I)$, and its complement.

The integral on $\mathbb{R}^3/\Omega$ can be computed as a surface integral. Thus,

$$\begin{aligned}\int_{\mathbb{R}^3} \mathbf{E}_I^{'} : \nabla\Gamma \, d\mathbf{x} &= \int_{\Omega} \mathbf{E}_I^{'} : \nabla\Gamma \, d\mathbf{x} + \int_{\mathbb{R}^3/\Omega} \mathbf{E}_I^{'} : \nabla\Gamma \, d\mathbf{x} \\ &= \int_{\Omega} \mathbf{E}_I^{'} : \nabla\Gamma \, d\mathbf{x} - \int_{\partial\Omega} \mathbf{E}_I^{'} : \hat{\mathbf{n}} \otimes \Gamma \, d\mathbf{s} \,, \end{aligned} \tag{2.40}$$

where $\hat{\mathbf{n}}$ denotes the outward normal to the surface $\partial\Omega$. The last equality follows from the fact that $\nabla^2 \bar{V}_{\tilde{\delta}}^I = 0$ on $\mathbb{R}^3/\Omega$.

The configurational force in equation (2.37) provides the generalized variational force with respect to both the internal positions of atoms as well as the external cell domain. In order to compute the force on any given atom, we restrict the compact support of Γ to only include the atom of interest. In order to compute the stresses associated with cell relaxation (keeping the fractional coordinates of atoms fixed), we restrict Γ to affine deformations. Thus, this provides a unified expression for geometry optimization corresponding to both internal ionic relaxations as well as cell relaxation. We further note that, while we derived the configurational force for the case of pseudopotential calculations, the derived expression is equally applicable for all-electron calculations by using $V_{ps}^J = \bar{V}_{\tilde{\delta}}^J$.

2.3.3 Finite-element discretization

Among numerical discretization techniques, the plane-wave discretization has been the most popular and widely used in orbital-free DFT [1, 86] as it naturally lends itself to the evaluation of the extended interactions in electrostatic energy and kernel kinetic energy functionals using Fourier transforms. Further, the plane wave basis offers systematic convergence with exponential convergence in the number of basis functions. However, as noted previously, the plane-wave basis also suffers from notable drawbacks. Importantly, plane-wave discretization is restricted to periodic geometries and boundary conditions which introduces a significant limitation, especially in the study of defects in bulk materials [56]. Further, the plane-wave basis has a uniform spatial resolution, and thus is not amenable to adaptive coarse-graining. Moreover, the use of plane-wave discretization involves the numerical evaluation of Fourier transforms whose scalability is limited on parallel computing platforms.

In order to circumvent these limitations of the plane-wave basis, there is an increasing focus on developing real-space discretization techniques for orbital-free DFT based on finite-difference discretization [89–91] and finite-element discretization [53, 88]. In particular, the finite-element basis [100], which is a piecewise continuous polynomial basis, has many features of a desirable basis in electronic structure calculations. While being a complete basis, the finite-element basis naturally allows for the consideration of complex geometries and boundary conditions, is amenable to unstructured coarse-graining, and exhibits good scalability on massively parallel computing platforms. Moreover, the adaptive nature of the finite-element discretization also enables the consideration of all-electron orbital-free DFT calculations that are widely used in studies of warm dense matter [79, 80, 82]. Further, recent numerical studies have shown that by using a higher-order finite-element discretization significant computational savings can be realized for both orbital-free DFT [88] and Kohn-Sham DFT calculations [61, 70], effectively overcoming the degree of freedom disadvantage of the finite-element basis in comparison to the plane-wave basis.

Let $\mathcal{Y}_h$ denote the finite-element subspace of $\mathcal{Y}$, where h represents the finite-element mesh size. The discrete problem of computing the ground-state energy for a given positions of atoms, corresponding to equation (2.30), is given by the constrained variational problem:

$$\begin{aligned} E_0(\mathbf{R}) = \quad & \min_{u_h \in \mathcal{Y}_h} \max_{\phi_h \in \mathcal{Y}_h} \min_{{\omega^s_{\alpha_j}}_h \in \mathcal{Y}_h} \max_{{\omega^s_{\beta_j}}_h \in \mathcal{Y}_h} \mathcal{L}(u_h, \phi_h, \omega_{\alpha_h}, \omega_{\beta_h}; \mathbf{R}) \\ & \text{subject to} : \int u_h^2(\mathbf{x})\, d\mathbf{x} = N \,. \end{aligned} \tag{2.41}$$

In the above, u_h, ϕ_h, $\omega_{\alpha h}$ and ω_{β_h} denote the finite-element discretized fields corresponding to square-root electron-density, electrostatic potential, and kernel potentials, respectively. We restrict our finite-element discretization such that atoms are located on the nodes of the finite-element mesh. In order to compute the finite-element discretized solution of $\bar{V}^J_{\tilde{\delta}}$, we represent $\tilde{\delta}(\mathbf{x} - \mathbf{R}_J)$ as a point charge on the finite-element node located at $\mathbf{R}_J$, and the finite-element discretization provides a regularization for $\bar{V}^J_{\tilde{\delta}}$. Previous investigations have suggested that such an approach provides optimal rates of convergence of the ground-state energy (cf. [61, 88] for a discussion).

The finite-element basis functions also provide the generator of the deformations of the underlying space in the isoparametric formulation, where the same finite-element shape functions are used to discretize both the spatial domain as well as the fields prescribed over the domain. Thus, the configurational force associated with the location of any node in the finite-element mesh can be computed by substituting for Γ, in equation (2.37), the finite-element shape function associated with the node. Thus, the configurational force on any finite-element node located at an atom location corresponds to the variational ionic force, which are used to drive the internal atomic relaxation. The forces on the finite-element nodes that do not correspond to an atom location represent the generalized force of the energy with respect to the location of the finite-element nodes, and these can be used to obtain the optimal location of the finite-element nodes—a basis adaptation technique.

We note that the local real-space variational formulation in section 2.3.1, where the extended interactions in the electrostatic energy and kernel functionals are reformulated as local variational problems, is essential for the finite-element discretization of the formulation.

2.4 Numerical Implementation

In this section, we present the details of the numerical implementation of the finite-element discretization of the real-space formulation of orbital-free DFT discussed in section 2.3. Subsequently, we discuss the solution procedure for the resulting discrete coupled equations in square-root electron-density, electrostatic potential and kernel potentials.

2.4.1 Finite-element basis

A finite-element discretization using linear tetrahedral finite-elements has been the most widely used discretization technique for a wide range of partial differential equations. Linear tetrahedral elements are well suited for problems involving complex geometries and moderate levels of accuracy. However in electronic structure calculations, where the desired accuracy is commensurate with chemical accuracy, linear finite elements are computationally inefficient requiring of the order of hundred thousand basis functions per atom to achieve chemical accuracy. A recent study [88] has demonstrated the significant computational savings—of the order of 1000-fold compared to linear finite-elements—that can be realized by using higher-order finite-element discretizations. Thus, in the present work we use higher-order hexahedral finite elements, where the basis functions are constructed as a tensor product of basis functions in one-dimension [100].

2.4.2 Solution procedure

The discrete variational problem in equation (2.41) involves the computation of the following fields—square-root electron-density, electrostatic potential and kernel potentials. Two solution procedures, suggested in prior efforts [88], for solving this discrete variational problem include: (i) a simultaneous solution of all the discrete fields in the problem; (ii) a nested solution procedure, where for every trial square-root electron-density the discrete electrostatic and kernel potential fields are computed. Given the non-linear nature of the problem, the simultaneous approach is very sensitive to the starting guess and often suffers from lack of robust convergence, especially for large-scale problems. The nested solution approach, on the other hand, while constituting a robust solution procedure, is computationally inefficient due to the huge computational costs incurred in computing the kernel potentials which involves the solution of a series of Helmholtz equations (cf. equation (2.27)). Thus, in the present work, we will recast the local variational problem in equation (2.41) as the following fixed point iteration problem:

$$\begin{aligned} \{\bar{u}_h, \bar{\phi}_h\} = \quad & arg \min_{u_h} arg \max_{\phi_h} \mathcal{L}(u_h, \phi_h, \bar{\omega}_{\alpha_h}, \bar{\omega}_{\beta_h}; \mathbf{R}) \\ & \text{subject to} : \int u_h^2(\mathbf{x})\, d\mathbf{x} = N. \end{aligned} \tag{2.42a}$$

$$\{\bar{\omega}_{\alpha_h}, \bar{\omega}_{\beta_h}\} = arg \min_{\omega_{\alpha_h}} arg \max_{\omega_{\beta_h}} \mathcal{L}(\bar{u}_h, \bar{\phi}_h, \omega_{\alpha_h}, \omega_{\beta_h}; \mathbf{R})\,. \tag{2.42b}$$

We solve this fixed point iteration problem using a mixing scheme, and, in particular, we employ the Anderson mixing scheme [101] with full history in this work. Our numerical investigations suggest that the fixed point iteration converges, typically, in less than ten self-consistent iterations even for large-scale problems, thus, providing a numerically efficient and robust solution procedure for the solution of the local variational orbital-free DFT problem. We note that this idea of fixed point iteration has independently and simultaneously been investigated by another group in the context of finite difference discretization [91], and have resulted in similar findings.

In the fixed point iteration problem, we employ a simultaneous solution procedure to solve the non-linear saddle point variational problem in u_h and ϕ_h (equation (2.42a)). We employ an inexact Newton solver provided by the PETSc package [102] with field split preconditioning and generalized-minimal residual method (GMRES) [103] as the linear solver. The discrete Helmholtz equations in equation (2.42b) are solved by employing block Jacobi preconditioning and using GMRES as the linear solver. An efficient and scalable parallel implementation of the solution procedure has been developed to take advantage of the parallel computing resources for conducting the large-scale simulations reported in this work.

2.5 Results and Discussion

In this section, we discuss the numerical studies on Al, Mg and Al-Mg intermetallics to investigate the accuracy and transferability of the real-space formulation of orbital-free DFT (RS-OFDFT) proposed in section 2.3. Wherever applicable, we benchmark the real-space orbital-free DFT calculations with plane-wave based orbital-free DFT calculations conducted using PROFESS [1], and compare with Kohn-Sham DFT (KS-DFT) calculations conducted using the plane-wave based ABINIT code [104]. Further, we demonstrate the usefulness of the proposed real-space formulation in studying the electronic structure of isolated defects.

2.5.1 General calculation details

In all the real-space orbital-free DFT calculations reported in this section, we use the local reformulation of the density-dependent WGC [2] kinetic energy functional proposed in section 2.3.1, the local density approximation (LDA) [3] for the exchange-correlation energy, and bulk derived local pseudopotentials (BLPS) [94] for Al and Mg. Cell stresses and ionic forces are calculated using the unified variational formulation of configurational forces developed in section 2.3.2. In the second order Taylor expansion of the density-dependent WGC functional about the bulk electron density (cf. Section 2.2), we only retain the K_{12} term for the computation of bulk properties as the contributions from K_{12} dominate those of K_{11} for bulk materials systems. However, in the calculations involving mono-vacancies, where significant

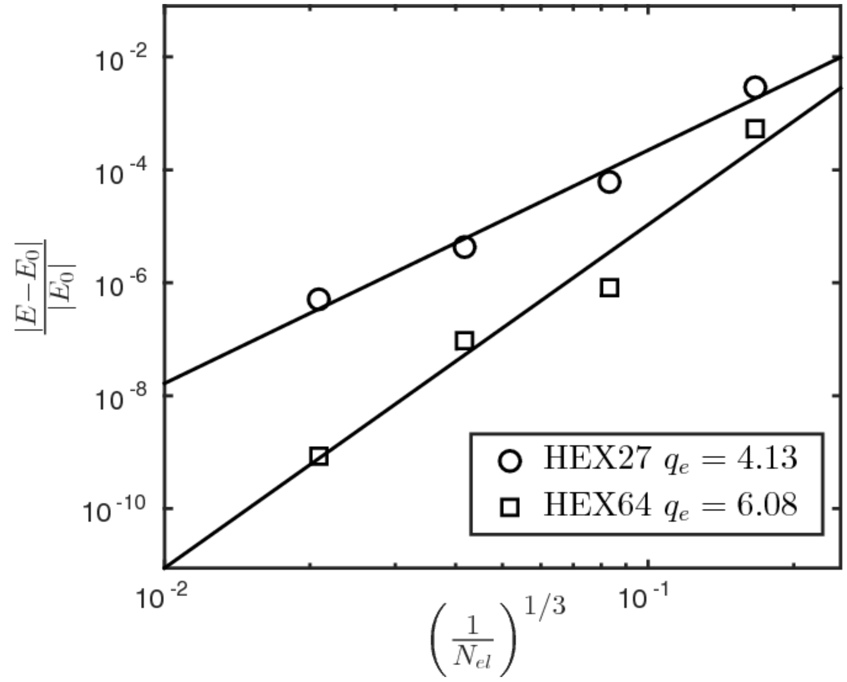

Figure 2.1: Convergence of the finite-element approximation in the energy of a fcc Al unit cell with lattice constant $a = 7.2$ Bohr.

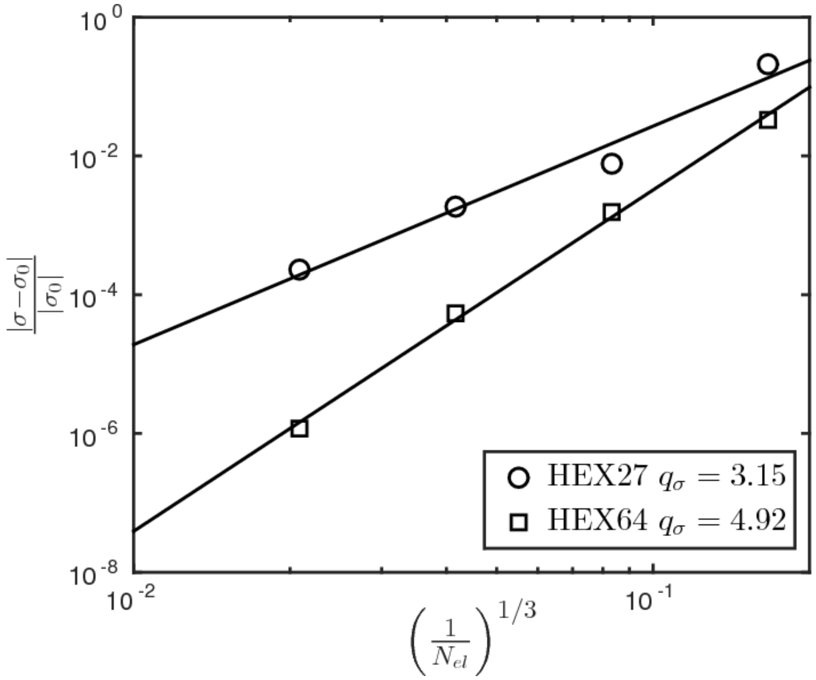

Figure 2.2: Convergence of the finite-element approximation in the hydrostatic stress of a fcc Al unit cell with lattice constant $a = 7.2$ Bohr.

spatial perturbations in the electronic structure are present, we use the full second order Taylor expansion of the density dependent WGC functional. We recall from section 2.3.1 that in order to obtain a local real-space reformulation of the extended interactions in the kinetic energy functionals, the kernels (K_0, K_1, K_{11}, K_{12}) are approximated using a sum of m partial fractions where the coefficients of the partial fractions are computed using a best fit approximation (cf. equation (2.25)). These best fit approximations for $m = 4, 5, 6$ that are employed in the present work are given in the supplemental material. It has been shown in recent studies that $m = 4$ suffices for Al [54, 91]. However, we find that $m = 6$ is required to obtain the desired accuracy in the bulk properties of Mg, and Table 2.2 shows the comparison between the kernel approximation with $m = 6$ and plane-wave based orbital-free DFT calculations conducted using PROFESS [1] for Mg. Thus, we use the best fit approximation of the kernels with $m = 4$ for Al, and employ the approximation with $m = 6$ for Mg and Al-Mg intermetallics. Henceforth, we will refer by RS-OFDFT-FE the real-space orbital-DFT calculations conducted by employing the local formulation and finite element discretization proposed in section 2.3.

The KS-DFT calculations used to assess the accuracy and transferability of the proposed real-space orbital-free DFT formalism are performed using the LDA exchange correlation functional [3]. The KS-DFT calculations are conducted using both local BLPS as well as the non-local Troullier-Martins pseudopotential (TM-NLPS) [105] in order to assess the accuracy and transferability of both the model kinetic energy functionals in orbital-free DFT as well as the local pseudopotentials to which the orbital-free DFT formalism is restricted to. The TM-NLPS for Al and Mg are generated using the fhi98PP code [106]. Within the fhi98PP code, we use the following inputs: $3d$ angular momentum channel as the local pseudopotential component for both Al and Mg, default core cutoff radii for the $3s$, $3p$, and $3d$ angular momentum channels, which are {1.790, 1.974, 2.124} Bohr and {2.087, 2.476, 2.476} Bohr for Al and Mg respectively, and the LDA [3] exchange-correlation. For brevity, henceforth, we refer to the KS-DFT calculations with BLPS and TM-NLPS as KS-BLPS and KS-NLPS, respectively.

In all the RS-OFDFT-FE calculations reported in this work, the finite-element discretization, order of the finite-elements, numerical quadrature rules and stopping tolerances are chosen such that we obtain 1 meV/ atom accuracy in energies, 1×10^{-7} Hartree Bohr^{-3} accuracy in cell stresses and 1×10^{-5} Hartree Bohr^{-1} accuracy in ionic forces. Similar accuracies in energies, stresses and ionic forces are achieved for KS-DFT calculations by choosing the appropriate k-point mesh, plane-wave energy cutoff, and stopping tolerances within ABINIT's framework. All calculations involving geometry optimization are conducted until cell stresses and ionic forces are below threshold values of 5×10^{-7} Hartree Bohr^{-3} and 5×10^{-5} Hartree Bohr^{-1}, respectively.

2.5.2 Convergence of finite-element discretization

We now study the convergence of energy and stresses with respect to the finite-element discretization of the proposed real-space orbital-free DFT formulation. In a prior study on the computational efficiency afforded by higher-order finite-element discretization in orbital-free DFT [88], it was shown that second and third-order finite-elements offer an optimal choice between accuracy and computational efficiency. Thus, in the present study, we limit our convergence studies to HEX27 and HEX64 finite-elements, which correspond to second- and third-order finite-elements. As a benchmark system, we consider a stressed fcc Al unit cell with a lattice constant $a = 7.2$ Bohr. We first construct a coarse finite-element mesh and subsequently perform a uniform subdivision to obtain a sequence of increasingly refined meshes. We denote by h the measure of the size of the finite-element. For these sequence of meshes, we hold the cell geometry fixed and compute the discrete ground-state energy, E_h, and hydrostatic stress, σ_h. The extrapolation procedure proposed in Motamarri et. al [88] allows us to estimate the ground-state energy and hydrostatic stress in the limit as $h \to 0$, denoted by E_0 and σ_0. To this end, the energy and hydrostatic stress computed from the sequence of meshes using HEX64 finite-elements are fitted to expressions of the form

$$\begin{aligned} |E_0 - E_h| &= C_e \left(\frac{1}{N_{el}}\right)^{\frac{q_e}{3}} , \\ |\sigma_0 - \sigma_h| &= C_\sigma \left(\frac{1}{N_{el}}\right)^{\frac{q_\sigma}{3}} , \end{aligned} \tag{2.43}$$

to determine E_0, q_e, $\sigma_0, \& \, q_\sigma$. In the above expression, N_{el} denotes the number of elements in a finite-element mesh. We subsequently use E_0 and σ_0 as the exact values of the ground-state energy and hydrostatic stress, respectively, for the benchmark system. Figures 2.1 and 2.2 show the relative errors in energy and hydrostatic stress plotted against $\left(\frac{1}{N_{el}}\right)^{\frac{1}{3}}$, which represents a measure of h. We note that the slopes of these curves provide the rates of convergence of the finite-element approximation for energy and stresses. These results show that we obtain close to optimal rates of convergence in energy of $\mathcal{O}(h^{2k})$, where k is polynomial interpolation order ($k = 2$ for HEX27 and $k = 3$ for HEX64). Further, we obtain close to $\mathcal{O}(h^{2k-1})$ convergence in the stresses, which represents optimal convergence for stresses. The results also suggest that higher accuracies in energy and stress are obtained with HEX64 in comparison to HEX27. Thus, we will employ HEX64 finite-elements for the remainder of our study.

2.5.3 Bulk properties of Al, Mg and Al-Mg intermetallics

We now study the accuracy and transferability of the proposed real-space formulation of orbital-free DFT for bulk properties of Al, Mg and Al-Mg intermetallics. To this end, we begin with the phase stability study of Al and Mg, where we compute the difference in the ground-state energy of a stable phase and the ground-state energy

Table 2.1: The energy difference in eV between a stable phase and the most stable phase for Al and Mg computed using RS-OFDFT-FE and KS-DFT with TM-NLPS.

Al	fcc	hcp	bcc	sc	dia
RS-OFDFT-FE	0^1	0.016	0.075	0.339	0.843
KS-NLPS	0	0.038	0.106	0.400	0.819
Mg	**hcp**	**fcc**	**bcc**	**sc**	**dia**
RS-OFDFT-FE	0	0.003	0.019	0.343	0.847
KS-NLPS	0	0.014	0.030	0.400	0.822

Table 2.2: Bulk properties of Al and Mg: Equilibrium ground-state energy per atom ($E_{\min}$ in eV), volume per atom (V_0 in $\mathring{A}^3$) and bulk modulus (B_0 in GPa) computed using RS-OFDFT-FE, PROFESS, and KS-DFT with BLPS and TM-NLPS.

Al[1]	RS-OFDFT-FE	PROFESS	KS-BLPS	KS-NLPS
$E_{\min}$	-57.935	-57.936	-57.954	-57.207
V_0	15.68	15.68	15.62	15.55
B_0	81.7	81.5	84.1	83.6
Mg[2]	**RS-OFDFT-FE**	**PROFESS**	**KS-BLPS**	**KS-NLPS**
$E_{\min}$	-24.647	-24.647	-24.678	-24.514
V_0	21.40	21.43	21.18	21.26
B_0	36.8	36.6	38.5	38.6

of the most stable phase. The results for Al and Mg are shown in Table 2.1, and are compared against those obtained with KS-DFT employing TM-NLPS. We note that RS-OFDFT-FE correctly predicts the most stable phases of Al and Mg being fcc and hcp, respectively. Further, the stability ordering of the various phases computed using RS-OFDFT-FE is consistent with KS-DFT TM-NLPS calculations. Moreover, the energy differences between the various stable phases and the most stable phase computed using RS-OFDFT-FE are in close agreement with KS-DFT calculations.

We next consider bulk properties of Al, Mg and Al-Mg intermetallics. To this end, for each system, we first optimize cell geometry and ionic positions to determine the equilibrium cell structure, equilibrium volume (V_0) and ground-state energy ($E_{\min}$). We subsequently compute the bulk modulus given by [97]

$$B = V \frac{\partial^2 E}{\partial V^2}\bigg|_{V=V_0} , \tag{2.44}$$

where E denotes the ground-state energy of a unit-cell with volume V. To compute the bulk modulus, we vary the cell volume by applying a volumetric deformation to the relaxed (equilibrium) unit-cell, which transforms the equilibrium cell vectors $\{\mathbf{c}_1\,, \mathbf{c}_2\,, \mathbf{c}_3\}$ to $\{\mathbf{c}'_1\,, \mathbf{c}'_2\,, \mathbf{c}'_3\}$ and are given by

$$c'_{ij} = c_{ij}\,(1+\eta)\,. \tag{2.45}$$

While keeping the cell structure fixed, we calculate the ground-state energy for each η between -0.01 to 0.01 in steps of 0.002 and fit a cubic polynomial to the $E-V$ data. We subsequently compute the bulk modulus, using equation (2.44), at the equilibrium volume, V_0. The computed bulk properties—ground-state energy, equilibrium volume and bulk modulus at equilibrium—for Al and Mg are given in Table 2.2, and those of Al-Mg intermetallics (Al_3Mg, $Mg_{13}Al_{14}$, $Mg_{17}Al_{12}$, and $Mg_{23}Al_{30}$) are given in Table 2.3. These results suggest that the bulk properties of Al, Mg and Al-Mg intermetallics computed using RS-OFDFT-FE are in good agreement with PROFESS and KS-DFT calculations.

Table 2.3: Bulk properties of Al-Mg intermetallics: Equilibrium ground-state energy per primitive cell ($E_{\min}$ in eV), volume of primitive cell (V_0 in $\mathring{A}^3$), and bulk modulus (B_0 in GPa) computed using RS-OFDFT-FE, PROFESS, and KS-DFT with BLPS and TM-NLPS.

Al_3Mg	RS-OFDFT-FE	PROFESS	KS-BLPS	KS-NLPS
$E_{\min}$	-198.492	-198.496	-198.575	-196.162
V_0	67.23	67.31	67.13	66.52
B_0	69.2	67.0	67.6	71.0
$Mg_{13}Al_{14}$	RS-OFDFT-FE	PROFESS	KS-BLPS	KS-NLPS
$E_{\min}$	-1130.083	-1130.100	-1130.972	-1117.936
V_0	494.77	494.73	498.19	492.73
B_0	53.1	52.1	54.7	54.8
$Mg_{17}Al_{12}$	RS-OFDFT-FE	PROFESS	KS-BLPS	KS-NLPS
$E_{\min}$	-1114.446	-1114.526	-1116.185	-1104.012
V_0	545.32	544.85	543.67	544.21
B_0	51.1	52.3	55.2	54.4
$Mg_{23}Al_{30}$	RS-OFDFT-FE	PROFESS	KS-BLPS	KS-NLPS
$E_{\min}$	-2306.785	-2306.762	-2307.989	-2281.082
V_0	953.87	952.55	963.72	957.46
B_0	64.2	60.9	60.5	60.5

Finally, we consider the formation energies of Al-Mg intermetallics. In addition to the Al-Mg intermetallics for which we computed the bulk properties, we also compute the formation energy of the β' alloy. The β' alloy has a disorder in 10 out of 879 sites with each site having 0.5 chance of being occupied by either Al or Mg. In our simulations, we consider the two limits where all 10 sites are occupied by either Al or Mg and refer to these as β'(Al) and β'(Mg), respectively. For these two systems, we do not provide KS-DFT results as they are computationally prohibitive. The formation energies for the range of Al-Mg intermetallics are reported in Table 2.4. Our results suggest that the formation energies predicted by RS-OFDFT-FE are in good agreement with PROFESS calculations, and in close agreement with KS-DFT calculations.

Table 2.4: Formation energy per atom (eV/atom) of Al-Mg intermetallics calculated using RS-OFDFT-FE, PROFESS, and KS-DFT with TM-NLPS.

Method	Al_3Mg	$Mg_{13}Al_{14}$	$Mg_{17}Al_{12}$	$Mg_{23}Al_{30}$	β'(Al)	β'(Mg)
RS-OFDFT-FE	-0.010	0.053	-0.008	-0.035	-0.026	-0.020
PROFESS	-0.011	0.052	-0.011	-0.034	-0.029	-0.023
KS-NLPS	-0.007	0.061	-0.027	-0.019	-	-

2.5.4 Configurational forces and atomic displacements

As a next step in our study of the accuracy and transferability of RS-OFDFT-FE, we compute the configurational forces on atoms that are perturbed from their equilibrium positions and compare these with Kohn-Sham DFT calculations. We investigate the accuracy of the forces in both fcc Al and hcp Mg. We begin by considering the relaxed Al fcc unit cell, and the relaxed Mg hcp unit cell. In the relaxed Al fcc unit cell, we perturb the face-centered atom with fractional coordinates 0, $\frac{1}{2}$, $\frac{1}{2}$ by 0.1 Bohr in the [0 1 0] direction. In the relaxed Mg hcp unit cell, we perturb the atom with fractional coordinates $\frac{2}{3}$, $\frac{1}{3}$, $\frac{1}{2}$ by 0.1 Bohr in the $[\bar{2}\ \bar{1}\ 3\ 0]$ direction (directions in hcp Mg are represented using *Miller-Bravais* indices). The configurational forces on the perturbed atoms are computed using RS-OFDFT-FE, and compared against KS-DFT calculations. The computed restoring forces, along $[0\ \bar{1}\ 0]$ for the Al system and along $[2\ 1\ \bar{3}\ 0]$ for the Mg system, are reported in Table 2.5. We note that the computed restoring forces from RS-OFDFT-FE are in good agreement with PROFESS and KS-DFT calculations.

As a more stringent test of accuracy and transferability, we consider the atomic relaxations around a mono-vacancy in fcc Al and hcp Mg. In the case of mono-vacancy in Al, we consider a supercell containing 3 × 3 × 3 fcc Al unit cells and remove an atom to create a mono-vacancy. We calculate the forces on the neighboring atoms of the mono-vacancy, and their relaxation displacements upon ionic relaxation using both RS-OFDFT-FE and KS-DFT calculations. Periodic boundary conditions are employed in these calculations. Table 2.6 reports the computed force and relaxation displacement in Al on the nearest neighboring atom, which experiences the largest ionic force and relaxation. In the case of a mono-vacancy in Mg, we consider a supercell containing 3 × 3 × 2 hcp unit cells, and Table 2.7 reports the ionic force and relaxation displacement on the neighboring atom that has the largest force in the presence of the vacancy. As is evident from the results, the ionic forces and relaxed displacements for a mono-vacancy in Al and Mg computed using RS-OFDFT-FE are in good agreement with PROFESS, and in close agreement with KS-DFT calculations. These results suggest that the proposed real-space orbital-free DFT formulation provides a good approximation to KS-DFT for Al-Mg materials systems.

Table 2.5: Restoring force (eV/Bohr) on the perturbed atom in fcc Al and hcp Mg unit cells computed using RS-OFDFT-FE, PROFESS, and KS-DFT calculations.

	RS-OFDFT-FE	PROFESS	KS-BLPS	KS-NLPS
Al	0.148	0.137	0.134	0.126
Mg	0.019	0.019	0.018	0.019

Table 2.6: Ionic forces (eV/Bohr) and relaxation displacement (Bohr) on the nearest neighboring atom to a mono-vacancy in a periodic 3 × 3 × 3 fcc Al supercell, calculated using RS-OFDFT-FE, PROFESS, and KS-DFT. f and d denote the magnitudes of ionic force and relaxation displacement. $\angle\mathbf{f}$ and $\angle\mathbf{d}$ denote the angles (in degrees) of the force and displacement vectors with respect to the KS-NLPS force and displacement vectors.

	RS-OFDFT-FE	PROFESS	KS-BLPS	KS-NLPS
f	0.141	0.146	0.130	0.119
d	9.90×10^{-2}	9.75×10^{-2}	9.47×10^{-2}	8.90×10^{-2}
$\angle\mathbf{f}$	0.00	0.00	0.00	0.00
$\angle\mathbf{d}$	0.15	0.00	0.00	0.00

2.5.5 Cell-size studies on a mono-vacancy in Al

Prior Fourier-space calculations using OF-DFT and WGC Functional [84], and KS-DFT calculations [107] have suggested that cell-sizes containing ∼ 256 lattice sites

Table 2.7: Ionic forces (eV/Bohr) and relaxation displacement (Bohr) on the nearest neighboring atom to a mono-vacancy in a periodic $3 \times 3 \times 2$ hcp Mg supercell, calculated using RS-OFDFT-FE, PROFESS, and KS-DFT.

	RS-OFDFT-FE	PROFESS	KS-BLPS	KS-NLPS
f	0.059	0.060	0.053	0.046
d	8.26×10^{-2}	8.64×10^{-2}	7.00×10^{-2}	5.83×10^{-2}
$\angle\mathbf{f}$	5.11	4.73	2.75	0.0
$\angle\mathbf{d}$	5.66	5.27	3.58	0.0

are sufficient to obtain a well-converged (to within 3 meV) mono-vacancy formation energy in fcc Al. These Fourier-space calculations, which employ periodic boundary conditions, compute the properties of a periodic array of vacancies. On the other hand, real-space calculations on isolated mono-vacancies in bulk, computed using the recently developed coarse-graining techniques for orbital-free DFT [54, 99], suggest that cell-size effects in mono-vacancy calculations are present up to cell-sizes of $\sim 10^3$ atoms. Although both approaches give similar converged vacancy formation energies, this discrepancy in the cell-size effects has thus far remained an open question.

In order to understand the source of this discrepancy, we conduct a cell-size study of the mono-vacancy formation energy in Al using RS-OFDFT-FE with two types of boundary conditions: (i) periodic boundary conditions on electronic fields; (ii) Dirichlet boundary conditions on electronic fields with values corresponding to that of a perfect crystal. These Dirichlet boundary conditions, which we refer to as bulk Dirichlet boundary conditions, correspond to the scenario where perturbations in the electronic structure due to the mono-vacancy vanish on the boundary of the computational domain, and the electronic structure beyond the computational domain corresponds to that of the bulk. We note that periodic boundary conditions mimic the widely used Fourier-space calculations on point defects, whereas the bulk Dirichlet boundary conditions correspond to simulating an isolated point defect embedded in bulk. We note that the local real-space formulation of orbital-free DFT and the finite-element basis are key to being able to consider these boundary conditions.

We compute the vacancy formation at constant volume as [97, 108]

$$E_{vf} = E\left(N-1, 1, \frac{N-1}{N}\Omega\right) - \frac{N-1}{N} E\left(N, 0, \Omega\right) , \tag{2.46}$$

where $E\left(N,0,\Omega\right)$ denotes the energy of perfect crystal containing N atoms occupying a volume Ω, and $E(N-1, 1, \frac{N-1}{N}\Omega)$ denotes energy of a computational cell containing $N-1$ atoms and one vacancy occupying a volume $\frac{N-1}{N}\Omega$. For both periodic boundary conditions and bulk Dirichlet boundary conditions, the lattice site where the vacancy is created is chosen to be the farthest site from the domain boundary. As we are primarily interested in the cell-size effects of the electronic structure, we do not consider ionic relaxations in this part of our study. Table 2.8 shows the unrelaxed mono-vacancy formation energies for different cell sizes computed using RS-OFDFT-FE using both periodic boundary conditions and bulk Dirichlet boundary conditions. We note that the mono-vacancy formation energies using both sets of boundary conditions converge to the same value, and this is also in good agreement with PROFESS and KS-DFT calculations (cf. Table 2.9). However, it is interesting to note that the mono-vacancy formation energies with periodic boundary conditions are well converged (to within 10 meV) by $3 \times 3 \times 3$ cell-size (108 atoms), whereas we required a $6 \times 6 \times 6$ cell-size (864 atoms) to achieve a converged formation energy with bulk Dirichlet boundary conditions.

In order to understand this boundary condition dependence of the cell-size effects, we compute the perturbations in the electronic fields due to the presence of the mono-vacancy by subtracting from the electronic fields corresponding to the mono-vacancy the electronic fields of a perfect crystal. To this end, we define the normalized

Table 2.8: Unrelaxed mono-vacancy formation energies for Al computed using RS-OFDFT-FE with periodic boundary conditions (E_{vf}^{p} in eV) and bulk Dirichlet boundary conditions (E_{vf}^{bD} in eV).

Cell size	N	E_{vf}^{bD}	E_{vf}^{p}
2x2x2	32	-0.390	0.955
3x3x3	108	0.864	0.915
4x4x4	256	0.971	0.908
5x5x5	500	0.944	-
6x6x6	864	0.918	-
7x7x7	1372	0.914	-

Table 2.9: Unrelaxed mono-vacancy formation energies (E_{vf} in eV) for Al computed using PROFESS [1], and KS-DFT on a $3 \times 3 \times 3$ computational cell.

	E_{vf}
PROFESS	0.903
KS-DFT-BLPS	0.815
KS-DFT-NLPS	0.811

perturbations in the electronic fields computed on the finite-element mesh to be

$$\begin{aligned}
u_h^c &= \left(u_h - u_h^p\right) / \mathrm{v}_{\mathrm{av}}\left(u_h^p\right) \;, \\
\phi_h^c &= \left(\phi_h - \phi_h^p\right) / \mathrm{v}_{\mathrm{av}}\left(\phi_h^p\right) \;, \\
k_{\alpha,h}^c &= \left(\sum_{j=1}^{m} \omega_{\alpha_j,h} - \sum_{j=1}^{m} \omega_{\alpha_j,h}^p\right) / \mathrm{v}_{\mathrm{av}}\left(\sum_{j=1}^{m} \omega_{\alpha_j,h}^p\right) \;, \\
k_{\beta,h}^c &= \left(\sum_{j=1}^{m} \omega_{\beta_j,h} - \sum_{j=1}^{m} \omega_{\beta_j,h}^p\right) / \mathrm{v}_{\mathrm{av}}\left(\sum_{j=1}^{m} \omega_{\beta_j,h}^p\right) \;.
\end{aligned} \tag{2.47}$$

In the above, $\{u_h, \phi_h, \omega_{\alpha_j,h}, \omega_{\beta_j,h}\}$ and $\{u_h^p, \phi_h^p, \omega_{\alpha_j,h}^p, \omega_{\beta_j,h}^p\}$ denote the electronic fields in the computational domain with the vacancy and those without the vacancy (perfect crystal), respectively. $\mathrm{v}_{\mathrm{av}}(.)$ denotes the volume average of an electronic field over the computational cell. As a representative metric, in the definition of $k_{\alpha,h}^c$ and $k_{\beta,h}^c$ we only consider the kernel potentials corresponding to K_0. Figures 2.3 and 2.4 shows the normalized corrector fields for the mono-vacancy, computed using periodic boundary conditions, along the face-diagonal of the periodic boundary. It is interesting to note from these results that the perturbations in the electronic structure due to the vacancy are significant up to $6 \times 6 \times 6$ computational cells. Thus, although the vacancy formation energy appears converged by $3 \times 3 \times 3$ computational cell while using periodic boundary conditions, the electronic fields are not converged till a cell-size of $6 \times 6 \times 6$ computational cell. On the other hand, the cell-size convergence in mono-vacancy formation energy suggested by the bulk Dirichlet boundary conditions is inline with the convergence of electronic fields. These results unambiguously demonstrate that the cell-size effects in the electronic structure of defects are larger than those suggested by a cell-size study of defect formation energies employing periodic boundary conditions. Using bulk Dirichlet boundary conditions for the cell-size study of defect formation energies provides a more accurate estimate of the cell-size effects in the electronic structure of defects, and the extent of electronic structure perturbations due to a defect. Further, while periodic boundary conditions are limited to the study of point defects, bulk Dirichlet boundary conditions can be used to also study defects like isolated dislocations [56], whose geometry does not admit periodic boundary conditions.

2.6 Summary

We have developed a local real-space formulation of orbital-free DFT with WGC kinetic energy functionals by reformulating the extended interactions in electrostatic and kinetic energy functionals as local variational problems in auxiliary potentials. The proposed real-space formulation readily extends to all-electron orbital-free DFT calculations that are commonly employed in warm dense matter calculations. Building on the proposed real-space formulation we have developed a unified variational framework for computing configurational forces associated with both ionic and cell relaxations. Further, we also proposed a numerically efficient approach for the so-

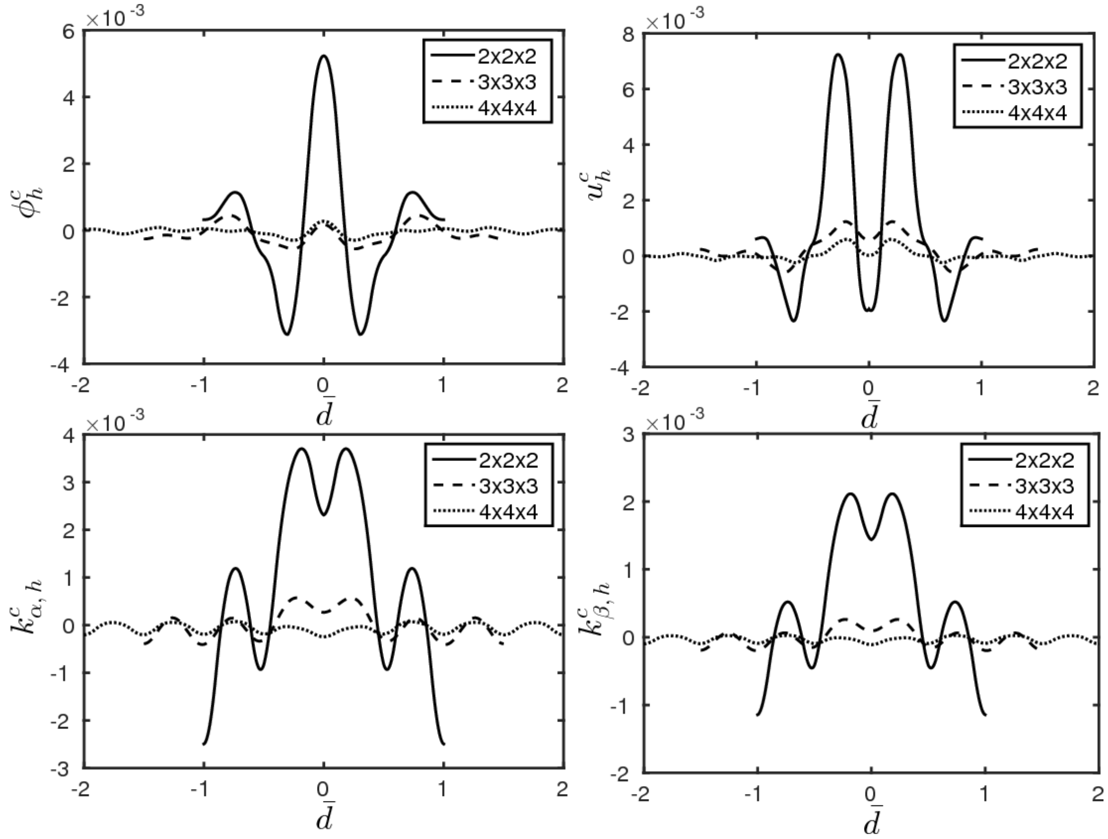

Figure 2.3: Normalized corrector fields for a mono-vacancy, computed with periodic boundary conditions, along the face diagonal on the computational domain boundary. The abscissa $\bar{d}$ represents a normalized coordinate along the face diagonal. Results for computational cell sizes from $2 \times 2 \times 2$ to $4 \times 4 \times 4$ are shown.

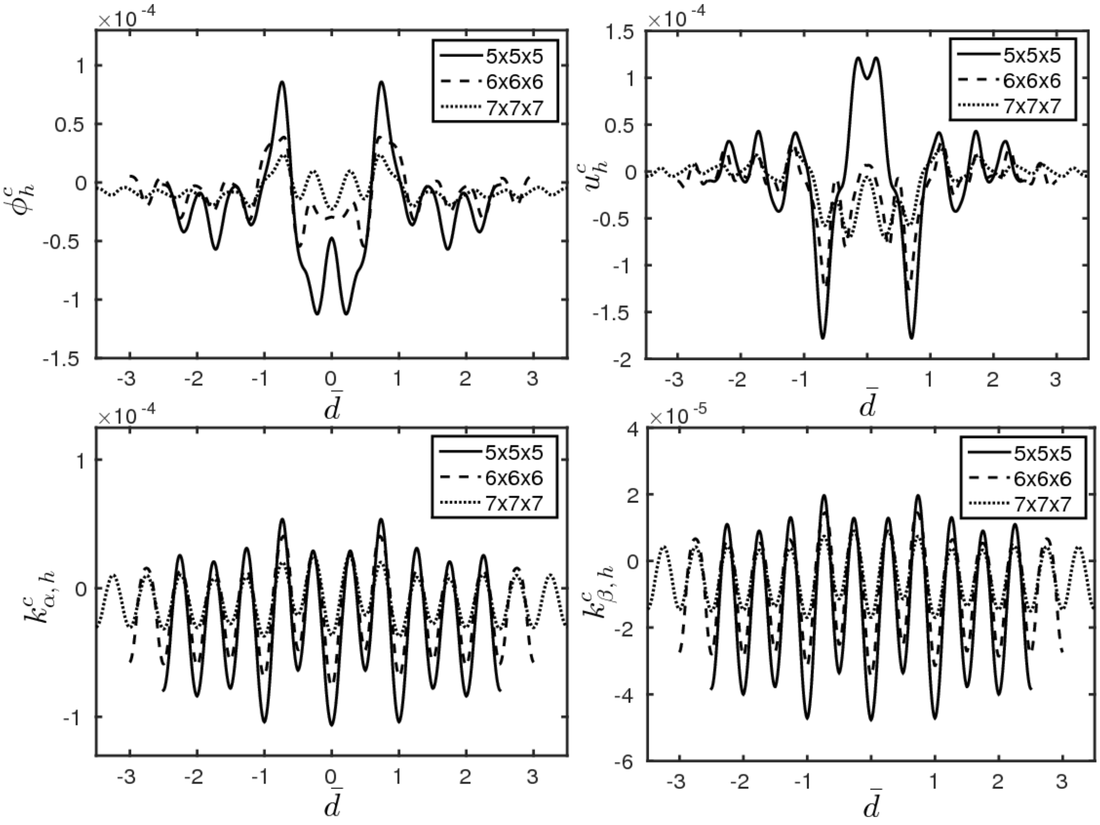

Figure 2.4: Normalized corrector fields for a mono-vacancy, computed with periodic boundary conditions, along the face diagonal on the computational domain boundary, for cell sizes ranging from $5 \times 5 \times 5$ to $7 \times 7 \times 7$.

lution of ground-state orbital-free DFT problem, by recasting the local saddle point problem in the electronic fields—electron density and auxiliary potential fields—as a fixed point iteration problem and employing a self-consistent iteration procedure. We have employed a finite-element basis for the numerical discretization of the proposed real-space formulation of orbital-free DFT. Our numerical convergence studies indicate that we obtain close to optimal rates of convergence in both ground-state energy and configurational forces with respect to the finite-element discretization.

We subsequently investigated the accuracy and transferability of the proposed real-space formulation of orbital-free DFT for Al-Mg materials system. To this end, we conducted a wide range of studies on Al, Mg and Al-Mg intermetallics, including computation of bulk properties for these systems, formation energies of Al-Mg intermetallics, and ionic forces in bulk and in the presence of point defects. Our studies indicate that orbital-free DFT and the proposed real-space formulation is in good agreement with Kohn-Sham DFT calculations using both local pseudopotentials as well as non-local pseudpotentials, thus providing an alternate linear-scaling approach for electronic structure studies in Al-Mg materials system. We finally investigated the cell-size effects in the electronic structure of a mono-vacancy in Al, and demonstrated that the cell-size convergence in the vacancy formation energy computed by employing periodic boundary conditions is not commensurate with the convergence of the electronic fields. On the other hand, the true cell-size effects in the electronic structure are revealed by employing the bulk Dirichlet boundary conditions, where the perturbations in the electronic fields due to the defect vanish on the boundary of the computational domain. Our studies indicate that the true cell-size effects are much larger than those suggested by periodic calculations even for simple defects like point defects. We note that the proposed real-space formulation and the finite-element basis are crucial to employing the bulk Dirichlet boundary conditions that are otherwise inaccessible using Fourier based formulations. The proposed formulation, besides being amenable to complex geometries, boundary conditions, and providing excellent scalability on parallel computing platforms, also enables coarse-graining techniques like the quasi-continuum reduction [99, 109] to conduct large-scale electronic structure calculations on the energetics of extended defects in Al-Mg materials system, and is an important direction for future studies.

CHAPTER III

Orbital-Free Density Functional Theory Calculations on the Energetics of Dislocations in Al-Mg Materials System

3.1 Introduction

This work is composed of two parts. First, we study core energetics of an isolated screw dislocation in face-centered-cubic (fcc) Aluminum [55] using the local real-space orbital-free DFT formulation (RS-OFDFT) discussed in chapter II. Second, using the same approach we study the core energetics of basal edge and basal screw dislocations in hexagonal-close-packed (hcp) Magnesium. In all the above dislocation systems, we estimate the core size of the isolated dislocation directly from the energetics and subsequently study the effect of external macroscopic deformation on the dislocation core energy.

3.2 Isolated Dislocation Energetics in Aluminum

In this section, we present our study on an isolated screw dislocation in Aluminum using RS-OFDFT. We adopt the approach proposed in [56], where bulk Dirichlet boundary conditions have been applied on the electronic fields to simulate an isolated edge dislocation embedded in the bulk in Aluminum. Following along similar lines, we compute the core size of the isolated screw dislocation in Aluminum directly from energetics, by identifying the region up to which the contribution from electronic structure perturbations (beyond those that can be accounted for in a nonlinear continuum theory) is significant to the energetics. The dislocation energy corresponding to this core size, computed from the proposed electronic structure calculations, is identified as the core energy. Further, we study the influence of external macroscopic deformations on the dislocation core energy and core structure for a wide range of macroscopic deformations. The RS-OFDFT calculations are conducted using the following choices: Wang-Govind-Carter (WGC) model for the kinetic energy functional [2] (second order Taylor expansion of the density dependent kernel, cf. [2]), a local density approximation (LDA) for the exchange-correlation energy [3], and the Goodwin-Needs-Heine pseudopotential [4]. For the finite-element discretization, we use quadratic hexahedral elements, where the basis functions are constructed as a tensor product of basis functions in one dimension. Numerical parameters like the finite-element mesh size, quadrature rules and stopping tolerances for iterative solvers are chosen such that the error in the computed dislocation energies per unit length of the dislocation line is less than 0.001 eV/Å. Atomic relaxations are performed till the force components in all directions on the atoms are less than 2.5×10^{-3} eV/Å.

3.2.1 Dislocation core size and core energy

We begin by estimating the core size of a perfect screw dislocation in face-centered-cubic (fcc) Aluminum explicitly from the energetics, and subsequently calculate the core energy for the perfect screw dislocation as well as the core energy after atomic relaxation. The coordinate system, X — Y — Z axes (or equivalently 1—2—3), is aligned along $[1\ 1\ \bar{2}]$—$[1\ 1\ 1]$—$[1\ \bar{1}\ 0]$ crystallographic directions. With this coordinate system, we create a perfect fcc crystal of size $R\sqrt{6}a_0 \times 2R\sqrt{3}a_0 \times \frac{a_0}{\sqrt{2}}$, where a_0

denotes the lattice parameter and R is an integer-valued scaling factor which sets the simulation domain size. Then we introduce a perfect screw dislocation with Burgers vector $\mathbf{b} = \frac{a_0}{2}[1\bar{1}0]$ and line direction along $[1\ \bar{1}\ 0]$ at the center of the simulation domain by applying isotropic Volterra displacement fields [5] of a screw dislocation to the positions of atoms. We employ the bulk Dirichlet boundary conditions on electronic fields, proposed in [56], to simulate the isolated screw dislocation in bulk. More specifically, in the X and Y directions, we employ Dirichlet boundary conditions on the electronic fields comprising of electron density, electrostatic potential and kernel potentials, and, in the Z direction, we use periodic boundary conditions on these fields. The Dirichlet boundary values for the electronic fields are determined using the Cauchy-Born approximation, wherein the values are obtained by projection of orbital-free DFT computed electronic fields on periodic unit cells which are deformed using the elastic field of the screw dislocation. These boundary conditions on the electronic fields correspond to an isolated dislocation in bulk with the electronic structure on the boundary of (and outside of) the simulation domain given by the Cauchy-Born hypothesis. The local real space formulation along with the finite-element discretization are crucial to realizing these bulk Dirichlet boundary conditions. Using these boundary conditions, we compute the electronic-structure and ground-state energy of the perfect screw dislocation for varying simulation domains with $R = 2$, 3, 4, 5, 7 while keeping the atomic positions fixed. This enables us to unambiguously delineate the contribution from electronic-structure perturbations to the dislocation energy, the origins of which are quantum mechanical in nature and are beyond the scope of any homogenized non-linear continuum theory, and also identify the region where this contribution is significant. Figure 3.1 shows the contours of the electron density for $R = 4$. For each of these simulation domains, the dislocation energy (E_{d}) is computed as

$$E_{\mathrm{d}}(N, V) = E_{\mathrm{disloc}}(N, V) - E_0(N, V), \tag{3.1}$$

where $E_{\text{disloc}}(N, V)$ denotes the energy of a dislocation system containing N atoms with a volume V, and $E_0(N, V)$ denotes energy of a perfect crystal of the same volume and containing the same number of atoms. From a thermodynamic standpoint, E_{d} is the dislocation formation energy at constant volume. We note that there is no volume change due to the perfect screw dislocation Volterra field. Table 3.1 shows the computed dislocation energies for the various domains. We note that the domain-size is measured to be $\sqrt{3}R|\mathbf{b}|$, which is the distance from dislocation line to the boundary along $[1\ 1\ \bar{2}]$. In order to identify the region in which the electronic-structure perturbations arising from the dislocation are significant, we consider the dislocation energy change for every successive increase in the domain size, and denote this change by ΔE_{d}. This has two contributions: (i) the elastic energy of the region between the two domains, which we denote by $\Delta E_{\text{d}}^{\text{elas}}$; (ii) contribution from electronic-structure changes due to the change in the location of the bulk Dirichlet boundary conditions on electronic fields, which we denote by $\Delta E_{\text{d}}^{\text{elec}}$. $\Delta E_{\text{d}}^{\text{elas}}$ is computed using the Cauchy-Born approximation, wherein the elastic energy density at each point is computed from RS-OFDFT calculations on periodic unit-cells deformed by screw dislocation elastic fields. We note that $\Delta E_{\text{d}}^{\text{elas}}$, thus computed, corresponds to the elastic contributions from the non-linear continuum elastic theory derived from OFDFT. We subsequently infer $\Delta E_{\text{d}}^{\text{elec}}$, by subtracting $\Delta E_{\text{d}}^{\text{elas}}$ from ΔE_{d}. The computed $\Delta E_{\text{d}}^{\text{elas}}$ and $\Delta E_{\text{d}}^{\text{elec}}$ are reported in Table 3.1, where the computed values are accurate up to 0.001 eV. We find that $\Delta E_{\text{d}}^{\text{elec}}$ remains significant in comparison to $\Delta E_{\text{d}}^{\text{elas}}$, i.e. more than 10 % of $\Delta E_{\text{d}}^{\text{elas}}$, until a domain-size of $\approx 7|\mathbf{b}|$. This suggests that the electronic-structure perturbations due to the dislocation are significant up to $\approx 7|\mathbf{b}|$ from the dislocation line, which represents the core size of the perfect screw dislocation. Graphically, this is also evident from figure 3.2, with the energy of the dislocation deviating from the logarithmic dependence for domain sizes below $7|\mathbf{b}|$. Importantly, we note that this domain size is much larger than previous core size estimates based on contin-

Table 3.1: Computed dislocation energy of perfect screw dislocation in Aluminum for varying domain-sizes, where N denotes the number of atoms in the simulation domain. ΔE_{d} denotes the change in the dislocation energy from the previous domain-size. $\Delta E_{\mathrm{d}}^{\mathrm{elas}}$ and $\Delta E_{\mathrm{d}}^{\mathrm{elec}}$ denote the elastic and electronic contributions to ΔE_{d}.

Domain size ($R\sqrt{3}\|\mathbf{b}\|$)	N (atoms)	E_{d} (eV)	ΔE_{d} (eV)	$\Delta E_{\mathrm{d}}^{\mathrm{elas}}$ (eV)	$\Delta E_{\mathrm{d}}^{\mathrm{elec}}$ (eV)
$3.5\|\mathbf{b}\|$	96	0.837	-	-	-
$5.2\|\mathbf{b}\|$	216	0.891	0.054	0.100	-0.046
$6.9\|\mathbf{b}\|$	384	0.943	0.052	0.069	-0.017
$8.7\|\mathbf{b}\|$	600	0.996	0.053	0.051	0.002
$12.1\|\mathbf{b}\|$	1176	1.079	0.083	0.080	0.003

uum displacement or strain fields of $\sim 1-3|\mathbf{b}|$ [5, 110, 111], underscoring the longer ranged nature of electronic structure perturbations from defects than previously believed, and its potential significance in governing the energetics of dislocations. The present finding is consistent with a recent electronic structure study on edge dislocation in Aluminum by [56], wherein the core size was computed to be $10|\mathbf{b}|$. We note that real-space studies on point defects have also shown strong cell-size effects owing to the electronic structure perturbations from the defect [52, 54, 99, 112, 113].

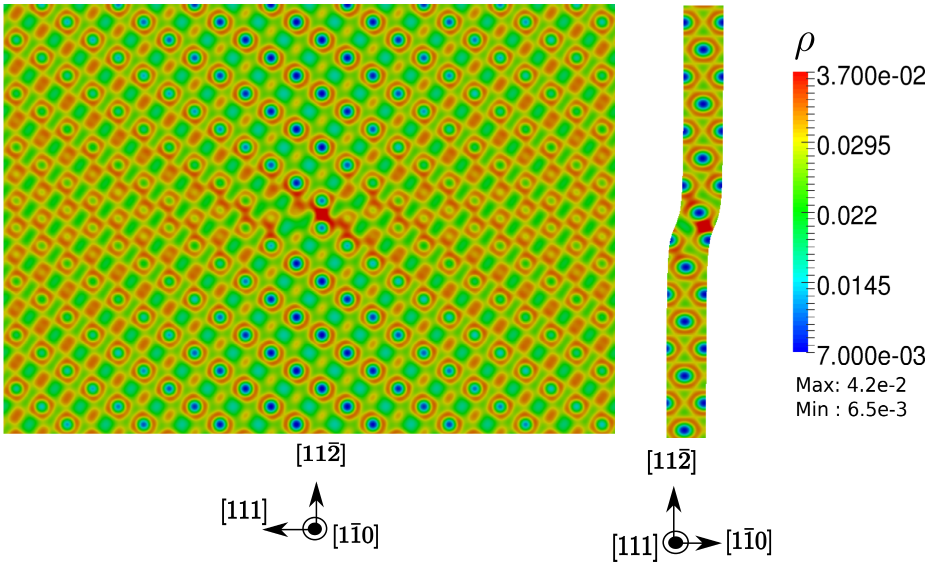

(a) (b)

Figure 3.1: Electron density contours on a) a $(1\bar{1}0)$ plane, and b) a (111) plane of a perfect screw dislocation in Aluminum. The (111) plane passes through the dislocation center.

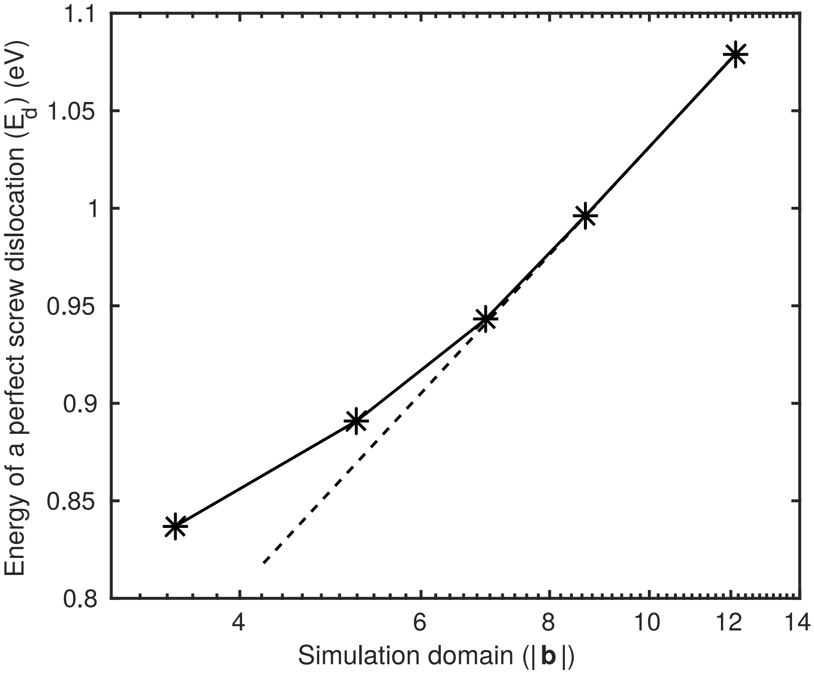

Figure 3.2: Semi-log plot of dislocation formation energy of the perfect screw dislocation in Aluminum as a function of simulation domain size. The dashed line demonstrates the asymptotic logarithmic divergence of the computed dislocation energies, as expected from continuum estimates, beyond simulation domains of $\approx 7|\mathbf{b}|$.

Next we investigate the relaxed core structure of the screw dislocation by relaxing the positions of atoms interior to the simulation domain, while holding fixed the positions of atoms on the Dirichlet boundary. We find that the relaxed structure and the corresponding reduction in the energy from the perfect screw core energy (denoted by $E_{\mathrm{d}}^{\mathrm{relax}}$) are sensitive to the simulation domain size up to the domain size of $8.7|\mathbf{b}|$. Beyond $8.7|\mathbf{b}|$, the change in the core structure is negligible and the change in $E_{\mathrm{d}}^{\mathrm{relax}}$ is within the tolerance 0.001 eV/Å. This suggests that electronic structure perturbations are not significant beyond $8.7|\mathbf{b}|$ for the relaxed screw dislocation representing Shockley partials. Thus, we consider $8.7|\mathbf{b}|$ to be the core size of the relaxed screw dislocation, and the dislocation energy corresponding to this core size as the dislocation core energy of the Shockley partials. The core energy of Shockley partials is computed to be 0.811 eV, or, equivalently, the core energy per unit length of dislocation line is 0.284 eV/Å, and $E_{\mathrm{d}}^{\mathrm{relax}}$ is 0.065 eV/Å. Figure 3.3 shows the edge and screw components of the differential displacements [114] and indicates the approximate location of the Shockley partials. The partial separation distance computed from the edge-component differential displacement (DD) plot is 6.59 Å (2.3 $|\mathbf{b}|$), and that computed from the screw-component differential displacement plot is 8.24 Å (2.9 $|\mathbf{b}|$). An uncertainty magnitude equal to twice the spacing between atomic planes in the X direction, which is $\frac{a_0}{\sqrt{6}} = 1.65$ Å (or 0.58 $|\mathbf{b}|$) is expected in computing the partial separation using this procedure. Comparing the partial separation distance with other DFT studies on a screw dislocation in Aluminum [44, 47], we are in good agreement with these studies that have reported partial separation distances between 5.0–7.5 Å.

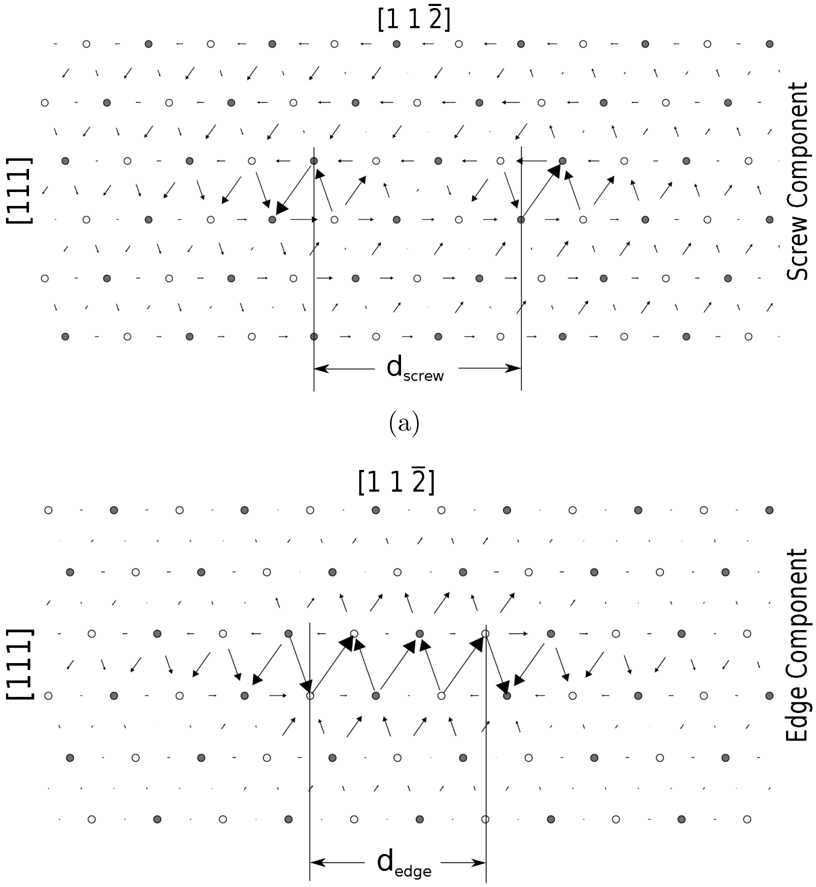

(a)

(b)

Figure 3.3: Differential displacement plots of the a) screw and b) edge components of Shockley partials of a screw dislocation in Aluminum.

3.2.2 Effect of macroscopic deformations

This study is motivated from recent investigations which suggest that macroscopic deformations can play a significant role in governing the electronic structure and subsequently the energetics of defects [115–118]. In the recent study on an edge dislocation in Aluminum [56, 57], it was observed that the core energy of the edge dislocation strongly depends on the external macroscopic deformation. In the present work, we perform a similar investigation on a screw dislocation in Aluminum to understand the effect of macroscopic deformation on its core energy and core structure. We begin with a perfect screw dislocation in a $8.7|\mathbf{b}|$ simulation domain, which corresponds to the core size of the Shockley partials determined in Section 3.2.1. On that simulation domain, we apply an affine deformation corresponding to a macroscopic strain $\boldsymbol{\epsilon}$, and, while holding the positions of the atoms fixed, we compute the electronic structure and the relaxed positions of atoms. The dislocation core energy, following equation (3.1), is computed as a function of macroscopic strain

$$E_{\text{c}}(\boldsymbol{\epsilon}) = E_{\text{disloc}}(\boldsymbol{\epsilon}) - E_0(\boldsymbol{\epsilon}), \tag{3.2}$$

where $E_{\text{disloc}}(\boldsymbol{\epsilon})$ denotes the ground-state energy of the $8.7|\mathbf{b}|$ simulation domain containing the dislocation under an affine deformation corresponding to macroscopic strain $\boldsymbol{\epsilon}$, and $E_0(\boldsymbol{\epsilon})$ denotes the energy of a perfect crystal under the same affine deformation, containing the same number of atoms and occupying the same volume.

We begin by studying the effect of macroscopic volumetric strain ϵ_v, corresponding to equi-triaxial strain, on the core energy and the core structure of screw dislocation Shockley partials. In this study, we consider volumetric strains of -5%, -2%, -1%, 1%, 2% and 5%. Figure 3.4 shows the core energy (per unit length of dislocation line) for the different volumetric strains. The core energy changed monotonically and almost linearly from 0.34 eV/Å at -5% volumetric strain to 0.24 eV/Å at 5%

volumetric strain, showing a strong dependence on volumetric strain, which is in sharp contrast to widely used continuum based dislocation models where the dislocation core energy is assumed to be independent of macroscopic deformation. However, for the range of volumetric strains considered, the core structure only changed marginally. In particular, the partial separation distance in the edge-component DD plots is found to be 2.3–2.6 $|\mathbf{b}|$, and the partial separation distance in the screw-component DD plot remained unchanged at 2.9 $|\mathbf{b}|$. We note that $|\mathbf{b}|$ used here to quantify the partial separation distance is computed with respect to the fcc lattice under the applied macroscopic strain.

We next study the influence of macroscopic uniaxial strains along the coordinate directions, $[1\ 1\ \bar{2}]$—$[1\ 1\ 1]$—$[1\ \bar{1}\ 0]$. For each of the coordinate directions we consider uniaxial strain values of -1.64%,-0.66%,-0.33%, 0.33%, 0.66% and 1.64%. Figures 3.5(a), 3.5(b), and 3.6 show the core energy dependence on ϵ_{11} (uniaxial strain along $[1\ 1\ \bar{2}]$), ϵ_{22} (uniaxial strain along $[1\ 1\ 1]$) and ϵ_{33} (uniaxial strain along $[1\ \bar{1}\ 0]$), respectively. Similar to volumetric strain, the core energy dependence on uniaxial strains, for the range of strains considered in this study, is found to be monotonically decreasing from compressive to tensile strains. However, the core energy dependence on ϵ_{33} is significantly weaker compared to the other two uniaxial strains. Interestingly, the monotonic and almost linear dependence of the screw dislocation core energy on uniaxial strains is in contrast to the edge dislocation results [56, 57], where the core energy dependency on uniaxial strains was found to be non-monotonic and non-linear. This suggests that the dislocation character can play an important role in influencing the dependence of core energies on macroscopic deformation. In contrast to the effect of volumetric strains, we find that ϵ_{22} and ϵ_{33} uniaxial strains have a more significant influence on the core structure of a screw dislocation, while the ϵ_{11} uniaxial strain has a smaller influence compared to ϵ_{22} and ϵ_{33} strains. For the range of uniaxial strains considered in this study, the partial separation distance in the edge-component DD plots varies monotonically in going from compressive to tensile strains. The ranges of the variation for ϵ_{11}, ϵ_{22} and ϵ_{33} strains are 2.3–2.1$|\mathbf{b}|$, 2.6–1.7$|\mathbf{b}|$, and 2.1–2.6 $|\mathbf{b}|$ respectively. The screw component partial separation distance remained unchanged for all uniaxial strains. These changes in the core structure cannot be rationalized using the linear elastic theory as these uniaxial strains do not result in any glide forces on the Shockley partials, thus underscoring the role of electronic structure in governing the core structure and energetics.

Finally, we consider the influence of macroscopic shear strains ϵ_{12} and ϵ_{13}. We have not considered the ϵ_{23} strain, as this results in a net glide force on the screw dislocation and can result in dislocation glide upon overcoming the small Peierls barrier ($\approx$ 11 MPa, cf. [46]). We considered shear strains of -0.66%,-0.33%, 0.33% and 0.66% in this study. Figure 3.7 shows the computed core energy dependence on ϵ_{12} and ϵ_{13} shear strains. We observe that the core energy dependence on ϵ_{13} is weak and symmetric, whereas the core energy dependence on ϵ_{12} strain is significant and is non-symmetric. This significant difference can be rationalized by taking note of the linear elastic forces on the Shockley partials due to these macroscopic shear strains. The ϵ_{13} shear strain causes climb forces to act on the screw components of Shockley partials. When the sign of ϵ_{13} is changed, the force direction is reversed but it has a symmetric influence on the core structure, which leads to the observed symmetry in the core energy dependence on ϵ_{13}. On the other hand, ϵ_{12} shear strain results in equal and opposite glide forces on the edge component of Shockley partials, which can either increase or decrease the partial separation distance depending on the sign of ϵ_{12} shear strain. This leads to the asymmetry in the core energy dependence on ϵ_{12}. This rationalization is also supported by investigating the change in the core-structure. For the ϵ_{12} strain, the partial separation in the edge-component of the DD plot changes considerably from 1.7 $|\mathbf{b}|$ at $\epsilon_{12} = 0.66\%$ to 2.9 $|\mathbf{b}|$ at $\epsilon_{12} = -0.66\%$ (cf. figure 3.8). On the other hand for ϵ_{13} strain, the partial separation distances are found to be unchanged for equal and opposite strains.

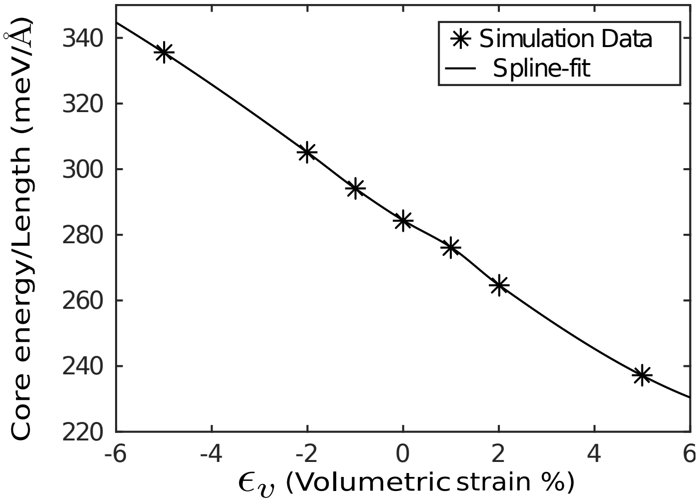

Figure 3.4: Core-energy per unit length of dislocation line of relaxed Shockley partials of screw dislocation in Aluminum as a function of volumetric strain.

3.3 Isolated Dislocation Energetics in Magnesium

On similar lines as the screw dislocation core energetics study in Section 3.2, we now present our study on isolated basal edge and screw dislocations in Magnesium using RS-OFDFT. We adopt the aforementioned bulk Dirichlet boundary conditions on the electronic fields to simulate isolated basal edge dislocation and basal screw dislocation in the bulk in Magnesium, and first estimate the core size of the isolated perfect dislocations. Next, we study the influence of external macroscopic deformations on the dislocation core energy for a wide range of macroscopic deformations. The RS-OFDFT calculations are conducted using the following choices: Wang-Govind-Carter (WGC) model for the kinetic energy functional [2] (second order Taylor expansion of the density dependent kernel, cf. [2]), a local density approximation (LDA) for the exchange-correlation energy [3], and a analytic form of local pseudopotential for Magnesium [119]. We use the same numerical parameters (finite element discretization and solver tolerances) as that used for the screw dislocation core energetics study in Section 3.2.

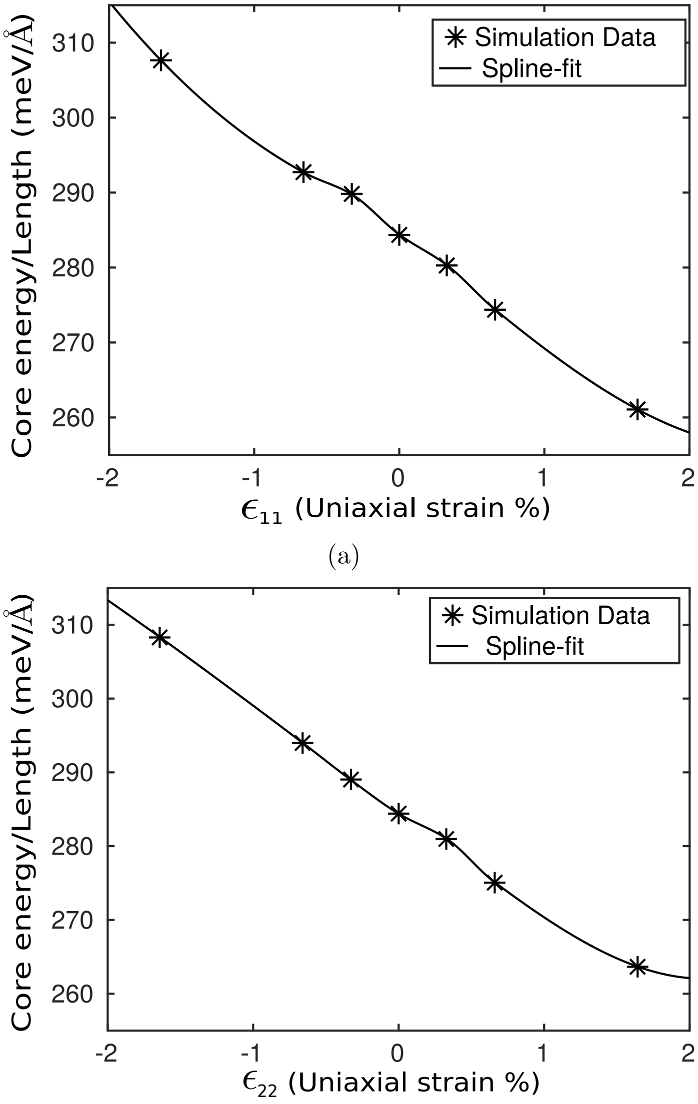

(a)

(b)

Figure 3.5: Core-energy per unit length of dislocation line of relaxed Shockley partials of screw dislocation in Aluminum as a function of uniaxial strains: (a) ϵ_{11}; (b) ϵ_{22}.

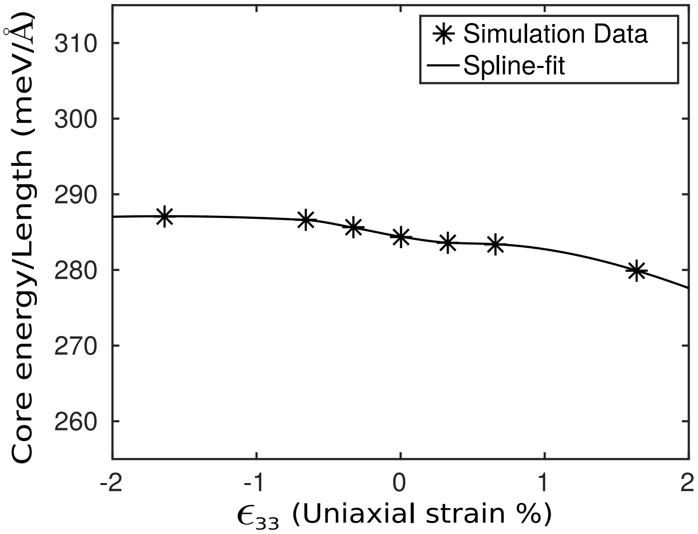

Figure 3.6: Core-energy per unit length of dislocation line of relaxed Shockley partials of screw dislocation in Aluminum as a function of ϵ_{33} uniaxial strain.

3.3.1 Dislocation core size and core energy

We first estimate the core size of the perfect basal edge and basal screw dislocations in hexagonal-close-packed (hcp) Magnesium explicitly from the energetics, and subsequently calculate the core energy of the perfect dislocations as well as the core energy after atomic relaxation. For the dislocation core-size study of the basal edge dislocation, the computational domain is set up by aligning the coordinate system, X — Y — Z axes (or equivalently 1—2—3) along $[2\bar{1}\bar{1}0]$—$[0001]$—$[0\bar{1}10]$ crystallographic directions respectively. Next, we chose a perfect crystal of size $2Ra_0 \times Rc_0 \times \sqrt{3}a_0$,where a_0 and c_0 denotes the lattice parameters of the hcp Mg crystal and R is an integer-valued scaling factor used to consider a sequence of increasing simulation domain sizes. A perfect edge dislocation with Burgers vector $\mathbf{b} = \frac{1}{3}[2\bar{1}\bar{1}0]$ is introduced at the center of the simulation domain by applying anisotropic elastic displacement fields [5] to the positions of atoms. Next we apply mixed periodic and Dirichlet boundary conditions similar to the case of screw dislocation in Aluminum, discussed previously in Section 3.2.1, and compute the electronic-structure and dislocation energy E_d (cf. equation 3.1) of the perfect edge dislocation for varying simulation

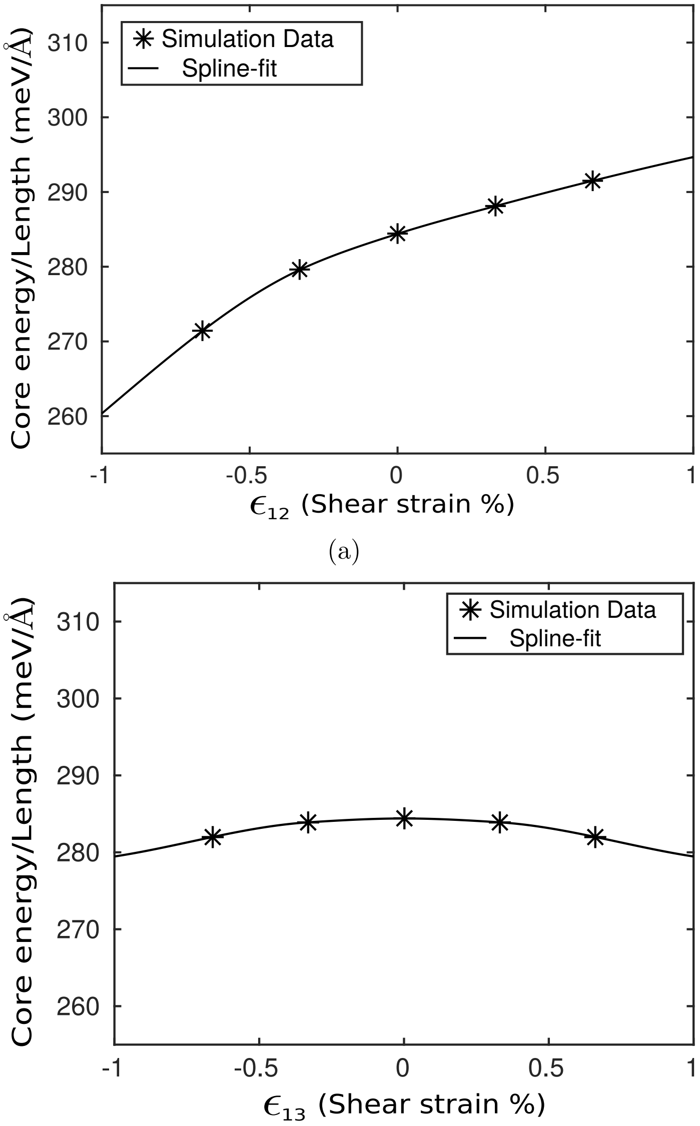

(a)

(b)

Figure 3.7: Core-energy per unit length of dislocation line of relaxed Shockley partials of screw dislocation in Aluminum as a function of shear strains: (a) ϵ_{12}; (b) ϵ_{13}.

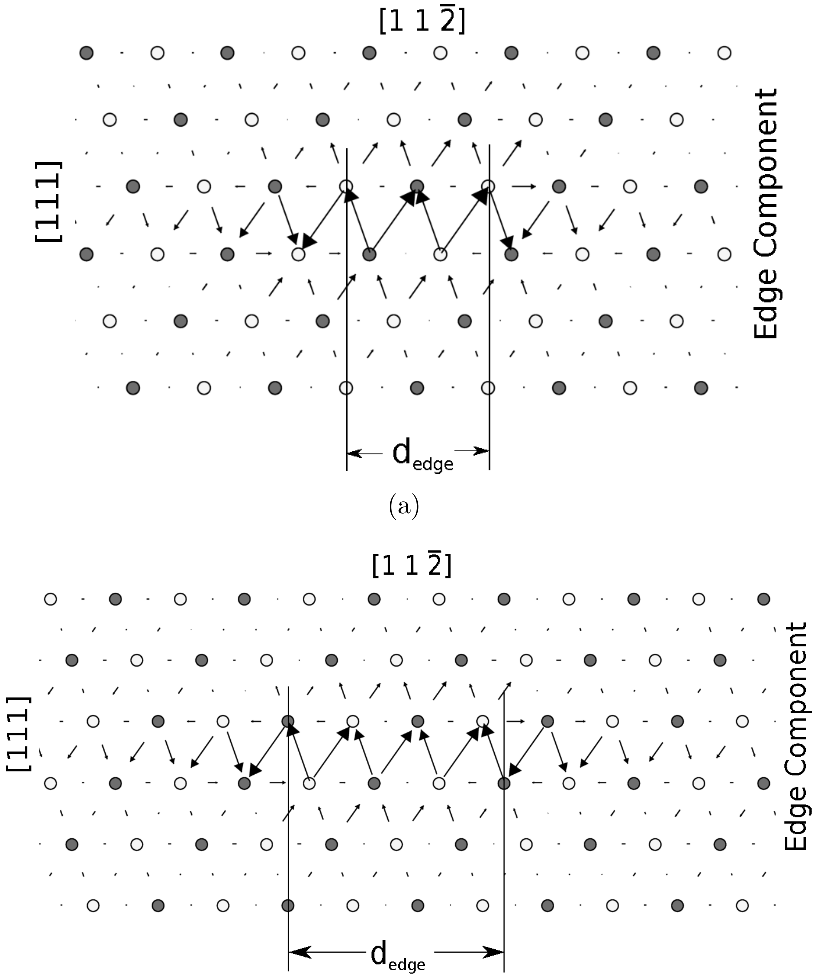

(a)

(b)

Figure 3.8: Differential displacement plots of the edge components of Shockley partials: (a) ϵ_{12} = 0.66% ; (b) ϵ_{12} = -0.66%.

Table 3.2: Computed dislocation energy of perfect basal edge dislocation in Magnesium for varying domain-sizes, where N denotes the number of atoms in the simulation domain. ΔE_{d} denotes the change in the dislocation energy from the previous domain-size. $\Delta E_{\mathrm{d}}^{\mathrm{elas}}$ and $\Delta E_{\mathrm{d}}^{\mathrm{elec}}$ denote the elastic and electronic contributions to ΔE_{d}.

Domain size	N (atoms)	E_{d} (eV)	ΔE_{d} (eV)	$\Delta E_{\mathrm{d}}^{\mathrm{elas}}$ (eV)	$\Delta E_{\mathrm{d}}^{\mathrm{elec}}$ (eV)
$4.1\lvert\mathbf{b}\rvert$	119	2.325	-	-	-
$6.1\lvert\mathbf{b}\rvert$	275	2.729	0.404	0.344	0.060
$8.1\lvert\mathbf{b}\rvert$	495	2.995	0.266	0.241	0.025
$10.2\lvert\mathbf{b}\rvert$	779	3.194	0.199	0.188	0.011
$14.3\lvert\mathbf{b}\rvert$	1539	3.489	0.295	0.290	0.005

domains with $R = 4, 6, 8, 10, 14$. The computed dislocation energies for the various domains are presented in Table 3.2. From Table 3.2, we observe that the ratio of ΔE_d^{elec} in relation to ΔE_d^{elas} is non-negligible until a domain-size of $8.1|\mathbf{b}|$, suggesting that the electronic-structure perturbations are significant up to distances as far as $8|\mathbf{b}|$ from the dislocation line. Graphically, this is also evident from figure 3.10, with the energy of the dislocation deviating from the logarithmic dependence for domain sizes below $8|\mathbf{b}|$. The computed core-energy for perfect basal edge dislocation is 2.995 eV , or, equivalently, the core-energy per unit length of dislocation line is 0.556 eV/Å.

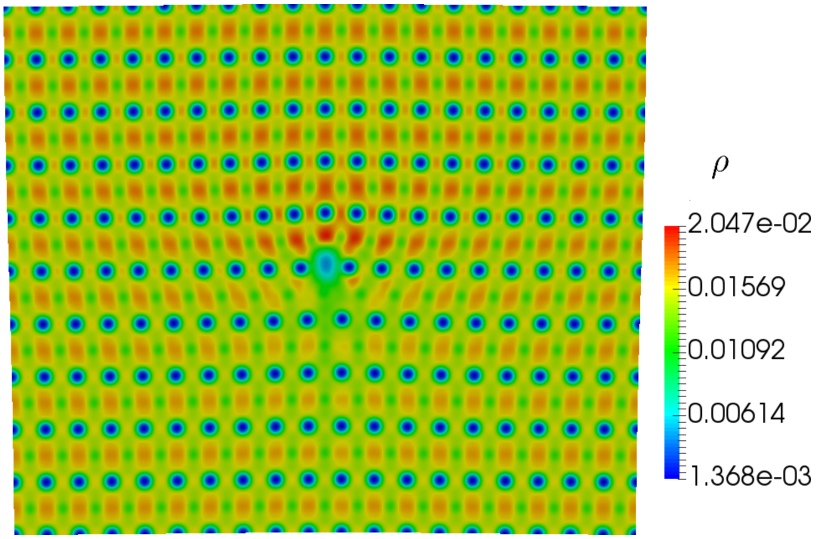

Figure 3.9: Electron density contours on $(0\bar{1}10)$ plane of a perfect basal edge dislocation in Magnesium.

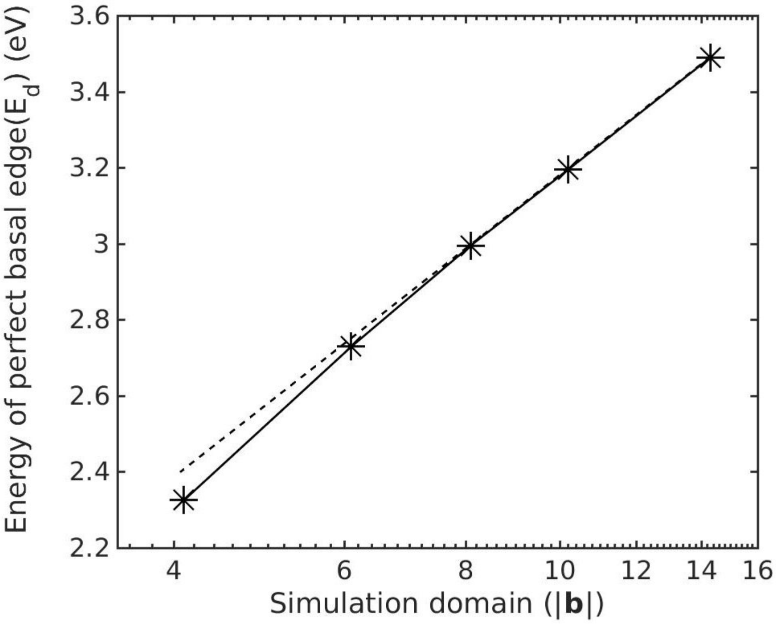

Figure 3.10: Semi-log plot of dislocation formation energy of the basal edge dislocation in Magnesium as a function of simulation domain size. The dashed line demonstrates the asymptotic logarithmic divergence of the computed dislocation energies, as expected from continuum estimates, beyond simulation domains of $\approx 8|\mathbf{b}|$.

We subsequently study the core-size of the basal screw dislocation, where we first align the coordinate axes 1—2—3 along $[01\bar{1}0]$—$[0001]$—$[2\bar{1}\bar{1}0]$ crystallographic directions. Next, we chose a perfect crystal of size $R\sqrt{3}a_0 \times Rc_0 \times a_0$ to consider sequence of increasing simulation domain sizes similar to the basal edge dislocation case. A perfect screw dislocation with Burgers vector $\mathbf{b} = \frac{1}{3}[2\bar{1}\bar{1}0]$ is introduced at the center of the simulation domain by applying anisotropic elastic displacement fields [5] to the positions of atoms. Next we apply mixed periodic and Dirichlet bulk boundary conditions, and compute the electronic-structure and dislocation energy E_d (cf. equation 3.1) of the perfect basal screw dislocation for varying simulation domains with $R = 4,\ 6,\ 8,\ 10,\ 12,\ 14$. The computed dislocation energies for the various domains are presented in Table 3.3. From Table 3.3, we observe that the ratio of ΔE_d^{elec} in relation to ΔE_d^{elas} is non-negligible until a domain-size of $11.4|\mathbf{b}|$, suggesting that the electronic-structure perturbations are significant up to distances as far as

Table 3.3: Computed dislocation energy of perfect basal screw dislocation in Magnesium for varying domain-sizes, where N denotes the number of atoms in the simulation domain. ΔE_{d} denotes the change in the dislocation energy from the previous domain-size. $\Delta E_{\mathrm{d}}^{\mathrm{elas}}$ and $\Delta E_{\mathrm{d}}^{\mathrm{elec}}$ denote the elastic and electronic contributions to ΔE_{d}.

Domain size	N (atoms)	E_{d} (eV)	ΔE_{d} (eV)	$\Delta E_{\mathrm{d}}^{\mathrm{elas}}$ (eV)	$\Delta E_{\mathrm{d}}^{\mathrm{elec}}$ (eV)
$3.8\|\mathbf{b}\|$	64	1.059	-	-	-
$5.7\|\mathbf{b}\|$	144	1.193	0.134	0.146	-0.012
$7.6\|\mathbf{b}\|$	256	1.290	0.097	0.104	-0.007
$9.5\|\mathbf{b}\|$	400	1.350	0.060	0.081	-0.021
$11.4\|\mathbf{b}\|$	576	1.435	0.085	0.066	0.019
$13.3\|\mathbf{b}\|$	784	1.492	0.057	0.056	0.001

$11|\mathbf{b}|$ from the dislocation line. Graphically, this is also evident from figure 3.11, with the energy of the dislocation deviating from the logarithmic dependence for domain sizes below $11|\mathbf{b}|$. The computed core-energy for perfect basal screw dislocation is 1.435 eV , or, equivalently, the core-energy per unit length of dislocation line is 0.461 eV/Å. The estimated perfect dislocation core sizes of 8–$11|\mathbf{b}|$ for basal dislocations in Magnesium are commensurate with the estimated core sizes of 7–10 $|\mathbf{b}|$ for dislocations in Aluminum (cf. Section 3.2.1).

Next we investigate the relaxed core structures of the basal edge and basal screw dislocation by relaxing the positions of atoms interior to the simulation domain, while holding fixed the positions of atoms on the Dirichlet boundary. We find that the relaxed structures and the corresponding reduction in the energy from the perfect dislocation core energy (denoted by $E_{\mathrm{d}}^{\mathrm{relax}}$) are sensitive to the simulation domain size beyond the estimated core sizes of the unrelaxed dislocation— $8|\mathbf{b}|$ and 11 $|\mathbf{b}|$ for basal edge and screw dislocations respectively. In particular, for the basal edge dislocation we find that beyond 14.3 $|\mathbf{b}|$, the change in the core structure is negligible and the change in $E_{\mathrm{d}}^{\mathrm{relax}}$ is within the tolerance 0.001 eV/Å. Similarly, for the basal screw dislocation we find that beyond 13.3 $|\mathbf{b}|$, the change in $E_{\mathrm{d}}^{\mathrm{relax}}$ is within the tolerance 0.001 eV/Å. Thus, we consider $14.3|\mathbf{b}|$ and 13.3 $|\mathbf{b}|$ to be the core sizes

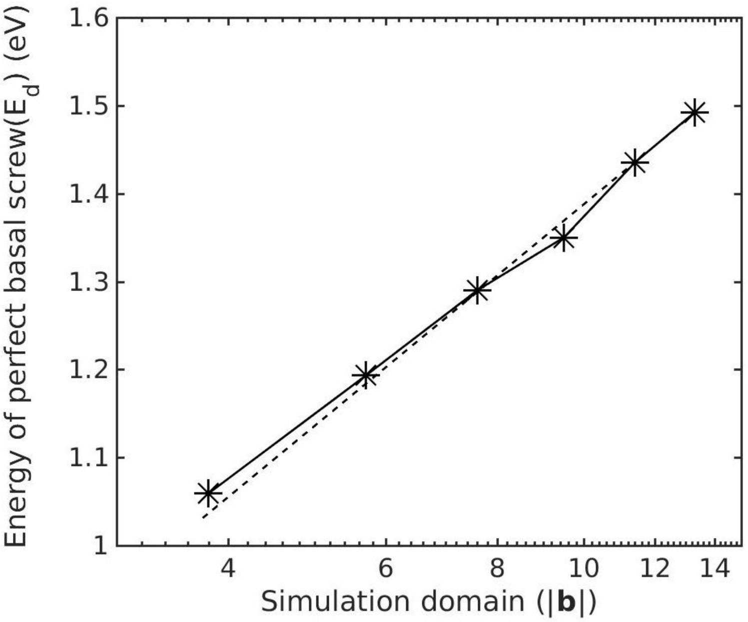

Figure 3.11: Semi-log plot of dislocation formation energy of the basal screw dislocation in Magnesium as a function of simulation domain size. The dashed line demonstrates the asymptotic logarithmic divergence of the computed dislocation energies, as expected from continuum estimates, beyond simulation domains of $\approx 11|\mathbf{b}|$.

of the relaxed basal edge dislocation and basal screw dislocations respectively. The core energy of Shockley partials for basal edge dislocation is computed to be 0.624 eV/Å($E_{\mathrm{d}}^{\mathrm{relax}} = 0.023$ eV/Å) and that for basal screw dislocation is computed to be 0.449 eV/Å($E_{\mathrm{d}}^{\mathrm{relax}} = 0.030$ eV/Å) . Figures 3.12 and 3.13 shows the edge and screw components of the differential displacements [114] of the basal edge and basal screw Schockley partials respectively. The partial separation distance is computed as the average of the partial separation distances from the edge and screw component differential displacement (DD) plots. For the basal edge dislocation, we find the partial separation distance to be 19.5 Å (6.3 $|\mathbf{b}|$), and for the basal screw dislocation it is 10.1 Å (3.2 $|\mathbf{b}|$). This is in good agreement with other DFT studies on basal edge and basal screw dislocations in Magnesium [45, 120], that have reported partial separation distances between 22–27 Å for basal edge dislocation and 12–15 Å for basal screw dislocation.

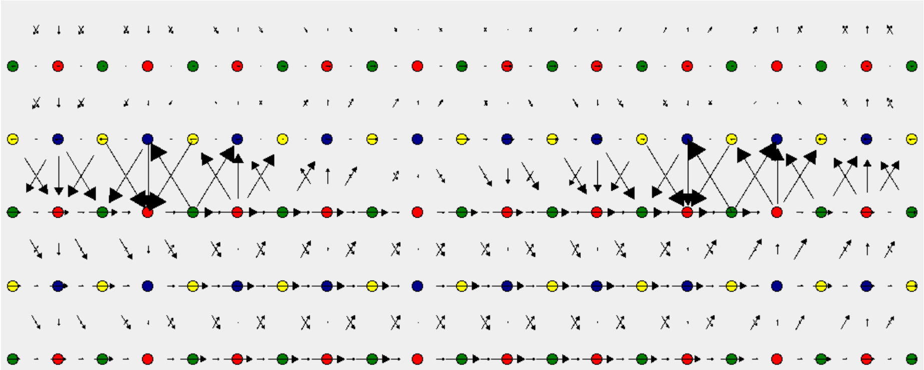

(a)

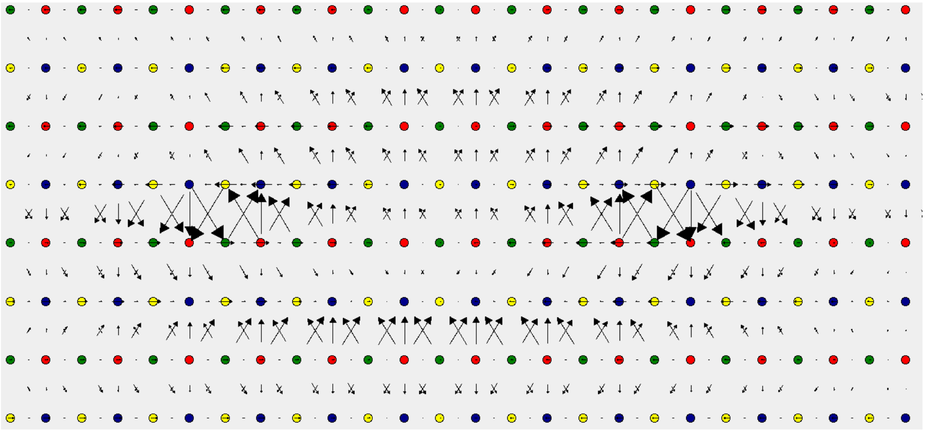

(b)

Figure 3.12: Differential displacement plots of the a) edge and b) screw components of Shockley partials of basal edge dislocation in Magnesium. The differential displacement plot is projected on the $(0\bar{1}10)$ plane.

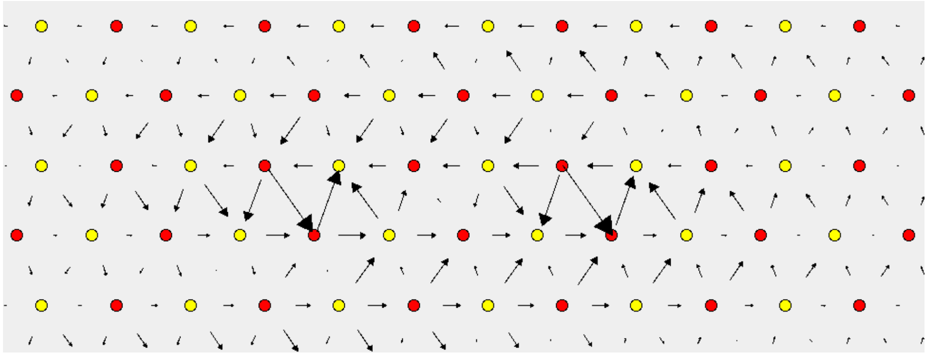

(a)

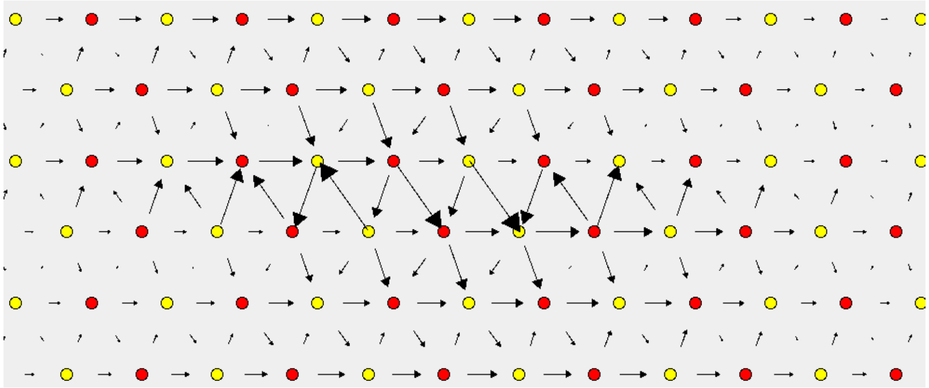

(b)

Figure 3.13: Differential displacement plots of the a) screw and b) edge components of Shockley partials of basal screw dislocation in Magnesium. The differential displacement plot is projected on the $(2\bar{1}\bar{1}0)$ plane.

3.3.2 Effect of macroscopic deformations

We now study the effect of macroscopic deformation on the core energy of basal edge and basal screw dislocations in Magnesium. Similar studies were performed on screw dislocation in Aluminum in Section 3.2.2 and on edge dislocation in Aluminum in [56, 57]. For both basal edge and basal screw dislocations, we consider a simulation domain corresponding to the core size of the relaxed Shockley partials— $14.3|\mathbf{b}|$ and $13.3\ |\mathbf{b}|$ for basal edge and basal screw dislocations respectively. On that simulation domain, we apply an affine deformation corresponding to a macroscopic strain $\boldsymbol{\epsilon}$, and, while holding the positions of the atoms fixed, we compute the electronic structure and the relaxed positions of atoms. Finally, the dislocation core energy, $E_{\text{disloc}}(\boldsymbol{\epsilon})$ is computed as a function of macroscopic strain using equation 3.2.

We first study the influence of macroscopic uniaxial strains along the coordinate directions, $[2\bar{1}\bar{1}0]$—$[0001]$—$[0\bar{1}10]$ for the basal edge dislocation and along $[01\bar{1}0]$—$[0001]$—$[2\bar{1}\bar{1}0]$ for the basal screw dislocation. For each of the coordinate directions we consider uniaxial strain values of -0.66%,-0.33%, 0.33%, and 0.66%. Figures 3.14(a), 3.14(b), and 3.15 show the core energy dependence of the basal edge dislocation on ϵ_{11} (uniaxial strain along $[2\bar{1}\bar{1}0]$), ϵ_{22} (uniaxial strain along $[0001]$) and ϵ_{33} (uniaxial strain along $[0\bar{1}10]$), respectively. Figures 3.17(a) and 3.17(b)(b) shows the core energy dependence of the basal screw dislocation on ϵ_{11} (uniaxial strain along $[01\bar{1}0]$) and ϵ_{22} (uniaxial strain along $[0001]$) respectively. In the case of the basal edge dislocation, the core energy dependence on uniaxial strains for the range of strains considered in this study is found to be in general non-monotonic and non-linear except for the ϵ_{11} strain, where the core energy dependence monotonically decreases from compressive to tensile strain. In the case of the basal screw dislocation, the core energy dependence on uniaxial strains is non-monotonic and non-linear for the ϵ_{11} strain whereas for the ϵ_{22} strain the core energy dependence monotonically decreases from compressive to tensile strain and demonstrates almost linear dependence. The core energy dependence for the ϵ_{22} is weaker than that for the ϵ_{11} strain. Interestingly, we observe that the slope of the core energy dependence for ϵ_{11} at zero strain has a positive sign in contrast to negative slope obtained in general for uniaxial strains in the case of basal edge dislocation in Magnesium and edge and screw dislocations in Aluminum.

Next, we consider the influence of the Ecsaig shear strain, which results in equal and opposite glide forces on the Shockley partials, leading to asymmetry in the core energy dependence as seen previously in the case of dislocations in Aluminum. In the case of basal edge dislocation, the relevant Ecsaig shear strain is the ϵ_{23} strain, and in the case of basal screw dislocation, the relevant Ecsaig shear strain is the ϵ_{12} strain. We consider shear strain values of -0.66%,-0.33%, 0.33%, and 0.66%. Figures 3.16 and 3.18 show the core energy dependence on Ecsaig shear strains for basal edge and screw dislocations respectively. Similar to previous observations in the case of dislocations in Aluminum, we observe significant and non-symmetric dependence of the core energy on the Ecsaig shear strains.

3.4 Core-force on an infinite straight dislocation

The studies in Sections 3.2.2 and 3.3.2 of the present work and Iyer et al. [56] demonstrate that the core energy of a dislocation is significantly dependent on macroscopic deformations. This core energy dependence on the macroscopic deformation results in an additional configurational force on the dislocation, beyond the Peach-Koehler force, which we refer to as the *core-force*. The core-force on a unit line segment of an infinite straight dislocation due to an external strain field $\boldsymbol{\epsilon}^{\mathrm{ext}}$ is given by

$$f_{\mathrm{c},i}(\boldsymbol{\epsilon}^{\mathrm{ext}}) = -\frac{\partial E_{\mathrm{c}}(\boldsymbol{\epsilon}^{\mathrm{ext}})}{\partial \epsilon_{kl}^{\mathrm{ext}}} \frac{\partial \epsilon_{kl}^{\mathrm{ext}}}{\partial x_i}, \tag{3.3}$$

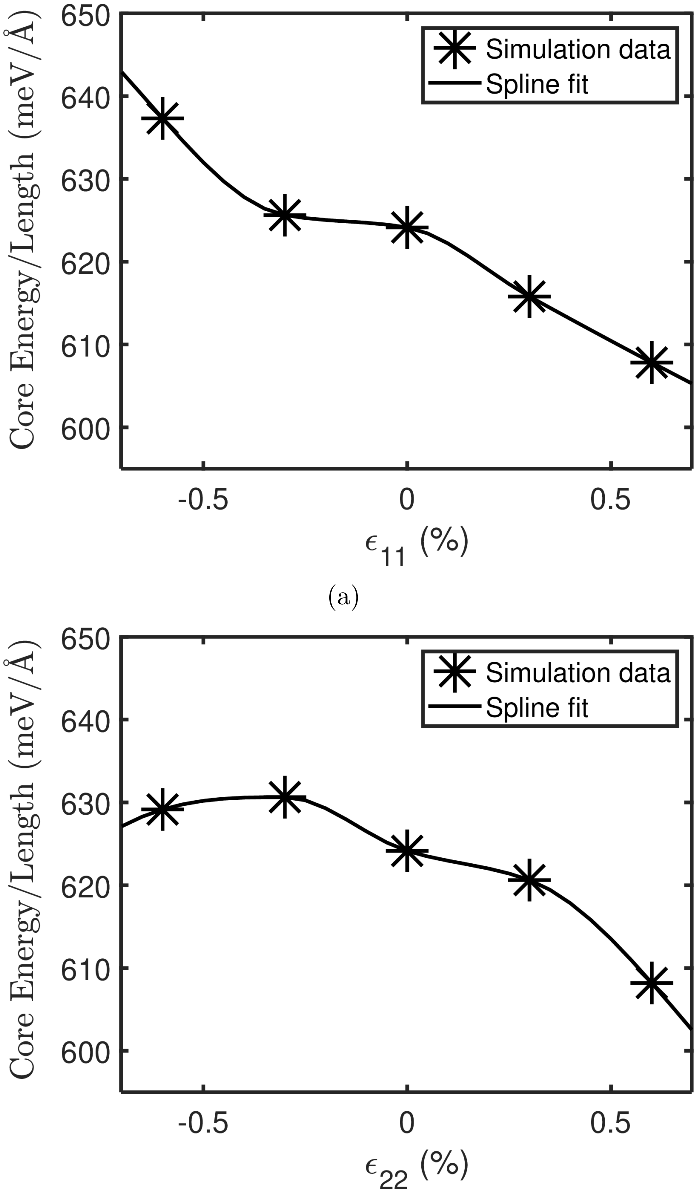

(a)

(b)

Figure 3.14: Basal edge dislocation in Magnesium: core-energy per unit length of dislocation line of relaxed Shockley partials as a function of uniaxial strains: (a) ϵ_{11}; (b) ϵ_{22}

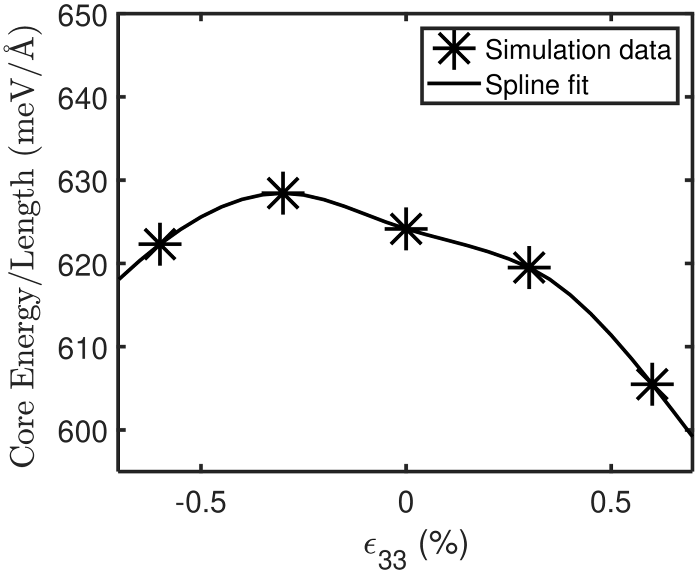

Figure 3.15: Basal edge dislocation in Magnesium: core-energy per unit length of dislocation line of relaxed Shockley partial as a function of ϵ_{33} uniaxial strain.

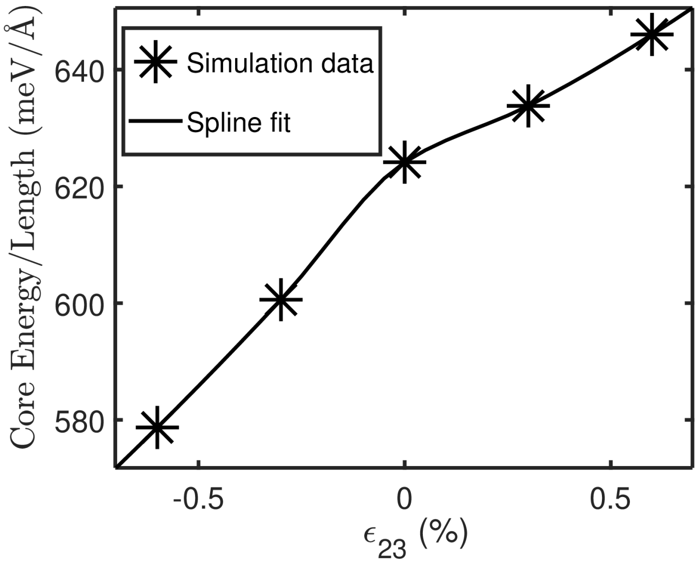

Figure 3.16: Basal edge dislocation in Magnesium: core-energy per unit length of dislocation line of relaxed Shockley partials as a function of Ecsaig shear strain ϵ_{23}.

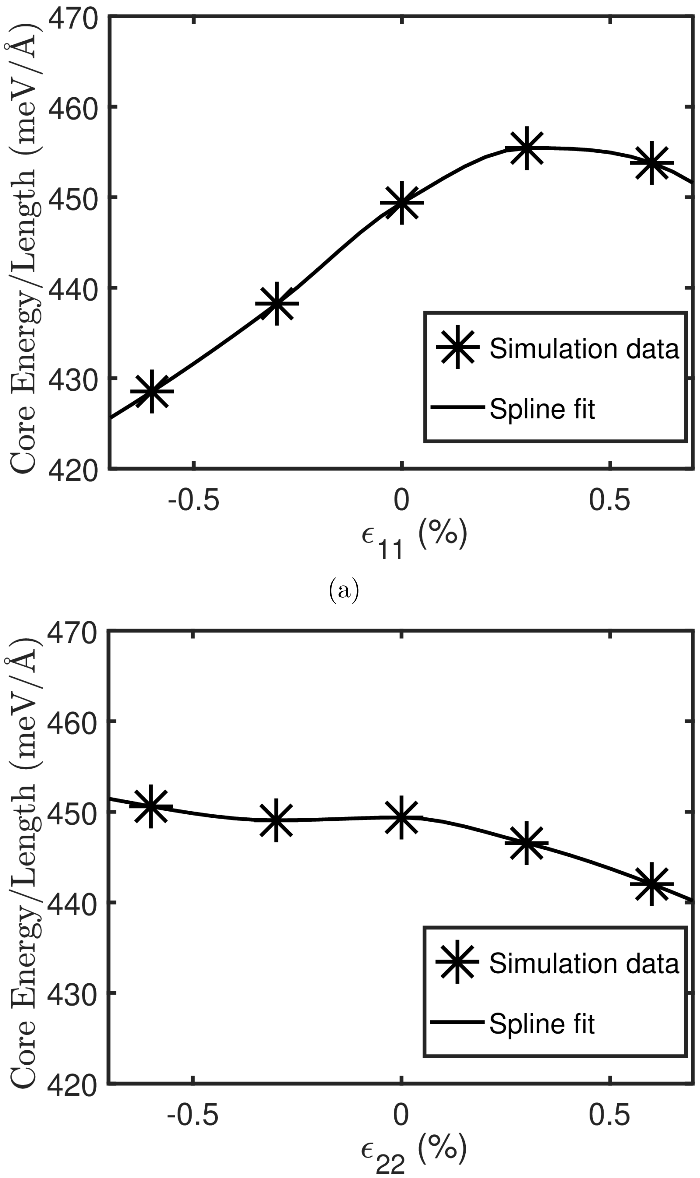

(a)

(b)

Figure 3.17: Basal screw dislocation in Magnesium: core-energy per unit length of dislocation line of relaxed Shockley partials as a function of uniaxial strains: (a) ϵ_{11}; (b) ϵ_{22}.

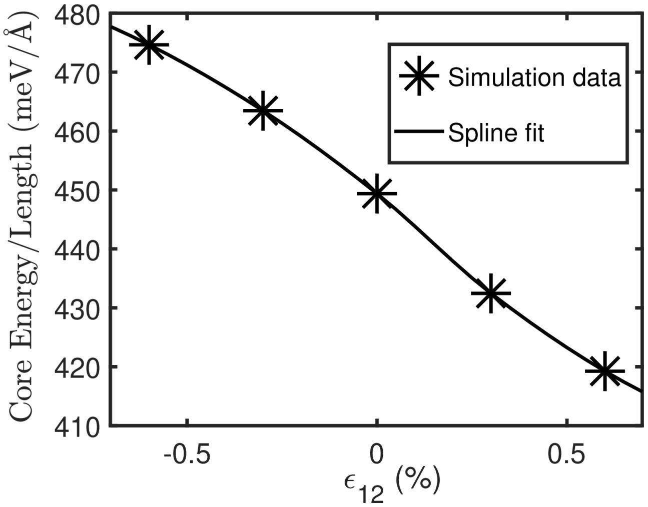

Figure 3.18: Basal screw dislocation in Magnesium: core-energy per unit length of dislocation line of relaxed Shockley partials as a function of Ecsaig shear strain ϵ_{12}.

where $E_c(\boldsymbol{\epsilon}^{\text{ext}})$ is the core energy of the dislocation per unit-length. In the above expression, the core size is assumed to be smaller than the length scale on which $\boldsymbol{\epsilon}^{\text{ext}}$ varies.

We note that the core-force on an infinite straight dislocation depends on the spatial gradient of the strain field. Thus, the core-force can play an important role in governing the dislocation behavior in regions of inhomogeneous deformations, such as the case of multiple interacting dislocations which has been widely studied using 3D discrete dislocation dynamics calculations (cf. Arsenlis and Parks [10], Arsenlis et al. [11], Bulatov et al. [13], Kubin et al. [14], Schwarz [18], Zbib et al. [19]) to predict macroscopic deformation response in crystalline materials. Apart from this, core forces may be significant in other physical scenarios involving dislocations in an external inhomogeneous strain field, such as interaction of dislocations with other defects like grain boundaries and precipitates (cf. [121–124]). In the next section, we develop a general framework for computing the core-force on a dislocation line segment in an aggregate of dislocations.

3.5 Summary

In summary, we studied the core structure and core energetics of an isolated screw dislocation in Aluminum and isolated basal edge and screw dislocations in Magnesium using a local real-space formulation of orbital-free DFT with finite-element discretization (RS-OFDFT). This study is complementary to an earlier RS-OFDFT study by [56, 57] on an isolated edge dislocation in Aluminum. In order to directly compute the core energetics, we employed mixed boundary conditions corresponding to an isolated dislocation embedded in the bulk—i.e., periodic boundary conditions along the dislocation line and bulk Dirichlet boundary conditions on the electronic fields obtained from the Cauchy-Born hypothesis along the boundary on the other two directions for fixed atomic positions on the boundary that are determined based on the elastic field of the dislocation. The local real-space formulation and the finite-element discretization are essential to realizing these boundary conditions, which are not accessible using the widely employed plane-wave discretization in electronic structure calculations. We computed the dislocation energies of a perfect dislocation in each dislocation type for a series of increasing domain sizes, and identified the region up to which the perturbations in the electronic structure are significant to the dislocation energetics. This allowed us to unambiguously characterize the core size, where the physics cannot be described using a homogenized continuum theory. We estimate, from an energetic viewpoint, the core size of the perfect screw dislocation in Aluminum to be $\approx 7\ |\mathbf{b}|$, and core sizes of basal edge and screw dislocations in Magnesium to be $\approx 8\ |\mathbf{b}|$ and $\approx 11\ |\mathbf{b}|$ respectively. These core sizes corresponds well with the estimated core size of $\approx 10\ |\mathbf{b}|$ for the perfect edge dislocation in Aluminum [56]. Significantly, these core sizes are much larger than the conventional estimates of 1–3 $|\mathbf{b}|$ based on displacement fields underlining the longer ranged nature of quantum mechanical perturbations in the energetics due to the dislocation core in comparison to displacement field deviation from elastic estimates. Upon ionic relaxation, the perfect screw dislocation in Aluminum and perfect basal edge and screw dislocations in Magnesium dissociated into two Shockley partials with partial separation distances comparing closely with other estimates from prior electronic structure studies. We also computed the core energy under externally applied affine volumetric, uniaxial and shear deformations, and found that, in general for dislocations in both Aluminum and Magnesium, the core energy was strongly dependent on the macroscopic deformations with non-zero slopes at zero deformation. Similar observations were reported for the core energetics of edge dislocation in Aluminum [56, 57]. This suggests that the dependence of the core energy on macroscopic deformations is a fundamental characteristic of dislocation energetics.

CHAPTER IV

Core-Force Model: Connecting Dislocation Core Energetics to Mesoscale Dislocation Behaviour

In this chapter, first in Section 4.1 a continuum model for an arbitrary aggregate of dislocations is developed, which takes into account the core energy dependence on macroscopic deformation, and the resulting additional configurational forces on the dislocations are derived. Next in Section 4.2, using case studies of dislocation–dislocation interactions, we demonstrate the significance of these additional configurational forces in relation to the elastic Peach-Koehler force. Finally in Section 4.3, using discrete dislocation dynamics (DDD) case studies, significant influence of the additional configurational forces on elementary dislocation mechanisms in Aluminum such as critical stress of a Frank-Read source and structure of a dislocation binary junction are demonstrated.

4.1 Core-energetics based forces for an aggregate of dislocations

In this section, we first develop an electronic-structure informed energetics model for an aggregate of dislocations in an isotropic infinite elastic continua, and subsequently, we obtain the forces in a discrete setting from variations of the total energy with respect to the degrees of freedom. In particular, we focus on the contribution to the forces arising from the core energy dependence on macroscopic deformations. In the present work, we have used RS-OFDFT calculations from Section 3.2 and Iyer et al. [56], Das et al. [57] to inform the core energetics model for Aluminum, however, the framework developed here is not materials system or data specific, and can be used with other materials systems and core energetics data from other studies. We note that recent DDD models have used core energetics information (cf. [15, 125]) from atomistic calculations resulting in additional force terms beyond the linear elastic Peach-Koehler force. However, the core energy is assumed to be a constant in these models, whereas it is evident from our study that the core energy can have a strong dependence on macroscopic strains. As noted in Section 3.4, for a simple case of an infinite edge dislocation, this dependence on macroscopic deformation results in another additional force that is proportional to external strain gradients and the slope of the core energy dependence on macroscopic strains (cf. equation (3.3)). In regions of inhomogeneous deformations with large strain gradients, this additional force can be significant as will be evident from the case studies presented in Section 4.2. Moreover, in Appendix B, we demonstrate that the slopes of the core energy dependence on macroscopic strains in Aluminum computed using atomistic calculations are sensitive to the choice of the interatomic potential, which underscores the need for quantum-mechanical calculations to compute the core energetics.

Broadly, this section comprises of two main parts, and is supported by Appendix B. Section 4.1.1 discusses the choice of the underlying linear elastic model, the partitioning of the total energy of the system into core and elastic energies, and the assumptions which go into developing the core energetics model for an arbitrary dislocation aggregate. Appendix B discusses the post-processing of the core energy data from RS-OFDFT calculations to remove the elastic effects consistent with the energy partition and tabulates the relevant information. In Section 4.1.2, we consider a dislocation network discretized into straight segments, and derive the forces on the nodes of the segments using linear shape functions.

4.1.1 Energetics model

We start by considering the elastic energy of the dislocation aggregate. We model the entire aggregate of dislocations as a collection of dislocation loops[1], and denote this by C. In an infinite isotropic elastic continua, using classical linear elastic theory of dislocations for small displacements, the stress field due to C at a spatial point $\mathbf{x}$ is expressed in terms of the line integral [5, 126],

$$\begin{aligned}\sigma^C_{\alpha\beta}(\mathbf{x}) =& \frac{\mu}{8\pi}\oint_C \partial_i\partial_p\partial_p R\left[b'_m\varepsilon_{im\alpha}\,\mathrm{d}x'_\beta + b'_m\varepsilon_{im\beta}\,\mathrm{d}x'_\alpha\right] \\ &+\frac{\mu}{4\pi(1-\nu)}\oint_C b'_m\varepsilon_{imk}\left(\partial_i\partial_\alpha\partial_\beta R - \delta_{\alpha\beta}\partial_i\partial_p\partial_p R\right)\mathrm{d}x'_k\,, \end{aligned} \tag{4.1}$$

where ε_{ijk} denotes the cyclic tensor, $\partial_i \equiv \frac{\partial}{\partial x_i}$, $R = \|\mathbf{x} - \mathbf{x}'\|$, $\mathbf{b}' = \mathbf{b}(\mathbf{x}')$ is the Burgers vectors at $\mathbf{x}'$, and μ and ν are the isotropic shear modulus and Poisson's ratio, respectively. The total elastic energy of C, denoted by E^C_{el}, is expressed as a double line integral [5, 126, 127],

$$\begin{aligned}E^C_{\mathrm{el}} =& -\frac{\mu}{8\pi}\oint_C\oint_C \partial_k\partial_k R\, b_i b'_j\,\mathrm{d}x_i\,\mathrm{d}x'_j - \frac{\mu}{4\pi(1-\nu)}\oint_C\oint_C \partial_i\partial_j R\, b_i b'_j\,\mathrm{d}x_k\,\mathrm{d}x'_k \\ &+\frac{\mu}{4\pi(1-\nu)}\left[\oint_C\oint_C \partial_k\partial_k R\, b_i b'_i\,\mathrm{d}x_j\,\mathrm{d}x'_j - \nu\oint_C\oint_C \partial_k\partial_k R\, b_i b'_j\,\mathrm{d}x_j\,\mathrm{d}x'_i\right]\,, \end{aligned} \tag{4.2}$$

where $\mathbf{b} = \mathbf{b}(\mathbf{x})$ and $\mathbf{b}' = \mathbf{b}(\mathbf{x}')$ are the Burgers vectors at $\mathbf{x}$ and $\mathbf{x}'$, respectively. We note that the partial derivatives of R appearing in the integrand of the above expressions for stress and energy become singular as $R \to 0$. In order to circumvent this issue, non-singular linear elastic theories [126, 128–130] have been proposed to remove the singularity in the elastic fields. Gradient elasticity theories [32–34] are also

---

[1] We are interested in dislocation loops as dislocation lines cannot terminate inside the crystal.

inherently non-singular, but we do not use them here as our focus is to investigate the forces from electronic structure effects at the dislocation core beyond what is captured by the classical linear elasticity theory. Among the non-singular formulations by Cai et al. [126], Brown [128], Gavazza and Barnett [129], Indenbom and Lothe [130], the formulations of Gavazza and Barnett [129] and Cai et al. [126], have the desirable variational property, i.e., the Peach-Koehler force on any point on the dislocation line is equal to the derivative of the total elastic energy with respect to its spatial position. In the Gavazza and Barnett [129] formulation, a tubular region around the dislocation is excluded from the elastic energy calculation, while in the Cai et al. [126] formulation, the Burgers vector is smeared using an isotropic spreading function characterized by a parameter a that quantifies the spread radius. In developing our model, we adopt the latter formulation as the former has difficulty dealing with dislocation lines with sharp corners which can be encountered at situations like junction nodes or cross-slip nodes. The total elastic energy of C using the non-singular formulation of Cai et al. [126] is given by

$$\begin{aligned} E^C_{\mathrm{el}}(a) = &-\frac{\mu}{8\pi}\oint_C\oint_C \partial_k\partial_k R_a b_i b'_j \,\mathrm{d}x_i\,\mathrm{d}x'_j - \frac{\mu}{4\pi(1-\nu)}\oint_C\oint_C \partial_i\partial_j R_a b_i b'_j \,\mathrm{d}x_k\,\mathrm{d}x'_k \\ &+\frac{\mu}{4\pi(1-\nu)}\left[\oint_C\oint_C \partial_k\partial_k R_a b_i b'_i \,\mathrm{d}x_j\,\mathrm{d}x'_j - \nu\oint_C\oint_C \partial_k\partial_k R_a b_i b'_j \,\mathrm{d}x_j\,\mathrm{d}x'_i\right], \quad (4.3) \end{aligned}$$

where $R_a = \sqrt{R^2 + a^2}$. Choosing $a > 0$, the spatial derivatives of R_a are no longer singular, and we assume this going forward. We refer to Cai et al. [126] for the non-singular expression for the stress field, which, analogous to equation (4.1), is expressed as a line integral. The non-singular stress field can be expressed in a condensed manner as

$$\sigma^C_{\alpha\beta}(\mathbf{x}; a) = \oint_C \bar{\sigma}_{\alpha\beta}\left(\boldsymbol{\xi}(\mathbf{x}'(s')), \mathbf{b}(\mathbf{x}'(s')), \mathbf{x} - \mathbf{x}'(s'); a\right) \mathrm{d}s', \quad (4.4)$$

where $\bar{\sigma}_{\alpha\beta}$ denotes the per unit-length contribution to the stress field at the spatial point $\mathbf{x}$ from the dislocation line at $\mathbf{x}'(s')$, with s' being the length parametric variable of C. The other dependencies of $\bar{\sigma}_{\alpha\beta}$ are $\boldsymbol{\xi}(\mathbf{x}')$, which is the tangent line direction at $\mathbf{x}'$ such that $\boldsymbol{\xi}(\mathbf{x}')\mathrm{d}s' = \mathrm{d}\mathbf{x}'$, and $\mathbf{b}(\mathbf{x}')$ is the Burgers vector at $\mathbf{x}'$. The dependency on the isotropic elastic constants, μ and ν, is implicit. Similarly, the non-singular strain field is also expressed as

$$\epsilon^C_{\alpha\beta}(\mathbf{x};a) = \oint_C \bar{\epsilon}_{\alpha\beta}\left(\boldsymbol{\xi}(\mathbf{x}'(s')), \mathbf{b}(\mathbf{x}'(s')), \mathbf{x}-\mathbf{x}'(s'); a\right)\mathrm{d}s' \,, \tag{4.5}$$

where $\bar{\epsilon}_{\alpha\beta}$ is the per unit-length contribution to the strain field at spatial point $\mathbf{x}$ from the dislocation line at $\mathbf{x}'(s')$, with the same dependencies as the stress field. This representation for the strain field will be used in the subsequent development of the core energetics model. We note that this representation can also be extended to the anisotropic case, where the anisotropic stress and strain fields of a dislocation loop are expressed as a line integral [131], as well as to gradient elasticity theories [33, 34].

4.1.1.1 Non-elastic core energetics model

We now develop a model that accounts for the dislocation core energy in the total energy of C, and its dependence on macroscopic strain, which is informed by the core energetics data obtained from RS-OFDFT electronic structure calculations. To this end, we refer to the total energy of C inside the tubular domain corresponding to the core-size (core-domain) as the core energy, and denote this by E^C_{c}. A portion of E^C_{c} is the non-singular elastic energy of the core-domain, which we denote as $E^C_{\mathrm{cel}}(a)$ (core-domain elastic energy or elastic core-energy). We refer to the remaining part of the core energy as the non-elastic core-energy, denoted by $E^C_{\mathrm{cnel}}(a)$, which includes contributions from atomistic and quantum mechanical effects inside the dislocation core. Thus, we have the following partitioning for the the core energy:

$$E_{\mathrm{c}}^{C} = E_{\mathrm{cel}}^{C}(a) + E_{\mathrm{cnel}}^{C}(a). \tag{4.6}$$

We note that as E_{cel}^{C} depends on the choice of the spread radius (a) in the non-singular approximation, E_{cnel}^{C} also depends on a. Changing a changes the partitioning of total core energy E_{c}^{C}, but this has no effect on the dislocation properties (energy and forces) as these are governed by E_{c}^{C}, which is informed from electronic structure calculations and is independent of a. Furthermore, the energy outside the core-domain is solely elastic energy and is independent of the spread radius a—the non-singular elastic fields converge to the classical elastic fields at distances beyond a, and commonly used values of a, $a < 2|\mathbf{b}|$ [15, 125], are much smaller than the RS-OFDFT calculated core-size of 7–10 $|\mathbf{b}|$. Thus, the total energy of C, which we denote as E_{tot}^{C}, is independent of a, and is given by

$$E_{\mathrm{tot}}^{C} = E_{\mathrm{el}}^{C}(a) + E_{\mathrm{cnel}}^{C}(a)\,. \tag{4.7}$$

We now present a model for E_{c}^{C} using reasonable approximations, where the model is directly informed by the core-energetics data from RS-OFDFT, and we subsequently extract the non-elastic core-energy $E_{\mathrm{cnel}}^{C}(a)$ using the partitioning in equation (4.6). In our model, we ignore the non-elastic effects arising from the direct core-core interactions between any two points on C, which is a reasonable approximation as the average separation between dislocations in DDD simulations is larger than the RS-OFDFT estimated core-size of 7–10 $|\mathbf{b}|$. Under this approximation, E_{c}^{C} can be expressed as a line integral on C. Further, we approximate the core energy per unit length at any point $\mathbf{x}(s)$ with that of an infinite straight dislocation having the same local Burgers vector ($\mathbf{b}(s)$), the same tangent line direction ($\boldsymbol{\xi}(s)$), and embedded in the same macroscopic environment, i.e., the infinite straight dislocation subjected to the same external strain field as being felt by the dislocation core at $\mathbf{x}(s)$. In other words, we ignore the possible explicit dependence of E_{c}^{C} on the curvature of C. Thus, under these approximations, the core energy is given by

$$E_{\mathrm{c}}^{C} = \oint_{C} E_{\mathrm{c}}^{\mathrm{str}}(\boldsymbol{\xi}(s), \mathbf{b}(s), \boldsymbol{\epsilon}^{\mathrm{ext}_{\mathrm{loc}}}(\mathbf{x}(s) + \mathbf{x}_{\mathrm{c}}))\,\mathrm{d}s, \qquad \mathbf{x}_{\mathrm{c}} \in \Omega_{\mathrm{c}}\,, \tag{4.8}$$

where $E_{\mathrm{c}}^{\mathrm{str}}$ denotes core energy per unit length of an infinite straight dislocation. In the above expression, $\boldsymbol{\epsilon}^{\mathrm{ext}_{\mathrm{loc}}}(\mathbf{x}(s) + \mathbf{x}_{\mathrm{c}})$ denotes the external strain field experienced by all points $\mathbf{x}_{\mathrm{c}}$ in the dislocation core domain Ω_{c}, where $\mathbf{x}_{\mathrm{c}}$ is the position vector with respect to the core center at $\mathbf{x}(s)$. The external strain field is due to the entire dislocation network C excluding the dislocation lines at and near the dislocation core, which is computed using a cut-off procedure that will be discussed subsequently. The symbol "loc" is used to denote that the strain tensor is expressed in a local coordinate frame at $\mathbf{x}(s)$, which is aligned such that the axis labelled '1' lies on the slip plane at $\mathbf{x}(s)$ and is perpendicular to $\boldsymbol{\xi}(s)$, axis labelled '2' is perpendicular to the slip plane, and the axis labelled '3' is along $\boldsymbol{\xi}(s)$. This choice of the local coordinate axes is the same as those employed in RS-OFDFT calculations and thus allows an immediate parametrization of the core energy dependence on macroscopic strains from the RS-OFDFT core energetics data. The transformation of the strain tensor field $\bar{\boldsymbol{\epsilon}}$ (the integrand in equation (4.5)) from the global frame to the local frame is given by

$$\begin{aligned} &\bar{\epsilon}_{\alpha\beta}^{\mathrm{loc}}\left(\boldsymbol{\xi}(s'), \mathbf{b}(s'), \mathbf{x} - \mathbf{x}'(s')\right) = \\ &\qquad R_{k\alpha}(\boldsymbol{\xi}(s), \mathbf{b}(s)) R_{l\beta}(\boldsymbol{\xi}(s), \mathbf{b}(s)) \bar{\epsilon}_{kl}\left(\boldsymbol{\xi}(s'), \mathbf{b}(s'), \mathbf{x} - \mathbf{x}'(s')\right), \end{aligned} \tag{4.9}$$

where the rotation matrix $\mathbf{R}(\boldsymbol{\xi}(s), \mathbf{b}(s))$ maps the components of any vector in the local coordinate frame at $\mathbf{x}(s)$ to the components of the same vector in the global coordinate frame. We note that the dependency on the smearing parameter, a, is ignored in the above expression as the separation between the dislocations is assumed to be larger than a. Using equations (4.5) and (4.9), as the rotation matrix is independent of s', the external strain field in the local coordinate frame, $\boldsymbol{\epsilon}^{\text{ext}_{\text{loc}}}(\mathbf{x})$, is given by

$$\epsilon_{\alpha\beta}^{\text{ext}_{\text{loc}}}(\mathbf{x}) = \int_{C-\rho_{\text{cut}}} \bar{\epsilon}_{\alpha\beta}^{\text{loc}}\left(\boldsymbol{\xi}(s'), \mathbf{b}(s'), \mathbf{x} - \mathbf{x}'(s')\right)\, \mathrm{d}s', \tag{4.10}$$

where ρ_{cut} is a small cut-off radius characterizing a spherical region centered at $\mathbf{x}(s)$, and the dislocation lines inside this region are excluded in evaluating the above line integral. We note that the use of this cut-off approach is solely to restrict the sources of the external strain field to those outside of the dislocation core, and is not an attempt to regularize the external strain field at the core as the regularization is already achieved by virtue of the non-singular elastic model. We further note that the external strain field in the above expression is considered to be independent of a, as the average separation distance in DDD calculations is greater than the values used for a, beyond which the strain fields are independent of the choice of a. Thus, by extension, E_{c}^{C} is also independent of the choice of a. We now consider reasonable simplifications to equations (4.8) and (4.10), which enable us to use the available RS-OFDFT data to inform the core energy.

Simplification (1): In equation (4.8), the core energy per unit length of the straight dislocation, $E_{\text{c}}^{\text{str}}$, in all generality, is a function of the external strain field at all points inside the core. However, parametrizing $E_{\text{c}}^{\text{str}}$ in the strain field function space is intractable. A reasonable approximation will be to simplify this dependence to a homogeneous mean-field strain dependence. To this end, we simplify the dependence to the external strain field at the dislocation line ($\mathbf{x}_{\text{c}} = \mathbf{0}$), given by

$$E_{\text{c}}^{C} = \oint_{C} E_{\text{c}}^{\text{str}}(\boldsymbol{\xi}(s), \mathbf{b}(s), \boldsymbol{\epsilon}^{\text{ext}_{\text{loc}}}(\mathbf{x}(s)))\, \mathrm{d}s\,. \tag{4.11}$$

We note that this approximation is reasonable when the distance between dislocations is much larger than the core-size.

Simplification (2): We note that the dependence of $E_{\mathrm{c}}^{\mathrm{str}}$ on $\boldsymbol{\xi}(s)$ and $\mathbf{b}(s)$ arises from the changing character for the dislocation that depends on the angle between the line direction and the Burgers vector, given by

$$\theta(s) = \arccos\left(\frac{\boldsymbol{\xi}(s)\cdot\mathbf{b}(s)}{\|\mathbf{b}(s)\|}\right) . \tag{4.12}$$

Parametrizing $E_{\mathrm{c}}^{\mathrm{str}}$ as a function of $\theta(s)$ can be very tedious and time consuming especially using electronic structure calculations. To this end, we adopt the commonly used approximation, where the core energy of a dislocation with mixed character is interpolated from the core energies of the edge and screw dislocations as

$$\begin{aligned} &E_{\mathrm{c}}^{\mathrm{str}}(\boldsymbol{\xi}(s), \mathbf{b}(s), \boldsymbol{\epsilon}^{\mathrm{ext}_{\mathrm{loc}}}(\mathbf{x}(s))) = \\ &\qquad E_{\mathrm{c}}^{\mathrm{edge}}(\boldsymbol{\epsilon}^{\mathrm{ext}_{\mathrm{loc}}}(\mathbf{x}(s)))\sin^2(\theta(s)) + E_{\mathrm{c}}^{\mathrm{screw}}(\boldsymbol{\epsilon}^{\mathrm{ext}_{\mathrm{loc}}}(\mathbf{x}(s)))\cos^2(\theta(s)) . \end{aligned} \tag{4.13}$$

Simplification (3): In general, the dependence of $E_{\mathrm{c}}^{\mathrm{str}}$ on $\boldsymbol{\epsilon}^{\mathrm{ext}_{\mathrm{loc}}}$ can be non-linear. However, when the distance between dislocations is sufficiently large, the external strain fields at the dislocation line are small. Thus, we can further simplify the dependence of $E_{\mathrm{c}}^{\mathrm{str}}$ on $\boldsymbol{\epsilon}^{\mathrm{ext}_{\mathrm{loc}}}$ by using a Taylor expansion to first order about $\boldsymbol{\epsilon}^{\mathrm{ext}_{\mathrm{loc}}} = 0$ as

$$\begin{aligned} E_{\mathrm{c}}^{C} = \oint_{C} \big[&E_{\mathrm{c}}^{\mathrm{str}}(\boldsymbol{\xi}(s), \mathbf{b}(s), \boldsymbol{\epsilon}^{\mathrm{ext}_{\mathrm{loc}}}(\mathbf{x}(s)) = \mathbf{0}) \\ &+ S_{\alpha\beta}(\boldsymbol{\xi}(s), \mathbf{b}(s))\epsilon_{\alpha\beta}^{\mathrm{ext}_{\mathrm{loc}}}(\mathbf{x}(s))\big] \,\mathrm{d}s , \end{aligned} \tag{4.14}$$

where $S_{\alpha\beta}(\boldsymbol{\xi}(s), \mathbf{b}(s))$ is the slope of the core energy dependence on external strain evaluated at zero strain,

$$S_{\alpha\beta}(\boldsymbol{\xi}(s),\mathbf{b}(s)) = \left.\frac{\partial E_{\mathrm{c}}^{\mathrm{str}}\left(\boldsymbol{\xi}(s),\mathbf{b}(s),\boldsymbol{\epsilon}^{\mathrm{ext_{loc}}}\right)}{\partial \epsilon_{\alpha\beta}^{\mathrm{ext_{loc}}}}\right|_{\boldsymbol{\epsilon}^{\mathrm{ext_{loc}}}=\mathbf{0}}. \tag{4.15}$$

The values of the slopes for dislocations with mixed character are evaluated, using equation (4.13), from the slopes of the pure edge and screw dislocations, which, in turn, are available using RS-OFDFT calculations.

Next, using the partition in equation (4.6), we obtain $E_{\mathrm{cnel}}^{C}(a)$ from E_{c}^{C} by subtracting the non-singular linear elastic energy. The values of the slopes at zero strain in equation (4.15) are also accordingly obtained by removing the contribution from the non-singular elastic energy. We refer to Appendix B for details of this post-processing. Finally, as a counterpart of equation (4.11), we obtain

$$E_{\mathrm{cnel}}^{C}(a) = \oint_C E_{\mathrm{cnel}}^{\mathrm{str}}(\boldsymbol{\xi}(s),\mathbf{b}(s),\boldsymbol{\epsilon}^{\mathrm{ext_{loc}}}(\mathbf{x}(s));a)\,\mathrm{d}s\,, \tag{4.16}$$

and as the counterpart of the linearized equations (4.14), we obtain

$$\begin{aligned} E_{\mathrm{cnel}}^{C}(a) = \oint_C & \Big[E_{\mathrm{cnel}}^{\mathrm{str}}(\boldsymbol{\xi}(s),\mathbf{b}(s),\boldsymbol{\epsilon}^{\mathrm{ext_{loc}}}(\mathbf{x}(s))=\mathbf{0};a) \\ & +\hat{S}_{\alpha\beta}(\boldsymbol{\xi}(s),\mathbf{b}(s);a)\epsilon_{\alpha\beta}^{\mathrm{ext_{loc}}}(\mathbf{x}(s))\Big]\,\mathrm{d}s\,, \end{aligned} \tag{4.17}$$

where

$$\hat{S}_{\alpha\beta}(\boldsymbol{\xi}(s),\mathbf{b}(s);a) = \left.\frac{\partial E_{\mathrm{cnel}}^{\mathrm{str}}\left(\boldsymbol{\xi}(s),\mathbf{b}(s),\boldsymbol{\epsilon}^{\mathrm{ext_{loc}}};a\right)}{\partial \epsilon_{\alpha\beta}^{\mathrm{ext_{loc}}}}\right|_{\boldsymbol{\epsilon}^{\mathrm{ext_{loc}}}=\mathbf{0}}. \tag{4.18}$$

We note that an important limitation of the aforementioned model stems from neglecting direct interactions between dislocation cores at different points on the dislocation aggregate. This is a reasonable assumption when distances between the dislocations are much larger compared to the core-size. However, there are practical situations where this assumption fails—e.g. when radius of curvature of the dislocation line is comparable to core-size, dislocations passing each other at distances less than core size, and dislocation core reactions like annihilation and junction formation. In such situations, the energetics have to be obtained from direct electronic structure calculations of the dislocation-dislocation interactions, which are still out of reach for such large systems. We note that, even for these situations, the energetics model developed here is an improvement over existing models that ignore the core energy dependence on external strains.

4.1.2 Derivation of nodal core force in a discretized network of dislocation line segments

In a 3D nodal discrete dislocation network, it is common to discretize the dislocation line into straight line segments forming discretized polygonal loops. The network is represented by a set of nodes with position vectors $\{\mathbf{r}^i\}$, which are connected by straight segments. The other set of degrees of freedom corresponds to $\mathbf{b}^{ij}$, which denotes the perfect dislocation Burgers vector of line-segment $\mathbf{l}^{ij} = \mathbf{r}^j - \mathbf{r}^i$ pointing from node i to node j. Here ij denotes the index of the line segment, $\mathbf{l}^{ij}$. Overall, we denote the network as $C \equiv \{\mathbf{r}^i, \mathbf{b}^{ij}\}$. Constraints are imposed on $\mathbf{b}^{ij}$ and the nodal connections such that the Burgers vector at each node is conserved, and dislocation lines cannot end in the crystal. Additionally, $\mathbf{b}^{ij}$ are assumed to be constant when the nodal positions $\{\mathbf{r}^i\}$ are updated without changing the node connectivity. We refer to [10, 11, 13] for a comprehensive description of the 3D DDD implementation including mobility laws, time integration, topological rearrangements, treatment of dislocation core reactions, and computational strategies. In this study, we are concerned with the nodal forces arising from non-elastic core energy contributions.

Applying the core energetics model we developed in Section 4.1.1 to a discrete dislocation network $C \equiv \{\mathbf{r}^i, \mathbf{b}^{ij}\}$, we obtain the non-elastic core energetics as (cf.

equation (4.16)),

$$E^C_{\text{cnel}}(a) = \sum_{ij \in U} \int_0^{L_{ij}} E^{\text{str}}_{\text{cnel}}(\boldsymbol{\xi}^{ij}, \mathbf{b}^{ij}, \boldsymbol{\epsilon}^{\text{ext}_{\text{loc}}}(\mathbf{x}^{ij}(s_{ij})); a)\, \mathrm{d}s_{ij}\,. \tag{4.19}$$

In the above, $L_{ij} = \|\mathbf{l}^{ij}\|$ is the length of $\mathbf{l}^{ij}$, $\boldsymbol{\xi}^{ij} = \frac{\mathbf{l}^{ij}}{\|\mathbf{l}^{ij}\|}$ is the unit vector corresponding to $\mathbf{l}^{ij}$, $\mathbf{x}^{ij}(s_{ij})$ is the position vector of a point on $\mathbf{l}^{ij}$, parametrized by s_{ij}, which is the parametric length coordinate of $\mathbf{l}^{ij}$ measured from node i towards node j. The index ij is summed over the set U, which represents the collection of all distinct line segments in the dislocation network. In particular, ij and ji are *not* considered as distinct as they refer to the same segment but with reversed directions for the unit vector and Burgers vector. Further, for computing the external strain field, we follow a more convenient cut-off procedure suited to the segment discretization rather than the spherical cut-off procedure used in equation (4.10). This is given by

$$\boldsymbol{\epsilon}^{\text{ext}_{\text{loc}}}(\mathbf{x}^{ij}(s_{ij})) = \sum_{kl \in U'_{ij}} \boldsymbol{\epsilon}^{kl_{\text{loc}}}(\boldsymbol{\xi}^{kl}, \mathbf{b}^{kl}, \mathbf{x}^{ij}(s_{ij})), \tag{4.20}$$

where $\boldsymbol{\epsilon}^{kl_{\text{loc}}}(\boldsymbol{\xi}^{kl}, \mathbf{b}^{kl}, \mathbf{x}^{ij}(s_{ij}))$ is the strain field contribution of $\mathbf{l}^{kl}$ segment at the spatial point $\mathbf{x}^{ij}(s_{ij})$, expressed in the local frame attached to $\mathbf{l}^{ij}$ in which the electronic structure core-energetics data is available, and the set U'_{ij} comprises of all distinct line segments in the network excepting those that have i or j as one of their nodes. In other words, the set U'_{ij} excludes the segment $\mathbf{l}^{ij}$ and its immediate neighbours. We note that this approach and the spherical cut-off approach converge to the same external strain field as $\max_{ij\in U} L_{ij} \to 0$ and $\rho_{\text{cut}} \to 0$, respectively. In the above expression, $\boldsymbol{\epsilon}^{kl_{\text{loc}}}(\boldsymbol{\xi}^{kl}, \mathbf{b}^{kl}, \mathbf{x}^{ij}(s_{ij}))$ is expressed using equation (4.9) as

$$\epsilon^{kl_{\text{loc}}}_{\alpha\beta}(\boldsymbol{\xi}^{kl}, \mathbf{b}^{kl}, \mathbf{x}^{ij}(s_{ij})) = R_{\eta\alpha}(\boldsymbol{\xi}^{ij}, \mathbf{b}^{ij}) R_{\omega\beta}(\boldsymbol{\xi}^{ij}, \mathbf{b}^{ij}) \epsilon^{kl}_{\eta\omega}(\boldsymbol{\xi}^{kl}, \mathbf{b}^{kl}, \mathbf{x}^{ij}(s_{ij}))\,, \tag{4.21}$$

which transforms the strain field contribution from $\mathbf{l}^{kl}$ segment at the spatial point

$\mathbf{x}^{ij}(s_{ij})$ in the global frame to the local frame attached to $\mathbf{l}^{ij}$. Next, we substitute equation (4.20) in equation (4.19), and linearize the dependence of the non-elastic core energy on the external macroscopic strain using equations (4.17) and (4.18), to simplify $E^{C}_{\text{cnel}}(a)$ as

$$\begin{aligned} E^{C}_{\text{cnel}}(a) &= \sum_{ij\,\in U} \int_0^{L_{ij}} E^{\text{str}}_{\text{cnel}}(\boldsymbol{\xi}^{ij}, \mathbf{b}^{ij}, \boldsymbol{\epsilon}^{\text{ext}_{\text{loc}}}(\mathbf{x}^{ij}(s_{ij})); a)\, \mathrm{d}s_{ij}, \\ &\approx \sum_{ij\,\in U} E^{\text{str}}_{\text{cnel}}(\boldsymbol{\xi}^{ij}, \mathbf{b}^{ij}, \mathbf{0}; a) L_{ij} \\ &\quad + \sum_{ij\,\in U} \sum_{kl\,\in U'_{ij}} \hat{S}_{\alpha\beta}(\boldsymbol{\xi}^{ij}, \mathbf{b}^{ij}; a) \int_0^{L_{ij}} \epsilon^{kl_{\text{loc}}}_{\alpha\beta}(\boldsymbol{\xi}^{kl}, \mathbf{b}^{kl}, \mathbf{x}^{ij}(s_{ij}))\, \mathrm{d}s_{ij}\,. \end{aligned} \tag{4.22}$$

For keeping the subsequent analysis concise, we rewrite the above expression in a condensed form as

$$E^{C}_{\text{cnel}}(a) = \sum_{ij\,\in U} T^{ij}_{\text{self}} + \sum_{ij\,\in U} \sum_{kl\,\in U'_{ij}} T^{(ij,kl)}_{\text{ext}}\,. \tag{4.23}$$

The force on node i, $\mathbf{F}^i$, is the negative derivative of the total energy with respect to the position $\mathbf{r}^i$, i.e.,

$$\begin{aligned} \mathbf{F}^i &= -\frac{\partial E^{C}_{\text{el}}(a)}{\partial \mathbf{r}^i} - \frac{\partial E^{C}_{\text{cnel}}(a)}{\partial \mathbf{r}^i} \\ &= \mathbf{F}^i_{\text{el}} + \mathbf{F}^i_{\text{c}}, \end{aligned} \tag{4.24}$$

where $\mathbf{F}^i_{\text{el}}$ and $\mathbf{F}^i_{\text{c}}$ are the nodal elastic force and core force contributions. $\mathbf{F}^i_{\text{el}}$, has been analytically determined in previous literature [11, 126] for the non-singular elastic formulation, by applying the principle of virtual work and using the Peach-Koehler formula. The focus in this study is on obtaining the expressions for $\mathbf{F}^i_{\text{c}}$. Using the representation in (4.23), $\mathbf{F}_{\mathrm{c}}^{i}$ is given by

$$\mathbf{F}_{\mathrm{c}}^{i} = -\frac{\partial E_{\mathrm{cnel}}^{C}(a)}{\partial \mathbf{r}^{i}} = \sum_{j} \mathbf{f}_{\mathrm{cs}}^{\{i\}j} + \sum_{j} \sum_{kl \in U'_{ij}} \mathbf{f}_{\mathrm{ce}}^{(\{i\}j,kl)} + \sum_{j} \sum_{kl \in U'_{ij}} \tilde{\mathbf{f}}_{\mathrm{ce}}^{(\{i\}j,kl)}, \tag{4.25a}$$

$$\mathbf{f}_{\mathrm{cs}}^{\{i\}j} = -\frac{\partial T_{\mathrm{self}}^{ij}}{\partial \mathbf{r}^{i}}; \quad \mathbf{f}_{\mathrm{ce}}^{(\{i\}j,kl)} = -\frac{\partial T_{\mathrm{ext}}^{(ij,kl)}}{\partial \mathbf{r}^{i}}; \quad \tilde{\mathbf{f}}_{\mathrm{ce}}^{(\{i\}j,kl)} = -\frac{\partial T_{\mathrm{ext}}^{(kl,ij)}}{\partial \mathbf{r}^{i}}, \tag{4.25b}$$

where j runs over all nodes which have a connection to node i, and the superscript notation '$\{i\}$' denotes that the force is with respect to perturbation of node i. In the above, the first term, $\mathbf{f}_{\mathrm{cs}}^{\{i\}j}$, is force resulting from change in T_{self}^{ij} due to perturbation of $\mathbf{r}^{i}$, but this does not account for the force resulting from the core energy dependence on external macroscopic strains. We note that this term is already incorporated into current DDD implementations [11, 15], but, we still analyze it here for the sake of completeness. The next two terms in the nodal force manifest from the core energy dependence on external strain, and these are not considered in current DDD implementations. To elaborate, $\mathbf{f}_{\mathrm{ce}}^{(\{i\}j,kl)}$ is the contribution to $\mathbf{F}_{\mathrm{c}}^{i}$ arising from the core energy change of segment $\mathbf{l}^{ij}$ due its dependence on the external strain field of another segment $\mathbf{l}^{kl}$ ($kl \in U'_{ij}$), and $\tilde{\mathbf{f}}_{\mathrm{ce}}^{(\{i\}j,kl)}$ is the contribution arising from the core energy change of the segment $\mathbf{l}^{kl}$ ($kl \in U'_{ij}$) due to its dependence on the strain field of $\mathbf{l}^{ij}$.

We now derive the expressions for each of the terms contributing to $\mathbf{F}_{\mathrm{c}}^{i}$ from the first order perturbations in T_{self}^{ij}, $T_{\mathrm{ext}}^{(ij,kl)}$ and $T_{\mathrm{ext}}^{(kl,ij)}$ resulting from a perturbation of the nodal position $\mathbf{r}^{i}$, while holding the other nodes fixed. Noting that the segments are always constrained to remain straight, we define a linear shape function attached to node i having a compact support over all segments $\mathbf{l}^{ij}$ attached to it,

$$N_i(\mathbf{x}^{ij}(s_{ij})) = \frac{\|\mathbf{x}^{ij}(s_{ij}) - \mathbf{r}_j\|}{\|\mathbf{r}_i - \mathbf{r}_j\|}, \tag{4.26}$$

which can also be expressed as

$$N_i(s_{ij}) = \frac{L_{ij} - s_{ij}}{L_{ij}} \,. \tag{4.27}$$

We first start with computing the first order perturbations in T^{ij}_{self} with respect to $\mathbf{r}^i$, and aim to write them in the form

$$\delta T^{ij}_{\text{self}} = -\mathbf{f}^{\{i\}j}_{\text{cs}} \cdot \delta \mathbf{r}^i \,. \tag{4.28}$$

Using equations (4.22) and (4.23),

$$\begin{aligned}\delta T^{ij}_{\text{self}} =& \frac{\partial E^{\text{str}}_{\text{cnel}}(\boldsymbol{\xi}^{ij}, \mathbf{b}^{ij}, \mathbf{0}; a)}{\partial \xi^{ij}_\alpha} \frac{\partial \xi^{ij}_\alpha}{\partial r^i_\beta} \delta r^i_\beta L_{ij} - E^{\text{str}}_{\text{cnel}}(\boldsymbol{\xi}^{ij}, \mathbf{b}^{ij}, \mathbf{0}; a) \xi^{ij}_\beta \delta r^i_\beta \\ =& \frac{\partial E^{\text{str}}_{\text{cnel}}(\boldsymbol{\xi}^{ij}, \mathbf{b}^{ij}, \mathbf{0}; a)}{\partial \xi^{ij}_\alpha} \{\xi^{ij}_\alpha \xi^{ij}_\beta - \delta_{\alpha\beta}\} \delta r^i_\beta - E^{\text{str}}_{\text{cnel}}(\boldsymbol{\xi}^{ij}, \mathbf{b}^{ij}, \mathbf{0}; a) \xi^{ij}_\beta \delta r^i_\beta \,, \end{aligned} \tag{4.29}$$

where $\delta_{\alpha\beta}$ denotes the Kronecker delta function. Comparing equations (4.28) and (4.29), we can extract the force vector

$$f^{\{i\}j}_{\text{cs},\beta} = \frac{\partial E^{\text{str}}_{\text{cnel}}(\boldsymbol{\xi}^{ij}, \mathbf{b}^{ij}, \mathbf{0}; a)}{\partial \xi^{ij}_\alpha} \{\delta_{\alpha\beta} - \xi^{ij}_\alpha \xi^{ij}_\beta\} + E^{\text{str}}_{\text{cnel}}(\boldsymbol{\xi}^{ij}, \mathbf{b}^{ij}, \mathbf{0}; a) \xi^{ij}_\beta \,, \tag{4.30}$$

where the first term is the contribution to the force which tends to rotate the line segment orientation to lower its core energy, while the second term represents a line tension force to reduce the length of the segment. Next, we consider the perturbations in $T^{(ij,kl)}_{\text{ext}}$ with respect to $\mathbf{r}^i$. From equations (4.22), (4.23) and (4.21), $T^{(ij,kl)}_{\text{ext}}$ is given by

$$T^{(ij,kl)}_{\text{ext}} = \hat{S}_{\alpha\beta}(\boldsymbol{\xi}^{ij}, \mathbf{b}^{ij}; a) R_{\eta\alpha}(\boldsymbol{\xi}^{ij}, \mathbf{b}^{ij}) R_{\omega\beta}(\boldsymbol{\xi}^{ij}, \mathbf{b}^{ij}) \int_0^{L_{ij}} \epsilon^{kl}_{\eta\omega}(\boldsymbol{\xi}^{kl}, \mathbf{b}^{kl}, \mathbf{x}^{ij}(s_{ij}))\, \mathrm{d}s_{ij}. \tag{4.31}$$

The first order perturbations in $T^{(ij,kl)}_{\text{ext}}$ with respect to $\mathbf{r}^i$ results from the following perturbations, given by

$$\begin{aligned}
\delta \hat{S}_{\alpha\beta}(\boldsymbol{\xi}^{ij}, \mathbf{b}^{ij}; a) =& \frac{\partial \hat{S}_{\alpha\beta}(\boldsymbol{\xi}^{ij}, \mathbf{b}^{ij}; a)}{\partial \xi_p^{ij}} \frac{\partial \xi_p^{ij}}{\partial r_q^i} \delta r_q^i \\
=& \frac{\partial \hat{S}_{\alpha\beta}(\boldsymbol{\xi}^{ij}, \mathbf{b}^{ij}; a)}{\partial \xi_p^{ij}} \frac{\{\xi_p^{ij}\xi_q^{ij} - \delta_{pq}\}}{L_{ij}} \delta r_q^i \\
=& - t^{\hat{S}}_{\alpha\beta q} \delta r_q^i \,,
\end{aligned} \tag{4.32a}$$

$$\begin{aligned}
\delta \left(R_{\eta\alpha}(\boldsymbol{\xi}^{ij}, \mathbf{b}^{ij}) R_{\omega\beta}(\boldsymbol{\xi}^{ij}, \mathbf{b}^{ij}) \right) =& \left[\frac{\partial R_{\eta\alpha}(\boldsymbol{\xi}^{ij}, \mathbf{b}^{ij})}{\partial \xi_p^{ij}} R_{\omega\beta}(\boldsymbol{\xi}^{ij}, \mathbf{b}^{ij}) \right. \\
& \left. + R_{\eta\alpha}(\boldsymbol{\xi}^{ij}, \mathbf{b}^{ij}) \frac{\partial R_{\omega\beta}(\boldsymbol{\xi}^{ij}, \mathbf{b}^{ij})}{\partial \xi_p^{ij}} \right] \frac{\partial \xi_p^{ij}}{\partial r_q^i} \delta r_q^i \\
=& \left[\frac{\partial R_{\eta\alpha}(\boldsymbol{\xi}^{ij}, \mathbf{b}^{ij})}{\partial \xi_p^{ij}} R_{\omega\beta}(\boldsymbol{\xi}^{ij}, \mathbf{b}^{ij}) \right. \\
& \left. + R_{\eta\alpha}(\boldsymbol{\xi}^{ij}, \mathbf{b}^{ij}) \frac{\partial R_{\omega\beta}(\boldsymbol{\xi}^{ij}, \mathbf{b}^{ij})}{\partial \xi_p^{ij}} \right] \frac{\{\xi_p^{ij}\xi_q^{ij} - \delta_{pq}\}}{L_{ij}} \delta r_q^i \\
=& - t^{R}_{\alpha\beta\omega\eta q} \delta r_q^i \,,
\end{aligned} \tag{4.32b}$$

$$\begin{aligned}
\delta \left(\int_0^{L_{ij}} \epsilon^{kl}_{\eta\omega}(\boldsymbol{\xi}^{kl}, \mathbf{b}^{kl}, \mathbf{x}^{ij}(s_{ij}))\, \mathrm{d}s_{ij} \right) =& \left[\int_0^{L_{ij}} \frac{\partial \epsilon^{kl}_{\eta\omega}(\boldsymbol{\xi}^{kl}, \mathbf{b}^{kl}, \mathbf{x}^{ij}(s_{ij}))}{\partial x_q^{ij}} N_i(s_{ij})\, \mathrm{d}s_{ij} \right. \\
& \left. - \frac{\xi_q^{ij}}{L_{ij}} \int_0^{L_{ij}} \epsilon^{kl}_{\eta\omega}(\boldsymbol{\xi}^{kl}, \mathbf{b}^{kl}, \mathbf{x}^{ij}(s_{ij}))\, \mathrm{d}s_{ij} \right] \delta r_q^i \\
=& - \left(t^{\epsilon_1}_{\eta\omega q} + t^{\epsilon_2}_{\eta\omega q} \right) \delta r_q^i \,.
\end{aligned} \tag{4.32c}$$

In the above, the first contributions results from the orientation dependence of the slopes of the core energy vs external macroscopic strain, originating from the difference in the slopes of the edge and screw dislocations. The second term results from the orientation dependence of the rotation matrix, which is solely geometric in nature. The third contribution is composed of two terms. The first term results from the perturbations to the spatial positions of the points on segment $\mathbf{l}^{ij}$, which then perturbs the external strain field experienced by these points. The second term captures the contribution arising from the change in the length of $\mathbf{l}^{ij}$. In the above perturbations, we used the fact that the position of segment $\mathbf{l}^{kl}$ remains unchanged with respect to perturbations of $\mathbf{r}^i$ owing to the cut-off procedure. Using equations (4.32) and (4.25), we arrive at the force

$$\begin{aligned}f_{\mathrm{ce},q}^{(\{i\}j,kl)} = {} & t_{\alpha\beta q}^{\hat{S}} R_{\eta\alpha}(\boldsymbol{\xi}^{ij},\mathbf{b}^{ij}) R_{\omega\beta}(\boldsymbol{\xi}^{ij},\mathbf{b}^{ij}) \int_0^{L_{ij}} \epsilon_{\eta\omega}^{kl}(\boldsymbol{\xi}^{kl},\mathbf{b}^{kl},\mathbf{x}^{ij}(s_{ij}))\,\mathrm{d}s_{ij} \\ & + t_{\alpha\beta\omega\eta q}^{R} \hat{S}_{\alpha\beta}(\boldsymbol{\xi}^{ij},\mathbf{b}^{ij};a) \int_0^{L_{ij}} \epsilon_{\eta\omega}^{kl}(\boldsymbol{\xi}^{kl},\mathbf{b}^{kl},\mathbf{x}^{ij}(s_{ij}))\,\mathrm{d}s_{ij} \\ & + t_{\eta\omega q}^{\epsilon_1} \hat{S}_{\alpha\beta}(\boldsymbol{\xi}^{ij},\mathbf{b}^{ij};a) R_{\eta\alpha}(\boldsymbol{\xi}^{ij},\mathbf{b}^{ij}) R_{\omega\beta}(\boldsymbol{\xi}^{ij},\mathbf{b}^{ij}) \\ & + t_{\eta\omega q}^{\epsilon_2} \hat{S}_{\alpha\beta}(\boldsymbol{\xi}^{ij},\mathbf{b}^{ij};a) R_{\eta\alpha}(\boldsymbol{\xi}^{ij},\mathbf{b}^{ij}) R_{\omega\beta}(\boldsymbol{\xi}^{ij},\mathbf{b}^{ij}). \quad (4.33)\end{aligned}$$

Next, we consider first order perturbations of $T_{\mathrm{ext}}^{(kl,ij)}$ with respect to $\mathbf{r}^i$. Using equations (4.31) and (4.5), we have

$$\begin{aligned}T_{\mathrm{ext}}^{(kl,ij)} = {} & \hat{S}_{\alpha\beta}(\boldsymbol{\xi}^{kl},\mathbf{b}^{kl};a) R_{\eta\alpha}(\boldsymbol{\xi}^{kl},\mathbf{b}^{kl}) R_{\omega\beta}(\boldsymbol{\xi}^{kl},\mathbf{b}^{kl}) \int_0^{L_{kl}} \epsilon_{\eta\omega}^{ij}(\boldsymbol{\xi}^{ij},\mathbf{b}^{ij},\mathbf{x}^{kl}(s_{kl}))\,\mathrm{d}s_{kl} \\ = {} & \hat{S}_{\alpha\beta}(\boldsymbol{\xi}^{kl},\mathbf{b}^{kl};a) R_{\eta\alpha}(\boldsymbol{\xi}^{kl},\mathbf{b}^{kl}) R_{\omega\beta}(\boldsymbol{\xi}^{kl},\mathbf{b}^{kl}) \\ & \int_0^{L_{kl}} \int_0^{L_{ij}} \bar{\epsilon}_{\eta\omega}^{ij}(\boldsymbol{\xi}^{ij},\mathbf{b}^{ij},\mathbf{x}^{kl}(s_{kl}) - \mathbf{x}^{ij}(s_{ij}))\,\mathrm{d}s_{ij}\mathrm{d}s_{kl} \\ = {} & D_{\eta\omega} \int_0^{L_{kl}} \int_0^{L_{ij}} \bar{\epsilon}_{\eta\omega}^{ij}(\boldsymbol{\xi}^{ij},\mathbf{b}^{ij},\mathbf{x}^{kl}(s_{kl}) - \mathbf{x}^{ij}(s_{ij}))\,\mathrm{d}s_{ij}\mathrm{d}s_{kl}\,, \quad (4.34)\end{aligned}$$

and

$$\begin{aligned}\delta T_{\mathrm{ext}}^{(kl,ij)} = {} & D_{\eta\omega} \frac{\{\xi_p^{ij}\xi_q^{ij} - \delta_{pq}\}}{L_{ij}} \int_0^{L_{kl}} \int_0^{L_{ij}} \frac{\partial \bar{\epsilon}_{\eta\omega}^{ij}(\boldsymbol{\xi}^{ij},\mathbf{b}^{ij},\mathbf{x}^{kl}(s_{kl}) - \mathbf{x}^{ij}(s_{ij}))}{\partial \xi_p^{ij}}\,\mathrm{d}s_{ij}\mathrm{d}s_{kl}\,\delta r_q^i \\ & + D_{\eta\omega} \int_0^{L_{kl}} \int_0^{L_{ij}} \frac{\partial \bar{\epsilon}_{\eta\omega}^{ij}(\boldsymbol{\xi}^{ij},\mathbf{b}^{ij},\mathbf{x}^{kl}(s_{kl}) - \mathbf{x}^{ij}(s_{ij}))}{\partial x_q^{ij}} N_i(s_{ij})\,\mathrm{d}s_{ij}\mathrm{d}s_{kl}\,\delta r_q^i \\ & - D_{\eta\omega} \frac{\xi_q^{ij}}{L_{ij}} \int_0^{L_{kl}} \int_0^{L_{ij}} \bar{\epsilon}_{\eta\omega}^{ij}(\boldsymbol{\xi}^{ij},\mathbf{b}^{ij},\mathbf{x}^{kl}(s_{kl}) - \mathbf{x}^{ij}(s_{ij}))\,\mathrm{d}s_{ij}\mathrm{d}s_{kl}\,\delta r_q^i \\ = {} & -\tilde{f}_{\mathrm{ce},q}^{(\{i\}j,kl)} \delta r_q^i\,. \quad (4.35)\end{aligned}$$

In the above, the first term results from the perturbation in the core energy of $\mathbf{l}^{kl}$

due to the perturbation in the strain field of segment $\mathbf{l}^{ij}$'s resulting from a change in its orientation. The second and the third term manifest from the perturbations in the strain field of segment $\mathbf{l}^{ij}$ associated with its position and length, respectively. In summary, equations (4.30), (4.33), and (4.35) provide the various contributions to the nodal core force $\mathbf{F}_{\mathrm{c}}^{i}$ in equation (4.25). In Appendix C, we extend the above analysis to the case where the perfect dislocations are dissociated into partials.

The various terms in the nodal core force can broadly be divided into three types based on their dependence on the strain field. These three types are: (I) terms which are proportional to the spatial gradients of the strain field, (II) which are proportional to the strain field or its gradients with respect to the dislocation orientation, and (III) which are independent of the strain field. Starting with type-(I) contributions, we note that they arise from the core energy dependence on external strain and perturbations in the external strain due to perturbations in the displacement vector connecting the dislocation source (producing the external strain) to the core location (cf. third term in equation (4.33) and second term in equation (4.35)). Next, the type-(II) contributions also arise from the core energy dependence on external strain, but, due to perturbations in the length and orientation of the dislocation segments (cf. first, second and fourth terms in equation (4.33), and first and third terms in equation (4.35)). Finally, type-(III) contributions (cf. equation (4.30)) manifest from the perturbations of the core energy solely due to perturbation in the length and orientation of dislocation segments without accounting for any dependence of the core energy on the external strain. We note that the current DDD frameworks (cf. [11, 15]) only account for type-(III) contributions to the core force. Further, these three different types of force contributions have different decay behavior in dislocation interactions. Type-(I) contributions are proportional to the spatial gradient of the strain field, thus are short-ranged decaying as $\mathcal{O}(\frac{1}{d^2})$, where d is the distance between the two interacting dislocation segments $ij \in U$ and $kl \in U'_{ij}$. On the other hand, type-(II) contributions are long-ranged decaying as $\mathcal{O}(\frac{1}{d})$ (the same decay of the elastic force), while type-(III) contributions do not depend on d. Thus, we expect type-(I) contributions to be significant in comparison with the elastic force at smaller distances. In Section 4.2, we use case studies to numerically compare the type-(I) core force contributions with the elastic force for a wide range of dislocation interactions. Studies that also include non-trivial type-(II) contributions are considered in the DDD case studies in Section 4.3.

4.2 Static case studies using core-energetics based forces

In this section, we consider case studies involving pairs of simple dislocation structures in fcc Al to find the spatial extent to which the core force contribution (cf. Section 4.1.2) is significant in comparison to the longer ranged Peach-Koehler force. In our case studies, we consider the systems as an aggregate of dislocation loops [2] only allowing for rigid body translations of the individual loops. In other words, we do not allow any changes in the shape, size and orientation of the dislocation loops. A full-fledged treatment without any restrictions on the degrees of freedom requires the efficient implementation of the core force in a 3D DDD framework, which we will pursue in a future work. Further, in these case studies, we treat the dislocations as perfect dislocations for computing the non-singular elastic fields. This is a reasonable assumption here, as the combined elastic fields of the partials converges to that of the perfect dislocation elastic fields beyond the core size.

We denote the ith loop in a system of n loops as C_i. Following Section 4.1.2, the core force on the dislocation loop C_i (denoted as $\mathbf{F}^i_{\mathrm{c}}$) corresponding to its rigid body

---

[2] Infinite straight dislocations can be treated as loops with radius approaching infinity.

translations, while keeping other loops fixed, is obtained as

$$\mathbf{F}_{\mathrm{c}}^{i} = \oint_{C_i} \mathbf{f}_{\mathrm{c}}^{i}(\mathbf{x}^i(s_i))\,\mathrm{d}s_i = \oint_{C_i} \left\{ \sum_{j\neq i} \mathbf{f}_{\mathrm{ce}}^{(i,j)}(\mathbf{x}^i(s_i)) + \sum_{j\neq i} \tilde{\mathbf{f}}_{\mathrm{ce}}^{(i,j)}(\mathbf{x}^i(s_i)) \right\} \mathrm{d}s_i\,, \tag{4.36}$$

where

$$\begin{split} f_{\mathrm{ce},q}^{(i,j)}(\mathbf{x}^i(s_i)) = -\hat{S}_{\alpha\beta}\left(\boldsymbol{\xi}^i(s_i), \mathbf{b}^i; a\right) R_{\eta\alpha}\left(\boldsymbol{\xi}^i(s_i), \mathbf{b}^i\right) R_{\omega\beta}\left(\boldsymbol{\xi}^i(s_i), \mathbf{b}^i\right) \\ \oint_{C_j} \frac{\partial \bar{\epsilon}^j_{\eta\omega}(\boldsymbol{\xi}^j(s_j), \mathbf{b}^j, \mathbf{x}^i(s_i) - \mathbf{x}^j(s_j))}{\partial x^i_q}\,\mathrm{d}s_j, \end{split} \tag{4.37}$$

and

$$\begin{split} \tilde{f}_{\mathrm{ce},q}^{(i,j)}(\mathbf{x}^i(s_i)) = -\oint_{C_j} \hat{S}_{\alpha\beta}\left(\boldsymbol{\xi}^j(s_j), \mathbf{b}^j; a\right) R_{\eta\alpha}\left(\boldsymbol{\xi}^j(s_j), \mathbf{b}^j\right) R_{\omega\beta}\left(\boldsymbol{\xi}^j(s_j), \mathbf{b}^j\right) \\ \frac{\partial \bar{\epsilon}^i_{\eta\omega}(\boldsymbol{\xi}^i(s_i), \mathbf{b}^i, \mathbf{x}^j(s_j) - \mathbf{x}^i(s_i))}{\partial x^i_q}\,\mathrm{d}s_j\,. \end{split} \tag{4.38}$$

In the above, $\boldsymbol{\xi}^i(s_i)$ is the tangent line direction at $\mathbf{x}^i(s_i)$ on C_i, $\mathbf{b}^i$ is the Burgers vector of C_i, and $\bar{\boldsymbol{\epsilon}}^i(\boldsymbol{\xi}^i(s_i), \mathbf{b}^i, \mathbf{x}-\mathbf{x}^i(s_i))$ is the per unit-length strain field contribution at $\mathbf{x}$ due to the dislocation line at a point $\mathbf{x}^i(s_i)$ on loop C_i. Based on the classification of core force contributions in Section 4.1.2, the above core force corresponds to the type-(I) contribution arising from pairwise interactions of loops C_i with C_j.

We now undertake a numerical study on assessing the significance of the core force in comparison to the Peach-Koehler force. To this end, we consider the following case studies: (i) interaction of a straight edge dislocation with a low-angle tilt grain boundary, (ii) interaction of a circular glide loop with a low-angle tilt grain boundary (iii) interaction of two circular glide loops, and (iv) interaction of a circular glide dislocation loop with a straight edge dislocation. The schematics of the geometry are shown in figure 4.1. The Burgers vectors of the dislocations are defined with respect to line directions taken as the following: along $[11\bar{2}]$ for straight edge dislocations, and for the glide loops, the line direction curls around the [111] direction in the right hand sense. In each of these case studies, the forces are evaluated with respect to translational perturbations of the blue-colored dislocation system, while keeping the red-colored dislocation system fixed. The values of the fcc Al material constants used in the calculations are obtained from RS-OFDFT, which are provided in Table B.1. The value of the smearing parameter, a, in the non-singular elastic formulation is chosen to be $1|\mathbf{b}|$ for all the case studies. Corresponding to this choice of a, Table B.3 provides the values of the non-elastic core energy and its slopes with respect to external macroscopic strains.

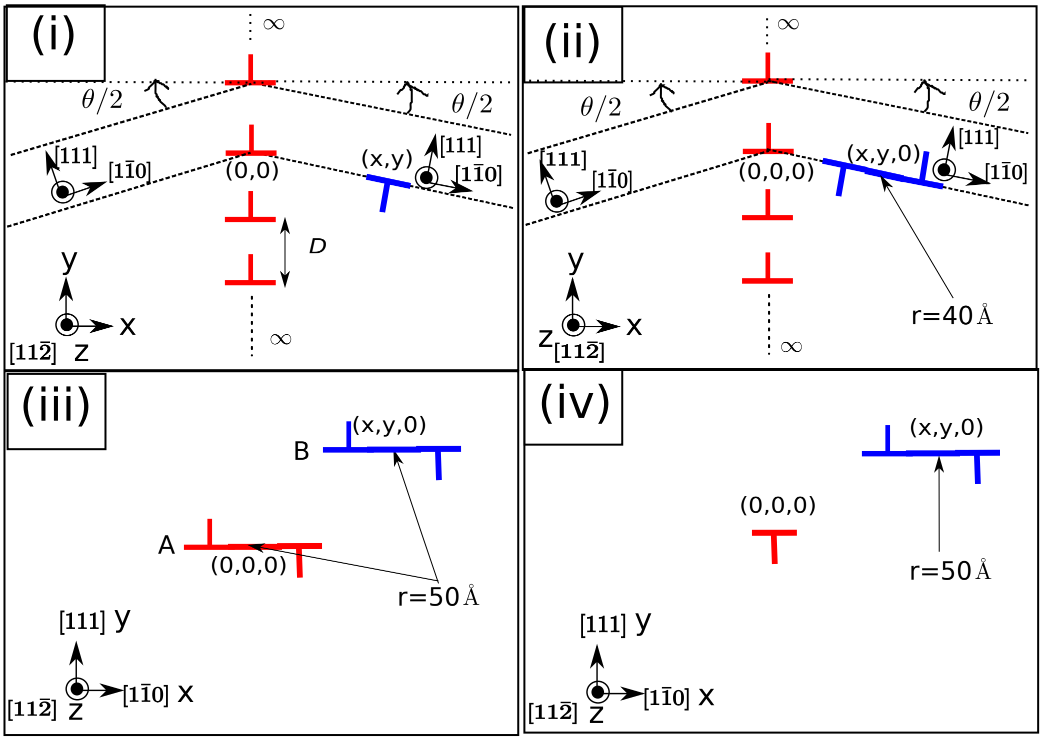

Figure 4.1: Schematic of the case studies.

Case study (i): We consider the interaction between a $\frac{a_0}{2}[1\bar{1}0]$ low-angle tilt grain boundary (LATGB) with tilt axis $[11\bar{2}]$, and a straight negative edge dislocation with Burgers vector $\frac{-a_0}{2}[1\bar{1}0]$. LATGB's are conventionally modeled as an uniformly spaced array of edge dislocations up to tilt angles of $\approx 15^\circ$ [132]). We denote the tilt angle as θ, as shown in figure 4.1. The relationship between θ and the dislocation array spacing, denoted as D, is given by

$$D = \frac{|\mathbf{b}^{arr}|}{2\sin(\theta/2)}\,, \tag{4.39}$$

where $\mathbf{b}^{arr} = \frac{a_0}{2}[1\bar{1}0]$ is the Burgers vector of each edge dislocation in the array. We consider two tilt angles of $\theta = 4°$ and $\theta = 10°$. In both these systems, we evaluate the Peach-Koehler force and the core force per unit length on the straight edge dislocation. The quantity of interest to us is the ratio of glide component (along $[1\bar{1}0]$ on the rotated frame) of the core force, $F_{\mathrm{c}}^{\mathrm{str,gl}}$, to the glide component of the Peach-Koehler force, $F_{\mathrm{PK}}^{\mathrm{str,gl}}$, with a regularization (c_0), given by

$$R_{\mathrm{str}}(\{x,y\}) = \left(\frac{|F_{\mathrm{c}}^{\mathrm{str,gl}}(\{x,y\})|}{|F_{\mathrm{PK}}^{\mathrm{str,gl}}(\{x,y\})| + c_0}\right)\,, \tag{4.40}$$

where $\{x,y\}$ is the position of the straight edge dislocation in the un-rotated frame attached to the GB. The regularization is used to avoid singularities in the ratio at the points where $F_{\mathrm{PK}}^{\mathrm{str,gl}}$ vanishes. The value of c_0, a positive regularization constant, is chosen to be

$$c_0 = 10 \times |\mathrm{PN_f}|\,, \tag{4.41}$$

where $\mathrm{PN_f}$ is the Peierls-Nabarro force per unit length of the straight edge dislocation computed using the Peierls stress to be 1.6 MPa [46]. Figures 4.2(a) and 4.2(b) show the contour plots of $\log_{10}(R_{\mathrm{str}}(\{x,y\}))$ for tilt angles of $\theta = 4°$ and $\theta = 10°$, respectively. For better presentability of the contour, we truncate the range of $\log_{10}(R_{\mathrm{str}}(\{x,y\}))$ to $[-3,3]$, the values to the left and right of this range being fixed at -3 and 3, respectively. We also adopt this truncation procedure for the subsequent case studies. In the contour plots, the regions of interest are those with

$\log_{10}\left(R_{\text{str}}(\{x,y\})\right) > -1$, which from equation (4.40) correspond to

$$|F_{\text{c}}^{\text{str,gl}}(\{x,y\})| > \frac{|F_{\text{PK}}^{\text{str,gl}}(\{x,y\})|}{10} \quad \& \quad |F_{\text{c}}^{\text{str,gl}}(\{x,y\})| > |\text{PN}_{\text{f}}|. \tag{4.42}$$

In the x direction, these regions extend upto $x = 4$ nm from the grain boundary in figure 4.2(a), and $x = 2$ nm from the grain boundary in figure 4.2(b). In the y direction, these regions almost completely fills up the separation between the dislocations in the GB. There are also areas inside these regions with separation distances of < 2 nm, where $\log_{10}\left(R_{\text{str}}(\{x,y\})\right) > 0$. Here, the core force is greater in magnitude compared to the Peach-Koehler force, and is also greater than ten times the Peierls-Nabarro force. Thus, we can expect the core force to influence the physical processes involved in dislocation–GB interactions like dislocation pile-up, dislocation absorption and dislocation transmission that play an important role in governing mechanical properties of polycrystalline materials.

Case study (ii): In this case study, we consider the interaction between a $\frac{a_0}{2}[1\bar{1}0]$ LATGB with tilt axis $[11\bar{2}]$, and a circular (111) glide loop of radius 40 Å with Burgers vector $\frac{-a_0}{2}[1\bar{1}0]$. We evaluate the total Peach-Koehler force and core force on the dislocation loop for two different values of LATGB tilt angles of $\theta = 4°$ and $\theta = 10°$. As in the previous case study, we consider the regularized ratio of glide component of the core force on the loop, $F_{\text{c}}^{\text{loop,gl}}$, to the glide component of the Peach-Koehler force on the loop, $F_{\text{PK}}^{\text{loop,gl}}$, given by

$$R_{\text{loop}}(\{x,y\}) = \left(\frac{|F_{\text{c}}^{\text{loop,gl}}(\{x,y\})|}{|F_{\text{PK}}^{\text{loop,gl}}(\{x,y\})| + c_0}\right), \tag{4.43}$$

where

$$c_0 = 10 \times \text{Per}_{\text{loop}} \times |\text{PN}_{\text{f}}|, \tag{4.44}$$

with Per_{loop} denoting the perimeter of the circular glide loop. Figures 4.3(a) and 4.3(b)

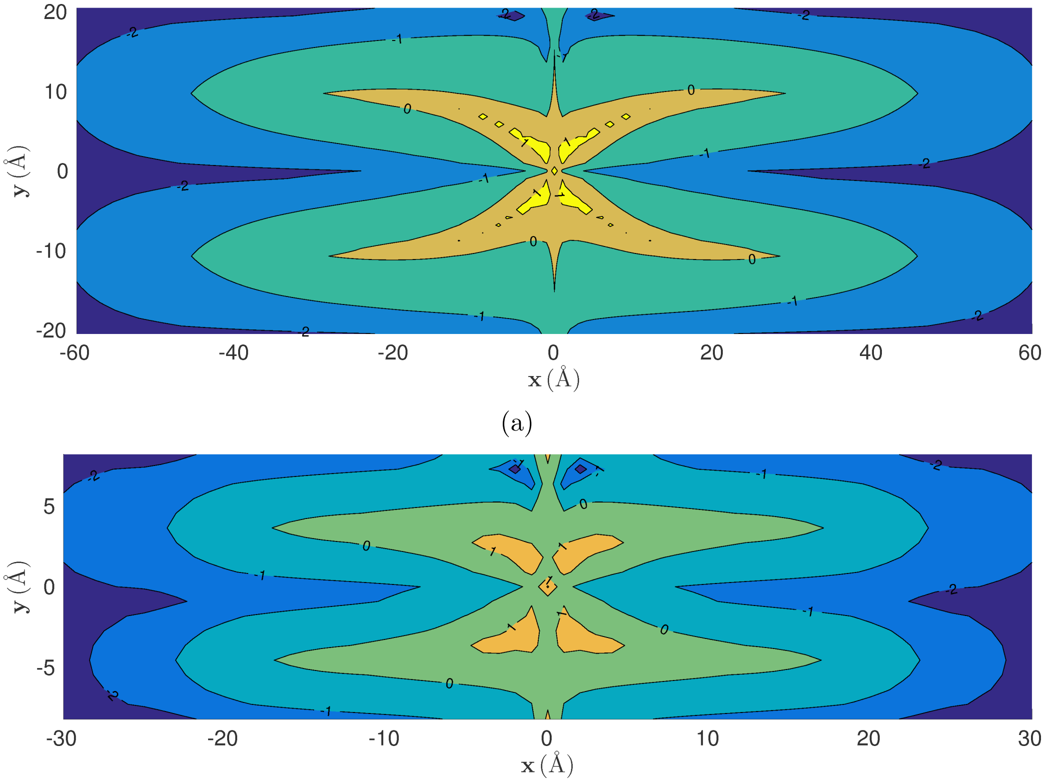

(a)

(b)

Figure 4.2: Case study (i): Contour plot of $\log_{10}(R_{\text{str}}(\{x,y\}))$ for the interaction between a straight edge dislocation and a low-angle title grain boundary for tilt angles a) $\theta = 4°$ b) $\theta = 10°$. The range of the y-axis in these plots is $[-\frac{D}{2}, \frac{D}{2}]$.

show the contour plots for tilt angles of $\theta = 4^\circ$ and $\theta = 10^\circ$, respectively. The regions with $\log_{10}\left(R_{\text{loop}}(\{x, y\})\right) > -1$ extend up to distances of 4–6 nm between the loop center and the LATGB.

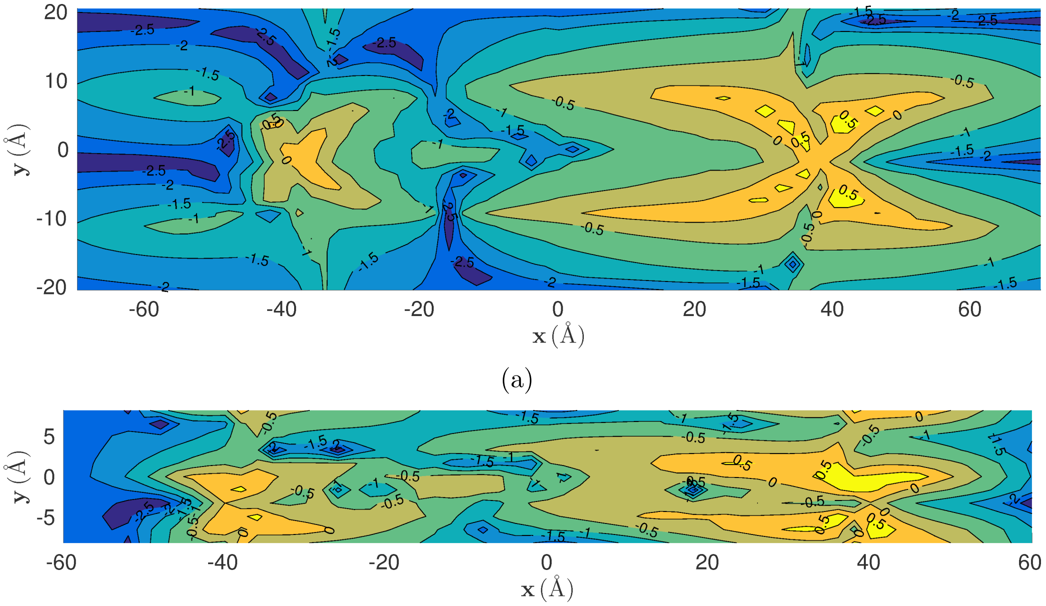

(a)

(b)

Figure 4.3: Case study (ii): Contour plot of $\log_{10}\left(R_{\text{loop}}(\{x, y\})\right)$ for the interaction between a glide loop and a low-angle tilt grain boundary for tilt angles a) $\theta = 4^\circ$ b) $\theta = 10^\circ$. The range of the y-axis in these plots is $[-\frac{D}{2}, \frac{D}{2}]$.

Case study (iii): Here we consider the interaction between two circular (111) glide loops of radius 50 Å with equal Burgers vector $\frac{a_0}{2}[1\bar{1}0]$. The center of the loop A is fixed at the origin $\{0, 0, 0\}$, while loop B's center is located at a variable position $\{x, y, 0\}$. We compute $F_{\text{c}}^{\text{loop,gl}}$ and $F_{\text{PK}}^{\text{loop,gl}}$ on glide loop B, and obtain the contour plot of $\log_{10}\left(R_{\text{loop}}(\{x, y\})\right)$ using equations (4.43) and (4.44), which is shown in figure 4.4. We observe that the regions with $\log_{10}\left(R_{\text{loop}}(\{x, y\})\right) > -1$ extend up to very significant distances of ≈ 15 nm between the loop centers.

Case study (iv): In the final case study, we consider the interaction between a circular (111) glide loop of radius 50 Å with Burgers vector $\frac{a_0}{2}[1\bar{1}0]$, and a straight negative edge dislocation with Burgers vector $\frac{-a_0}{2}[1\bar{1}0]$. The straight edge dislocation is fixed at the origin while the glide loop's center has a variable position, $\{x, y, 0\}$.

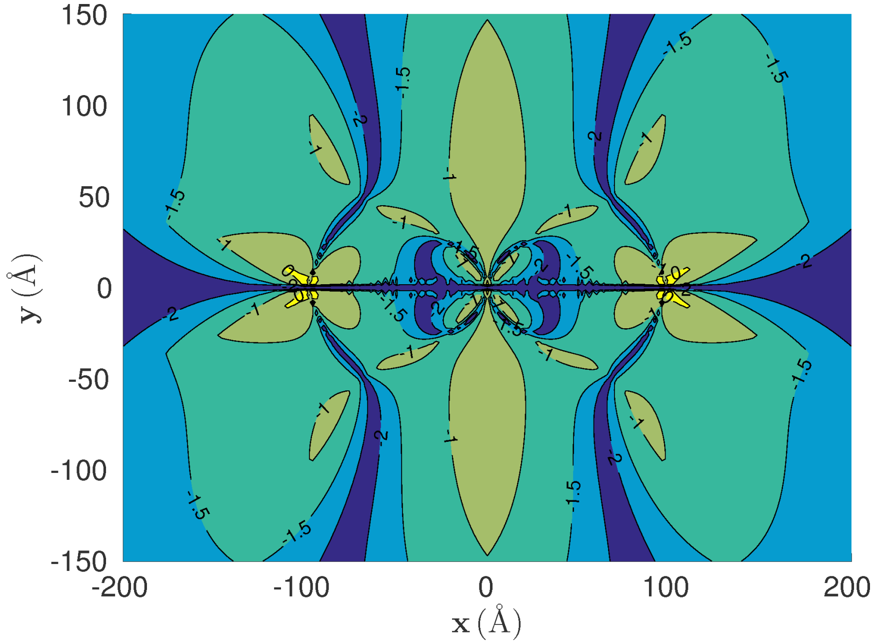

Figure 4.4: Case study (iii): Contour plot of $\log_{10}(R_{\text{loop}}(\{x, y\}))$ for the interaction between two glide loops.

We compute $F_{\text{c}}^{\text{loop,gl}}$ and $F_{\text{PK}}^{\text{loop,gl}}$ on the glide loop. Figure 4.5 shows the contour plot of $\log_{10}(R_{\text{loop}}(\{x, y\}))$. We observe that core force are considerable up to distances of $\approx$ 10 nm between the glide loop center and the straight edge dislocation.

4.3 Dislocation dynamics case studies with core-energetics based nodal core force

In this section, we consider discrete dislocation dynamics case studies to investigate the influence of incorporating the nodal core force derived in Section 4.1.2. In particular, we incorporated the equations 4.25–4.35 into DDLab [133], a MATLAB based 3D DDD code for small scale DDD simulations. The DDD model used in DDLab is similar to that used in the widely used ParaDiS DDD code [11] for large-scale DDD simulations. The underlying elastic model in DDLab is the non-singular elastic formulation by [126]. We note that both DDLab and ParaDis already incorporate the self core force term ((cf. equation 4.30)) but lack the interaction core force terms

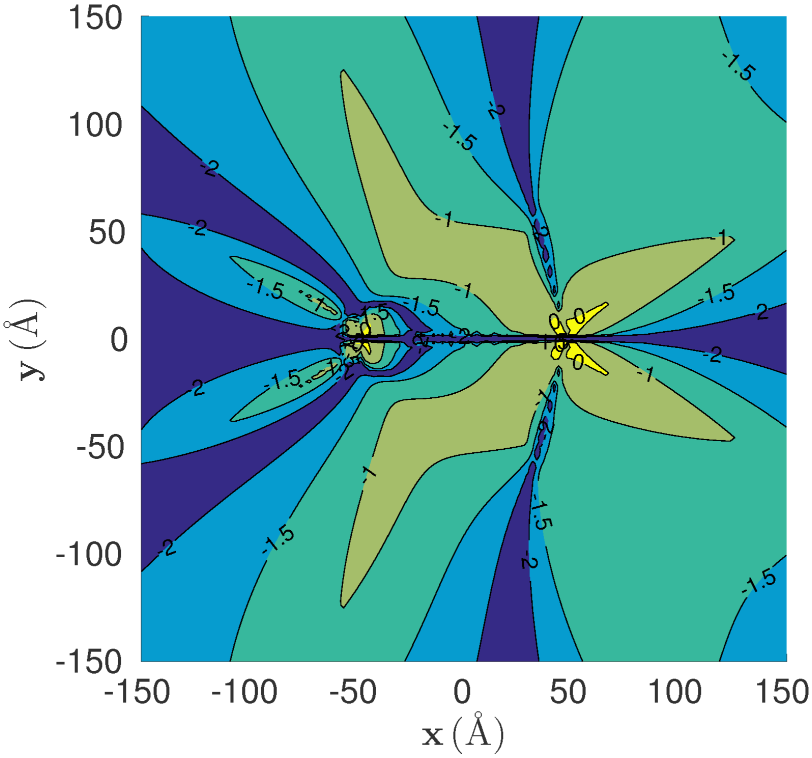

Figure 4.5: Case study (iv): Contour plot of $\log_{10}(R_{\text{loop}}(\{x, y\}))$ for the interaction between a glide loop and a straight edge dislocation.

resulting from the core energy dependence on external macroscopic strain.

Here, we consider two case studies of dislocation hardening mechanisms in fcc Aluminum— a Frank-Read source and a dislocation binary junction. The values of the RS-OFDFT calculated fcc Al material constants used in the case studies are provided in Table B.1 (cf. Appendix B). The value of the smearing parameter, a, in the non-singular elastic formulation is chosen to be $15|\mathbf{b}|$. Corresponding to the above choice of a, the values of the non-elastic core energy and its slopes with respect to external macroscopic strains are recomputed by following the post-processing approach discussed in Appendix B.

First, we consider the Frank-Read source case study. Frank-Read source is a dislocation multiplication mechanism [5, 134] which involves repeated bowing out and generation of dislocations from an initial pinned dislocation line segment beyond a certain critical applied stress. In the present case study, we investigate the influence of incorporating OFDFT core energetics informed nodal core force on the critical applied stress predictions via DDD simulations. We consider fcc Aluminum crystal with coordinate axes X–Y–Z aligned along [100]—[010]—[001] crystallographic directions and introduce an initial straight dislocation line pinned at $(-L/2; -L/2; 0)$ and $(L/2; L/2; 0)$, where the parameter L controls the pinning distance. $(0; 0; 0)$ is a mobile node at the center. The Burgers vector of the dislocation line is $\mathbf{b} = \frac{a_0}{2}[10\bar{1}]$ and the specified glide plane is (111). The default FCC mobility parameters in DDLab are used. Next we apply a certain external stress state, $\sigma\mu\mathbf{A}$, whose magnitude is controlled by the dimensionless scalar σ. μ is the isotropic shear modulus and $\mathbf{A}$ is a 3×3 matrix with $\mathbf{A}(1,3) = \mathbf{A}(3,1) = 1.0$, all other entries being zero. We define critical stress, σ_c as the value of σ which makes the dislocation line bow beyond a certain empirical measure. The empirical criteria for critical stress we use here is the maximum distance of any node in the bowed dislocation line from the center of the initial pinned dislocation line. When this exceeds the length of the initial pinned dislocation length, we consider critical stress to be reached. Figure 4.6 shows the numerically computed critical stress for various initial pinned lengths using three different approaches—(A) DDLab code without any modifications to $\mathbf{F}_c$, which only has the self core force term (cf. equation 4.30) but the core energies are determined based on a heuristic used by DDLab, (B) modified DDLab code where the self core force term is informed from OFDFT calculated dislocation core energetics for Aluminum, and (C) modified DDLab code which incorporates OFDFT core-energetics informed self as well interaction core force terms (cf. equations 4.25–4.35). We observe significant differences in the calculated critical stress between route (A) and route (B) as well as between routes (B) and route (C). This underlines the significant influence of quantum mechanically informed self and interaction nodal core force terms in relation to the original DDD model, which includes only the self core force with heuristically set core energies.

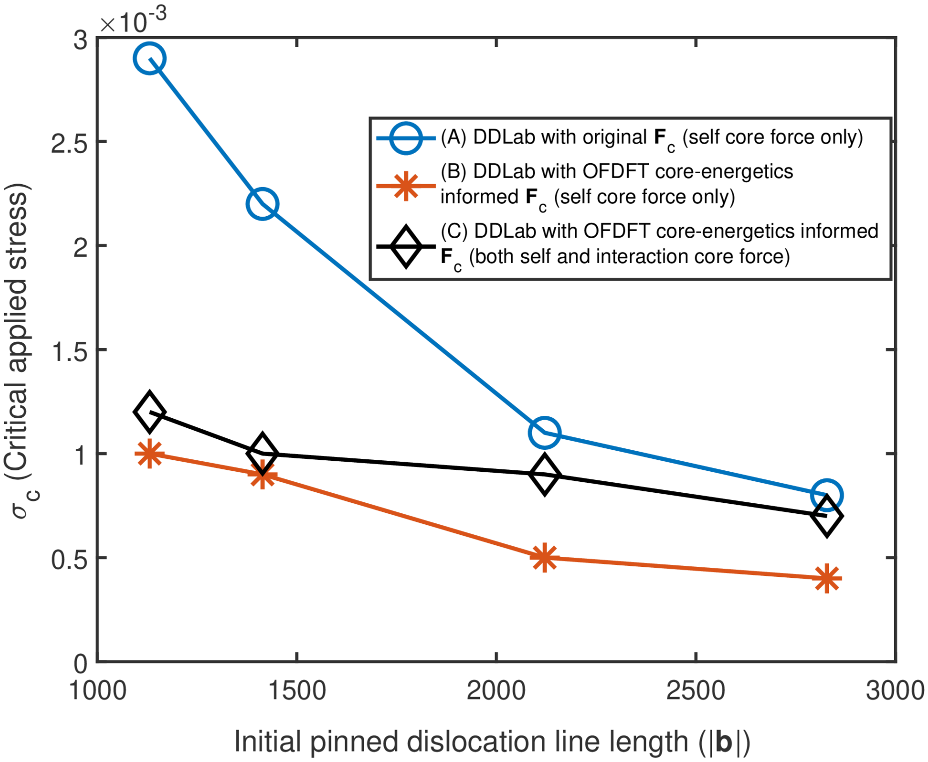

Figure 4.6: Influence of nodal core force on critical stress of a Frank-Read source.

We now consider the second case study— dislocation binary junction in fcc Aluminum. When two dislocations on different glide planes approach each other, under certain conditions of orientation and Burgers vectors they form a binary junction. Such junctions play an important role in strain hardening [135, 136]. Important binary junction characteristics are the equilibrium junction length and the critical stress required to cause dissociation of the junction. In the current case study, we focus on the influence of nodal core force on equilibrium junction length. Similar to the previous case study, the coordinate axes X–Y–Z are aligned along [100]—[010]—[001] crystallographic direction. We consider two pinned dislocation line segments— one (denoted as dislocation 1) on the (111) plane and the other (denoted as dislocation 2) on the $(11\bar{1})$ plane. The Burgers vectors of dislocation 1 and dislocation 2 are $\mathbf{b}_1 = \frac{a_0}{2}[10\bar{1}]$ and $\mathbf{b}_2 = \frac{a_0}{2}[011]$ respectively. We choose orientations for dislocation 1 and dislocation 2 such that the two dislocations interact and form a binary junction

Table 4.1: Influence of nodal core force on equilibrium junction lengths of a binary dislocation junction in fcc Aluminum.

(A) DDLab with original $\mathbf{F}_c$ (self core force only)	301 $\lvert\mathbf{b}\rvert$
(B) DDLab with OFDFT core-energetics informed $\mathbf{F}_c$ (self core force only)	556 $\lvert\mathbf{b}\rvert$
(C) DDLab with OFDFT core-energetics informed $\mathbf{F}_c$ (self and interaction core force)	495 $\lvert\mathbf{b}\rvert$

along the intersection of their glide planes. In particular, following are the positions of the end nodes for dislocation 1 ($(-1597.3\|\mathbf{b}_1\|, 1092.7\|\mathbf{b}_1\|, 504.6\|\mathbf{b}_1\|)$ and $(1597.3\|\mathbf{b}_1\|, -1092.7\|\mathbf{b}_1\|, -504.6\|\mathbf{b}_1\|)$) and dislocation 2 ($(339.5\|\mathbf{b}_2\|, 1213.6\|\mathbf{b}_2\|, 1553.1\|\mathbf{b}_2\|)$ and $(-339.5\|\mathbf{b}_2\| , -1213.6\|\mathbf{b}_2\| , -1553.1\|\mathbf{b}_2\|)$). Table 4.1 shows the numerically computed equilibrium junction lengths computed using three different routes similar to the previous case study. We observe significant influence on the equilibrium junction lengths due to incorporation of OFDFT core-energetics informed nodal self and interaction core force. In particular, between routes (A) and (B), there is a 85% change in the equilibrium junction length, and between routes (B) and (C) there is further change of 11% in the equilibrium junction length.

4.4 Summary

We developed an energetics model for a dislocation aggregate, denoted by C, in an isotropic infinite elastic continua, which incorporates the dependence of the core energetics on macroscopic deformations. The underlying elastic model is chosen to be the non-singular elastic formulation by [126]. Under the physically reasonable assumption that the core size is smaller than the structural length-scales of the dislocation aggregate, the core energetics of isolated edge and screw dislocations are used to describe the total core energy, which is expressed as a line integral on C. The core energy per unit length at each point on C depends on the external strain field at the point resulting from all parts of C excepting a chosen cut-off region around the point. Further, we subtract the non-singular elastic effects from the total core energy to obtain the non-elastic core energy that is dependent on external strain. Next, we extended the developed energetics model to a nodal dislocation network, and derived the nodal force associated with the non-elastic core energy contribution, which we referred to as the nodal core force.

Next, we considered case studies to compare the magnitude of the Peach-Koehler force with the magnitude of the core force contribution arising from the macroscopic deformation dependence of the core energy. These case studies involved interactions of grain boundary-straight dislocation, grain boundary-glide loop, glide loop-glide loop and glide loop-straight dislocation in fcc Aluminum. Numerically computing the Peach-Koehler and core force along the slip direction in these case studies, we found that even up to distances of 10-15 nm between dislocations, the magnitude of the core force is significant with respect to the Peach-Koehler force (being at least 10% of the Peach-Koehler force), while also being larger than the Peierls-Nabarro force. Furthermore, for some configurations with distances of < 2 nm, the magnitude of the core force was found to be comparable or more than the elastic force.

Finally, we incorporated the nodal core force into DDLab, a MATLAB based 3D DDD framework, and studied the influence of nodal core force on two different case studies involving dislocation mechanisms in fcc Aluminum. The first case study investigated the influence of nodal core force on critical stress of a Frank-Read source while the second case study investigated the influence of nodal core force on the equilibrium junction length of a dislocation binary junction. In both of these case studies, we observed significant influence of both self as well as interaction nodal core force terms on the computed quantities.

Based on the analysis of the core force expressions and the results of the above case studies, we anticipate that the core force may influence macroscale predictions of plasticity via large-scale DDD simulations. The nodal core force expressions developed here can be readily incorporated into DDD implementations as demonstrated here for small scale DDD simulations of elementary mechanisms of dislocation enabled hardening in fcc crystal. However, extending this to large-scale bulk plasticity simulations using DDD codes like ParaDis requires a computationally efficient implementation of the nodal core force terms in these frameworks. In this regard, the asymptotic behavior of various terms contributing to the core force can be exploited, along with obtaining analytical expressions, which will be pursued in a subsequent work.

CHAPTER V

Extensions to Large-Scale Kohn-Sham Density Functional Theory: Computational Methods and Benchmarks

5.1 Introduction and previous work

So far in the current thesis, the electronic structure method development and calculations have focussed on orbital-free DFT, which is shown to provide good accuracy in comparison to the more accurate Kohn-Sham DFT (KSDFT) for material systems close to uniform electron gas like Aluminum and Magnesium. However, obtaining the dislocation core energetics for material systems where orbital-free DFT kinetic energy functionals are not well developed or are not sufficiently accurate, such as transition metals and covalently bonded systems, requires the use of Kohn-Sham DFT for studying such systems. Importantly, in the context of electronic structure studies of dislocations there so far has not been any direct quantitative comparison of dislocation core energetics between OFDFT and KSDFT. Furthermore, electronic structure study of dislocation-solute interactions in Aluminum and Magnesium [50, 58–60] is very critical for alloy design, but OFDFT may not be transferable for the various solute types. However, the computational cost of KSDFT scales asymptotically cubically with respect to number of atoms and thus accurate KSDFT calculations are routinely limited to materials systems with at most a few thousands of electrons restricting the system sizes to a few hundred atoms. In this regard, the focus of the current chapter is the development of a capability to perform accurate and large-scale KSDFT calculations using large parallel computers on dislocations in generic metallic systems with system sizes ranging up to 10,000 atoms.

Traditionally, the widely used KSDFT codes employ either plane-waves [104, 137–139] or atomic-orbital type basis sets [140–144] for DFT calculations. However, the use of plane-wave basis restricts simulation domains to be periodic. Further, these basis sets do not exhibit good parallel scalability, severely limiting the range of materials systems that can be studied. On the other hand, atomic orbital type basis sets are not systematically convergent for generic materials systems. Thus, to overcome the above limitations, there has been an increasing thrust in the development of systematically improvable and scalable real-space discretization techniques like finite-elements [61, 145–157], finite-difference [158–163], wavelets [164], psinc functions [165], and other reduced order basis techniques [166, 167].

In this work, we focus on real-space adaptive spectral finite-element (FE) discretization of Kohn-Sham DFT which affords excellent parallel scalability. The current endeavour is composed of two steps. The first step [63][1] extends previous work on local real-space variational formulation of Kohn-Sham DFT [61, 62], which handles all-electron and pseudopotential calculations in the same framework while accommodating periodic, non-periodic and semi-periodic boundary conditions. In [61], the advantage of higher-order spectral finite-elements in conjunction with Chebyshev filtering approach [168] in significantly improving the computational efficiency of DFT calculations has been demonstrated. Here, we focus on reducing the computational prefactor by using efficient numerical strategies, which include: (i) optimized FE cell level matrix operations during the Chebyshev filtering procedure; (ii) Cholesky fac-

---

[1] Phani Motamarri and Sambit Das are co-first authors.

torization based Gram-Schmidt orthonormalization; (iii) mixed precision arithmetic, and (iv) spectrum splitting based Rayleigh-Ritz procedure. We note that the use of these techniques delays the onset of cubic scaling computational complexity to very large system sizes. These strategies enabled systematically convergent, computationally efficient and massively parallel DFT calculations (demonstrated up to $192,000$ MPI tasks) on material systems with tens of thousands of electrons for both metallic and insulating systems. This part of the work has resulted in the development of the DFT-FE open-source software, a massively parallel adaptive finite-element code for large-scale density functional theory calculations.

In the second step of this work [64], we focus on acceleration of DFT-FE using Graphics Processing Units (GPUs). Our implementation innovations on GPUs that significantly reduce the data movement costs and increase arithmetic intensity lead to significant speedups of 20x factor with respect to CPUs. Using the GPU nodes on the Summit supercomputer, we demonstrate an unprecedented sustained performance of 46 PFLOPS (27.8% peak FP64 performance) on a dislocation system in Magnesium containing 105,080 electrons using 3,800 GPU nodes of Summit supercomputer, which is the highest performance to-date among DFT codes.

5.1.1 Governing equations in DFT

We consider a materials system with N_e electrons and N_a atoms whose position vectors are denoted by $\mathbf{R} = \{\mathbf{R}_1,\, \mathbf{R}_2,\, \cdots \mathbf{R}_{N_a}\}$. Neglecting spin, the variational problem of evaluating the ground-state properties in density functional theory is equivalent to solving the N lowest eigenvalues of the following non-linear eigenvalue problem [67]:

$$\left(-\frac{1}{2}\nabla^2 + V_{\text{eff}}(\rho, \mathbf{R})\right)\psi_i = \epsilon_i \psi_i, \qquad i = 1, 2, \cdots N \quad \text{with} \quad N > \frac{N_e}{2}\,, \tag{5.1}$$

where ϵ_i and ψ_i denote the eigenvalues and corresponding eigenfunctions (also referred to as the canonical wavefunctions) of the Hamiltonian, respectively. For clarity and notational convenience, the case of spin independent Hamiltonian is discussed here. However, extension to spin-dependent Hamiltonians [169] is straightforward, and incorporated in DFT-FE. The electron density ρ in equation (5.1) can be expressed in terms of the orbital occupancy function $f(\epsilon, \mu)$ and the canonical wavefunctions as

$$\rho(\mathbf{x}) = 2\sum_{i=1}^{N} f(\epsilon_i, \mu)|\psi_i(\mathbf{x})|^2 \ . \tag{5.2}$$

The range of $f(\epsilon_i, \mu)$ lies in the interval $[0, 1]$, and μ represents the Fermi-energy. In material systems with large number of eigenstates around the Fermi energy, the numerical instabilities that may arise in the solution of the non-linear Kohn-Sham eigenvalue problem are avoided by using a smooth orbital occupancy function. In DFT-FE, f is represented by the Fermi-Dirac distribution [138, 170] given by

$$f(\epsilon, \mu) = \frac{1}{1 + \exp\left(\frac{\epsilon-\mu}{\sigma}\right)} \ . \tag{5.3}$$

In the above, $\sigma = k_B T$ denotes the regularization parameter with k_B denoting the Boltzmann constant and T representing the finite temperature. We note that as $\sigma \to 0$, the Fermi-Dirac distribution tends to the Heaviside function. The constraint on the total number of electrons in the system (N_e) determines the Fermi-energy μ, and is given by

$$\int \rho(\mathbf{x})\, d\mathbf{x} = 2\sum_{i} f(\epsilon_i, \mu) = N_e \, . \tag{5.4}$$

We note that $f(\epsilon_i, \mu)$ is denoted as f_i in the remainder of the manuscript. The effective single-electron potential, $V_{\text{eff}}(\rho, \mathbf{R})$, in the Hamiltonian in equation (5.1) is given by

$$V_{\text{eff}}(\rho, \mathbf{R}) = V_{\text{xc}}(\rho) + V_{\text{el}}(\rho, \mathbf{R}) = \frac{\delta E_{\text{xc}}}{\delta \rho} + \frac{\delta E_{\text{el}}}{\delta \rho} \tag{5.5}$$

In the above, $V_{\mathrm{xc}}(\rho)$ denotes the exchange-correlation potential that accounts for quantum-mechanical interactions between electrons [171], and is given by the first variational derivative of the exchange-correlation energy E_{xc}. We adopt the generalized gradient approximation (GGA) [93, 169] for the exchange correlation functional description throughout the manuscript. However other forms of functionals involving local density (LDA, LSDA) are also incorporated in DFT-FE. In the case of GGA, the exchange-correlation energy is given by

$$E_{\mathrm{xc}}(\rho) = \int \epsilon_{\mathrm{xc}}(\rho, \nabla\rho)\rho(\mathbf{x})\, d\mathbf{x}. \tag{5.6}$$

Numerous forms for $\epsilon_{\mathrm{xc}}(\rho, \nabla\rho)$ have been proposed, and the three widely used forms are Becke (B88) [172], Perdew and Wang (PW91) [173] and Perdew, Burke and Enzerhof (PBE) [174].

The term $V_{\mathrm{el}}(\rho)$, in the effective single-electron potential (equation (5.5)), accounts for the electrostatic interactions. In particular, it is the variational derivative of the classical electrostatic interaction energy between electrons and nuclei, E_{el}, which can further be decomposed as

$$E_{\mathrm{el}}(\rho, \mathbf{R}) = E_{\mathrm{H}}(\rho) + E_{\mathrm{ext}}(\rho, \mathbf{R}) + E_{\mathrm{zz}}(\mathbf{R})\,. \tag{5.7}$$

In the above, E_{H}, E_{ext} and E_{zz} denote the electrostatic interaction energy between electrons (Hartree energy), interaction energy between nuclei and electrons, and repulsive energy between nuclei, respectively. These are given by

$$\begin{aligned} E_{\mathrm{H}} =& \frac{1}{2}\int\int \frac{\rho(\mathbf{x})\rho(\mathbf{y})}{|\mathbf{x}-\mathbf{y}|}\, d\mathbf{x}\, d\mathbf{y}, \quad E_{\mathrm{ext}} = -\sum_J \int \rho(\mathbf{x}) \frac{Z_J}{|\mathbf{x}-\mathbf{R}_J|}\, d\mathbf{x}, \\ E_{\mathrm{zz}} =& \frac{1}{2}\sum_{I,J\neq I} \frac{Z_I Z_J}{|\mathbf{R}_I - \mathbf{R}_J|}, \end{aligned} \tag{5.8}$$

where Z_I denotes the charge on the I^{th} nucleus. In the case of non-periodic boundary conditions representing an isolated atomic system, all integrals in equations (5.8) are over $\mathbb{R}^3$, and the summations include all the atoms in the system. In the case of periodic boundary conditions representing an infinite periodic crystal, all integrals involving $\mathbf{x}$ in equation (5.8) are over the periodic domain (supercell), whereas the integrals involving $\mathbf{y}$ are over $\mathbb{R}^3$. Further, the summation over I is on atoms in the periodic domain, and the summation over J extends over all the lattice sites. Henceforth, unless otherwise specified, we will adopt this convention. Next, we define the nuclear charge distribution $b(\mathbf{x},\mathbf{R}) = -\sum_I Z_I \tilde{\delta}(|\mathbf{x}-\mathbf{R}_I|)$ with $\tilde{\delta}(\mathbf{x}-\mathbf{R}_I)$ denoting a regularized Dirac distribution centered at $\mathbf{R}_I$ (and similarly $b(\mathbf{y},\mathbf{R}) = -\sum_J Z_J \tilde{\delta}(|\mathbf{y}-\mathbf{R}_J|)$) to reformulate the repulsive energy $E_{\text{zz}}(\mathbf{R})$ as

$$\begin{aligned} E_{zz} &= \frac{1}{2}\int\int \frac{b(\mathbf{x},\mathbf{R})\, b(\mathbf{y},\mathbf{R})}{|\mathbf{x}-\mathbf{y}|}\, d\mathbf{x}\, d\mathbf{y} \; - E_{\text{self}} \\ &= \frac{1}{2}\int\int \left(\frac{b(\mathbf{x},\mathbf{R})\, b(\mathbf{y},\mathbf{R})}{|\mathbf{x}-\mathbf{y}|} - \sum_I \frac{Z_I^2 \tilde{\delta}(|\mathbf{x}-\mathbf{R}_I|)\tilde{\delta}(|\mathbf{y}-\mathbf{R}_I|)}{|\mathbf{x}-\mathbf{y}|} \right) d\mathbf{x}\, d\mathbf{y}\,, \end{aligned} \tag{5.9}$$

where E_{self} denotes the self energy of the nuclear charges which depends only on the nuclear charge distribution.

The tightly bound core electrons close to the nucleus of an atom do not influence chemical bonding in many materials systems, and, thus, may not play a significant role in governing many materials properties. Hence, it is a common practice to adopt the pseudopotential approach, where valence electronic wavefunctions are computed in an effective potential generated by the the nucleus and the core electrons. The pseudopotential is often defined by the operator $\mathcal{V}_{\text{PS}} = \mathcal{V}_{\text{loc}} + \mathcal{V}_{\text{nl}} = \sum_J (\mathcal{V}_{\text{loc}}^J + \mathcal{V}_{\text{nl}}^J)$, where $\mathcal{V}_{\text{loc}}^J$ and $\mathcal{V}_{\text{nl}}^J$ denote the local and non-local part of the pseudopotential operator for an atom J, respectively. Further, in the case of norm-conserving pseudopotentials, $\mathcal{V}_{\text{nl}}^J$ can be constructed as a separable pseudopotential operator [169, 175] of the form $\sum_{lpm} |\chi_{lpm}\rangle\, h_{lp}\, \langle\chi_{lpm}|$, with $|\chi_{lpm}\rangle$ denoting the pseudopotential projector. Here l

denotes the azimuthal quantum number, p denotes the index corresponding to the projector component for a given l while m denotes the magnetic quantum number with h_{lp} denoting the pseudopotential constant. Using the representation of the operator $\mathcal{V}_{PS}$ in the $\mathbf{x}$ basis, E_{ext} in pseudopotential Kohn-Sham DFT can be expressed as

$$E_{\text{ext}} = 2\sum_{i=1}^{N} \int\int f_i\, \psi_i^*(\mathbf{x})\, V_{\text{PS}}(\mathbf{x},\mathbf{y},\mathbf{R})\, \psi_i(\mathbf{y})\, d\mathbf{y}\, d\mathbf{x}\,. \tag{5.10}$$

Norm conserving pseudopotentials are employed in DFT-FE, where the action of the nonlocal psuedopotential operator on a wavefunction is given by

$$V_{\text{nl}}\,\psi_i := \int V_{\text{nl}}(\mathbf{x},\mathbf{y},\mathbf{R})\psi_i(\mathbf{y})\, d\mathbf{y} = \sum_J \sum_{lp} \sum_m C_{lpm}^{J,i}\; h_{lp}^J\; \chi_{lpm}^J(\mathbf{x},\mathbf{R}_J)\,, \tag{5.11}$$

$$\text{with} \qquad C_{lpm}^{J,i} = \int \chi_{lpm}^J(\mathbf{x},\mathbf{R}_J)\psi_i(\mathbf{x})\, d\mathbf{x}, \qquad \frac{1}{h_{lp}^J} = \left\langle \xi_{lm}^J \right|, \chi_{lpm}^J \left|\right\rangle. \tag{5.12}$$

In the above, $\left|\xi_{lm}^J\right\rangle$ denotes the single atom pseudo-wavefunction. Note that h_{lp}^J does not depend on the magnetic quantum number m as the spherical harmonics associated with angular variables in the inner product (5.12) are normalized to unity. We remark that equation (5.11) reduces to Troullier-Martins (TM) pseudopotential [176] in the Kleinman-Bylander form [175] for one projector component, i.e. $p = 1$ for every l, while in the case of optimized norm conserving Vanderbilt pseudopotential (ONCV) [177] there are two projector components ($p = 1,\, 2$) for every l. Both TM and ONCV norm-conserving pseudopotentials are implemented in DFT-FE. We further note that the accuracy of ONCV pseudopotentials are shown to be on par with PAW approaches widely employed in DFT codes [178].

We note that the various components of the electrostatic interaction energy in (5.8) and (5.9) are non-local in real-space, and these extended interactions are reformulated as local variational problems as discussed in [61, 87]. To this end, we define the electrostatic potential corresponding to the I^{th} nuclear charge $Z_I\tilde{\delta}(|\mathbf{x}-\mathbf{R}_I|)$ to be

$\bar{V}^I_{\tilde{\delta}}(\mathbf{x})$ and the electrostatic potential corresponding to the total charge distribution $(\rho + b)$ to be $\varphi(\mathbf{x}, \mathbf{R})$, and these potentials are given by:

$$\bar{V}^I_{\tilde{\delta}}(\mathbf{x}) = \int \frac{-Z_I \tilde{\delta}(|\mathbf{y} - \mathbf{R}_I|)}{|\mathbf{x} - \mathbf{y}|}\, d\mathbf{y}, \quad \varphi(\mathbf{x}, \mathbf{R}) = \int \frac{\rho(\mathbf{y}) + b(\mathbf{y}, \mathbf{R})}{|\mathbf{x} - \mathbf{y}|}\, d\mathbf{y}\,. \tag{5.13}$$

Noting that the kernel corresponding to these extended interactions is the Green's function of the Laplace operator, these potentials can be efficiently computed by taking recourse to the solution of a Poisson problem. Using the potentials defined in (5.13) and the expressions for different components of electrostatic energy in (5.8)-(5.10), we can rewrite the electrostatic energy $E_{\text{el}} = E_H + E_{\text{ext}} + E_{zz}$ as [52, 62]

$$\begin{aligned} E_{\text{el}} = {} & \frac{1}{2}\int (\rho(\mathbf{x}) \; + \; b(\mathbf{x}, \mathbf{R}))\, \varphi(\mathbf{x}, \mathbf{R})\, d\mathbf{x} - \frac{1}{2}\sum_I \int -Z_I \tilde{\delta}(|\mathbf{x} - \mathbf{R}_I|) \bar{V}^I_{\tilde{\delta}}(\mathbf{x})\, d\mathbf{x} \\ & + \sum_J \int \left(V^J_{\text{loc}}(|\mathbf{x} - \mathbf{R}_J|) - \bar{V}^J_{\tilde{\delta}}(|\mathbf{x} - \mathbf{R}_J|)\right) \rho(\mathbf{x})\, d\mathbf{x} \\ & + 2\sum_{i=1}^{N} \int\!\!\int f_i\, \psi_i^*(\mathbf{x})\, V_{\text{nl}}(\mathbf{x}, \mathbf{y})\, \psi_i(\mathbf{y})\, d\mathbf{y}\, d\mathbf{x}\,. \end{aligned}$$

Finally, for given positions of nuclei, the reformulated governing equations for the Kohn-Sham DFT problem are:

$$\left(-\frac{1}{2}\nabla^2 + V_{\text{xc}} + \varphi + \sum_J (V^J_{\text{loc}} - \bar{V}^J_{\tilde{\delta}}) + V_{\text{nl}}\right) \psi_i = \epsilon_i\, \psi_i, \tag{5.14a}$$

$$-\frac{1}{4\pi}\nabla^2\, \varphi(\mathbf{x}, \mathbf{R}) = \rho(\mathbf{x}) + b(\mathbf{x}, \mathbf{R})\,, \quad -\frac{1}{4\pi}\nabla^2\, \bar{V}^I_{\tilde{\delta}}(\mathbf{x}, \mathbf{R}_I) = -Z_I \tilde{\delta}(|\mathbf{x} - \mathbf{R}_I|)\,, \tag{5.14b}$$

$$2\sum_i f(\epsilon_i, \mu) = N_e\,, \quad \rho(\mathbf{x}) = 2\sum_i f(\epsilon_i, \mu) |\psi_i(\mathbf{x})|^2. \tag{5.14c}$$

Though, the above equations (5.14) and (5.14) represent a pseudopotential treatment, we note that an all-electron treatment can be realized by setting $V^J_{\text{loc}} = \bar{V}^J_{\tilde{\delta}}$ and $V_{\text{nl}} = 0$. We further remark that the equations (5.14) and (5.14) are equally valid for both periodic and non-periodic systems with appropriate boundary conditions. In a non-periodic setting, the simulation domain corresponds to a large enough domain, containing the compact support of the wavefunctions, with Dirichlet boundary conditions. In periodic calculations, it corresponds to a supercell with periodic boundary conditions.

5.1.2 Variational formulation

The Kohn-Sham governing equations discussed in the previous subsection are the Euler-Lagrange equations of a local variational Kohn-Sham problem that corresponds to the computation of the electronic ground-state free energy for a given position of atoms. The variational problem can be formulated in terms of wavefunctions, fractional occupancies and the electrostatic potentials as given by [62]:

$$\begin{aligned}\mathcal{F}_0(\mathbf{R}) = &\min_{\boldsymbol{f}\in[0,1]^N} \min_{\boldsymbol{\Psi}\in(\mathcal{Y})^N} \max_{\varphi\in\mathcal{Y}} \mathcal{L}(\boldsymbol{f},\boldsymbol{\Psi},\varphi;\mathbf{R}) \\ &\text{such that} \quad \int \psi_i^*\psi_j \, d\mathbf{x} = \delta_{ij}, \;\; 2\sum_i f_i = N_e \,,\end{aligned} \tag{5.15}$$

$$\text{where} \quad \mathcal{L}(\boldsymbol{f},\boldsymbol{\Psi},\varphi;\mathbf{R}) = \widetilde{\mathcal{L}}(\boldsymbol{f},\boldsymbol{\Psi}) + \min_{\mathcal{V}\in(H^1(\mathbb{R}^3))^{N_a}} \mathcal{L}_{\mathrm{el}}(\boldsymbol{f},\boldsymbol{\Psi},\varphi,\mathcal{V};\mathbf{R}) \,,$$

$$\text{with} \;\; \widetilde{\mathcal{L}}(\boldsymbol{f},\boldsymbol{\Psi}) = T_{\mathrm{s}}(\boldsymbol{f},\boldsymbol{\Psi}) + E_{\mathrm{xc}}(\rho) + E_{\mathrm{ent}}(\boldsymbol{f}). \tag{5.16}$$

We note that $\boldsymbol{\Psi} = \{\psi_1(\mathbf{x}), \psi_2(\mathbf{x}), \psi_3(\mathbf{x}), \cdots, \psi_N(\mathbf{x})\}$, and $\boldsymbol{f} = \{f_1, f_2, f_3 \cdots f_N\}$ denotes the vector of orbital occupancy factors, while $\mathcal{V} = \{V^1, V^2, \cdots, V^{N_a}\}$ denotes the vector containing the trial electrostatic potentials corresponding to all nuclear charges in the simulation domain. Here, $T_{\mathrm{s}}(\boldsymbol{f},\boldsymbol{\Psi})$ denotes the kinetic energy of non-interacting electrons and $E_{\mathrm{ent}}(\boldsymbol{f})$ denotes the electronic entropy contribution, and the corresponding expressions are given by

$$T_{\mathrm{s}}(\boldsymbol{f},\boldsymbol{\Psi}) = 2\sum_{i=1}^{N}\int f_i\,\psi_i^*(\mathbf{x})\left(-\frac{1}{2}\nabla^2\right)\psi_i(\mathbf{x})\,d\mathbf{x}\,, \tag{5.17}$$

$$E_{\mathrm{ent}} = -2\,\sigma\sum_{i=1}^{N}\left[f_i\ln f_i + (1-f_i)\ln(1-f_i)\right]\,. \tag{5.18}$$

The energy functional corresponding to electrostatic energy, $\mathcal{L}_{\mathrm{el}}$, can be expressed in the local form as [62]

$$\begin{aligned}
&\mathcal{L}_{\mathrm{el}}(\boldsymbol{f},\boldsymbol{\Psi},\varphi,\mathcal{V},\mathbf{R}) = \int\left[-\frac{1}{8\pi}|\nabla\varphi(\mathbf{x})|^2 + (\rho(\mathbf{x})+b(\mathbf{x},\mathbf{R}))\varphi(\mathbf{x})\right]\,d\mathbf{x}\\
&+\sum_I\int\left[\frac{1}{8\pi}|\nabla V^I(\mathbf{x})|^2 + Z_I\tilde{\delta}(|\mathbf{x}-\mathbf{R}_I|)V^I(\mathbf{x})\right]\,d\mathbf{x}\\
&+\sum_J\int\left(V_{\mathrm{loc}}^J(|\mathbf{x}-\mathbf{R}_J|) - \bar{V}_{\tilde{\delta}}^J(|\mathbf{x}-\mathbf{R}_J|)\right)\rho(\mathbf{x})\,d\mathbf{x}\\
&+2\sum_{i=1}^{N}\int\int f_i\,\psi_i^*(\mathbf{x})V_{\mathrm{nl}}(\mathbf{x},\mathbf{y},\mathbf{R})\,\psi_i(\mathbf{y})\,d\mathbf{y}\,d\mathbf{x}\,,
\end{aligned} \tag{5.19}$$

where $\bar{V}_{\tilde{\delta}}^J$ denotes the electrostatic potential corresponding to the J^{th} nuclear charge (see equation (5.13)), or analogously

$$\bar{\mathcal{V}}_\delta = \{\bar{V}_{\tilde{\delta}}^1, \bar{V}_{\tilde{\delta}}^2, \cdots, \bar{V}_{\tilde{\delta}}^{N_a}\} = arg\min_{\mathcal{V}\in(H^1(\mathbb{R}^3))^{N_a}}\mathcal{L}_{\mathrm{el}}(\boldsymbol{f},\boldsymbol{\Psi},\varphi,\mathcal{V};\mathbf{R}). \tag{5.20}$$

Further, we note that, $\mathcal{Y}$ in equation (5.15) denotes a suitable function space that guarantees the existence of minimizers. We remark that numerical computations involve the use of bounded domains, which in non-periodic calculations correspond to a large enough domain containing the compact support of the wavefunctions, and, in periodic calculations, correspond to the super-cell[2]. Denoting such an appropriate bounded domain by Ω subsequently, $\mathcal{Y} = H_0^1(\Omega)$ in the case of non-periodic problems,

---

[2] while the variational problem in equation (5.15) is presented for super-cells in the case of periodic calculations, it can be extended to periodic unit-cells using the Bloch Ansatz as discussed in [62].

and $\mathcal{Y} = H^1_{per}(\Omega)$ in the case of periodic problems.

5.1.3 Discrete Kohn-Sham DFT equations

We introduce here the finite-element (FE) discretization of the Kohn-Sham DFT problem by representing various electronic fields in the FE basis, a piece-wise polynomial basis generated from the FE discretization [100]. In particular, we employ C^0 continuous Lagrange polynomial basis interpolated over Gauss-Lobatto-Legendre nodal points. The FE discretization of the Kohn-Sham DFT problem described here is along the lines of our prior work [61] and is briefly discussed here, highlighting the important differences in this work. We specifically note here that the real-space formulation of Kohn-Sham DFT as presented in equation (5.15) results in a saddle point problem (min-max problem) in the electronic fields. Thus, it is possible that the electronic ground-state energy obtained from a single FE discretization of all the solution fields in the Kohn-Sham DFT problem can be non-variational. To address this, we seek to solve the electrostatic problem to a more stringent accuracy than the Kohn-Sham eigenvalue problem. To this end, we consider two FE triangulations for representing the wavefunctions and the electrostatic potentials, namely $\mathcal{T}^h$ and $\mathcal{T}^{h_{el}}$ with the characteristic mesh-sizes denoted by h and h_{el}, respectively. We consider $\mathcal{T}^{h_{el}}$ to be a uniform subdivision of $\mathcal{T}^h$. Denoting the subspaces spanned by the FE basis corresponding to triangulations $\mathcal{T}^h$ and $\mathcal{T}^{h_{el}}$ to be $\mathbb{V}^M_h$ (with dimension M) and $\mathbb{V}^{M_{el}}_{h_{el}}$ (with dimension $M_{el} > M$), we note that $\mathbb{V}^M_h \subset \mathbb{V}^{M_{el}}_{h_{el}}$. Finally, the representation of the various fields in the Kohn-Sham problem (5.14)—the wavefunctions and the electrostatic potentials—in the FE basis is given by

$$\psi^h_i(\mathbf{x}) = \sum_{j=1}^{M} N^h_j(\mathbf{x})\psi^j_i \ , \quad \varphi^{h_{el}}(\mathbf{x}) = \sum_{j=1}^{M_{el}} N^{h_{el}}_j(\mathbf{x})\varphi^j \, , \quad \bar{V}^{J^{h_{el}}}_{\tilde{\delta}}(\mathbf{x}) = \sum_{j=1}^{M_{el}} N^{h_{el}}_j(\mathbf{x})\bar{V}^{J^j}_{\tilde{\delta}} \ , \tag{5.21}$$

where $N_j^h : 1 \leq j \leq M$ denotes the FE basis spanning $\mathbb{V}_h^M$ and $N_j^{h_{el}} : 1 \leq j \leq M_{el}$ denotes the FE basis spanning $\mathbb{V}_{h_{el}}^{M_{el}}$. We note that ψ_i^h, $\varphi^{h_{el}}$ and $\bar{V}_{\tilde{\delta}}^{J^{h_{el}}}$ denote the FE discretized fields, with ψ_i^j, φ^j and $\bar{V}_{\tilde{\delta}}^{Jj}$ denoting the coefficients in the expansion of the i^{th} discretized wavefunction and the electrostatic potentials, which also correspond to the nodal values of the respective fields at the j^{th} node on the FE mesh.

The FE discretization of the Kohn-Sham eigenvalue problem (5.14) results in a generalized eigenvalue problem given by $\mathbf{H}\hat{\boldsymbol{\Psi}}_i = \epsilon_i^h \mathbf{M}\hat{\boldsymbol{\Psi}}_i$ where $\mathbf{H}$ denotes the discrete Hamiltonian matrix with matrix elements H_{jk}, $\mathbf{M}$ denotes the overlap matrix (or commonly referred to as the mass matrix in finite element literature) with matrix elements M_{jk}, and ϵ_i^h denotes the i^{th} eigenvalue corresponding to the discrete eigenvector $\hat{\boldsymbol{\Psi}}_i$. The expression for the discrete Hamiltonian matrix, $\mathrm{H}_{jk} = \mathrm{H}_{jk}^{\mathrm{loc}} + \mathrm{H}_{jk}^{\mathrm{nl}}$, is given in terms of

$$\mathrm{H}_{jk}^{\mathrm{loc}} = \frac{1}{2}\int_{\Omega} \nabla N_j^h(\mathbf{x}).\nabla N_k^h(\mathbf{x})\, d\mathbf{x} + \int_{\Omega} V_{\mathrm{eff,loc}}^h(\mathbf{x},\mathbf{R})\, N_j^h(\mathbf{x}) N_k^h(\mathbf{x})\, d\mathbf{x}\,. \tag{5.22}$$

In the above, $V_{\mathrm{eff,loc}}^h$ denotes the local part of the effective single-electron potential computed in the FE basis as the sum of discretized exchange-correlation potential V_{xc}^h, total electrostatic potential $\varphi^{h_{el}}(\mathbf{x})$ and the local pseudopotential term as follows:

$$V_{\mathrm{eff,loc}}^h(\mathbf{x},\mathbf{R}) = V_{\mathrm{xc}}^h(\mathbf{x}) + \varphi^{h_{el}}(\mathbf{x}) + \sum_J \Big(V_{\mathrm{loc}}^J(|\mathbf{x}-\mathbf{R}_J|) - \bar{V}_{\tilde{\delta}}^{J^{h_{el}}}(|\mathbf{x}-\mathbf{R}_J|) \Big)\,. \tag{5.23}$$

In the case of all-electron calculations, $V_{\mathrm{eff,loc}}^h(\mathbf{x},\mathbf{R}) = V_{\mathrm{xc}}^h(\mathbf{x}) + \varphi^{h_{el}}(\mathbf{x})$ and $\mathrm{H}_{jk}^{\mathrm{nl}}$ is zero. In the case of pseudopotential calculations, H_{jk}^{nl} is given by

$$\mathrm{H}_{jk}^{\mathrm{nl}} = \sum_{J=1}^{N_a}\sum_{lpm} C_{lpm,j}^J h_{lp}^J C_{lpm,k}^J\,, \quad \text{where} \quad C_{lpm,j}^J = \int_{\Omega} \chi_{lpm}^J(\mathbf{x},\mathbf{R}_J) N_j^h(\mathbf{x})\, d\mathbf{x}\,. \tag{5.24}$$

Finally, the matrix elements of the overlap matrix $\mathbf{M}$ are given by

$$\mathrm{M}_{jk} = \int_{\Omega} N_j^h(\mathbf{x}) N_k^h(\mathbf{x})\, d\mathbf{x}. \tag{5.25}$$

We note that the matrices $\mathbf{H}^{\text{loc}}$ and $\mathbf{M}$ are sparse as the FE basis functions are local in real space and have a compact support (a finite region where the function is non-zero). Further, the vectors $C^J_{lpm,j}$ in $\mathbf{H}^{\text{nl}}$ are also sparse since the projectors $\chi^J_{lpm}(\mathbf{x}, \mathbf{R}_J)$ have a compact support, thus rendering a sparse structure to the discrete Hamiltonian $\mathbf{H}$.

In order to explore efficient solution strategies, it is desirable to transform the generalized eigenvalue problem into a standard eigenvalue problem. Since the matrix $\mathbf{M}$ is positive definite symmetric, there exists a unique positive definite symmetric square root of $\mathbf{M}$, and is denoted by $\mathbf{M}^{1/2}$. Hence, the following holds true:

$$\mathbf{H}\hat{\boldsymbol{\Psi}}_i = \epsilon_i^h \mathbf{M}\hat{\boldsymbol{\Psi}}_i \quad \Rightarrow \qquad \mathbf{H}\hat{\boldsymbol{\Psi}}_i = \epsilon_i^h \mathbf{M}^{1/2}\mathbf{M}^{1/2}\hat{\boldsymbol{\Psi}}_i \quad \Rightarrow \qquad \tilde{\mathbf{H}}\widetilde{\boldsymbol{\Psi}}_i = \epsilon_i^h \widetilde{\boldsymbol{\Psi}}_i\,, \tag{5.26}$$

$$\text{where} \quad \widetilde{\boldsymbol{\Psi}}_i = \mathbf{M}^{1/2}\hat{\boldsymbol{\Psi}}_i\,, \quad \tilde{\mathbf{H}} = \mathbf{M}^{-1/2}\mathbf{H}\mathbf{M}^{-1/2}\,. \tag{5.27}$$

We note that $\tilde{\mathbf{H}}$ is a Hermitian matrix, and (5.26) represents a standard Hermitian eigenvalue problem. The actual eigenvectors are recovered by the transformation $\hat{\boldsymbol{\Psi}}_i = \mathbf{M}^{-1/2}\widetilde{\boldsymbol{\Psi}}_i$. Furthermore, we note that the matrix $\mathbf{M}^{-1/2}$ can be evaluated with modest computational cost by using a spectral FE basis in conjunction with the use of Gauss-Lobatto-Legendre (GLL) quadrature for the evaluation of integrals in the overlap matrix, that renders the overlap matrix diagonal [61]. This renders the matrix $\tilde{\mathbf{H}}$ the same sparsity structure as the matrix $\mathbf{H}$.

Finally, for the given positions of nuclei, the discrete Kohn-Sham eigenvalue problem along with the discretized Poisson equations for the electrostatic potentials ($\varphi^{h_{el}}$

and $\bar{V}_{\tilde{\delta}}^{J^{h_{el}}}$) are to be solved self-consistently, and are given by:

$$\mathbf{M}^{-1/2}\mathbf{H}\mathbf{M}^{-1/2}\widetilde{\boldsymbol{\Psi}}_i = \epsilon_i^h \widetilde{\boldsymbol{\Psi}}_i\,, \tag{5.28a}$$

$$\sum_{j=1}^{M_{el}} \left[\frac{1}{4\pi}\int_{\Omega} \nabla N_i^{h_{el}}(\mathbf{x}).\nabla N_j^{h_{el}}(\mathbf{x})\; d\mathbf{x}\right]\varphi^j = \int_{\Omega} \left(\rho^h(\mathbf{x}) + b^{h_{el}}(\mathbf{x},\mathbf{R})\right) N_i^{h_{el}}(\mathbf{x})\,\mathrm{d}\mathbf{x}\,, \tag{5.28b}$$

$$\sum_{j=1}^{M_{el}} \left[\frac{1}{4\pi}\int_{\Omega_J} \nabla N_i^{h_{el}}(\mathbf{x}).\nabla N_j^{h_{el}}(\mathbf{x})\,\mathrm{d}\mathbf{x}\right]\bar{V}_{\tilde{\delta}}^{J^j} = \int_{\Omega_J} \left(b_J^{h_{el}}(|\mathbf{x}-\mathbf{R}_J|)\right) N_i^{h_{el}}(\mathbf{x})\; d\mathbf{x}\,, \quad \forall J\,, \tag{5.28c}$$

$$2\sum_i f(\epsilon_i^h,\mu) = N_e\,, \quad \rho^h(\mathbf{x}) = 2\sum_i f(\epsilon_i^h,\mu)|\psi_i^h(\mathbf{x})|^2\,. \tag{5.28d}$$

We note that the nuclear charges in DFT-FE implementation are located on the nodes of the FE triangulation, and are treated as point charges. Thus, the nuclear charge distribution in the discrete setting $b^{h_{el}}(\mathbf{x},\mathbf{R})$ in equation (5.28b) is given by $b^{h_{el}}(\mathbf{x},\mathbf{R}) = \sum_I b_I^{h_{el}}(|\mathbf{x}-\mathbf{R}_I|)$ with $b_I^{h_{el}} = -Z_I\delta(|\mathbf{x}-\mathbf{R}_I|)$ where $\delta(|\mathbf{x}-\mathbf{R}_I|)$ denotes the Dirac-delta distribution centered at the position of the atom $\mathbf{R}_I$. The boundary conditions used for the computation of the discrete potential field $\varphi^{h_{el}}(\mathbf{x})$ in equation (5.28b) are either homogeneous Dirichlet boundary conditions or periodic boundary conditions depending on whether the problem is non-periodic or periodic. Further, the discrete self potential $\bar{V}_{\tilde{\delta}}^{J^{h_{el}}}$ associated with individual nuclear charge J is solved using the discrete Poisson equation (5.28c) subject to Dirichlet boundary conditions with prescribed Coulomb potential applied on a domain Ω_J enclosing the atom J. After obtaining the electronic ground-state from the solution of the discrete Kohn-Sham problem (equations (5.28)), we compute the discrete total ground-state energy E^h in terms of the discrete solution fields $(\bar{\epsilon}_i^h, \bar{\rho}^h, \bar{\varphi}^{h_{el}}, \bar{V}_{\tilde{\delta}}^{I^{h_{el}}})$ as follows:

$$E^h = E^h_{\text{band}} - E^h_{\text{pot}} + E^h_{\text{xc}}(\bar{\rho}^h, \nabla\rho^h) + E^{h_{el}}_{\text{el}}\,, \tag{5.29}$$

where,

$$
\begin{aligned}
E^h_{\text{band}} &= 2\sum_i f(\bar{\epsilon}^h_i, \mu)\bar{\epsilon}^h_i\,, \quad E^h_{\text{pot}} = \int_\Omega \bar{\rho}^h(\mathbf{x})\left(V^h_{\text{xc}}(\mathbf{x}) + \bar{\varphi}^{h_{el}}(\mathbf{x})\right)\,d\mathbf{x}\,,\\
E^{h_{el}}_{\text{el}} &= \int_\Omega \left[-\frac{1}{8\pi}|\nabla\bar{\varphi}^{h_{el}}(\mathbf{x})|^2 + (\bar{\rho}^{h_{el}}(\mathbf{x}) + b^{h_{el}}(\mathbf{x},\mathbf{R}))\bar{\varphi}^{h_{el}}(\mathbf{x})\right]\,d\mathbf{x}\\
&\quad + \sum_I \int_{\mathbb{R}^3}\left[\frac{1}{8\pi}|\nabla\bar{V}^{I^{h_{el}}}_{\tilde{\delta}}(\mathbf{x})|^2 - b^{h_{el}}_I(|\mathbf{x}-\mathbf{R}_I|)\bar{V}^{I^{h_{el}}}_{\tilde{\delta}}(\mathbf{x})\right]\,d\mathbf{x}\,.
\end{aligned}
$$

5.2 Improvements in the SCF Algorithm for large-scale Kohn-Sham DFT calculations

The discrete nonlinear Hermitian eigenvalue problem is solved self-consistently along with Poisson equations (see equation (5.28)) to compute the Kohn-Sham ground-state solution. Algorithm 1 lists all the steps in the SCF procedure followed in DFT-FE. We use adaptive higher order spectral finite-elements in conjunction with computationally efficient and scalable Chebyshev filtered subspace iteration technique (ChFSI) [61, 179] to evaluate the occupied eigenspace of the discrete Kohn-Sham Hamiltonian. We further employ Anderson and Broyden schemes [101, 180] for electron-density mixing, and the finite-temperature Fermi-Dirac smearing [138] to avoid the charge sloshing associated with metallic systems.

The ChFSI procedure in Algorithm 1 involves the Chebyshev filtering (CF), orthonormalization (CholGS), and the Rayleigh-Ritz procedure (RR). We note that CF scales quadratically with number of atoms, while CholGS and RR scale cubically with number of atoms. Thus, for small to medium scale system sizes CF is the dominant computational cost, while for larger system sizes the computational cost of CholGS and RR dominates. To this end, the numerical implementation in DFT-FE focuses on reducing the prefactor and improving scalability of the ChFSI procedure by exploiting efficient methods and cache-friendly data-structures like FE cell level matrix-matrix multiplications, mixed precision strategies and spectrum splitting approach, as will be discussed subsequently. Furthermore, the electrostatic potentials are computed by solving a Poisson problem, which employs a matrix-free framework of the deal.II finite-element library [181, 182] in conjunction with a Jacobi preconditioned conjugate gradient solver. We note that the above matrix-free framework computes the matrix-vector product of the FE operator on the fly without ever storing it as a sparse matrix. Such on the fly computations benefit from significantly lower memory access costs and have been demonstrated to outperform global sparse-matrix based methods on modern computing architectures [181].

Algorithm 1 Self Consistent Field (SCF) iteration in DFT-FE

```
1: Compute the self-potentials ($\bar{V}_{\tilde{\delta}}^{J^{h_{el}}}$) corresponding to the nuclear charges by solving the discrete Poisson equations (5.28c).
2: Compute the discrete pseudopotential projector matrices $C^{J}_{lpm,j}$ (see equation (5.24)).
3: Start with an initial guess for $\rho^{h}_{\text{in}}(\mathbf{x})$, obtained from the superposition of single atom charge densities, and an initial guess for $\widetilde{\mathbf{\Psi}}$ using single-atom Kohn-Sham DFT wavefunctions.
4: [ES] Get the total electrostatic potential $\varphi^{h}(\mathbf{x}, \mathbf{R})$ by solving the discrete Poisson equation (5.28b).
5: Get effective potential, $V^{h}_{\text{eff,loc}}(\rho^{h}_{\text{in}}(\mathbf{x}), \mathbf{R}) = V^{h}_{\text{xc}} + \varphi^{h_{el}} + \sum_{J}(V^{J^{h}}_{\text{loc}} - \bar{V}_{\tilde{\delta}}^{J^{h_{el}}})$ (see equation (5.14)).
6: Compute the FE cell level Hamiltonian matrices corresponding to $H^{\text{loc}}_{jk}$ (see equation (5.22)).
7: Employ Chebyshev-filtered subspace iteration (ChFSI) method to get the occupied subspace spanning the $N (N > N_e/2)$ lowest eigenvectors of $\widetilde{\mathbf{H}}$ (see equation (5.26)).
    a: [CF] Chebyshev filtering of $\widetilde{\mathbf{\Psi}}$ (see Section 5.2.1).
    b: [CholGS] Orthonormalize the Chebyshev filtered basis $\widetilde{\mathbf{\Psi}}$ (call Algorithm 2 in Section 5.2.2).
    c: [RR] Perform the Rayleigh-Ritz procedure (call Algorithm 3 in Section 5.2.3).
8: [DC] Compute new output electron density, $\rho^{h}_{\text{out}}(\mathbf{x})$ (call Algorithm 4 in Section 5.2.3).
9: If $\left\|\rho^{h}_{\text{out}}(\mathbf{x}) - \rho^{h}_{\text{in}}(\mathbf{x})\right\| \leq$ tolerance, stop; Else, compute new $\rho^{h}_{\text{in}}(\mathbf{x})$ using a mixing scheme and go to step 4.
```

5.2.1 Chebyshev filtering

In DFT-FE, Chebyshev polynomial filtering technique [168] is used to adaptively approximate the wanted eigenspace (the lowest N occupied eigenfunctions) of the FE discretized Hamiltonian $\widetilde{\mathbf{H}}$ [61]. In practice, N is typically chosen as $N_e/2 + b$ to allow for finite-temperature Fermi-Dirac smearing, where b is usually $(5 - 10)\%$ of $N_e/2$. In a given SCF iteration step, a scaled Hamiltonian $\bar{\mathbf{H}}$ is obtained by scaling and shifting $\widetilde{\mathbf{H}}$ such that the unwanted spectrum of $\widetilde{\mathbf{H}}$ is mapped on to $[-1, 1]$, and the wanted spectrum is mapped on to $(-\infty, -1)$ to exploit the fast growth property of Chebyshev polynomials in this region. Subsequently, the action of a degree m Chebyshev polynomial filter, $T_m(\bar{\mathbf{H}})$, on the input subspace, $\widetilde{\boldsymbol{\Psi}}$, is computed recursively as

$$T_m(\bar{\mathbf{H}})\widetilde{\boldsymbol{\Psi}} = \left[2\bar{\mathbf{H}}T_{m-1}(\bar{\mathbf{H}}) - T_{m-2}(\bar{\mathbf{H}})\right]\widetilde{\boldsymbol{\Psi}}\,. \tag{5.30}$$

We use an adaptive filtering strategy in which multiple sweeps of ChFSI procedure are performed till the residual norm of the eigenpair closest to the Fermi energy reaches below a specified tolerance δ, chosen to between $1 \times 10^{-2} - 5 \times 10^{-2}$. Our numerical experiments in the case of pseudopotential electronic ground-state calculations show that while multiple calls to ChFSI are triggered in the first few SCF iterations, there is an overall reduction in the number of ChFSI calls (due to reduced number of SCF iterations) when employing the adaptive filtering strategy in comparison to employing a single sweep in all SCF iterations. We remark that despite using the adaptive filtering strategy, for atomic relaxations or molecular dynamics simulations, multiple Chebyshev filtering calls are typically not triggered as the wavefunctions from the previous electronic ground-state calculation are reused as a starting guess. We note that the choice of the Chebyshev polynomial degree m in equation (5.30) is based on the upper bound of the spectrum of $\widetilde{\mathbf{H}}$, which is governed by the smallest mesh size employed in the finite element discretization. A Chebyshev polynomial degree between 20–50 is typically used in DFT-FE for pseudopotential calculations, whereas significantly higher Chebyshev polynomial degrees ($\sim 500 - 1000$) are required for all-electron calculations.

5.2.1.1 Practical implementation aspects of Chebyshev filtering

The computational complexity of Chebyshev filtering scales as $\mathcal{O}(MN)$, where M is the size of the discretized Hamiltonian $\widetilde{\mathbf{H}}$ and N is the number of occupied states. Since Chebyshev filtering is the dominant computational cost in DFT-FE for small to medium sized systems (up to 20,000 electrons), we optimize the core kernel in the Chebyshev filtering procedure, which involves the computation of $\bar{\mathbf{H}}\mathbf{X}$ in equation (5.30), with $\mathbf{X}$ denoting a trial subspace in the course of the Chebyshev recursive iteration. To this end, we first explicitly compute and store the FE Hamiltonian matrices (cell level Hamiltonian matrices), and subsequently extract the cell level wavefunction matrices from the global wavefunction vectors $\mathbf{X}$. We then employ BLAS `Xgemm` routines to compute the matrix-matrix products involving cell Hamiltonian and wavefunction matrices, and assemble them to get the global wavefunction vectors. We note that global FE sparse matrix approaches, particularly when dealing with large number of wavefunction vectors, are more memory-bandwidth limited[3] and incur a higher communication cost[4] than the cell level matrix approach employed above.

In case of large problems with many thousands of wavefunction vectors, the peak memory during Chebyshev filtering can be quite high if implemented naively by filtering all the wavefunction vectors simultaneously, as multiple temporary memories of size $\mathbf{X}$ are needed in the course of the Chebyshev recursive iteration. Hence, to re-

---

[3] The cell level matrix approach is similar in spirit to matrix-free based approaches, which have been demonstrated to have lower memory access costs than global FE sparse-matrix based methods [181].

[4] The global FE sparse matrix framework in deal.II library currently does not take advantage of performing MPI communication of multiple vectors in a single communication call.

duce the peak memory, we use a blocked approach by filtering blocks of wavefunction vectors, $\mathbf{X}_b$ with block size denoted by B^f, based on the rationale that Chebyshev filtering can be performed on each wavefunction vector independently. Further, the blocked approach also allows us to take advantage of batched `Xgemm` [5] routines in $\widetilde{\mathbf{H}}\mathbf{X}_b$ to perform the aforementioned cell level matrix-matrix products concurrently on multiple threads, which we found to be faster than using multiple threads on standard `Xgemm` calls involving very skewed matrix dimensions when blocked approach is not used. Additionally, we use a single contiguous memory block to store the global wavefunction vectors as well as the block wavefunction vectors, where the data layout is such that for each degree of freedom the corresponding wavefunction values are stored contiguously. This leads to more cache-friendly data access while copying the data between the global wavefunction vectors and the cell wavefunction matrices. Furthermore, we exploit the fact that all wavefunction vectors have identical communication pattern to minimize the total number of MPI point-to-point communication calls in $\widetilde{\mathbf{H}}\mathbf{X}_b$, which reduces the network latency.

The optimal value of the Chebyshev filtering block size, B^f, depends on two competing factors—very small sizes lead to higher memory access overheads and communication latency, whereas very large sizes increase peak memory and reduce the efficiency of batched `Xgemm` routines. Based on numerical experiments, we find the optimal range of B^f to be between 300–400, which is set as the default in DFT-FE.

5.2.2 Cholesky factorization based Gram-Schmidt orthonormalization

ChFSI involves orthonormalization procedure after the Chebyshev filtering step to prevent the ill-conditioning of the filtered vectors in the course of the subspace iteration procedure. This procedure scales cubically with number of electrons and

---

[5] Batched operations are efficient for performing many small matrix-matrix multiplications concurrently on multiple threads. Currently such routines are available in vendor optimized BLAS libraries such as Intel MKL.

becomes one of the dominant computational costs in large-scale problems (greater than 20,000 electrons). To this end, we employ Cholesky factorization based Gram-Schmidt (CholGS) orthonormalization technique in DFT-FE. This is shown to be more efficient and scalable [164, 183] than the commonly used classical Gram-Schmidt procedure. Algorithm 2 shows the steps involved in the CholGS procedure. The $\mathcal{O}(N^2)$ dot products involved in classical Gram-Schmidt are replaced by more cache-friendly matrix-matrix multiplications in CholGS (steps 1 and 4). Furthermore, the single communication call involved in the computation of overlap matrix $\mathbf{S}$ in CholGS has a much lower communication latency in comparison to $\mathcal{O}(N^2)$ communication calls in classical Gram-Schmidt.

Algorithm 2 Cholesky-Gram-Schimdt (CholGS) orthonormalization

```
1: Compute overlap matrix, $\mathbf{S} = \widetilde{\boldsymbol{\Psi}}^{\dagger}\widetilde{\boldsymbol{\Psi}}$.   $(\mathcal{O}(MN^2))$
2: Perform Cholesky factorization of the overlap matrix, $\mathbf{S} = \mathbf{L}\mathbf{L}^{\dagger}$.   $(\mathcal{O}(N^3))$
3: Compute $\mathbf{L}^{-1}$.   $\mathcal{O}(N^3)$
4: Construct orthonormal basis: $\widetilde{\boldsymbol{\Psi}}^{\text{o}} = \widetilde{\boldsymbol{\Psi}}\mathbf{L}^{-\mathbf{1}^{\dagger}}$.   $(\mathcal{O}(MN^2))$
```

5.2.2.1 Parallel implementation aspects of CholGS in Algorithm 2

Computation of overlap matrix We first note that $\widetilde{\boldsymbol{\Psi}}$ is stored in parallel as a $M_{\text{loc}} \times N$ matrix, where M_{loc} is the number of FE nodes owned locally by a given MPI task. Accordingly, a straightforward approach to compute the overlap matrix $\mathbf{S}$ in step 1 involves the evaluation of local contributions of $\widetilde{\boldsymbol{\Psi}}^{\dagger}\widetilde{\boldsymbol{\Psi}}$ (a $N \times N$ matrix) on each MPI task, and then accumulating the local contributions to $\mathbf{S}$ using the `MPI_Allreduce` collective routine. However, this approach requires memory corresponding to a $N \times N$ matrix on each MPI task, and hence is not practically applicable for large-scale problems $\sim (N > 20,000)$. To avoid this large memory footprint in both storage of $\mathbf{S}$ as well as computation of the local contributions, we use the popular 2D cyclic block grid distribution of ScaLAPACK library [184] to distribute the memory of $\mathbf{S}$, and use a blocked approach to compute the local contributions of

$\widetilde{\mathbf{\Psi}}^{\dagger}\widetilde{\mathbf{\Psi}}$ to $\mathbf{S}$. Further in the blocked approach, we also exploit the Hermiticity of $\mathbf{S}$, by computing only the lower triangular portion of $\mathbf{S}$. Fig. 5.1 shows the schematic of the blocked approach with block size B^v, where $[i, N] \times [i, i + B^v]$ sub-matrices of $\mathbf{S}$ are computed successively one after another. Computation of each sub-matrix first involves computation of the local contribution in each MPI task by performing matrix-matrix multiplication between $[i, N] \times M_{\text{loc}}$ block of $\widetilde{\mathbf{\Psi}}^{\dagger}$ and $M_{\text{loc}} \times [i, i + B^v]$ of $\widetilde{\mathbf{\Psi}}$ using BLAS `Xgemm` routine, followed by accumulation of the local contributions using the `MPI_Allreduce` collective. Subsequently, the corresponding sub-matrix entries of the ScaLAPACK parallelized $\mathbf{S}$ are filled. Overall, the above blocked approach combined with ScaLAPACK parallelization of $\mathbf{S}$ provides both memory optimization and efficiency improvements.

Computation of inverse of Cholesky factor Cholesky factorization of $\mathbf{S}$ in step 2 and inversion of the Cholesky factor $\mathbf{L}$ in step 3 are performed using ScaLAPACK routines `pXpotrf` and `pXtrtri`, respectively. Based on the numerical experiments conducted on a large benchmark systems, we find that the steps 2 and 3 are a minor cost compared to other steps in CholGS. For instance, the cost of steps 2 and 3 combined contributed to about 7% of the total wall time for CholGS for a system containing 61,502 electrons (see Fig. 5.3).

Construction of orthonormal vectors Similar to step 1, computation of the orthonormalized basis $\widetilde{\mathbf{\Psi}}^{\text{o}}$ in step 4 also has a large memory footprint when performed simply as a matrix-matrix multiplication between the local portion ($M_{\text{loc}} \times N$ matrix) of the parallel distributed $\widetilde{\mathbf{\Psi}}$ and the full $\mathbf{L^{-1}}^{\dagger}$ ($N \times N$ matrix) on every MPI task. For large-scale problems this leads to a high peak memory due to storage of the full $\mathbf{L^{-1}}^{\dagger}$ on every MPI task, and also to store the computed $\widetilde{\mathbf{\Psi}}^{\text{o}}$, which requires the same memory size as $\widetilde{\mathbf{\Psi}}$. Hence, we compute $\widetilde{\mathbf{\Psi}}^{\text{o}}$ using two blocked levels to address both of these memory issues, as shown schematically in Fig. 5.2. First, we employ an outer blocked level over M_{loc} with block size B^d, which allows reuse of the memory of $\widetilde{\mathbf{\Psi}}$ to store $\widetilde{\mathbf{\Psi}}^{\text{o}}$. In particular, we compute $[i, i + B^d] \times [1, N]$ sub-matrices of $\widetilde{\mathbf{\Psi}}^{\text{o}}$ one after the other and copy the orthonormalized sub-matrices back on to $\widetilde{\mathbf{\Psi}}$, thereby requiring only an additional $B^d \times N$ memory. Secondly, we employ an inner blocked level where each $[i, i+B^d] \times [1, N]$ sub-matrix of $\widetilde{\mathbf{\Psi}}^{\text{o}}$ is further divided into $[i, i+B^d] \times [j, j+B^v]$ sub-matrices and successively computed. Similar to the blocked approach used in step 1, this inner blocked level removes the requirement to store the full $\mathbf{L^{-1}}^{\dagger}$ while also exploiting the triangular matrix property of $\mathbf{L^{-1}}^{\dagger}$. Each $[i, i + B^d] \times [j, j + B^v]$ sub-matrix in the inner blocked level is computed by performing a matrix-matrix multiplication between a $[i, i+B^d] \times [1, j+B^v]$ sub-matrix of $\widetilde{\mathbf{\Psi}}$ and a $[1, j+B^v] \times [j, j+B^v]$ sub-matrix of $\mathbf{L^{-1}}^{\dagger}$. We note that $\mathbf{L^{-1}}^{\dagger}$ is stored in a ScaLAPACK parallel format after the end of step 3. Thus to obtain the $[1, j + B^v] \times [j, j + B^v]$ sub-matrix of $\mathbf{L^{-1}}^{\dagger}$ in each MPI task, we first use the local portion of the parallel $\mathbf{L^{-1}}^{\dagger}$ to fill the corresponding entries in the sub-matrix and the rest as zeros, and subsequently use the `MPI_Allreduce` collective to gather and communicate the filled sub-matrix to all MPI tasks.

Remarks on block sizes We now discuss few considerations regarding the choice of optimal values for the block sizes B^v (used above in steps 1 and 4) and B^d (used above in step 4). Too small values of B^v will lead to computational overheads in the `Xgemm` calls due to the highly skewed matrix dimensions which are not cache-friendly, and, further, the total number of MPI collective communication calls will increase leading to higher communication latency. On the other hand too large values of B^v will deprecate the efficiency benefit of exploiting the Hermiticity of $\mathbf{S}$ in step 1 and the triangular matrix nature of $\mathbf{L^{-1}}^{\dagger}$ in step 4. Based on numerical experiments, we find that value of B^v between 350–500 is optimal. Similarly, the choice of B^d is based on two competing factors— too small values of B^d incur higher computational and communication overheads due to repeated access of $\mathbf{L^{-1}}^{\dagger}$ for every outer level block computation, whereas larger values increase the peak memory required in step 4. We

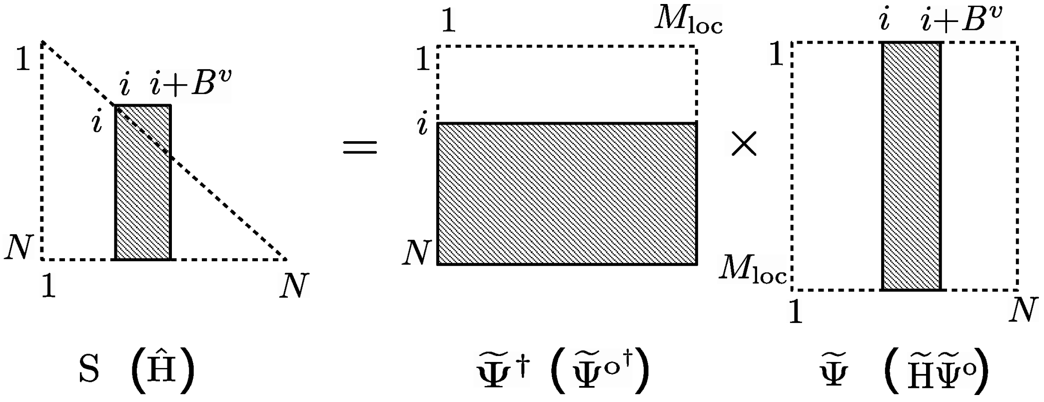

Figure 5.1: Blocked approach computation of lower triangular part of the Hermitian overlap matrix, $\mathbf{S} = \widetilde{\mathbf{\Psi}}^{\dagger}\widetilde{\mathbf{\Psi}}$ in Algorithm 2, and of the Hermitian projected Hamiltonian, $\hat{\mathbf{H}} = \widetilde{\mathbf{\Psi}}^{\mathbf{o}^{\dagger}}\widetilde{\mathbf{H}}\widetilde{\mathbf{\Psi}}^{\mathbf{o}}$ in Algorithm 3.

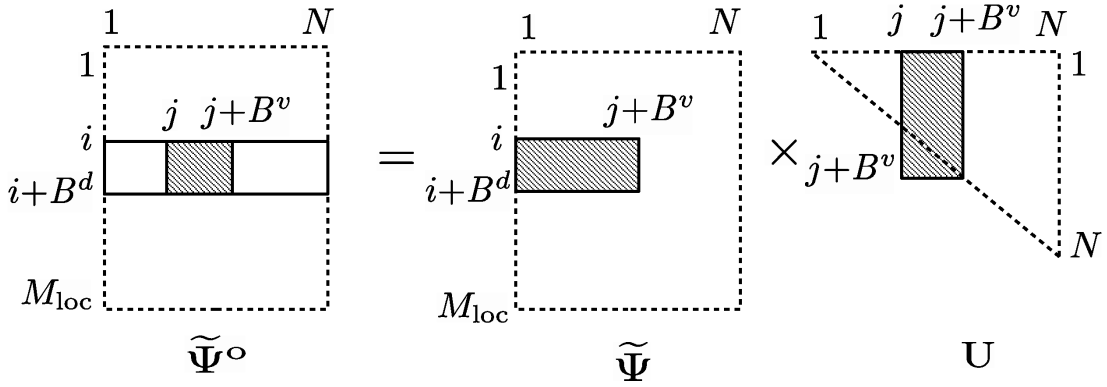

Figure 5.2: Two level blocked approach computation of $\widetilde{\mathbf{\Psi}}^{\mathbf{o}} = \widetilde{\mathbf{\Psi}}\mathbf{U}$, where $\mathbf{U}$ is an upper triangular matrix.

find that B^d values between 2000–3000 have very negligible overhead costs while still providing memory efficiency when M_{loc} is much larger than B^d.

5.2.2.2 Mixed precision approaches in CholGS

To further reduce the prefactor of the CholGS algorithm, we make use of mixed precision arithmetic in steps 1 and 4 of Algorithm 2, which are the dominant costs in the CholGS algorithm. Mixed precision approaches for orthonormalization in the context of electronic-structure calculations have been explored previously by [185]. We first develop a mixed precision approach for step 1, where the computation of the overlap matrix, $\mathbf{S}$ can be split into computation of the diagonal and the off-diagonal parts:

$$\mathbf{S} = \mathbf{S_d} + \mathbf{S_{od}}, \tag{5.31}$$

where $\mathbf{S_d}$ is a matrix containing the diagonal entries of $\mathbf{S}$. We take advantage of the fact that $\mathbf{S_{od}} \to \mathbf{0}$ as the SCF approaches convergence and hence compute $\mathbf{S_{od}}$ using single precision BLAS `Xgemm` routines, while the computation of diagonal entries of $\mathbf{S_d}$ is performed using double precision BLAS routines at negligible computational cost. Similarly, step 4 can be split into

$$\widetilde{\mathbf{\Psi}}^{\mathbf{o}} = \widetilde{\mathbf{\Psi}}\mathbf{L}_{\mathbf{d}}^{\mathbf{-1}^{\dagger}} + \widetilde{\mathbf{\Psi}}\mathbf{L}^{\mathbf{-1}^{\dagger}}_{\mathbf{od}}, \tag{5.32}$$

where $\mathbf{L}_{\mathbf{d}}^{\mathbf{-1}^{\dagger}}$ is a matrix containing the diagonal entries of $\mathbf{L}^{\mathbf{-1}^{\dagger}}$. Taking advantage of the fact that $\mathbf{L}_{\mathbf{od}}^{\mathbf{-1}^{\dagger}} \to \mathbf{0}$ as the SCF approaches convergence, we compute $\widetilde{\mathbf{\Psi}}\mathbf{L}_{\mathbf{od}}^{\mathbf{-1}^{\dagger}}$ using single precision BLAS `Xgemm` routines, while the computation of $\widetilde{\mathbf{\Psi}}\mathbf{L}_{\mathbf{d}}^{\mathbf{-1}^{\dagger}}$ is performed as a double precision scaling operation at negligible computational cost. We remark that, in addition to the reduction of computational costs, the use of mixed precision also reduces the communication costs in steps 1 and 4 as the `MPI_Allreduce` collectives employed in these steps communicate the relevant single precision data with half the MPI message size (bytes), in comparison to their double precision counterparts.

The computational cost reduction in steps 1 and 4 of the mixed precision approach is demonstrated in Fig. 5.3 for large-scale benchmark problems involving 39,900 and 61,502 electrons. We find this approach to be around 2 times faster in comparison to double precision approach. Furthermore, we also examine the accuracy and robustness of the mixed precision algorithm in the overall SCF convergence in Section 5.2.3.2, and is discussed in detail subsequently.

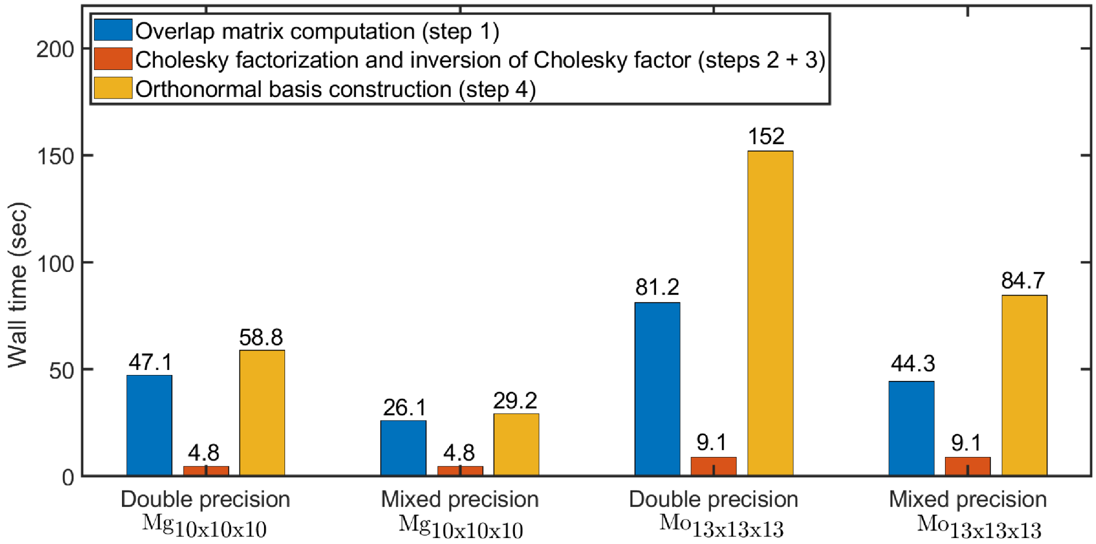

Figure 5.3: Comparison of CholGS algorithm (Algorithm 2) wall times for a single SCF step in using mixed precision arithmetic in steps 1 and 4. Case studies: (i) $\mathrm{Mg}_{10x10x10}$ with 39,990 electrons run on 51,200 MPI tasks and (ii) $\mathrm{Mo}_{13x13x13}$ with 61,502 electrons run on 64,000 MPI tasks.

5.2.3 Rayleigh-Ritz procedure and electron-density computation

Rayleigh-Ritz (RR) procedure in ChFSI involves the following steps: i) computation of the projected Hamiltonian, $\hat{\mathbf{H}} = \widetilde{\boldsymbol{\Psi}}^{\mathbf{o}^\dagger} \widetilde{\mathbf{H}} \widetilde{\boldsymbol{\Psi}}^{\mathbf{o}}$ into the space spanned by the orthonormalized wavefunctions $\widetilde{\boldsymbol{\Psi}}^{\mathbf{o}}$, ii) diagonalization of $\hat{\mathbf{H}}$: $\hat{\mathbf{H}}\mathbf{Q} = \mathbf{Q}\mathbf{D}$, where $\mathbf{D}$ contains all the eigenvalues of $\hat{\mathbf{H}}$ in ascending order and $\mathbf{Q}$ contains the corresponding eigenvectors, iii) subspace rotation of $\widetilde{\boldsymbol{\Psi}}^{\mathbf{o}}$: $\widetilde{\boldsymbol{\Psi}}^{\mathbf{R}} = \widetilde{\boldsymbol{\Psi}}^{\mathbf{o}}\mathbf{Q}$. Subsequently, the output electron-density at a point $\mathbf{x}$ belonging to a FE cell e is computed as

$$\begin{aligned} \rho^h_{\text{out}}(\mathbf{x}) =& 2\sum_{i=1}^{N} f(\epsilon^h_i, \mu)|\psi^h_i(\mathbf{x})|^2 \\ =& 2\sum_{i=1}^{N} \left[f(\epsilon^h_i, \mu) \left(\sum_{j=1}^{M_e} \psi_i^{e,j} N^e_j(\mathbf{x}) \right) \left(\sum_{k=1}^{M_e} \psi_i^{e,k^*} N^e_k(\mathbf{x}) \right) \right], \end{aligned} \tag{5.33}$$

where $\left\{ N^e_1(\mathbf{x}),\, N^e_2(\mathbf{x}),\, \cdots\, N^e_{M_e}(\mathbf{x}) \right\}$ denote the FE basis functions associated with the given cell (M_e denoting the number of nodes in the cell), and $\left\{ \psi_i^{e,1},\, \psi_i^{e,2},\, \cdots\, \psi_i^{e,M_e} \right\}$ denote the corresponding nodal values of the i^{th} wavefunction, $\boldsymbol{\psi}^h_i(\mathbf{x})$ in FE cell e.

Using the subspace rotated wavefunctions $\widetilde{\boldsymbol{\Psi}}^{\mathbf{R}}$, Equation 5.33 can be re-written as

$$\rho^h_{\text{out}}(\mathbf{x}) = 2\,\boldsymbol{n}^{\boldsymbol{e}^{\boldsymbol{T}}}(\mathbf{x})\hat{\boldsymbol{\Psi}}^{\mathbf{R}}_{\boldsymbol{e}} f\left(\mathbf{D},\mu\right)\hat{\boldsymbol{\Psi}}^{\mathbf{R}^{\dagger}}_{\boldsymbol{e}}\,\boldsymbol{n}^{\boldsymbol{e}}(\mathbf{x}), \tag{5.34}$$

where

$$\boldsymbol{n}^{\boldsymbol{e}}(\mathbf{x}) = \left[N^e_1(\mathbf{x})\, N^e_2(\mathbf{x})\, \cdots\, N^e_{M_e}(\mathbf{x})\right]^T, \tag{5.35}$$

and the matrix $\hat{\boldsymbol{\Psi}}^{\mathbf{R}}_{\boldsymbol{e}}$ contains the FE cell column vectors extracted from $\hat{\boldsymbol{\Psi}}^{\mathbf{R}}$ which is given by

$$\hat{\boldsymbol{\Psi}}^{\mathbf{R}} = \mathbf{M}^{-1/2}\widetilde{\boldsymbol{\Psi}}^{\mathbf{R}}. \tag{5.36}$$

In the above, the computational complexity of steps i), ii) and iii) of the Rayleigh-Ritz procedure scales as $\mathcal{O}(MN^2)$, $\mathcal{O}(N^3)$, and $\mathcal{O}(MN^2)$, respectively, while the electron-density computation scales as $\mathcal{O}(MN)$. Rayleigh-Ritz procedure is, thus, one of the significant bottlenecks for large-scale problems. To this end, we employ two strategies in DFT-FE: spectrum-splitting and mixed precision, to reduce the prefactor of Rayleigh-Ritz procedure, as discussed below.

5.2.3.1 Spectrum-splitting in RR

Algorithm 3 Spectrum-splitting based Rayleigh Ritz procedure (RR)

```
Compute $\hat{\mathbf{H}} = \widetilde{\boldsymbol{\Psi}}^{\mathbf{o}^{\dagger}}\widetilde{\mathbf{H}}\widetilde{\boldsymbol{\Psi}}^{\mathbf{o}}$.
Compute $N_{\text{fr}}$ largest eigenstates of $\hat{\mathbf{H}}$: $\hat{\mathbf{H}}\mathbf{Q}_{\mathbf{fr}} = \mathbf{Q}_{\mathbf{fr}}\mathbf{D}_{\mathbf{fr}}$.
Subspace rotation to compute fractionally occupied eigenstates: $\widetilde{\boldsymbol{\Psi}}^{\mathbf{R}}_{\mathbf{fr}} = \widetilde{\boldsymbol{\Psi}}^{\mathbf{o}}\mathbf{Q}_{\mathbf{fr}}$.
```

The key idea behind spectrum-splitting is that the eigenvalues and eigenvectors of the projected Hamiltonian $\hat{\mathbf{H}}$ with orbital occupancy function $f_i = 1$ are not explicitly necessary for the computation of the electron-density in equation (5.34). This can be exploited to achieve significant computational savings when most of the Kohn-Sham states are fully occupied as is the case for typically used Fermi-Dirac smearing temperatures $\sim$ 500 K. Such methods have been developed in previous works in the context of both pseudopotential [159, 186] and all-electron DFT [187] calculations, which we have adapted in DFT-FE. Furthermore, we additionally take advantage of spectrum-splitting to develop a mixed precision technique to reduce the computational cost of the projected Hamiltonian computation. We discuss below the implementation of the spectrum-splitting algorithm in DFT-FE.

Let N_{oc} denote the number of Kohn-Sham eigenstates with full occupancies ($f_i = 1$), and $N_{\text{fr}} = N - N_{\text{oc}}$ denote the number of remaining states with partial occupancies. We consider the following split in the diagonalization of $\hat{\mathbf{H}}$:

$$\hat{\mathbf{H}} = \left[\begin{array}{c|c} \mathbf{Q_{oc}} & \mathbf{Q_{fr}} \end{array}\right] \left[\begin{array}{c|c} \mathbf{D_{oc}} & \mathbf{0} \\ \hline \mathbf{0} & \mathbf{D_{fr}} \end{array}\right] \left[\begin{array}{c} \mathbf{Q}^{\dagger}_{\mathbf{oc}} \\ \hline \mathbf{Q}^{\dagger}_{\mathbf{fr}} \end{array}\right], \tag{5.37}$$

where $\mathbf{Q_{oc}}$ contains the eigenvectors corresponding to N_{oc} eigenvalues of $\hat{\mathbf{H}}$, which are stored as the diagonal entries of $\mathbf{D_{oc}}$. On the other hand, $\mathbf{Q_{fr}}$ contains the eigenvectors corresponding to remaining N_{fr} eigenvalues of $\hat{\mathbf{H}}$, which are stored as the diagonal entries of $\mathbf{D_{fr}}$. Similarly $f\left(\mathbf{D}, \mu\right)$ can be split as

$$f\left(\mathbf{D}, \mu\right) = \left[\begin{array}{c|c} f\left(\mathbf{D_{oc}}, \mu\right) & \mathbf{0} \\ \hline \mathbf{0} & f\left(\mathbf{D_{fr}}, \mu\right) \end{array}\right]. \tag{5.38}$$

Using the above equation (5.38) along with the scaling step in equation (5.36) and subspace rotation: $\widetilde{\mathbf{\Psi}}^{\mathbf{R}} = \widetilde{\mathbf{\Psi}}^{\mathbf{o}}\mathbf{Q}$, equation (5.34) can be written as

$$\rho^h_{\text{out}}(\mathbf{x}) = 2\,\boldsymbol{n}^{\boldsymbol{e}^{\boldsymbol{T}}}(\mathbf{x})\hat{\mathbf{\Psi}}^{\mathbf{o}}_{\boldsymbol{e}} \left[\begin{array}{c|c} \mathbf{Q_{oc}} & \mathbf{Q_{fr}} \end{array}\right] \left[\begin{array}{c|c} f\left(\mathbf{D_{oc}}, \mu\right) & \mathbf{0} \\ \hline \mathbf{0} & f\left(\mathbf{D_{fr}}, \mu\right) \end{array}\right] \left[\begin{array}{c} \mathbf{Q}^{\dagger}_{\mathbf{oc}} \\ \hline \mathbf{Q}^{\dagger}_{\mathbf{fr}} \end{array}\right] \hat{\mathbf{\Psi}}^{\mathbf{o}^{\dagger}}_{\boldsymbol{e}}\,\boldsymbol{n}^{\boldsymbol{e}}(\mathbf{x}), \tag{5.39}$$

where $\hat{\mathbf{\Psi}}^{\mathbf{o}}_{\boldsymbol{e}}$ denotes the FE cell level vectors of $\hat{\mathbf{\Psi}}^{\mathbf{o}} = \mathbf{M}^{-1/2}\widetilde{\mathbf{\Psi}}^{\mathbf{o}}$. We note that

$f\left(\mathbf{D_{oc}},\mu\right) = \mathbf{I_{oc}}$, an $N_{\text{oc}} \times N_{\text{oc}}$ identity matrix and hence equation (5.39) can be recast in the following way:

$$\begin{aligned}
\rho^h_{\text{out}}(\mathbf{x}) =& 2\,\boldsymbol{n}^{\boldsymbol{e}^{\boldsymbol{T}}}(\mathbf{x})\hat{\boldsymbol{\Psi}}^{\mathbf{o}}_{\boldsymbol{e}} \left[\begin{array}{c|c} \mathbf{Q_{oc}} & \mathbf{Q_{fr}} \end{array}\right] \left[\mathbf{I} + \left(\begin{array}{c|c} \mathbf{0} & \mathbf{0} \\ \hline \mathbf{0} & f\left(\mathbf{D_{fr}},\mu\right) - \mathbf{I_{fr}} \end{array}\right)\right] \left[\begin{array}{c} \mathbf{Q}^{\dagger}_{\mathbf{oc}} \\ \hline \mathbf{Q}^{\dagger}_{\mathbf{fr}} \end{array}\right] \hat{\boldsymbol{\Psi}}^{\mathbf{o}^{\dagger}}_{\boldsymbol{e}}\, \boldsymbol{n}^{\boldsymbol{e}}(\mathbf{x}) \\
=& 2\,\boldsymbol{n}^{\boldsymbol{e}^{\boldsymbol{T}}}(\mathbf{x}) \left[\hat{\boldsymbol{\Psi}}^{\mathbf{o}}_{\boldsymbol{e}}\hat{\boldsymbol{\Psi}}^{\mathbf{o}^{\dagger}}_{\boldsymbol{e}} + \hat{\boldsymbol{\Psi}}^{\mathbf{o}}_{\boldsymbol{e}}\mathbf{Q_{fr}}\left(f\left(\mathbf{D_{fr}},\mu\right) - \mathbf{I_{fr}}\right)\mathbf{Q}^{\dagger}_{\mathbf{fr}}\hat{\boldsymbol{\Psi}}^{\mathbf{o}^{\dagger}}_{\boldsymbol{e}}\right] \boldsymbol{n}^{\boldsymbol{e}}(\mathbf{x}) \\
=& 2\,\boldsymbol{n}^{\boldsymbol{e}^{\boldsymbol{T}}}(\mathbf{x}) \left[\hat{\boldsymbol{\Psi}}^{\mathbf{o}}_{\boldsymbol{e}}\hat{\boldsymbol{\Psi}}^{\mathbf{o}^{\dagger}}_{\boldsymbol{e}} + \hat{\boldsymbol{\Psi}}^{\mathbf{R}}_{\mathbf{fr},\boldsymbol{e}}\left(f\left(\mathbf{D_{fr}},\mu\right) - \mathbf{I_{fr}}\right)\hat{\boldsymbol{\Psi}}^{\mathbf{R}^{\dagger}}_{\mathbf{fr},\boldsymbol{e}}\right] \boldsymbol{n}^{\boldsymbol{e}}(\mathbf{x}), \qquad (5.40)
\end{aligned}$$

where $\hat{\boldsymbol{\Psi}}^{\mathbf{R}}_{\mathbf{fr},\boldsymbol{e}}$ denotes the FE cell level vectors of $\hat{\boldsymbol{\Psi}}^{\mathbf{R}}_{\mathbf{fr}} = \mathbf{M}^{-1/2}\widetilde{\boldsymbol{\Psi}}^{\mathbf{o}}\mathbf{Q_{fr}}$.

Algorithm 4 Electron-density computation (DC)

```
Compute Fermi-energy ($\mu$) using the constraint:
    $$2\left(N_{\text{oc}} + \sum_{i=N_{\text{oc}}}^{N} f(\epsilon^h_i,\mu)\right) = N_e.$$
Scale $\widetilde{\boldsymbol{\Psi}}^{\mathbf{o}}$ and $\widetilde{\boldsymbol{\Psi}}^{\mathbf{R}}_{\mathbf{fr}}$: $\hat{\boldsymbol{\Psi}}^{\mathbf{o}} = \mathbf{M}^{-1/2}\widetilde{\boldsymbol{\Psi}}^{\mathbf{o}}$, $\hat{\boldsymbol{\Psi}}^{\mathbf{R}}_{\mathbf{fr}} = \mathbf{M}^{-1/2}\widetilde{\boldsymbol{\Psi}}^{\mathbf{R}}_{\mathbf{fr}}$.
Compute electron density using equation (5.40):
    $$\rho^h_{\text{out}}(\mathbf{x}) = 2\,\boldsymbol{n}^{\boldsymbol{e}^{\boldsymbol{T}}}(\mathbf{x})\left[\hat{\boldsymbol{\Psi}}^{\mathbf{o}}_{\boldsymbol{e}}\hat{\boldsymbol{\Psi}}^{\mathbf{o}^{\dagger}}_{\boldsymbol{e}} + \hat{\boldsymbol{\Psi}}^{\mathbf{R}}_{\mathbf{fr},\boldsymbol{e}}\left(f\left(\mathbf{D_{fr}},\mu\right) - \mathbf{I_{fr}}\right)\hat{\boldsymbol{\Psi}}^{\mathbf{R}^{\dagger}}_{\mathbf{fr},\boldsymbol{e}}\right]\boldsymbol{n}^{\boldsymbol{e}}(\mathbf{x}).$$
```

In the above, it is evident that the electron-density computation requires only the N_{fr} largest eigenstates of $\hat{\mathbf{H}}$. Accordingly, the spectrum-splitting based algorithms for the Rayleigh-Ritz procedure and electron-density computation in DFT-FE are given in Algorithm 3 and Algorithm 4, respectively. Even with finite-temperature Fermi-Dirac smearing, N_{fr} is usually a small fraction of N. From our numerical experiments, we find that N_{fr} is 10–15% of N for metallic systems, and much smaller percentage ($< 5\%$) for insulating and semi-conducting systems. This translates to significant cost savings in the subspace rotation step as shown in Fig. 5.4. This is because the usual full subspace rotation: $\widetilde{\boldsymbol{\Psi}}^{\mathbf{R}} = \widetilde{\boldsymbol{\Psi}}^{\mathbf{o}}\mathbf{Q}$, which scales as $\mathcal{O}(MN^2)$ is

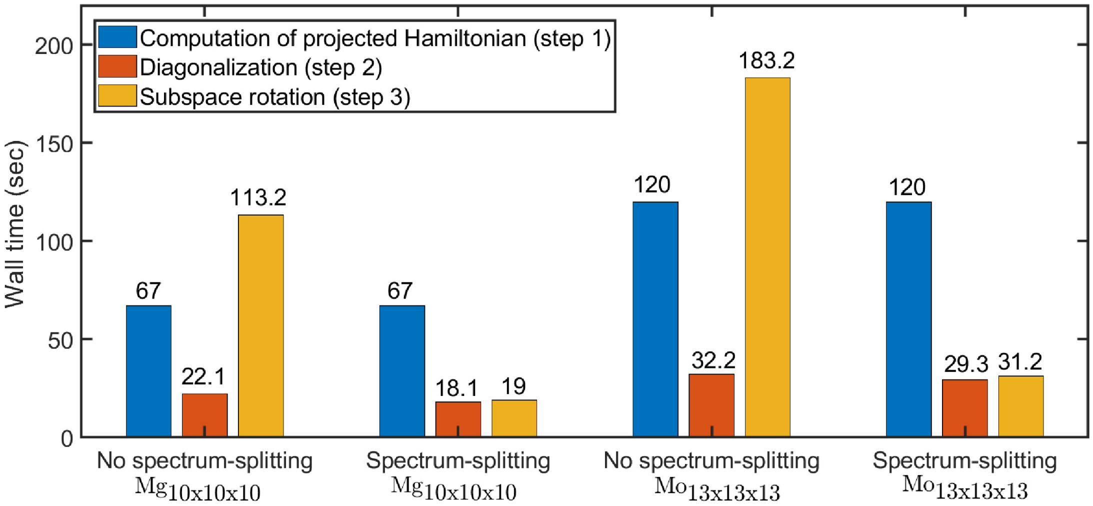

Figure 5.4: Comparison of Rayleigh-Ritz procedure wall times for a single SCF step by using spectrum-splitting (Algorithm 3). Case studies: (i) $\mathrm{Mg}_{10\mathrm{x}10\mathrm{x}10}$ with 39,990 electrons run on 51,200 MPI tasks and (ii) $\mathrm{Mo}_{13\mathrm{x}13\mathrm{x}13}$ with 61,502 electrons run on 64,000 MPI tasks. N_{fr} for both case studies is 15% of N

now replaced by a significantly cheaper partial subspace rotation step: $\widetilde{\boldsymbol{\Psi}}^{\mathbf{R}}_{\mathbf{fr}} = \widetilde{\boldsymbol{\Psi}}^{\mathbf{o}}\mathbf{Q}_{\mathbf{fr}}$ (step 3 of Algorithm 3), which scales as $\mathcal{O}(MNN_{\mathrm{fr}})$. Furthermore, step 2, which now amounts to a partial diagonalization of $\hat{\mathbf{H}}$ to compute the N_{fr} largest eigenstates, can be exploited to reduce diagonalization cost. In the literature, iterative approaches like LOBPCG [159], and inner Chebyshev filtering [186] are shown to be better than ScaLAPACK's direct eigensolver for partial diagonalization. However, iterative approaches may not be robust for metallic systems in the limit of vanishing band gaps. Hence in DFT-FE, we perform partial diagonalization using the ELPA library's [188–190] direct eigensolver, which is more scalable than ScaLAPACK's eigensolver and competes with the aforementioned iterative approaches with respect to minimum solution time. Fig. 5.4 shows the direct diagonalization times[6] (step 2) for very large system sizes with 39,990 electrons and 61,502 electrons.

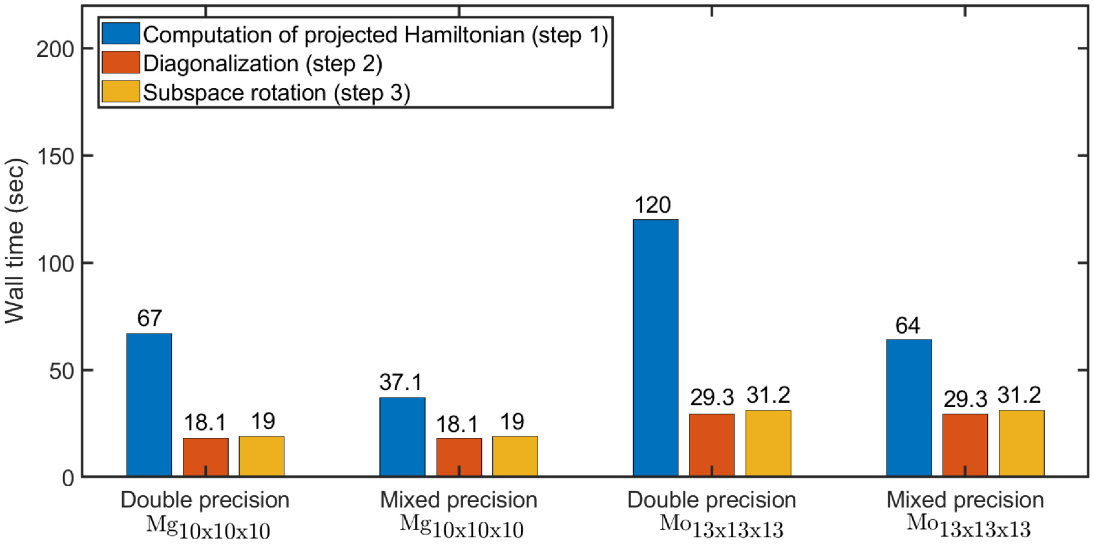

Figure 5.5: Comparison of Rayleigh-Ritz procedure (Algorithm 3) wall times for a single SCF step by using mixed precision arithmetic in the computation of projected Hamiltonian. Case studies: (i) $\mathrm{Mg}_{10x10x10}$ with 39,990 electrons run on 51,200 MPI tasks and (ii) $\mathrm{Mo}_{13x13x13}$ with 61,502 electrons run on 64,000 MPI tasks.

5.2.3.2 Mixed precision in RR

We observe that the computation of the projected Hamiltonian, $\hat{\mathbf{H}} = \widetilde{\boldsymbol{\Psi}}^{\mathbf{o}^\dagger}\widetilde{\mathbf{H}}\widetilde{\boldsymbol{\Psi}}^{\mathbf{o}}$ is the most dominant cost in the Rayleigh Ritz procedure using the spectrum-splitting technique (see Fig. 5.4). To this end, we develop a mixed precision algorithm to reduce the prefactor of the computation of $\hat{\mathbf{H}}$ and illustrate the procedure here. We first consider the following split of the orthonormalized wavefunctions $\widetilde{\boldsymbol{\Psi}}^{\mathbf{o}}$

$$\widetilde{\boldsymbol{\Psi}}^{\mathbf{o}} = \left[\widetilde{\boldsymbol{\Psi}}^{\mathbf{o}}_{\mathbf{oc}}\, \widetilde{\boldsymbol{\Psi}}^{\mathbf{o}}_{\mathbf{fr}}\right], \tag{5.41}$$

where the columns $\widetilde{\boldsymbol{\Psi}}^{\mathbf{o}}_{\mathbf{oc}}$ and $\widetilde{\boldsymbol{\Psi}}^{\mathbf{o}}_{\mathbf{fr}}$ contain the first N_{oc} and the remaining N_{fr} wavefunctions, respectively. We next rewrite the partial eigendecomposition of $\hat{\mathbf{H}} : \hat{\mathbf{H}}\mathbf{Q}_{\mathbf{fr}} =$

---

[6] The ELPA diagonalization times quoted here are run on NERSC Cori Intel KNL nodes which have 1.4 GHz clock frequency. On a higher clock frequency machine (eg: IBM Power and Intel Skylake architectures), these diagonalization timings are faster by a factor of 2–3 [190].

$\mathbf{Q_{fr}D_{fr}}$ (see step 2 of Algorithm 3) as

$$\left[\begin{array}{c|c} \hat{\mathbf{H}}_{\mathbf{oc-oc}} & \hat{\mathbf{H}}_{\mathbf{oc-fr}} \\ \hline \hat{\mathbf{H}}_{\mathbf{fr-oc}} & \hat{\mathbf{H}}_{\mathbf{fr-fr}} \end{array}\right] \left[\begin{array}{c} \mathbf{Q}^{\boldsymbol{a}}_{\mathbf{fr}} \\ \hline \mathbf{Q}^{\boldsymbol{b}}_{\mathbf{fr}} \end{array}\right] = \left[\begin{array}{c} \mathbf{Q}^{\boldsymbol{a}}_{\mathbf{fr}} \\ \hline \mathbf{Q}^{\boldsymbol{b}}_{\mathbf{fr}} \end{array}\right] \mathbf{D_{fr}}, \tag{5.42}$$

where $\hat{\mathbf{H}}_{\mathbf{oc-oc}} = \widetilde{\mathbf{\Psi}}^{\mathbf{o}\dagger}_{\mathbf{oc}}\widetilde{\mathbf{H}}\widetilde{\mathbf{\Psi}}^{\mathbf{o}}_{\mathbf{oc}}$, $\hat{\mathbf{H}}_{\mathbf{fr-fr}} = \widetilde{\mathbf{\Psi}}^{\mathbf{o}\dagger}_{\mathbf{fr}}\widetilde{\mathbf{H}}\widetilde{\mathbf{\Psi}}^{\mathbf{o}}_{\mathbf{fr}}$, $\hat{\mathbf{H}}_{\mathbf{fr-oc}} = \widetilde{\mathbf{\Psi}}^{\mathbf{o}\dagger}_{\mathbf{fr}}\widetilde{\mathbf{H}}\widetilde{\mathbf{\Psi}}^{\mathbf{o}}_{\mathbf{oc}}$, and $\hat{\mathbf{H}}_{\mathbf{oc-fr}} = \widetilde{\mathbf{\Psi}}^{\mathbf{o}\dagger}_{\mathbf{oc}}\widetilde{\mathbf{H}}\widetilde{\mathbf{\Psi}}^{\mathbf{o}}_{\mathbf{fr}}$. As the SCF approaches convergence, $\widetilde{\mathbf{\Psi}}^{\mathbf{o}}$ tends to the eigenfunctions of $\widetilde{\mathbf{H}}$, and hence the limiting behaviour of equation (5.42) can be written as

$$\left[\begin{array}{c|c} \hat{\mathbf{H}}_{\mathbf{oc-oc}} \rightarrow \mathbf{D_{oc}} & \hat{\mathbf{H}}_{\mathbf{oc-fr}} \rightarrow \mathbf{0} \\ \hline \hat{\mathbf{H}}_{\mathbf{fr-oc}} \rightarrow \mathbf{0} & \hat{\mathbf{H}}_{\mathbf{fr-fr}} \rightarrow \mathbf{D_{fr}} \end{array}\right] \left[\begin{array}{c} \mathbf{Q}^{\boldsymbol{a}}_{\mathbf{fr}} \rightarrow \mathbf{0} \\ \hline \mathbf{Q}^{\boldsymbol{b}}_{\mathbf{fr}} \rightarrow \mathbf{I_{fr}} \end{array}\right] = \left[\begin{array}{c} \mathbf{Q}^{\boldsymbol{a}}_{\mathbf{fr}} \rightarrow \mathbf{0} \\ \hline \mathbf{Q}^{\boldsymbol{b}}_{\mathbf{fr}} \rightarrow \mathbf{I_{fr}} \end{array}\right] \mathbf{D_{fr}}. \tag{5.43}$$

Using equation (5.43) the limiting behaviour of the partial eigendecomposition of $\hat{\mathbf{H}} : \hat{\mathbf{H}}\mathbf{Q_{fr}} = \mathbf{Q_{fr}D_{fr}}$ is written as

$$\hat{\mathbf{H}}_{\mathbf{fr-fr}}\mathbf{Q}^{\boldsymbol{b}}_{\mathbf{fr}} = \mathbf{Q}^{\boldsymbol{b}}_{\mathbf{fr}}\mathbf{D_{fr}}. \tag{5.44}$$

Equation (5.44) provides the rationale to design a mixed precision algorithm to compute $\hat{\mathbf{H}}$ by employing double precision BLAS `Xgemm` routine to compute the $\hat{\mathbf{H}}_{\mathbf{fr-fr}}$ sub-matrix, while all the other sub-matrices: $\hat{\mathbf{H}}_{\mathbf{oc-oc}}$, $\hat{\mathbf{H}}_{\mathbf{fr-oc}}$ and $\hat{\mathbf{H}}_{\mathbf{oc-fr}}$ are computed using single precision BLAS `Xgemm` routine. Since N_{fr} is typically less than 15% of N, the computation of $\hat{\mathbf{H}}_{\mathbf{fr-fr}}$ using double precision is a very small computational cost in this approach. This leads to overall computational savings by a factor of around 2 in computation of $\hat{\mathbf{H}}$ as shown in Fig. 5.5. Additionally, in Table 5.1, we examine the accuracy and robustness in employing mixed precision algorithms for both Rayleigh-Ritz and orthonormalization (see Section 5.2.2) steps on various benchmark systems in DFT-FE. These benchmark system are chosen such that the FE discretization errors are $\sim 10^{-4}$ Ha/atom in ground-state energy and $\sim 10^{-4}$

Ha/Bohr in ionic forces. The results in Table 5.1 show that number of SCFs do not change between mixed precision and double precision approaches, and further the mixed precision algorithms incur negligible errors in both energies and forces in comparison to the double precision calculations. Notably, these errors are about two orders of magnitude lower than the discretization errors.

In addition to using mixed precision in computation of $\hat{\mathbf{H}}$, we also use a blocked approach for memory and computational efficiency improvements. The computational efficiency improvement in using the blocked approach arises from exploiting the Hermiticity of $\hat{\mathbf{H}}$ as shown in Fig. 5.1. The implementation of the blocked approach used here is similar to the implementation of the blocked approach in the overlap matrix computation (see Section 5.2.2). Finally, we remark that the use of spectrum splitting technique in conjunction with the mixed precision algorithm in the Rayleigh-Ritz procedure provides efficiency gains by a factor of around 3 for the large benchmark systems considered in Fig. 5.4 and 5.5.

Table 5.1: Accuracy and robustness study of mixed precision computations in CholGS orthonormalization and Rayleigh-Ritz procedure on benchmark systems. Energy difference, maximum atomic force difference magnitude ($\max\limits_{1\leq i\leq N_a} \left\|\mathbf{f}^i_{\text{dp}} - \mathbf{f}^i_{\text{sp}}\right\|$) and total number of SCFs are reported with respect to double precision calculations. $\mathbf{f}^i_{\text{dp}}$ and $\mathbf{f}^i_{\text{sp}}$ denote atomic force on i^{th} atom for double precision and single precision calculations respectively. Discretization errors for the benchmark systems are $\sim 10^{-4}$ Ha/atom in ground-state energy and $\sim 10^{-4}$ Ha/Bohr in ionic forces. More details about the benchmark systems are given in Section 5.3.3.

System	Energy difference (Ha/atom)	Maximum force difference magnitude (Ha/Bohr)	Total SCFs (Double, Mixed)
Mg_{6x6x6}	7×10^{-12}	2×10^{-6}	(49, 49)
$\text{Cu}_{\text{4-shell}}$	5×10^{-12}	3×10^{-6}	(46, 46)
Mo_{6x6x6}	3×10^{-12}	7×10^{-7}	(49, 49)

5.2.4 Parallelization

The primary level of parallelization in the DFT–FE code is based on domain decomposition of the adaptive FE mesh into partitions and distributing them to different MPI tasks. This is accomplished through the deal.II finite element library with p4est [191]. We note that the FE basis is localized with a compact support on the cells shared by a FE node. Hence only the FE nodes on the processor boundaries need to be communicated, which has a significantly smaller communication cost in comparison to the all-to-all communication required in global basis sets like planewaves. This allows for excellent parallel scalability of DFT–FE, which we demonstrate subsequently in Section 5.3.2.

To further improve scalability, we implement a second level of parallelization over wavefunctions (band parallelization) in each of the key computational steps of the SCF iteration: Chebyshev filtering, CholGS (steps 1 and 4 of Algorithm 2), Rayleigh–Ritz procedure (steps 1 and 3 of Algorithm 3), and electron density computation. In particular, computations over the total number of wavefunctions ($\widetilde{\boldsymbol{\Psi}}$) are divided into groups of wavefunctions (band groups) and distributed among a group of MPI sub–communicators, with each sub–communicator doing computations on a single band group of size N_{b_i}, denoted by $\widetilde{\boldsymbol{\Psi}}_{\boldsymbol{b_i}}$, where i denotes the band group index. The use of band parallelization in Chebyshev filtering and electron density computation does not involve any inter band group communication of $\widetilde{\boldsymbol{\Psi}}_{\boldsymbol{b_i}}$'s. However, the computation of the electron density requires accumulation of the electron density contribution from each band group incurring a very small communication cost. Further, we exploit band parallelization in the computation of overlap matrix and orthonormal basis construction in CholGS as $\mathbf{S}_{\boldsymbol{b_i}} = \widetilde{\boldsymbol{\Psi}}^{\dagger}\widetilde{\boldsymbol{\Psi}}_{\boldsymbol{b_i}}$ and $\widetilde{\boldsymbol{\Psi}}^{\mathbf{o}}_{\boldsymbol{b_i}} = \widetilde{\boldsymbol{\Psi}}\mathbf{L}_{\mathbf{b_i}}^{\mathbf{-1}^{\dagger}}$, respectively. We note that $\mathbf{L}_{\mathbf{b_i}}^{\mathbf{-1}^{\dagger}}$ denotes $N \times N_{b_i}$ sub-matrix of $\mathbf{L}^{\mathbf{-1}^{\dagger}}$. Similarly, band parallelized computation of projected Hamiltonian in Rayleigh–Ritz procedure is performed as $\hat{\mathbf{H}}_{\boldsymbol{b_i}} = \widetilde{\boldsymbol{\Psi}}^{\mathbf{o}^{\dagger}}\widetilde{\mathbf{H}}\widetilde{\boldsymbol{\Psi}}^{\mathbf{o}}_{\boldsymbol{b_i}}$. We note that all-to-all communications of $\widetilde{\boldsymbol{\Psi}}_{\boldsymbol{b_i}}$'s and $\widetilde{\boldsymbol{\Psi}}^{\mathbf{o}}_{\boldsymbol{b_i}}$'s across band groups are performed before beginning the orthonormalization and Rayleigh-Ritz procedure, respectively. Furthermore, all-to-all communications of $\mathbf{S}_{\boldsymbol{b_i}}$'s and $\hat{\mathbf{H}}_{\boldsymbol{b_i}}$'s across band groups are also performed to compute the matrices $\mathbf{S}$ and $\hat{\mathbf{H}}$ ($N \times N$ dimensions). The above all-to-all communications involve large memory sizes, and hence the communication cost can increase significantly with increase in band parallelization groups, thus affecting parallel scaling efficiency. However, a modest amount of band parallelization can be combined with domain decomposition parallelization to extend the parallel scalability in DFT-FE, as discussed below. Additionally, we have also implemented parallelization over k points for problems involving multiple k-point sampling over the Brillouin zone in periodic calculations.

We now compare the scalability of three different parallelization approaches in DFT-FE: (i) only domain decomposition parallelization (P1), (ii) primarily band parallelization with just enough domain decomposition parallelization to fit the memory (P2), and (iii) domain decomposition parallelization till parallel scaling efficiency of $\sim 70\%$ followed by moderate band parallelization (P3). We conduct comparative studies on a large benchmark system containing 3999 atoms (39,990 electrons) using the above three approaches, and the results are shown in Fig. 5.6. We observe that only domain decomposition parallelization (P1) provides better parallel scalability than the primarily band parallelization approach (P2)—73% efficiency vs. 52% efficiency at 51,200 MPI. This is attributed to the significant increase in MPI collective communication cost of wavefunctions as the number of band parallelization groups increase. However, the use of band parallelization is beneficial for medium–large system sizes when appreciable scaling from domain decomposition parallelization has already been extracted, as is evident from Fig. 5.6, where the best parallel scaling efficiency is obtained for the combined parallelization approach (P3). In particular, we use domain decomposition parallelization till 51,200 MPI tasks (73% efficiency), and band parallelization using two band parallelization groups to achieve 49% efficiency at 102,400 MPI tasks. We remark that only 41% efficiency is achieved for the same 102,400 tasks by solely using domain decomposition parallelization approach (P1). Based on the above comparison, in the remainder of this work, we primarily use the combined parallelization approach (P3) to scale DFT-FE calculations, particularly for large system sizes.

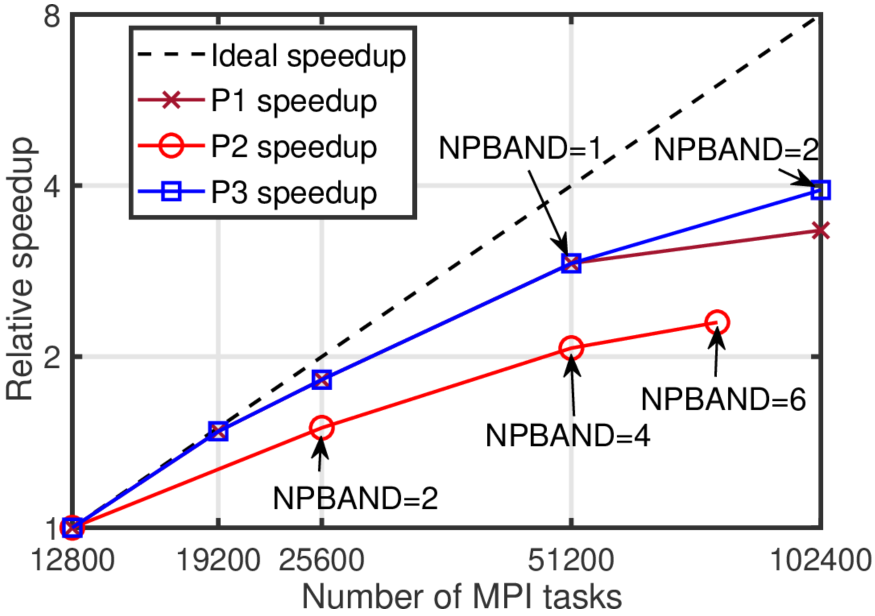

Figure 5.6: Comparison of parallel scalability of $Mg_{10x10x10}$ (39,990 electrons) using three different parallelization approaches: (P1) only domain decomposition parallelization, (P2) primarily band parallelization with minimal domain decomposition parallelization, and (P3) domain decomposition parallelization till parallel scaling efficiency of $\sim 70\%$ followed by moderate band parallelization. The number of band parallelization groups used in approaches P2 and P3 are denoted by NPBAND. This benchmark study comprised of ~ 94 million 4^{th} order FE basis functions.

5.3 Validation and performance benchmarking

In this section, we demonstrate the accuracy, parallel scaling performance and computational efficiency of the developed DFT-FE code on various benchmark systems involving pseudopotential DFT calculations. GGA [93] exchange correlation of the PBE form [174] is employed in all the calculations, and additionally ONCV [177] pseudopotentials from the SG15 database [192] are employed in all the calculations.

Further, we use Fermi-Dirac smearing with temperature $T = 500\ K$, and the n-stage Anderson mixing scheme [101] for mixing the electron-density in the SCF iteration procedure.

We first validate the accuracy of DFT-FE with widely used DFT basis sets on benchmark materials systems involving periodic and non-periodic pseudopotential DFT calculations. Second, we demonstrate the parallel scalability of DFT-FE on pseudopotential benchmark systems with sizes ranging from $2,550$ electrons to $39,990$ electrons. Third, we assess the computational efficiency of the DFT-FE code by comparing to popular plane-wave based codes—QUANTUM ESPRESSO (QE) [137, 193], and ABINIT [104]—on periodic and non-periodic pseudopotential benchmark systems with sizes ranging from $2,550$ to $20,470$ electrons. Finally, we also conduct large-scale DFT calculations on sizes ranging from $27,986$ to $61,502$ electrons using DFT-FE that are computationally prohibitive using plane-wave codes. The discretization parameters in the above computational efficiency studies are chosen to be commensurate with chemical accuracy (discretization errors of $\sim 10^{-4}$ Ha and $\sim 10^{-4}$ Ha/Bohr in energy per atom and ionic forces respectively), based on the validation studies on the same benchmark systems at smaller sizes.

All the numerical simulations with computational times reported in this work were executed on the Cori supercomputer at the National Energy Research Scientific Computing (NERSC) center. In particular, we used Cori's Phase II partition containing 9,688 compute nodes based on Intel Xeon Phi processors. Each compute node has the following specifications: single-socket Intel Xeon Phi 7250 ("Knights Landing") processor with 68 physical cores per node @ 1.4 GHz and 96 GB of memory per node. Cori uses a Cray Aries with Dragonfly topology for inter-node communication with 45.0 TB/s global peak bidirectional bandwidth.

The DFT-FE simulations reported in this section were run using 32 MPI tasks per node and 2 OpenMP threads (for `BLAS` operations), except for a few small system sizes (less than $3,000$ electrons) where using 64 MPI tasks per node and a single OpenMP thread was found to be more efficient. Similarly, QE and ABINIT simulations were run using optimal MPI tasks-OpenMP threads combinations based on the problem size— 32 MPI tasks per node and 2 OpenMP threads for smaller problem sizes (less than $3,000$ electrons), and 16/8 MPI tasks per node and 4 OpenMP threads for larger problem sizes where more memory per MPI task is required. Furthermore, MPI task to core binding was also appropriately set for all the above combinations. Our numerical experiments showed that using more than 4 OpenMP threads provided negligible performance gains in DFT-FE as well as in QE and ABINIT.

5.3.1 Validation

We consider three different benchmark systems: (i) hexagonal close packed (hcp) Mg periodic supercells with a mono-vacancy, (ii) body centered cubic (bcc) Mo periodic supercells with a mono-vacancy, and (iii) non-periodic Icosahedron Cu nanoparticles. In each of the benchmark systems, we take increasingly refined basis sets in DFT-FE and QE and compare the ground-state energy per atom, ionic forces, and cell stresses at two different accuracy levels: a) medium accuracy—discretization errors of $\sim 10^{-4}$ Ha/atom in ground-state energy, $\sim 10^{-4}$ Ha/Bohr in ionic forces, and $\sim 5 \times 10^{-6}$ Ha/Bohr^3 in cell stress (in periodic benchmark systems), which we consider as chemical accuracy; b) high accuracy—using a more refined basis set in both DFT-FE and QE to demonstrate much closer agreement between them. Further, we note that the validation studies for the aforementioned periodic benchmark systems are conducted using a Gamma point.

In the benchmark system involving Mg, we consider periodic supercells constructed from orthogonal unit cells (containing 4 atoms) of hcp Mg with lattice constants: $a = 5.882$ Bohr and $c = 9.586$ Bohr. We consider a mono-vacancy in two supercells: $2 \times 2 \times 2$ denoted by $\mathrm{Mg}_{2\mathrm{x}2\mathrm{x}2}$ containing 31 atoms (310 electrons) and

Table 5.2: Validation of DFT-FE with QE on pseudopotential benchmark systems at two different accuracy levels— medium accuracy and high accuracy. $\mathrm{FE_o}, h_1$ and h_2 denote the FE polynomial order, minimum element size and maximum element size (Bohr), respectively, in DFT-FE. E_{cut} denotes the plane-wave basis cut-off used in QE (Hartree). E_{g} denotes ground-state energy (Hartree/atom). $\Delta_{\max} f = \max_{1 \leq i \leq N_a} \left\| \mathbf{f}_i^{\mathrm{DFT-FE}} - \mathbf{f}_i^{\mathrm{QE}} \right\|$ (Hartree/Bohr), where $\mathbf{f}_i$ denotes the force on the i^{th} atom. $\Delta\sigma_h = \left| {\sigma_h}^{\mathrm{DFT-FE}} - {\sigma_h}^{\mathrm{QE}} \right|$ (Hartree/Bohr^3), where σ_h denotes the hydrostatic cell stress.

(a) Medium accuracy

System	DFT-FE ($\mathrm{FE_o}, h_1$, h_2)	DFT-FE E_g	QE E_{cut}	QE E_g	Differ. in forces & stress ($\Delta_{\max} f$, $\Delta\sigma_h$)
$\mathrm{Mg}_{\mathrm{2x2x2}}$	4, 0.46, 1.92	−54.3195364	45	−54.3195594	$\Delta_{\max} f = 2.1 \times 10^{-4}$ $\Delta\sigma_h = 3.7 \times 10^{-6}$
$\mathrm{Mg}_{\mathrm{4x4x4}}$	4, 0.46, 1.92	−54.3279442	45	−54.3279638	$\Delta_{\max} f = 3.3 \times 10^{-4}$ $\Delta\sigma_h = 4.6 \times 10^{-6}$
$\mathrm{Mo}_{\mathrm{2x2x2}}$	5, 0.74, 1.49	−68.5573334	20	−68.5573613	$\Delta_{\max} f = 1 \times 10^{-5}$ $\Delta\sigma_h = 1.6 \times 10^{-6}$
$\mathrm{Mo}_{\mathrm{4x4x4}}$	5, 0.74, 1.49	−68.5811483	20	−68.5811857	$\Delta_{\max} f = 2.1 \times 10^{-5}$ $\Delta\sigma_h = 1.9 \times 10^{-6}$
$\mathrm{Cu}_{\text{3-Shell}}$	4, 0.39, 12.5	−182.5870759	50	−182.5870221	$\Delta_{\max} f = 7.2 \times 10^{-5}$
$\mathrm{Cu}_{\text{4-Shell}}$	4, 0.39, 12.2	−182.5908621	50	−182.5908346	$\Delta_{\max} f = 1.4 \times 10^{-4}$

(b) High accuracy

System	DFT-FE ($\mathrm{FE_o}, h_1$, h_2)	DFT-FE E_g	QE E_{cut}	QE E_g	Differ. in forces & stress ($\Delta_{\max} f$, $\Delta\sigma_h$)
$\mathrm{Mg}_{\mathrm{2x2x2}}$	5, 0.24, 0.96	−54.3196337	55	−54.3196270	$\Delta_{\max} f = 4.6 \times 10^{-6}$ $\Delta\sigma_h = 2.7 \times 10^{-7}$
$\mathrm{Mg}_{\mathrm{4x4x4}}$	5, 0.24, 0.96	−54.3280448	55	−54.3280318	$\Delta_{\max} f = 7.9 \times 10^{-6}$ $\Delta\sigma_h = 2.6 \times 10^{-7}$
$\mathrm{Mo}_{\mathrm{2x2x2}}$	5, 0.37, 0.74	−68.5574282	50	−68.5574315	$\Delta_{\max} f = 4.5 \times 10^{-6}$ $\Delta\sigma_h = 1.1 \times 10^{-6}$
$\mathrm{Mo}_{\mathrm{4x4x4}}$	5, 0.37, 0.74	−68.5812495	50	−68.5812527	$\Delta_{\max} f = 6 \times 10^{-6}$ $\Delta\sigma_h = 9.8 \times 10^{-7}$
$\mathrm{Cu}_{\text{3-Shell}}$	5, 0.18, 12.5	−182.5872871	70	−182.5872868	$\Delta_{\max} f = 2.5 \times 10^{-5}$
$\mathrm{Cu}_{\text{4-Shell}}$	5, 0.18, 12.2	−182.5910308	70	−182.5910298	$\Delta_{\max} f = 3.5 \times 10^{-5}$

$4 \times 4 \times 4$ denoted by Mg_{4x4x4} containing 255 atoms (2,550 electrons). The relevant mesh parameters for DFT-FE and cut-off energies for QE are shown in Table 5.2. Table 5.2 also provides the comparison between DFT-FE and QE at medium and high accuracy levels. At the medium accuracy level, the agreement in ground-state energy is $\mathcal{O}(10^{-5})$ Ha/atom, ionic forces is $\mathcal{O}(10^{-4})$ Ha/Bohr, and hydrostatic stress is $\mathcal{O}(10^{-6})$ Hartree/Bohr^3. Similarly, at high accuracy level the agreement in ground-state energy is $\mathcal{O}(10^{-5})$ Ha/atom, ionic forces is $\mathcal{O}(10^{-5})$ Ha/Bohr, and hydrostatic stress is $\mathcal{O}(10^{-7})$ Hartree/Bohr^3. We additionally remark that Mg has a hard ONCV pseudopotential, which is reflected in basis set parameters.

Next, in the benchmark system involving Mo, we consider periodic supercells constructed from bcc Mo unit cells with lattice constant of 5.95 Bohr. We consider a mono-vacancy in two supercell sizes—$2\times2\times2$ denoted by Mo_{2x2x2} containing 15 atoms (210 electrons) and $4\times4\times4$ denoted by Mo_{4x4x4} containing 127 atoms (1,778 electrons). Table 5.2 shows the comparison between DFT-FE and QE, which demonstrates a similar excellent agreement as in the case of the Mg benchmark system. We note that the lower plane-wave cut-off or larger h_{min} in DFT-FE in comparison to the Mg benchmark system is attributed to Mo having a softer ONCV pseudopotential than Mg.

Finally, in benchmark system involving Cu, we consider three-dimensional non-periodic Icosahedron Cu nano-particles [194]. The Icosahedron nano-particles are constructed with nearest neighbour bond length of 6.8 Bohr and varying the number of shells. We consider two Cu nano-particle sizes: $\text{Cu}_{\text{3-Shell}}$ containing 147 atoms (2,793 electrons), $\text{Cu}_{\text{4-shell}}$ containing 309 atoms (5,871 electrons). For the DFT-FE simulations, we choose a non-periodic domain containing the Cu nano-particle and impose homogeneous Dirichlet boundary conditions on the boundary of the domain. On the other hand, for the QE simulations, we choose an artificial periodic domain containing the Cu nano-particle. The energy and forces are converged with respect to the domain size in both DFT-FE and QE simulations. Table 5.2 shows the comparison between DFT-FE and QE, which demonstrates excellent agreement between the two codes in a non-periodic setting.

Overall, from Table 5.2, we show excellent agreement between DFT-FE and QE for both medium and high accuracy calculations, with the difference between the codes systematically reducing with increasing discretization.

5.3.2 Parallel scaling performance

Here we demonstrate the parallel scalability of DFT-FE on various system sizes. We consider hexagonal close packed (hcp) Mg periodic super cells with a monovacancy, and study the strong scaling behavior using pseudopotential DFT calculations on three system sizes: (a) small—Mg_{4x4x4} (255 atoms, 2,550 electrons), (b) medium—Mg_{8x8x8} (2,047 atoms, 20,470 electrons), and (c) large—$\mathrm{Mg}_{10x10x10}$ (3,999 atoms, 39,990 electrons). In particular, we study the strong scaling behavior by measuring the relative speedup with increasing number of MPI tasks while keeping the discretization fixed for all the three systems. The speedup is measured relative to the wall time taken on 128 MPI tasks, 512 MPI tasks, 3,200 MPI tasks, 12,800 MPI tasks for C_{60} , Mg_{4x4x4}, Mg_{8x8x8} and $\mathrm{Mg}_{10x10x10}$ respectively. We note that further lower number of MPI tasks were not possible due to memory constraints. This is primarily because of low memory per core ($\sim$1.4 GB) of the many-core KNL architecture in the Cori supercomputer. Further, the FE mesh in the above studies is chosen such that the discretization errors in energy and forces are $\sim 10^{-4}$ Ha per atom and $\sim 10^{-4}$ Ha/Bohr, respectively.

We first consider Mg_{4x4x4}, the smallest of the three Mg hcp periodic supercell benchmarks considered in this study. As demonstrated in Fig. 5.7, we use domain decomposition parallelization to scale up to 4,096 MPI tasks at 75% efficiency, with an average of 1,629 dofs per MPI task. The corresponding wall time for a single SCF iteration step is 28 seconds. Such excellent parallel scalability is possible due to the aforementioned low communication cost in the FE discretized Hamiltonian matrix and wavefunction vector products involved in Chebyshev filtering. Next, we consider the parallel scalability of the medium to large system sizes: $\mathrm{Mg}_{8\mathrm{x}8\mathrm{x}8}$ and $\mathrm{Mg}_{10\mathrm{x}10\mathrm{x}10}$, which are shown in Fig. 5.8. Based on the comparison of three different parallelization strategies in Section 5.2.4 for achieving maximum parallel scalability for large system sizes, we use the parallelization strategy of combined domain decomposition and band parallelization. In particular, in the case of $\mathrm{Mg}_{8\mathrm{x}8\mathrm{x}8}$, we use domain decomposition parallelization from 3,200 to 32,000 MPI tasks and then use band parallelization with two band parallelization groups to further scale to 64,000 MPI tasks at 43% efficiency. At 64,000 MPI tasks, we use an average of 1,436 dofs per MPI task, and obtain a wall time of 91 seconds for a single SCF iteration step. Similarly, in the case of $\mathrm{Mg}_{10\mathrm{x}10\mathrm{x}10}$, we use domain decomposition parallelization till 51,200 MPI tasks, and then use band parallelization to further scale to 102,400 MPI tasks at 49% efficiency. At 102,400 MPI tasks, we use an average of 1,835 dofs per MPI task, and obtain a wall time of 237 seconds for a single SCF iteration step. The parallel scaling of the above medium to large system sizes is dependent on the scalability of the major computational steps: CF, CholGS and RR (section 5.2). We remark that in spite of the computational complexity of CF scaling quadratically in comparison to cubic scaling of CholGS and RR, CF's excellent parallel scalability afforded by FE discretization continues to be crucial for parallel scalability at medium to large system sizes. This is evident from Fig. 5.9 showing the strong scaling of the various computational steps in DFT-FE for $\mathrm{Mg}_{8\mathrm{x}8\mathrm{x}8}$ and $\mathrm{Mg}_{10\mathrm{x}10\mathrm{x}10}$, where we note that CF is still a significant portion of the total wall-times, and further CF also demonstrates excellent parallel scalability. Fig. 5.9 also demonstrates good parallel scaling of CholGS and RR steps, where the use of mixed precision arithmetic based algorithms play a key role in reducing communication costs. Overall, DFT-FE's massive parallel scalability, as demonstrated here, is a result of the locality of the FE basis as well as an effective parallel implementation of the various algorithms in DFT-FE, as discussed in section 5.2, that reduce communication costs and latency.

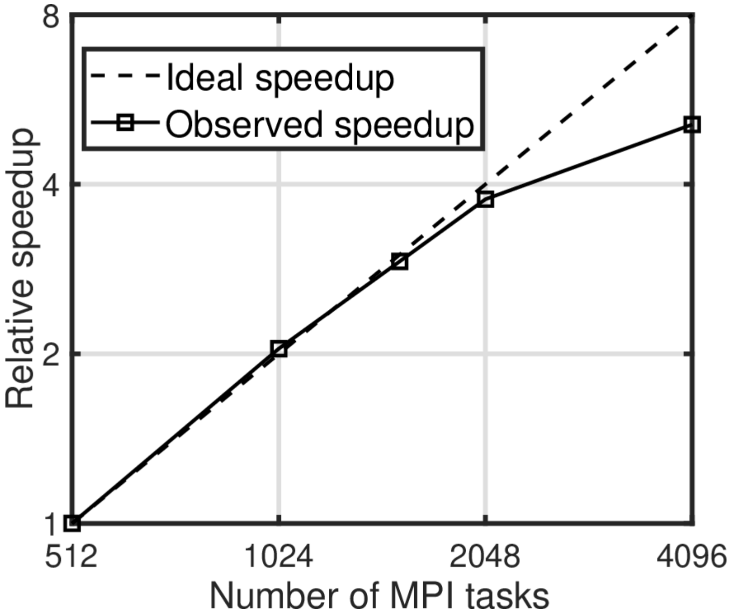

Figure 5.7: Strong parallel scaling using DFT-FE on a small system. Case study: $\mathrm{Mg}_{4\mathrm{x}4\mathrm{x}4}$ (255 atoms, 2,550 electrons).

5.3.3 Computational efficiency and wall time comparison with plane-wave codes

We now consider three different benchmark systems with sizes ranging from $2,550$ to $61,502$ electrons to compare the computational efficiency (CPU-time and minimum wall-time) of the DFT-FE code against the plane-wave codes—QUANTUM ESPRESSO (QE) v6.3 [137, 193], and ABINIT v8.8.4 [104]. In particular, we consider: (i) hexagonal close packed (hcp) Mg periodic super cells with a mono-vacancy, (ii) body centered cubic (bcc) Mo periodic super cells with a mono-vacancy, and (iii) non-periodic Icosahedron Cu nano-particles. The details on these benchmark systems are discussed previously in Section 5.3.1, with a wider range of system sizes considered here. We note that the FE mesh parameters and plane-wave cut-off energies in all

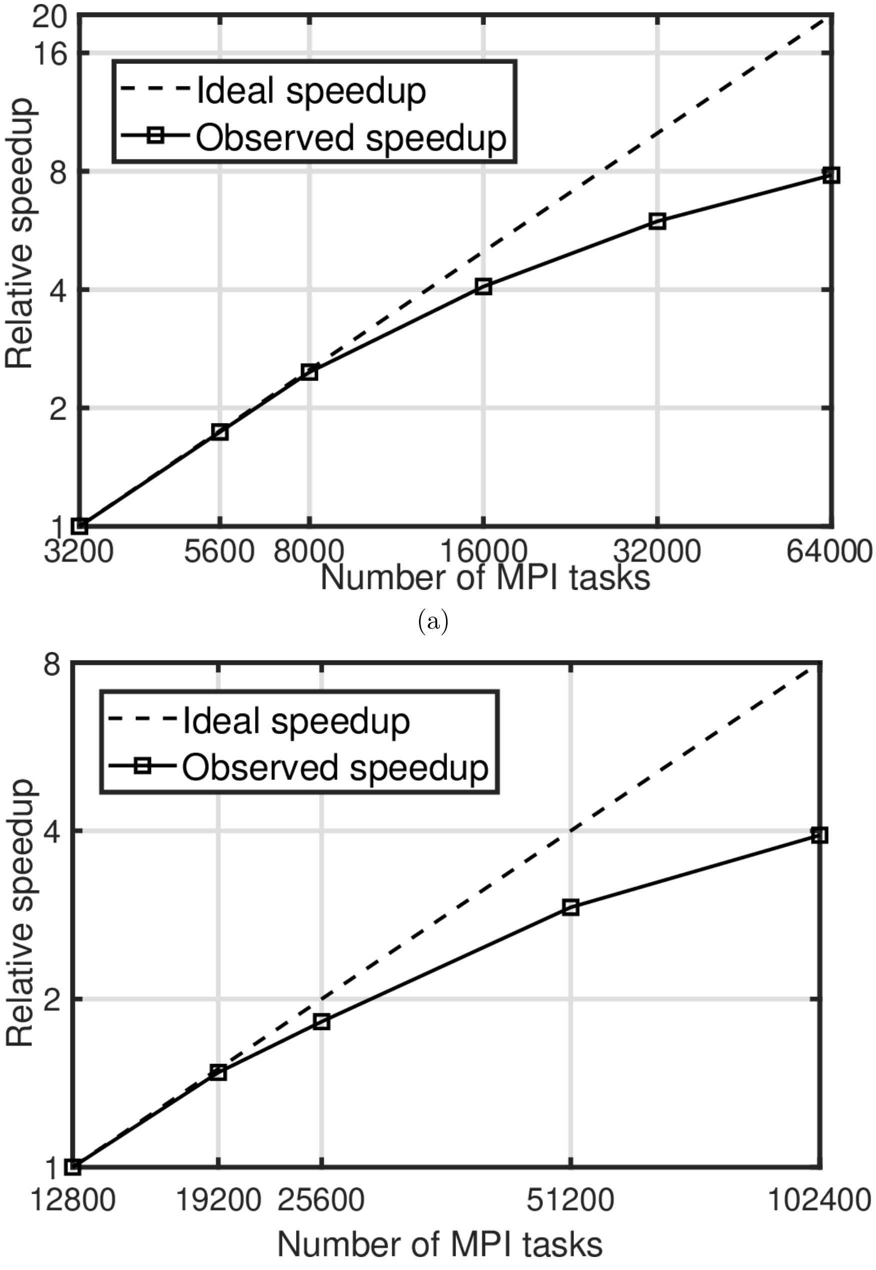

(a)

(b)

Figure 5.8: Strong parallel scaling using DFT-FE on larger system sizes. Case studies: a) Mg_{8x8x8} (2,047 atoms, 20,470 electrons), and b) $Mg_{10x10x10}$ (3,999 atoms, 39,990 electrons).

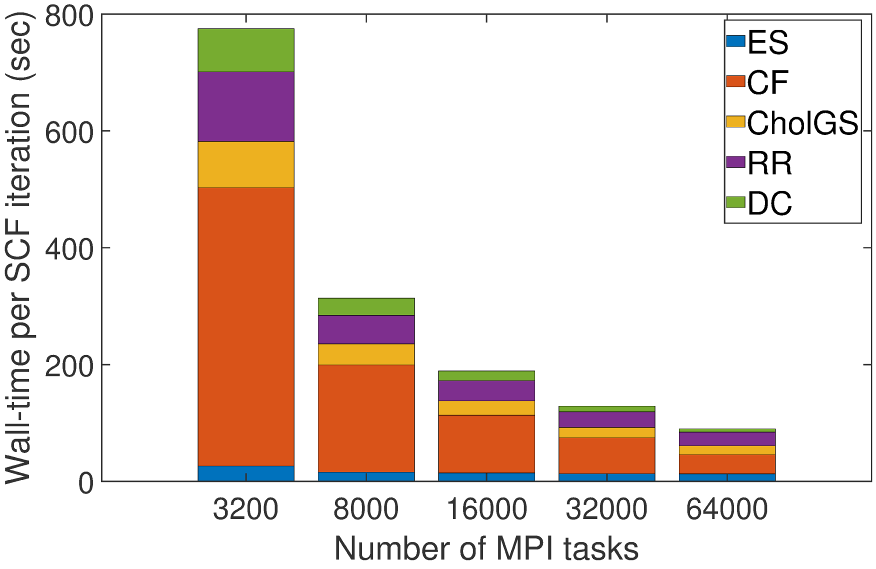

(a)

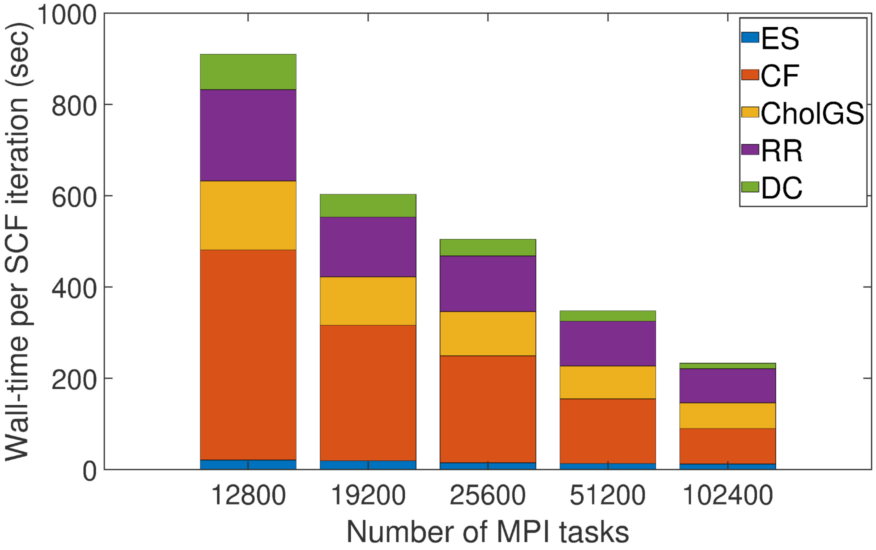

(b)

Figure 5.9: Breakdown of total wall-time per SCF iteration into the various computational steps in DFT-FE: a) ES (Total electrostatic potential solve), b) CF (Chebyshev filtering), c) CholGS (Cholesky-Gram-Schimdt Orthogonalization), d) RR (Rayleigh-Ritz procedure), and e) DC (Electron-density computation). Case studies: a) $\mathrm{Mg}_{8\mathrm{x}8\mathrm{x}8}$, and b) $\mathrm{Mg}_{10\mathrm{x}10\mathrm{x}10}$. The number of MPI tasks correspond to the strong scaling studies in Fig. 5.8.

the benchmark calculations are chosen to be commensurate with chemical accuracy, based on the validation studies on smaller system sizes for the same benchmark system types. We do not explicitly measure the discretization errors here as highly refined calculations required to do so will use significant computational resources given the many benchmark systems along with large sizes (up to $61,502$ electrons) considered here. Further, we note that all QE and ABINIT timings reported below are for an optimal combination of FFT grid parallelization and band parallelization.

The DFT-FE simulations for the above benchmark systems use the following values of Chebyshev polynomial degree m (see Section 5.2.1): $m = 45$ for benchmark systems (i) and (ii), and $m = 50$ for benchmark system (iii). Further, N_{fr}, which is used in the RR step (see Section 5.2.3), is chosen to be 15 % of N. Additionally, in all simulations (DFT-FE, QE and ABINIT) N is chosen as $N_e/2 + b$, with $b \sim 10\%$ of $N_e/2$ for benchmark systems (i) and (ii), and $b \sim 5\%$ of $N_e/2$ for benchmark system (iii).

CPU-time comparisons In Tables 5.3, 5.4, and 5.5 we compare the average computational CPU-times per SCF iteration step[7] in the above benchmark systems between DFT-FE and the plane-wave codes QE and ABINIT. The CPU-times are reported in Node-Hrs, which is obtained by multiplying the total number of compute nodes used with the average wall-time per SCF iteration measured in hours. We also compare the number of basis functions used to achieve the desired chemical accuracy in energy and forces. We note that all the simulations for Tables 5.3, 5.4, and 5.5 are run using the minimum number of compute nodes required to fit the peak memory of the simulation, and additionally remark that the dashes in the table corresponding to QE

---

[7] Measured by taking the average of a few SCF iteration steps after the first $2-3$ SCF iteration steps, which are excluded as their timings can be variable depending on the starting wavefunctions guess to the SCF procedure. Furthermore, for few system sizes ($< 10,000$ electrons) in each benchmark system, we verify that the choice of the DFT-FE parameters are adequate to achieve convergence in similar number of SCF iteration steps as taken by QE and ABINIT. We do not use advanced mixing strategies like Kerker preconditioning in QE and ABINIT simulations as such strategies are currently not implemented in DFT-FE.

and ABINIT benchmark simulations that are not performed as they are computationally prohibitive. First, we consider the periodic benchmark problems in Tables 5.3 and 5.4, where we observe that DFT-FE is more computationally efficient than both QE and ABINIT beyond system sizes of ~ 3000 electrons (300 atoms) for hcp Mg supercells, and $\sim 6,000$ electrons (428 atoms) for bcc Mo supercells. There are a couple of reasons for DFT-FE's efficiency gains over QE in spite of the number of basis functions advantage of plane-wave basis for periodic problems. Firstly, simulations for medium to large system sizes require more compute nodes to fit the peak memory on many-core architectures like the Cori KNL nodes. This increases the CPU-time of plane-wave codes, relative to DFT-FE, due to the better parallel scaling of DFT-FE. Secondly, the efficient and scalable numerical implementation CF, CholGS and RR in DFT-FE (see Section 5.2) is also a key factor. Next, we consider the non-periodic benchmark problem: Icosahedron nano-particles of varying sizes, in Table 5.5. Here we observe that that DFT-FE is more computationally efficient than QE beyond a very small system size of 147 atoms ($2,793$ electrons). We note that the spatial adaptivity of DFT-FE provides a key advantage in non-periodic systems where the FE mesh can be coarse-grained into the vacuum as opposed to a uniform spatial resolution of the plane-wave basis. Furthermore, the spatial adaptivity of the FE basis is also an advantage in systems having hard pseudopotentials such as Cu. Overall, from Tables 5.3, 5.4, and 5.5, we observe that DFT-FE's efficiency gains over QE increases with increasing system size, achieving efficiency gains of 5.7×, 12.4×, and 11.9× for $\mathrm{Mg}_{\mathrm{8x8x8}}$, $\mathrm{Mo}_{\mathrm{10x10x10}}$, and $\mathrm{Cu}_{\text{5-shell}}$, respectively, which are the largest benchmark systems considered for CPU-time comparison. We note that ABINIT is slower than QE for all benchmark systems considered here. Finally, another key observation is that due to the efficient numerical implementation of cubic-scaling CholGS and RR steps in DFT-FE, the range of close to quadratic scaling in computational complexity with respect to number of electrons (N_e) is extended to much larger system sizes—$\mathcal{O}(N_e^{2.12})$

up to $N_e = 39,990$ for hcp Mg super cells, $\mathcal{O}(N_e^{2.32})$ up to $N_e = 27,986$ for bcc Mo super cells, and $\mathcal{O}(N_e^{2.04})$ up to $N_e = 17,537$ for Cu nano-particles.

Table 5.3: CPU-time comparison of DFT-FE with QE and ABINIT: Average time per SCF iteration step in Node-Hrs. Benchmark system (i): hcp Mg periodic supercells with a mono-vacancy.

System	No. of atoms (No. of electrons)	FE basis	DFT-FE	Plane-wave basis	QE	ABINIT
$\text{Mg}_{4\text{x}4\text{x}4}$	255 (2,550)	6,673,513	0.3	530,051	0.1	0.3
$\text{Mg}_{6\text{x}6\text{x}6}$	863 (8,630)	19,852,441	3.3	1,788,771	4.4	20.2
$\text{Mg}_{8\text{x}8\text{x}8}$	2,047 (20,470)	45,954,505	21.6	4,240,071	123.5	-
$\text{Mg}_{10\text{x}10\text{x}10}$	3,999 (39,990)	93,972,153	103.4	-	-	-

Table 5.4: CPU-time comparison of DFT-FE with QE and ABINIT: Average time per SCF iteration step in Node-Hrs. Benchmark system (ii): bcc Mo periodic supercells with a mono-vacancy.

System	No. of atoms (No. of electrons)	FE basis	DFT-FE	Plane-wave basis	QE	ABINIT
$\text{Mo}_{6\text{x}6\text{x}6}$	431 (6034)	5,475,843	0.5	194,310	0.56	0.7
$\text{Mo}_{8\text{x}8\text{x}8}$	1,023 (14,322)	12,942,743	4.2	460,725	22.1	115.7
$\text{Mo}_{10\text{x}10\text{x}10}$	1,999 (27,986)	25,229,995	17.7	899,849	219.5	-

Table 5.5: CPU-time comparison of DFT-FE with QE and ABINIT: Average time per SCF iteration step in Node-Hrs. Benchmark system (iii): Cu Icosahedron nano-particles of varying sizes.

System	No. of atoms (No. of electrons)	FE basis	DFT-FE	Plane-wave basis	QE	ABINIT
$\text{Cu}_{3\text{-Shell}}$	147 (2793)	6,584,861	0.3	1,080,751	0.2	0.8
$\text{Cu}_{4\text{-Shell}}$	309 (5,871)	13,974,767	1.7	2,110,867	5.5	10.7
$\text{Cu}_{5\text{-Shell}}$	561 (10,659)	26,060,299	5.3	3,647,655	63.4	-
$\text{Cu}_{6\text{-Shell}}$	923 (17,537)	41,775,101	12.7	5,792,547	-	-

Wall-time comparisons Next, in Tables 5.6, 5.7, and 5.8 we compare the average minimum wall-times per SCF iteration step in the above benchmark systems between DFT-FE and QE, with the restriction that the parallel scaling efficiency is above

40%. We observe that DFT-FE wall-times are smaller than QE wall-times for all the benchmark systems considered. Furthermore, the speedups in DFT-FE over QE increases with system size, with substantial speedups of 9×, 16.1× and 6.9× for Mg_{8x8x8}, $\text{Mo}_{\text{10x10x10}}$, and $\text{Cu}_{\text{5-shell}}$, respectively. Even at the smallest system sizes DFT-FE is still significantly faster than QE, with speedups of 1.5×, 7.5× and 3.3× for Mg_{4x4x4}, Mo_{6x6x6}, and $\text{Cu}_{\text{3-shell}}$, respectively. Additionally, in Tables 5.6, 5.7, and 5.8, we also report some very large scale simulations conducted using DFT-FE: $\text{Mg}_{\text{10x10x10}}$, $\text{Mo}_{\text{13x13x13}}$, and $\text{Cu}_{\text{6-shell}}$, obtaining very modest minimum wall-times of 203, 277 and 70 seconds, respectively (with parallel scaling efficiencies above 40%). We note that such large system sizes are computationally prohibitive using QE, and thereby QE simulations for these systems are not performed. Finally, in Table 5.9 we show the breakdown of DFT-FE wall-times into key computational steps for the large system sizes in the above benchmark problems. Overall, we have demonstrated that DFT-FE is faster than plane-wave codes QE and ABINIT for system sizes beyond $2,000$ electrons with significant speedups at larger system sizes, and large-scale DFT simulations on generic material systems are practically feasible using DFT-FE for system sizes ranging up to $50,000$–$100,000$ electrons.

Table 5.6: Minimum wall-time comparison of DFT-FE with QE: Average time per SCF iteration step in seconds (rounded to the nearest whole number). Benchmark system (i): hcp Mg periodic supercells with a mono-vacancy.

System	No. of atoms (No. of electrons)	DFT-FE	QE
Mg_{4x4x4}	255 (2,550)	19	29
Mg_{6x6x6}	863 (8,630)	38	165
Mg_{8x8x8}	2,047 (20,470)	91	816
$\text{Mg}_{\text{10x10x10}}$	3,999 (39,990)	203	-

Table 5.7: Minimum wall-time comparison of DFT-FE with QE: Average time per SCF iteration step in seconds (rounded to the nearest whole number). Benchmark system (ii): bcc Mo periodic supercells with a mono-vacancy.

System	No. of atoms (No. of electrons)	DFT-FE	QE
Mo_{6x6x6}	431 (6,034)	23	173
Mo_{8x8x8}	1,023 (14,322)	52	549
$\text{Mo}_{\text{10x10x10}}$	1,999 (27,986)	117	1883
$\text{Mo}_{\text{13x13x13}}$	4,393 (61,502)	277	-

Table 5.8: Minimum wall-time comparison of DFT-FE with QE: Average time per SCF iteration step in seconds (rounded to the nearest whole number). Benchmark system (iii): Cu Icosahedron nano-particles of varying sizes.

System	No. of atoms (No. of electrons)	DFT-FE	QE
$\text{Cu}_{\text{3-Shell}}$	147 (2,793)	15	50
$\text{Cu}_{\text{4-Shell}}$	309 (5,871)	25	183
$\text{Cu}_{\text{5-Shell}}$	561 (10,659)	44	304
$\text{Cu}_{\text{6-Shell}}$	923 (17,537)	70	-

5.4 Strategies for acceleration of DFT-FE using Graphics Processing Units

In the last decade, with the slowing down of the Moore's law for central processing units (CPUs) there has been considerable interest in using Graphics Processing Units (GPUs) to accelerate electronic-structure calculations [195, 196]. However, efficiency on CPU architectures may not translate to efficiency on GPU architectures. This is because of two reasons— a) the massively parallel GPU architecture requires the computational algorithm to expose fine-grained parallelism in the computations, and b) data movement both inside the GPU and across GPUs is considerably slower than the compute on GPUs, and thus it is imperative to increase compute intensity (the ratio of compute to data movement) on GPUs to obtain high efficiency. We focus on these aspects to achieve significant GPU acceleration of DFT-FE. As will be evident

Table 5.9: Breakdown of average wall-time per SCF iteration step (in seconds, rounded to the nearest whole number) using DFT-FE for large systems into the following computational steps: a) ES (Total electrostatic potential solve), b) CF (Chebyshev filtering), c) CholGS (Cholesky-Gram-Schimdt Orthogonalization), d) RR (Rayleigh-Ritz procedure), e) DC (Electron-density computation) and f) O (other—Discrete Hamiltonian computation, electron density mixing, and computation of Fermi energy). "NDP" denotes number of domain decomposition MPI tasks, and "NBP" denotes number of band parallelization groups. Total number of MPI tasks is NDP times NBP.

(a) Setup of the benchmark simulations.

System	No. atoms	No. electrons	DOF's per atom	NDP (NBP)	Total MPI tasks
Mg_{8x8x8}	2,047	20,470	22,450	32,000 (2)	64,000
$\mathrm{Mg}_{10x10x10}$	3,999	39,990	23,499	51,200 (3)	153,600
$\mathrm{Mo}_{10x10x10}$	1,999	27,986	12,621	16,000 (3)	48,000
$\mathrm{Mo}_{13x13x13}$	4,393	61,502	12,594	48,000 (4)	192,000

(b) Breakdown of average wall-time per SCF iteration step.

System	ES	CF	CholGS	RR	DC	O	Total time
Mg_{8x8x8}	11	33	15	24	6	2	91
$\mathrm{Mg}_{10x10x10}$	12	63	53	63	9	3	203
$\mathrm{Mo}_{10x10x10}$	5	49	23	30	6	4	117
$\mathrm{Mo}_{13x13x13}$	7	80	80	97	9	4	277

below, the use of FE basis comes to our advantage in GPU acceleration of DFT-FE as it allows us to expose the fine-grained parallelism in compute across the FE cells.

5.4.1 GPU acceleration strategy in DFT-FE

We recollect the self consistent field (SCF) iteration (cf. Algorithm 1) for solving Kohn-Sham nonlinear eigenvalue problem by employing the Chebyshev filtered subspace iteration procedure (ChFSI) [61, 168] in each SCF iteration. Below we discuss the innovations on GPUs focused on improving arithmetic intensity and reducing data movement costs in the ChFSI algorithm.

To achieve maximum performance on GPUs, we have ported all computationally intensive steps in the ChFSI procedure to GPUs. Further, the algorithm is implemented such that we minimize CPU-GPU data transfers, which can be a rate limiting step relative to the high arithmetic performance on the GPU. In ChFSI procedure, all the key compute operations corresponding to CF, CholGS and RR are ported to GPUs using CUDA kernels, and cuBLAS library for the `Xgemm` operations. However, the Cholesky factorization and inversion steps in CholGS, and Hermitian matrix diagonalization step in RR are still performed on CPUs in parallel on a subset of the MPI ranks using the ELPA library [188]. These operations could not be performed on GPUs as the $\mathcal{O}(N^2)$ memory of the overlap ($\mathbf{S}$) and projected Hamiltonian ($\hat{\mathbf{H}}$) matrices would be too large to store in serial on a single GPU for very large scale problems considered in this work ($N \sim 60,000$). However, the cost of these operations on CPUs are much smaller compared to other steps. An important aspect of our implementation is that, by porting the aforementioned steps in ChFSI procedure to GPUs in conjunction with GPU porting of the electron-density computation (DC), we *completely eliminate* the otherwise required large data transfer of $\widetilde{\boldsymbol{\Psi}}$ between CPU and GPU during the SCF procedure.

We now briefly discuss the GPU acceleration of the key Chebyshev filtering step (CF) in the ChFSI procedure. As discussed in Section 5.2.1, the key computational kernel in CF are $\widetilde{\mathbf{H}}\mathbf{X}$ evaluations, which are performed using a blocked approach to reduce peak memory. To this end, blocks of B_f wavefunction vectors, denoted by $\mathbf{X_b}$, are filtered sequentially. We significantly reduce the memory access costs in $\widetilde{\mathbf{H}}\mathbf{X_b}$ by employing FE cell level dense matrix operations as shown in Fig. 5.10, instead of global sparse matrix approaches. The FE cell level matrix operations involving many small dense matrix-matrix multiplications are performed simultaneously for all cells on GPUs using cuBLAS's `XgemmStridedBatched` routine. Furthermore, as shown in Fig. 5.10, we structure the memory layout of $\mathbf{X_b}$ to ensure coalesced memory access across GPU threads, thereby significantly reducing memory access costs in extracting $\mathbf{X}_{\mathbf{b}}^{c_i}$ from $\mathbf{X_b}$ and in the assembly operation. Additionally, we minimize communication latencies and overheads in $\widetilde{\mathbf{H}}\mathbf{X_b}$ by exploiting the fact that all wavefunction vectors have identical MPI point-to-point communication pattern across the FE domain decomposition partition boundaries. This allows us to perform the MPI communication for all wavefunction vectors in $\mathbf{X_b}$ simultaneously, which incurs minimal network latency compared to communicating the wavefunction vectors one by one. The above optimization further benefits from the memory layout of $\mathbf{X_b}$ (see Fig. 5.10) when copying the wavefunctions data to and from the MPI buffer. Furthermore, we use FP32 (single precision) for this MPI communication and it has been observed to retain FP64 accuracy in ground-state solutions while reducing the communication cost by a factor of 2.

These implementation innovations lead to a high overall throughput for CF, as demonstrated in Fig. 5.11. Notably, we achieved 20.5% of the FP64 peak using block size $B_f = 200$ on a single Tesla V100 GPU of Summit. Overall, as demonstrated in Table 5.10, all the innovations discussed above have led to *substantial GPU acceleration*, with overall SCF iteration (including all steps) speedups of 19.6× on Summit nodes.

Table 5.10: GPU speedup of single SCF iteration step with respect to CPU on Summit nodes. Case study: 18,480 electrons Mg dislocation system using 140 nodes. CPU simulation used 40 MPI tasks per node, with each task bound to 1 CPU core (total 42 cores in each node). CPU linear algebra performed using IBM ESSL. GPU simulation used 18 MPI tasks across 6 GPUs on each node.

Step	Wall-time CPU (sec)	Wall-time GPU (sec)	Speedup
Single SCF Total	844.8	43.1	19.6×

5.4.2 Large-scale dislocation system benchmarks using GPUs

All simulations reported in this section are exectuted using the hybrid CPU-GPU architecture on the Summit supercomputer. Summit is currently the fastest supercomputer in the world, with 200.79 PFLOPS FP64 peak. Summit comprises

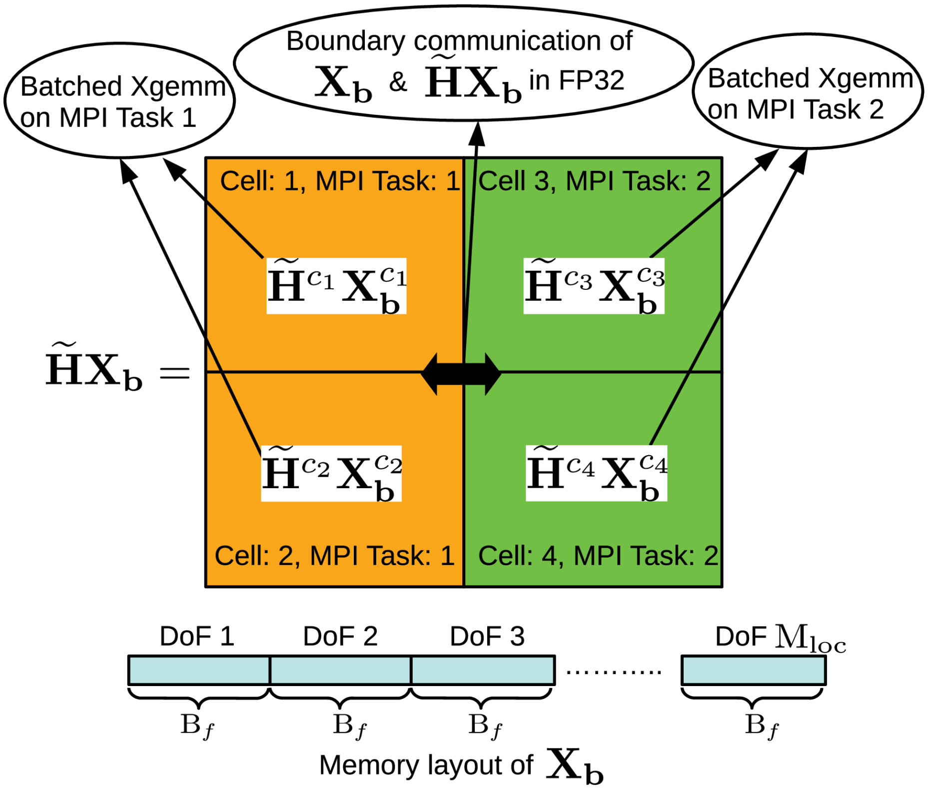

Figure 5.10: Schematic of $\tilde{\mathbf{H}}\mathbf{X_b}$ computation over four FE cells distributed over two MPI tasks using batched `Xgemm` operations. Memory layout of $\mathbf{X_b}$ where wavefunction values are stored contiguously for each degree of freedom provides coalesced memory access across GPU threads. M_{loc} denotes number of DoFs owned locally by a MPI task.

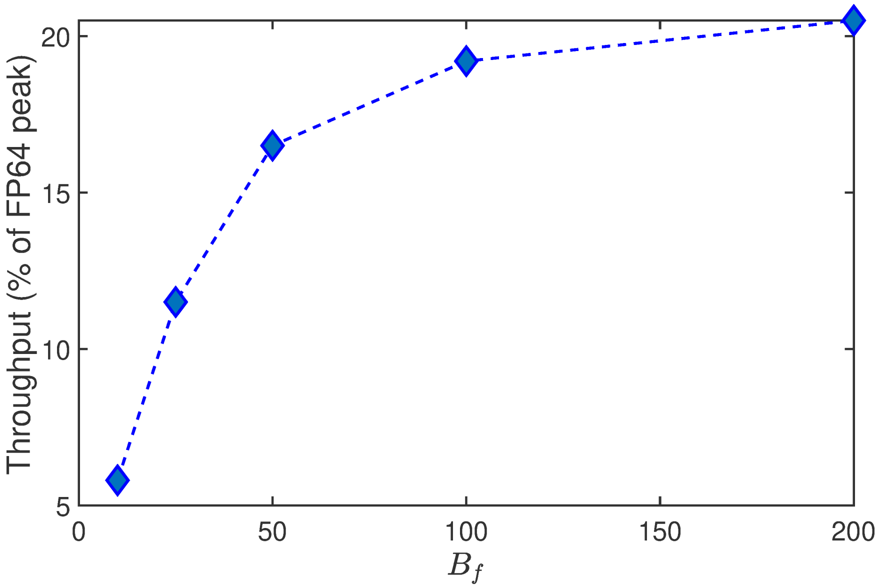

Figure 5.11: Chebyshev filtering (CF) throughput on a single Tesla V100 GPU of Summit using 3 MPI tasks (via Multi Process Service) for various block sizes (B_f). FP64 peak of Summit's Tesla V100: 7.3 TFLOPS. Case study: Mg super cell with mono-vacancy containing 310 electrons. FE Mesh DoFs: 254,097.

of 4,608 IBM Power System AC922 nodes with two IBM POWER9 processors (42 physical cores) and six NVIDIA Volta V100 GPUs in each node. Each node contains 512 GB of DDR4 memory for use by the POWER9 processors and 16 GB of HBM2 for each V100 GPU. Summit nodes are connected to a dual-rail EDR InfiniBand network providing a node injection bandwidth of 23 GB/s.

In a recent work on the effect of alloying elements on ductility in Mg (Mg) [60], it was shown that small energy difference between pyramidal I and II $< c + a >$ screw dislocations can be tuned to significantly improve the ductility of Mg. In order to use DFT calculations to guide the alloy design, it is imperative to compute the energy difference between pyramidal I and II $< c + a >$ screw dislocations ($\Delta \mathrm{E}_{\mathrm{I-II}}$) to an accuracy that is better than 10^{-4} Ha/Å [60]. Based on this motivation, here we choose an isolated pyramidal II $< c + a >$ screw dislocation in Mg, with system sizes ranging up to 105,080 electrons, as the benchmark problem on which we demonstrate the performance of DFT-FE. We consider three different system sizes: pyrIIScrewA

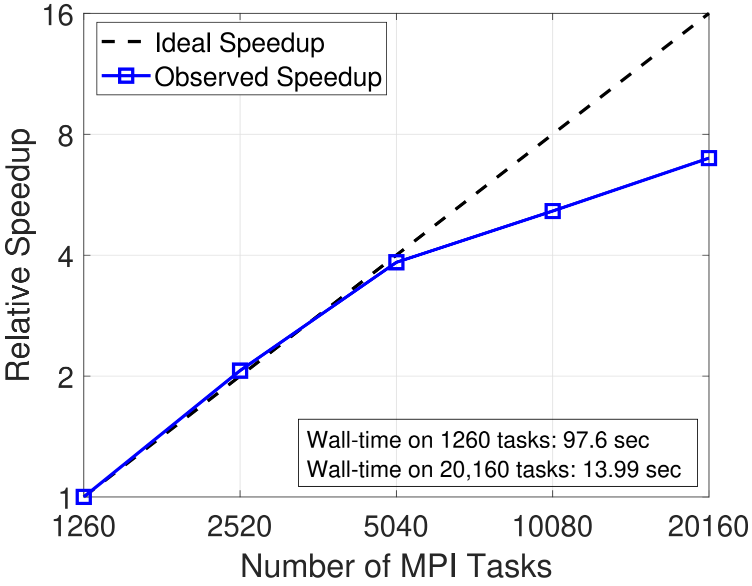

Figure 5.12: Strong scaling of wall-time per SCF iteration on Summit GPU nodes using DFT-FE. Case study: Mg dislocation system with 18,480 electrons (1,848 atoms). Each GPU is associated with 3 MPI tasks.

with 18,480 electrons (1,848 atoms), pyrIIScrewB with 61,640 electrons (6,164 atoms), and pyrIIScrewC with 105,080 electrons (10,508 atoms). Additionally, we have also considered pyramidal I and II screw dislocations on smaller computational domains with less than 1,000 atoms, where we conducted a convergence study with respect to FE discretization to determine the discretization parameters to achieve the targeted accuracy of better than 10^{-4} Ha/Å in $\Delta E_{\mathrm{I-II}}$. These discretization parameters have been used for pyrIIScrewA, pyrIIScrewB and pyrIIScrewC simulations.

First, we conduct a strong scaling study using Summit GPU nodes on the pyrIIScrewA system containing 18,480 electrons (1,848 Mg atoms) as shown in Fig. 5.12. We obtain 96% efficiency at 280 nodes (5,040 MPI tasks) with 11,000 DoFs per task. The wall-time per SCF iteration reduced from 97.6 sec on 1,260 MPI tasks to around 13.99 sec on 20,160 MPI tasks.

Next, we demonstrate the performance of DFT-FE on large-scale Mg dislocation systems: pyrIIScrewB with 61,640 electrons (6,164 Mg atoms), and pyrIIScrewC with

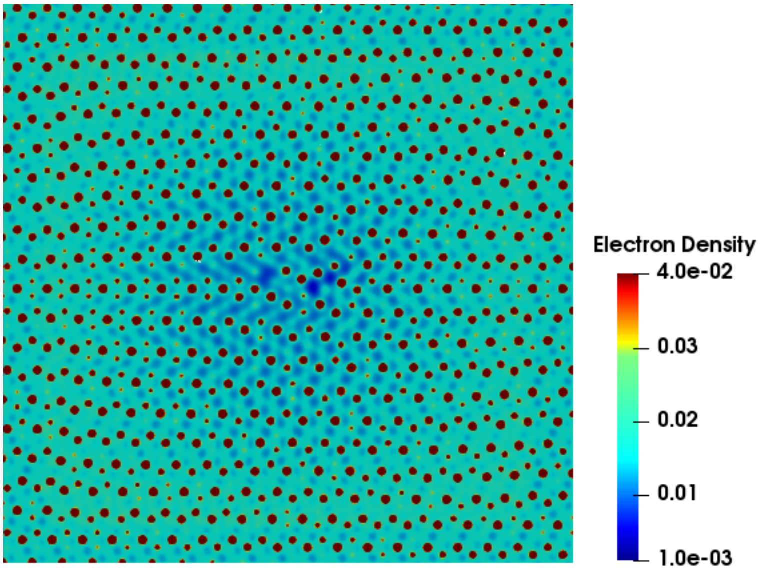

Figure 5.13: Electron density contour of pyramidal II screw dislocation system in Mg with 61,640 electrons (6,164 Mg atoms).

105,080 electrons (10,508 Mg atoms) using Summit GPU nodes. First, in Table 5.11, we report the time-to-solution and performance of the pyrIIScrewB system, which has been discretized with 179.03 million DoFs. This simulation achieved 16.7 PFLOPS (29.5% efficiency) sustained performance in the ground-state calculation involving 56 SCF iterations, and almost similar sustained performance of 14.7 PFLOPS (26.0% efficiency) over the entire run time of the program including initialization costs.

Table 5.11: Time-to-solution and performance of pyrIIScrewB (61,640 electrons) system. Simulation performed using 1,300 Summit nodes (FP64 peak: 56.65 PFLOPS). Breakdown of run time into initialization and ground-state calculation costs.

Procedure	Wall-time (sec)	FLOP count (PFLOP)	PFLOPS (% of FP64 peak)
Initialization	981	-	-
Ground-state	7377	123174	16.7 (29.5%)
Total	**8358**	**123174**	**14.7 (26.0%)**

Finally, in Table 5.12, we report the wall-time and sustained performance of a single SCF iteration step of the pyrIIScrewC system, the largest system size considered in this work with 105,080 electrons (10,508 Mg atoms) and discretized with 304.92 million DoFs (17.69 trillion wavefunction values). We note that the SCF wall-time

Table 5.12: Wall-time and sustained performance of a single SCF iteration step of pyrIIScrewC (105,080 electrons) system. Simulation performed using 3,800 Summit nodes (FP64 peak: 165.58 PFLOPS).

Step	Wall-time (sec)	FLOP count (PFLOP)	PFLOPS (% of FP64 peak)
Single SCF	142.7	6,563.7	46 (27.8%)

in Table 5.12 is obtained by taking the average over 10 calls to the ChFSI procedure, thus demonstrating sustainability of the performance. This simulation achieves two significant landmarks. First, the single SCF wall-time of 142.7 sec demonstrates that fast large-scale and chemically accurate Kohn-Sham DFT simulations of metallic systems reaching $\sim 100,000$ electrons are now possible. Second, we achieve an unprecedented sustained performance of 46 PFLOPS (27.8% efficiency) utilizing 3,800 nodes out of total 4,608 nodes on Summit.

The above benchmarks demonstrate that accurate Kohn-Sham DFT studies on dislocation energetics now becomes a reality, which can guide and accelerate the discovery of new light weight structural alloys.

5.5 Summary

In this work, we have developed DFT-FE (Density Functional Theory with Finite-Elements), an accurate, computationally efficient and scalable finite-element (FE) based code for large-scale first-principles based materials modeling using Kohn-Sham DFT. The DFT-FE code can conduct both pseudopotential and all-electron calculations on non-periodic, semi-periodic and periodic systems, which is a unique feature that has been possible due to the real-space formulation employed in this work in conjunction with the versatility of the FE basis. Besides the systematic convergence afforded by the FE basis, the spatial adaptivity of the FE basis (realized through 'p4est' library in deal.II package) and the higher-order spectral finite-elements employed in DFT-FE play an important role in the computational efficiency of the code.

The computational efficiency and scalability of the DFT-FE code can largely be attributed to the locality of the FE basis, the algorithms employed in the solution of the discrete Kohn-Sham problem, and a careful numerical implementation of the algorithms—minimizing floating point operations, communication costs and latency—some of which leverage the attributes of the FE basis. In particular, the solution to the Kohn-Sham problem is efficiently computed by: (i) employing Chebyshev filtered subspace iteration technique to compute the eigensubspace of interest; (ii) using Cholesky factorization based Gram-Schmidt orthonormalization (CholGS) to compute an orthonormal basis spanning the subspace; (iii) employing Rayleigh-Ritz (RR) procedure to diagonalize the Hamiltonian in the projected subspace and compute the electron density to continue the self-consistent field (SCF) iteration. We developed and implemented mixed precision arithmetic based algorithms for the various steps in the solution procedure, and also employed spectrum splitting technique, that significantly reduced the computational prefactors for CholGS and RR procedure by factors of around 2 and 3, respectively, for large-scale systems. Since the computational complexity of CholGS and RR procedure scale cubically with system size, these efficiency gains delay the onset of cubic computational complexity in DFT-FE to very large system sizes. Our numerical studies on benchmark problems demonstrate that DFT-FE exhibits close to quadratic-scaling in system size even for those as large as $40,000$ electrons. The scalability of DFT-FE has been tested on up to $192,000$ MPI tasks, with a parallel efficiency of 42% realized on a $\sim 60,000$ electron system. The locality of the FE basis is an important factor in the excellent parallel scalability of the DFT-FE code. However, a careful implementation of the various aspects of the algorithms—such as the use of elemental level matrix-matrix products and blocked approach in Chebyshev filtering, the use mixed precision arithmetic based algorithms in the CholGS and RR procedure—have been instrumental in reducing communication costs and latency, thus resulting in better scalability and reduced wall-times.

In order to assess the accuracy of DFT-FE with respect to state-of-the-art DFT codes, we have conducted a comprehensive comparison study with respect to QUANTUM ESPRESSO (QE), a widely used pseudopotential plane-wave code. The benchmark systems considered included periodic metallic systems and non-periodic nanoparticles of various sizes. Importantly, the agreement between DFT-FE and QE on ground-state energies, ionic forces and stresses was excellent, with the differences being significantly lower than the discretization errors of the codes.

In order to compare the computational efficiency and scalability afforded by DFT-FE with respect to widely used DFT codes, we conducted an extensive comparison study with QE using ONCV pseudopotentials. We used the CPU-time per SCF iteration on a wide range of benchmark problems as a metric to assess the computational efficiency, and the minimum wall-time (with at least $40-45\%$ parallel efficiency) as a metric to also assess the effectiveness of the scalability. These benchmark studies suggest that DFT-FE is more efficient than QE for periodic system sizes beyond 3,000 electrons. Furthermore, for larger systems ($10,659-20,470$ electrons), we find DFT-FE to be substantially more efficient than QE by $4.5-12\times$ in terms of CPU-times. We used the same benchmark systems to also compare the minimum wall-time per SCF iteration. Importantly, DFT-FE was significantly faster than QE for all the systems considered, with $1.5-7.5\times$ speedups for smaller system sizes ($2,550-6,034$ electrons) to $7-16\times$ speedups for larger system sizes ($14,322-20,470$ electrons). We also considered three very large periodic metallic systems with $27,986$, $39,990$ and $61,502$ electrons, where we achieve very modest average minimum wall-times per SCF iteration of 1.9, 3.4 and 4.6 minutes, respectively.

Finally, we have also accelerated DFT-FE using Graphics Processing Units (GPUs). We employed implementation strategies that significantly reduce the data movement costs and increase arithmetic intensity. This lead to significant speedups of 20x factor with respect to CPUs. Using the GPU nodes on the Summit supercomputer, we demonstrated an unprecedented sustained performance of 46 PFLOPS (27.8% peak FP64 performance) on a dislocation system in Mg containing 105,080 electrons using 3,800 GPU nodes of Summit supercomputer, which is the highest performance to-date among DFT codes.

Overall, DFT-FE provides a practical capability to perform accurate massively parallel large-scale pseudopotential DFT calculations (reaching 100,000 electrons) in generic material systems with arbitrary boundary conditions and complex geometries. An attractive feature of DFT-FE is also the ability to perform all-electron calculations in the same framework, which can aid transferability studies on pseudopotentials. Further, the framework, in principle, can support mixed pseudopotential and all-electron calculations, where some atoms are treated at the all-electron level and others are treated at the pseudopotential level. This can be useful in a wide range of applications from using all-electron calculations for certain atoms with unreliable pseudopotentials to the computation of spin Hamiltonian parameters that require an all-electron treatment around the defect states (e.g. NV center in diamond) [197]. Implementation of enriched finite-element basis [156] in DFT-FE, which can enable large-scale efficient all-electron DFT calculations, is currently being pursued. Further, implementation of advanced exchange-correlation functionals (hybrid and dispersion corrected), advanced mixing schemes, spin-orbit coupling, and implementation of polarizability and dielectric calculations in DFT-FE are other efforts that are being pursued.

CHAPTER VI

Conclusions

6.1 Summary

The present thesis developed computational methodologies in both orbital-free DFT and Kohn-Sham DFT to conduct large-scale real-space electronic-structure studies of core structure and core energetics of dislocations in Aluminum and Magnesium, and used the dislocation core energetics to develop a continuum model for an arbitrary aggregate of dislocations. The additional configurational forces resulting from the developed continuum model is incorporated into various case studies of dislocation–dislocation interactions in static as well as dislocation dynamics setting, where significant influence of the additional core-energetics informed configurational forces is demonstrated in relation to the elastic Peach-Koehler force.

The first part of the thesis (Chapter II) developed a local real-space formulation of orbital-free DFT with WGC kinetic energy functionals by reformulating the extended interactions in electrostatic and kinetic energy functionals as local variational problems in auxiliary potentials. Building on the proposed real-space formulation we have developed a unified variational framework for computing configurational forces associated with both ionic and cell relaxations. Further, we also proposed a numerically efficient approach for the solution of ground-state orbital-free DFT problem, and employed a finite-element basis for the numerical discretization of the proposed real-space formulation of orbital-free DFT. Our numerical convergence studies indicate that we obtain close to optimal rates of convergence in both ground-state energy and configurational forces with respect to the finite-element discretization. We subsequently demonstrated the accuracy and transferability of the proposed real-space formulation of orbital-free DFT for Aluminum-Magnesium materials system using various bulk and defect material systems. We finally investigated the cell-size effects in the electronic structure of a mono-vacancy in Aluminum, where we demonstrated that the true cell-size effects in the electronic structure are revealed by using bulk Dirichlet boundary conditions, where the perturbations in the electronic fields due to the defect vanish on the boundary of the computational domain. We note that the proposed real-space formulation and the finite-element basis are crucial to employing the bulk Dirichlet boundary conditions that are otherwise inaccessible using Fourier based formulations.

The second part of the thesis (Chapter III) studied the core structure and core energetics of dislocations in Aluminum and Magnesium using the real-space formulation of orbital-free DFT with finite-element discretization developed in Chapter II. In order to directly compute the core energetics, we employed mixed boundary conditions corresponding to an isolated dislocation embedded in the bulk—i.e., periodic boundary conditions along the dislocation line and bulk Dirichlet boundary conditions on the electronic fields obtained from the Cauchy-Born hypothesis along the boundary on the other two directions for fixed atomic positions on the boundary that are determined based on the elastic field of the dislocation. The local real-space formulation and the finite-element discretization are essential to realizing these boundary conditions, which are not accessible using the widely employed plane-wave discretization in electronic structure calculations. We computed the dislocation energies of a perfect dislocation in each dislocation type for a series of increasing domain sizes, and identified the region up to which the perturbations in the electronic structure are significant to the dislocation energetics. This allowed us to unambiguously characterize the core size of the perfect screw dislocation in Aluminum to be $\approx 7\ |\mathbf{b}|$, and core sizes of basal edge and basal screw dislocations in Magnesium to be $\approx 8\ |\mathbf{b}|$ and $\approx 11\ |\mathbf{b}|$ respectively. This core size corresponds well with the estimated core size of $\approx 10\ |\mathbf{b}|$ for the perfect edge dislocation in Aluminum [56]. Significantly, these core sizes are much larger than the conventional estimates of 1–3 $|\mathbf{b}|$ based on displacement fields underlining the longer ranged nature of quantum mechanical perturbations in the energetics due to the dislocation core in comparison to displacement field deviation from elastic estimates. Upon ionic relaxation, the perfect screw dislocation in Aluminum and perfect basal edge and basal screw dislocations in Magnesium dissociated into two Shockley partials with partial separation distances comparing closely with other estimates from prior electronic structure studies. We also computed the core energy under externally applied affine volumetric, uniaxial and shear deformations, and found that, in general for dislocations in both Aluminum and Magnesium, the core energy is strongly dependent on the macroscopic deformations with non-zero slopes at zero deformation. This suggests that the dependence of the core energy on macroscopic deformations is a fundamental characteristic of dislocation energetics.

The third part of this thesis (Chapter IV) used the dislocation core energetics to develop an continuum model for a dislocation aggregate, in an isotropic infinite elastic continua. This model incorporates the dependence of the core energetics on macroscopic deformations. The underlying elastic model is chosen to be the non-singular elastic formulation by [126]. Next, we extended the developed energetics model to a nodal dislocation network, and derived the nodal force associated with the core energy contribution not captured by the non-singular elastic formulatoin, which we referred to as the nodal core force. Next, we considered case studies to compare the magnitude of the Peach-Koehler force with the magnitude of the core force contribution arising from the macroscopic deformation dependence of the core energy. These case studies involved interactions of grain boundary-straight dislocation, grain boundary-glide loop, glide loop-glide loop and glide loop-straight dislocation in fcc Aluminum. Numerically computing the Peach-Koehler and core force along the slip direction in these case studies, we found that even up to distances of 10-15 nm between dislocations, the magnitude of the core force is significant with respect to the Peach-Koehler force (being at least 10% of the Peach-Koehler force), while also being larger than the Peierls-Nabarro force. Furthermore, for some configurations with distances of < 2 nm, the magnitude of the core force was found to be comparable or more than the elastic force. Finally, we incorporated the nodal core force into DDLab, a MATLAB based 3D DDD framework, and studied the influence of nodal core force on two different case studies involving dislocation mechanisms in fcc Aluminum. The first case study investigated the influence of nodal core force on critical stress of a Frank-Read source while the second case study investigated the influence of nodal core force on the equilibrium junction length of a dislocation binary junction. In both of these case studies, we observed significant influence of both self as well interaction nodal core force on the computed quantities.

The final part of the thesis (Chapter V) improved upon previous work on real-space adaptive spectral finite-element (FE) discretization of Kohn-Sham DFT [61, 62] to develop DFT-FE (Density Functional Theory with Finite-Elements), an accurate, computationally efficient and scalable finite-element (FE) based code for large-scale Kohn-Sham DFT calculations (reaching $\sim$ 100,000 electrons). The important numerical and implementation improvements made in this work are: (i) optimized FE cell level matrix operations during the Chebyshev filtering procedure; (ii) Cholesky factorization based Gram-Schmidt orthonormalization; (iii) mixed precision arithmetic based algorithms, and (iv) spectrum splitting based Rayleigh-Ritz procedure. In particular, the mixed precision and spectrum splitting algorithms reduced the computational prefactors for CholGS and RR procedure by factors of around 2 and 3, respectively, for large-scale systems. We demonstrate the accuracy of DFT-FE by comparing the energies, ionic forces and periodic cell stresses on a wide range of problems with QUANTUM ESPRESSO— a popularly used plane-wave DFT code. Further, we demonstrate that DFT-FE significantly outperforms widely used plane-wave codes—both in CPU-times and wall-times, and on both non-periodic and periodic systems—at systems sizes beyond a few thousand electrons, with over 5–10 fold speedups in systems with morethan 10,000 electrons. The benchmark studies also highlight the excellent parallel scalability of DFT-FE, with strong scaling demonstrated on up to 192,000 MPI tasks. Finally, we have also accelerated DFT-FE using Graphics Processing Units (GPUs), where we achieved significant speedups of 20x factor with respect to CPUs using the Summit supercomputer.

6.2 Future work and directions

Influence of core force on macroscale strain hardening via large-scale DDD simulations: In the present thesis, significant influence of core force is demonstrated on elementary strain hardening mechanisms in Aluminum— a Frank-Read source and a dislocation binary junction. This suggests that predictions of macroscale strain hardening behaviour in Aluminum and Aluminum alloys can be influenced by core force. However, the modified DDLab code used in the present thesis to study the above elementary mechanisms is not adequate for performing large scale DDD simulations. Thus, integrating the nodal core force from this work into large-scale, massively parallel DDD codes like ParaDiS is an important future direction. The major challenge in the implementation stems from developing a strategy to reduce the $\mathcal{O}(N^2)$ computational cost of calculating all the interaction core force, where N is the number of discrete dislocation line segments in the dislocation network. To that end, the asymptotic behavior of various terms contributing to the core force can be exploited, along with obtaining closed form expressions.

Study of dislocation core energetics in Aluminum and Magnesium using Kohn-Sham DFT: Large-scale Kohn-Sham DFT calculations of dislocation core energetics would provide more accurate prediction of dislocation core energetics in Aluminum and Magnesium in comparison to orbital-free DFT used in the present thesis. This is particularly important in the context of the core force expression developed in the present thesis, which contains terms that are proportional to the slope of the core energy dependence on macroscopic strains. The values of the slopes could be sensitive to the kinetic energy functional approximation in orbital-free DFT. The development of DFT-FE in the present thesis allows accurate and large scale Kohn-Sham DFT calculations of dislocation core energetics. To that end, development of an computational approach to apply Dirichlet bulk boundary conditions for isolated dislocations in the context of Kohn-Sham DFT is an important future direction. Furthermore, such a capability will allow electronic-structure study of dislocation core structure and core energetics in other metals like Ti (hcp) and Fe (bcc), which are of significant interest to the material science community.

APPENDICES

APPENDIX A

Partial Fraction Approximations of WGC Kernels

We now discuss the partial fraction approximations of the K_0, K_1, K_{11} and K_{12} kernel terms arising from the second order Taylor series expansion of the WGC [2] kinetic energy functional (cf. equations (2.9) and (2.25)) that are central to the local reformulation of the extended interactions in the kinetic energy functional. Following the procedure by Choly and Kaxiras [98], we seek to fit with a sum of partial fractions the Fourier transforms of the kernels given by $\hat{K}_0(\bar{q})$, $\hat{K}_1(\bar{q})$, $\hat{K}_{11}(\bar{q})$ and $\hat{K}_{12}(\bar{q})$ in a scaled Fourier space $\bar{q} = k/(2\bar{k}_F)$, where $\bar{k}_F = (3\pi^2\rho_0)^{1/3}$ and ρ_0 denotes the reference electron density, generally taken as the bulk average electron density. Taking into account the difference in asymptotic behavior of these kernels as $\bar{q} \to \infty$, two forms of partial fraction approximations are chosen, one for the K_0 kernel, and the second for all the remaining kernels. In particular, the forms of the partial fraction approximations for the kernels of interest are given by

$$\begin{aligned} \tilde{K}_0(\bar{q}) &= \sum_{j=1}^{m} \frac{\bar{q}^2 A_j}{\bar{q}^2 + B_j} \,, \\ \rho_0 \tilde{K}_1(\bar{q}) &= \sum_{j=1}^{m} \frac{A_j}{\bar{q}^2 + B_j} \,, \\ {\rho_0}^2 \tilde{K}_{11}(\bar{q}) &= \sum_{j=1}^{m} \frac{A_j}{\bar{q}^2 + B_j} \,, \\ {\rho_0}^2 \tilde{K}_{12}(\bar{q}) &= \sum_{j=1}^{m} \frac{A_j}{\bar{q}^2 + B_j} \,, \end{aligned} \tag{A.1}$$

where $\tilde{K}_0(\bar{q})$, $\tilde{K}_1(\bar{q})$, $\tilde{K}_{11}(\bar{q})$ and $\tilde{K}_{12}(\bar{q})$ are approximations to $\hat{K}_0(\bar{q})$, $\hat{K}_1(\bar{q})$, $\hat{K}_{11}(\bar{q})$ and $\hat{K}_{12}(\bar{q})$, respectively. We note that the A_js and B_js for each of the kernels are fitted independently, by employing a best fit approximation.

The kernels $\hat{K}_0(\bar{q})$, $\hat{K}_1(\bar{q})$, $\hat{K}_{11}(\bar{q})$ and $\hat{K}_{12}(\bar{q})$ for the second order Taylor series expansion of the density dependent WGC functional with parameters $\{\alpha, \beta\} = \{5/6 + \sqrt{5}/6, 5/6 - \sqrt{5}/6\}$ and $\gamma = 2.7$ are computed following the lines of [2], which involves the numerical solution of a series of ordinary differential equations. Choly and Kaxiras [98] have proposed the best fit approximation of these kernels using a sum of four partial fractions, i.e., $m = 4$. However, such a fit, while satisfactory for Al is found to be inadequate for Mg. Thus, we compute the best fit approximation of these kernels for $m = 5$ and $m = 6$. The best approximations for $m = 4$, $m = 5$ and $m = 6$ employed in this work are provided in Tables A.1, A.2 and A.3, respectively. The errors in the best fit approximation are shown in Figures A.1, A.2, A.3 and A.4.

Table A.1: Best fit approximation with $m = 4$ for the WGC kinetic energy functional kernels $\hat{K}_0(\bar{q})$, $\hat{K}_1(\bar{q})$, $\hat{K}_{11}(\bar{q})$, and $\hat{K}_{12}(\bar{q})$. Only odd indices are given. The even indices $j = 2$, and $j = 4$ satisfy the relations: $A_2 = A_1^*$, $A_4 = A_3^*$, $B_2 = B_1^*$, and $B_4 = B_3^*$, where '$*$' is the complex conjugate symbol.

		j=1	j=3
K_0	A_j	$0.108403 + i0.079657$	$-0.908403 + i0.439708$
	B_j	$-0.470923 - i0.465392$	$0.066051 - i0.259678$
$\rho_0 K_1$	A_j	$-0.030515 + i0.015027$	$0.028915 - i0.008817$
	B_j	$-0.597793 - i0.294130$	$-0.087917 - i0.164937$
${\rho_0}^2 K_{11}$	A_j	$0.008907 - i0.032841$	$-0.034974 + i0.009116$
	B_j	$-0.537986 - i0.233840$	$-0.041565 - i0.196662$
${\rho_0}^2 K_{12}$	A_j	$0.012423 - i0.034421$	$-0.031907 + i0.007392$
	B_j	$-0.511699 - i0.266195$	$-0.034031 - i0.188927$

Table A.2: Best fit approximation with $m = 5$ for the WGC kinetic energy functional kernels $\hat{K}_0(\bar{q})$, $\hat{K}_1(\bar{q})$, $\hat{K}_{11}(\bar{q})$, and $\hat{K}_{12}(\bar{q})$. Only odd indices are given. The even indices $j = 2$, and $j = 4$ satisfy the relations: $A_2 = A_1^*$, $A_4 = A_3^*$, $B_2 = B_1^*$, and $B_4 = B_3^*$.

		j=1	j=3	j=5
K_0	A_j	$-0.886 + i0.4146$	$0.08621 - i0.09572$	$-0.0004198 + i0.0$
	B_j	$0.06707 - i0.2503$	$-0.447 + i0.4122$	$0.2402 + i0.0$
$\rho_0 K_1$	A_j	$-0.008928 - i0.02575$	$0.03686 + i0.07371$	$-0.10395 + i0.0$
	B_j	$-0.7097 + i0.3011$	$-0.1313 + i0.3094$	$0.3323 + i0.0$
${\rho_0}^2 K_{11}$	A_j	$0.02388 - i0.03564$	$-0.01716 + i0.004228$	$0.02037 + i0.0$
	B_j	$-0.2272 + i0.2447$	$-0.7899 + i0.1762$	$0.09371 + i0.0$
${\rho_0}^2 K_{12}$	A_j	$0.02387 - i0.02923$	$-0.0172 + i0.002471$	$0.01633 + i0.0$
	B_j	$-0.2334 + i0.2403$	$-0.7962 + i0.1756$	$0.09016 + i0.0$

Table A.3: Best fit approximation with $m = 6$ for the WGC kinetic energy functional kernels $\hat{K}_0(\bar{q})$, $\hat{K}_1(\bar{q})$, $\hat{K}_{11}(\bar{q})$, and $\hat{K}_{12}(\bar{q})$. Only odd indices are given.The even indices $j = 2$, $j = 4$, and $j = 6$ satisfy the relations: $A_2 = A_1^*$, $A_4 = A_3^*$, $A_6 = A_5^*$, $B_2 = B_1^*$, $B_4 = B_3^*$, and $B_6 = B_5^*$.

		j=1	j=3	j=5
K_0	A_j	$0.09497 + i0.2248$	$0.01503 + i0.006301$	$-0.9100 + i0.2338$
	B_j	$-0.2711 - i0.4679$	$-0.7524 + i0.3445$	$0.09512 - i0.2323$
$\rho_0 K_1$	A_j	$0.004923 - i0.007041$	$-0.05719 - i0.009509$	$0.04444 - i0.01249$
	B_j	$-0.8584 + i0.222$	$-0.4359 - i0.391$	$-0.01699 + i0.2098$
${\rho_0}^2 K_{11}$	A_j	$-0.006501 - i0.007079$	$0.02922 + i0.03002$	$-0.02879 - i0.005261$
	B_j	$-0.9058 + i0.1325$	$-0.4807 + i0.3047$	$-0.04111 + i0.171$
${\rho_0}^2 K_{12}$	A_j	$-0.006068 - i0.007396$	$-0.02479 - i0.006033$	$0.02405 + i0.0302$
	B_j	$-0.9081 + i0.1324$	$-0.04396 + i0.1684$	$-0.4863 + i0.3013$

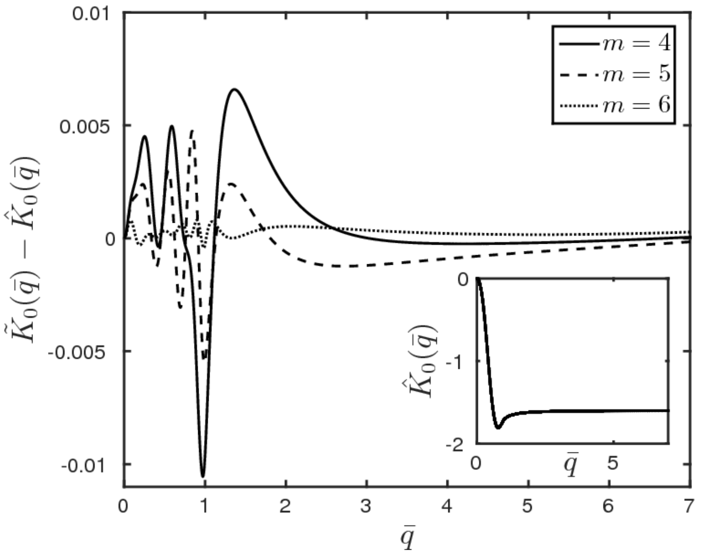

Figure A.1: Partial fraction approximation errors for WGC kernel, $\hat{K}_0(\bar{q})$.

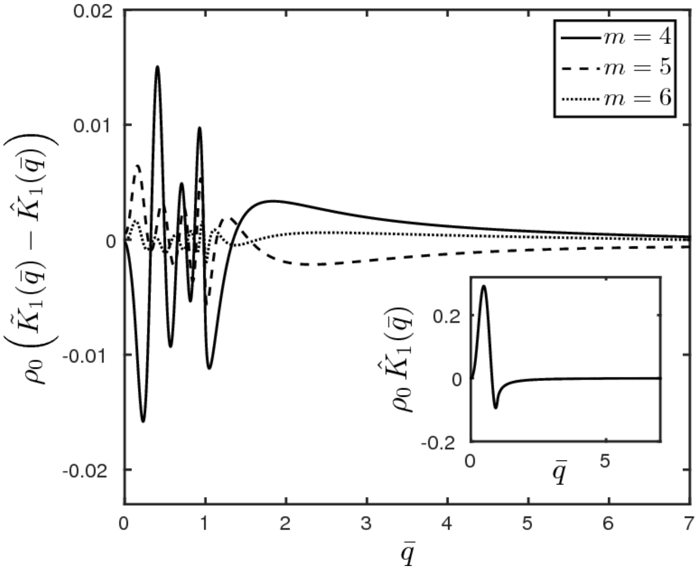

Figure A.2: Partial fraction approximation errors for WGC kernel, $\hat{K}_1(\bar{q})$.

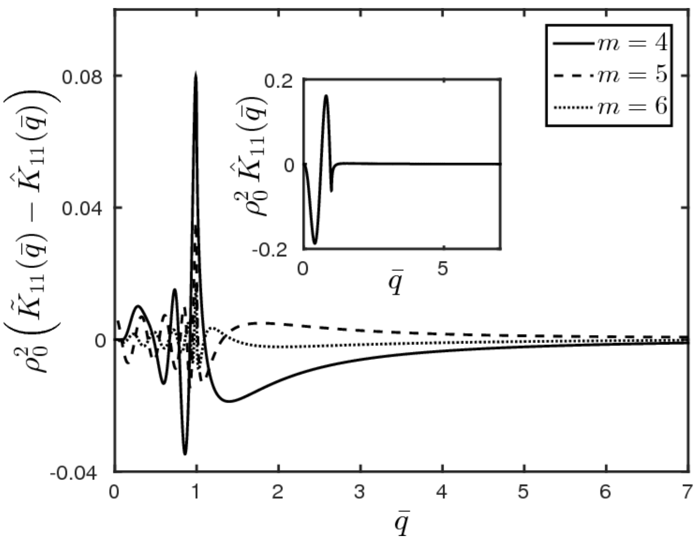

Figure A.3: Partial fraction approximation errors for WGC kernel, $\hat{K}_{11}(\bar{q})$.

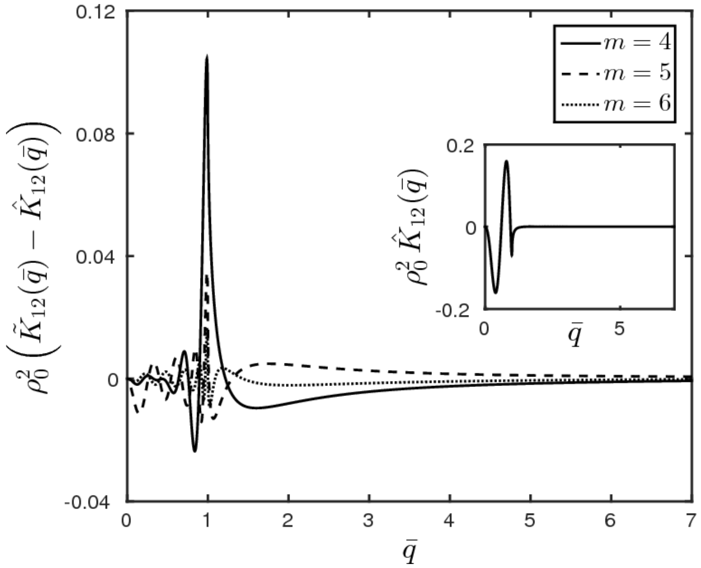

Figure A.4: Partial fraction approximation errors for WGC kernel, $\hat{K}_{12}(\bar{q})$.

APPENDIX B

Computation of Non-Elastic Core Energy From RS-OFDFT Dislocation Core Energetics Data

Here, we discuss the post-processing of the core-energetics data from RS-OFDFT calculations to estimate the non-elastic core energy of the dislocation aggregate, E^{C}_{cnel}. The non-elastic core energy is obtained by subtracting from the core energy of a dislocation aggregate, E^{C}_{c}, the elastic energy of the dislocation (cf. equation (4.6)). In the model presented in section 4.1.1, as the core energy of a dislocation aggregate is computed in terms of the core energies of straight edge and screw dislocations, $E^{\mathrm{edge/screw}}_{\mathrm{c}}(\boldsymbol{\epsilon}^{\mathrm{ext}})$ (cf. equation (4.13)), it is sufficient to compute the non-elastic core energies of straight edge and screw dislocations—$E^{\mathrm{edge/screw}}_{\mathrm{cnel}}(\boldsymbol{\epsilon}^{\mathrm{ext}})$.

To this end, we consider the domain corresponding to the dislocation core, denoted by Ω_{c}, as determined from RS-OFDFT calculations—10 $|\mathbf{b}|$ for the edge dislocation [56] and 8.7 $|\mathbf{b}|$ for the screw dislocation (cf. section 3.2) in Aluminum. The coordinate axes 1—2—3 are aligned such that the axis labelled ‘1’ lies on the slip plane and is perpendicular to the line direction, axis labelled ‘2’ is perpendicular to the slip plane, and the axis labelled ‘3’ is along the line direction. In the present work, as we restrict our model and study to a dislocation aggregate of perfect dislocations, though an extension to consider dissociated partials is possible following the lines of Martínez et al. [15], we subtract the non-singular elastic contribution of perfect dislocation from the RS-OFDFT core energy data that corresponds to relaxed Shockley partials. Thus, the energetics associated with core structure relaxation are present in the non-elastic core energy. Further, in the context of DDD calculations, the average distance between dislocations is much larger compared to the core size, beyond which the combined elastic fields of the Shockley partials converges to the elastic field of the perfect dislocation. We now consider the non-singular elastic energy of isolated straight edge and screw dislocations under an external homogeneous strain, $\boldsymbol{\epsilon}^{\mathrm{ext}}$, using a choice for a and the isotropic elastic constants for Al computed from RS-OFDFT (cf. Table B.1). The non-singular elastic energy per unit length of dislocation line in the domain Ω_{c} is given by

$$\begin{aligned} E_{\mathrm{cel}}^{\mathrm{edge/screw}}(\boldsymbol{\epsilon}^{\mathrm{ext}}; a) =& \frac{1}{2}\int_{\Omega_{\mathrm{c}}} \left(\boldsymbol{\sigma}^{\mathrm{d}}(\mathbf{x}_{\mathrm{c}}, a) + \boldsymbol{\sigma}^{\mathrm{ext}}\right) : \left(\boldsymbol{\epsilon}^{\mathrm{d}}(\mathbf{x}_{\mathrm{c}}, a) + \boldsymbol{\epsilon}^{\mathrm{ext}}\right) \mathrm{d}A \\ =& \frac{1}{2}\int_{\Omega_{\mathrm{c}}} \boldsymbol{\sigma}^{\mathrm{d}}(\mathbf{x}_{\mathrm{c}}, a) : \boldsymbol{\epsilon}^{\mathrm{d}}(\mathbf{x}_{\mathrm{c}}, a)\, \mathrm{d}A + \frac{1}{2}\int_{\Omega_{\mathrm{c}}} \boldsymbol{\sigma}^{\mathrm{ext}} : \boldsymbol{\epsilon}^{\mathrm{ext}}\, \mathrm{d}A \\ &+ \int_{\Omega_{\mathrm{c}}} \boldsymbol{\sigma}^{\mathrm{d}}(\mathbf{x}_{\mathrm{c}}, a) : \boldsymbol{\epsilon}^{\mathrm{ext}}\, \mathrm{d}A\,, \end{aligned} \tag{B.1}$$

where $\boldsymbol{\sigma}^{\mathrm{d}}(\mathbf{x}_{\mathrm{c}}, a)$ and $\boldsymbol{\epsilon}^{\mathrm{d}}(\mathbf{x}_{\mathrm{c}}, a)$ are the non-singular stress and strain fields, respectively, of the straight edge or screw dislocation at any point $\mathbf{x}_{\mathrm{c}} \in \Omega_{\mathrm{c}}$, and $\mathbf{x}_{\mathrm{c}}$ is measured with respect to the dislocation line. In the above, as we are interested in the regime of small external homogenous strains, we assume that $\boldsymbol{\sigma}^{\mathrm{d}}$ and $\boldsymbol{\epsilon}^{\mathrm{d}}$ are independent of $\boldsymbol{\epsilon}^{\mathrm{ext}}$.

Next, we turn to the core energies of the isolated straight edge and screw dislocations, and the estimation of the corresponding non-elastic core energies. While the core energy, $E_{\mathrm{c}}^{\mathrm{edge/screw}}(\boldsymbol{\epsilon}^{\mathrm{ext}})$, is defined as the total energy inside Ω_{c} measured with respect to the unstrained perfect crystal, the core-energetics data from RS-OFDFT calculations, presented in section 3.2, measure the excess energy with respect to a perfect crystal undergoing the same external homogenous strain (cf. equation (3.2)).

Thus, $E_{\mathrm{c}}^{\mathrm{edge/screw}}(\boldsymbol{\epsilon}^{\mathrm{ext}})$ is related to the RS-OFDFT core energetics data, which we denote by $E_{\mathrm{c,\,data}}^{\mathrm{edge/screw}}(\boldsymbol{\epsilon}^{\mathrm{ext}})$, as

$$E_{\mathrm{c}}^{\mathrm{edge/screw}}(\boldsymbol{\epsilon}^{\mathrm{ext}}) = E_{\mathrm{c,data}}^{\mathrm{edge/screw}}(\boldsymbol{\epsilon}^{\mathrm{ext}}) + \frac{1}{2}\int_{\Omega_{\mathrm{c}}} \boldsymbol{\sigma}^{\mathrm{ext}} : \boldsymbol{\epsilon}^{\mathrm{ext}}\,\mathrm{d}A\,. \tag{B.2}$$

The non-elastic core energy, following the partitioning in equation (4.6), is given by

$$E_{\mathrm{cnel}}^{\mathrm{edge/screw}}(\boldsymbol{\epsilon}^{\mathrm{ext}}) = E_{\mathrm{c}}^{\mathrm{edge/screw}}(\boldsymbol{\epsilon}^{\mathrm{ext}}) - E_{\mathrm{cel}}^{\mathrm{edge/screw}}(\boldsymbol{\epsilon}^{\mathrm{ext}})\,. \tag{B.3}$$

In the regime of small external homogeneous strains, linearizing the above equation about $\boldsymbol{\epsilon}^{\mathrm{ext}} = 0$ (cf. equations (4.14) - (4.15)), we obtain

$$\begin{aligned} E_{\mathrm{cnel}}^{\mathrm{edge/screw}}(\boldsymbol{\epsilon}^{\mathrm{ext}}; a) \;&\approx E_{\mathrm{cnel}}^{\mathrm{edge/screw}}(\boldsymbol{\epsilon}^{\mathrm{ext}} = \mathbf{0}; a) + \hat{S}_{\alpha\beta}^{\mathrm{edge/screw}}(a)\epsilon_{\alpha\beta}^{\mathrm{ext}} \\ &= \left(E_{\mathrm{c}}^{\mathrm{edge/screw}}(\boldsymbol{\epsilon}^{\mathrm{ext}} = \mathbf{0}) - \frac{1}{2}\int_{\Omega_{\mathrm{c}}} \boldsymbol{\sigma}^{\mathrm{d}}(\mathbf{x}_{\mathrm{c}}, a) : \boldsymbol{\epsilon}^{\mathrm{d}}(\mathbf{x}_{\mathrm{c}}, a)\,\mathrm{d}A\right) \\ &\quad + \left(S_{\alpha\beta}^{\mathrm{edge/screw}} - \int_{\Omega_{\mathrm{c}}} \sigma_{\alpha\beta}^{\mathrm{d}}(\mathbf{x}_{\mathrm{c}}, a)\,\mathrm{d}A\right)\epsilon_{\alpha\beta}^{\mathrm{ext}}\,. \end{aligned} \tag{B.4}$$

In the above, $\hat{S}_{\alpha\beta}^{\mathrm{edge/screw}} = \left.\frac{\partial E_{\mathrm{cnel}}^{\mathrm{edge/screw}}}{\partial \epsilon_{\alpha\beta}^{\mathrm{ext}}}\right|_{\boldsymbol{\epsilon}^{\mathrm{ext}}=\mathbf{0}}$ and $S_{\alpha\beta}^{\mathrm{edge/screw}} = \left.\frac{\partial E_{\mathrm{c}}^{\mathrm{edge/screw}}}{\partial \epsilon_{\alpha\beta}^{\mathrm{ext}}}\right|_{\boldsymbol{\epsilon}^{\mathrm{ext}}=\mathbf{0}}$. We note that, from equation (B.2), $E_{\mathrm{c}}^{\mathrm{edge/screw}}(\boldsymbol{\epsilon}^{\mathrm{ext}} = \mathbf{0}) = E_{\mathrm{c,data}}^{\mathrm{edge/screw}}(\boldsymbol{\epsilon}^{\mathrm{ext}} = \mathbf{0})$, and, further, $S_{\alpha\beta}^{\mathrm{edge/screw}} = \left.\frac{\partial E_{\mathrm{c,data}}^{\mathrm{edge/screw}}}{\partial \epsilon_{\alpha\beta}^{\mathrm{ext}}}\right|_{\boldsymbol{\epsilon}^{\mathrm{ext}}=\mathbf{0}}$. Thus, the values of $\mathbf{S}^{\mathrm{edge/screw}}$ are directly obtained from the RS-OFDFT calculations in this work for a screw dislocation in Section 3.2.2, and for an edge dislocation from Iyer et al. [56], Das et al. [57]. Although we lack the core energetics data for the shear strains causing the perfect edge or screw dislocations to glide, from symmetry, the slopes corresponding to these glide shear strains, S_{12}^{edge} and S_{23}^{screw}, should be zero. Table B.2 provides the data for $E_{\mathrm{c}}^{\mathrm{edge/screw}}(\boldsymbol{\epsilon}^{\mathrm{ext}} = \mathbf{0})$ and $\mathbf{S}^{\mathrm{edge/screw}}$. Table B.3 provides the corresponding non-elastic core energetics data, $E_{\mathrm{cnel}}^{\mathrm{edge/screw}}(\boldsymbol{\epsilon}^{\mathrm{ext}} = \mathbf{0})$ and $\hat{\mathbf{S}}^{\mathrm{edge/screw}}$, computed based on equation (B.4) using $a = 1|\mathbf{b}|$. We note that though the non-elastic core energy at

Table B.1: Material parameters of fcc Al computed using RS-OFDFT with Wang-Govind-Carter (WGC) kinetic energy functional [2], local density approximation (LDA) for the exchange-correlation energy [3], and Goodwin-Needs-Heine pseudopotential [4]. The isotropic elastics constants, μ and ν are computed from the fcc cubic elastic constants using Voigt average [5].

Cell relaxed lattice constant (Bohr)	7.63
Isotropic shear modulus, μ (GPa)	22
Isotropic Poisson's ratio, ν	0.35

Table B.2: Core energy of edge and screw dislocations in Al, and their slopes with respect to external strains at zero strain, directly obtained from RS-OFDFT calculations. All values are in eV/Å.

Edge		Screw	
$E_{\mathrm{c}}^{\mathrm{edge}}(\boldsymbol{\epsilon}^{\mathrm{ext}} = \mathbf{0})$	0.401	$E_{\mathrm{c}}^{\mathrm{screw}}(\boldsymbol{\epsilon}^{\mathrm{ext}} = \mathbf{0})$	0.284
S_{11}^{edge}	-2.3	S_{11}^{screw}	-1.4
S_{22}^{edge}	-2.2	S_{22}^{screw}	-1.2
S_{33}^{edge}	-1.0	S_{33}^{screw}	-0.3
S_{13}^{edge}	0.0	S_{13}^{screw}	0.0
S_{23}^{edge}	-2.9[1]	S_{12}^{screw}	1.3[1]
S_{12}^{edge}	-	S_{23}^{screw}	-

zero strain has a small value, the values of the slopes are considerable. Furthermore, we note that the values of $\hat{\mathbf{S}}^{\mathrm{edge/screw}}$ and $\mathbf{S}^{\mathrm{edge/screw}}$ are equal, which follows from equation (B.4) as

$$\int_{\Omega_{\mathrm{c}}} \boldsymbol{\sigma}^{\mathrm{d}}(\mathbf{x}_{\mathrm{c}}, a)\, \mathrm{d}A = \mathbf{0}\,, \tag{B.5}$$

which in turn is readily observed from the anti-symmetries in the analytical expressions for the stress fields of the perfect edge and screw dislocations [126]. Finally, in Table B.4, we have also provided values of $\mathbf{S}^{\mathrm{edge/screw}}$ computed using atomistic calculations. Comparing with Table B.2, we observe that they vary widely based on the choice of the EAM potential, which underscores the need for electronic structure calculations to compute these quantities.

Table B.3: Non-elastic core energy of edge and screw dislocations in Al, and their slopes with respect to external strains at zero strain, obtained from the RS-OFDFT data by subtracting the non-singular elastic contribution with smearing parameter $a = 1|\mathbf{b}|$. All values are in eV/Å.

Edge		Screw	
$E^{\text{edge}}_{\text{cnel}}(\boldsymbol{\epsilon}^{\text{ext}} = \mathbf{0})$	0.046	$E^{\text{screw}}_{\text{cnel}}(\boldsymbol{\epsilon}^{\text{ext}} = \mathbf{0})$	0.024
$\hat{S}^{\text{edge}}_{11}$	-2.3	$\hat{S}^{\text{screw}}_{11}$	-1.4
$\hat{S}^{\text{edge}}_{22}$	-2.2	$\hat{S}^{\text{screw}}_{22}$	-1.2
$\hat{S}^{\text{edge}}_{33}$	-1.0	$\hat{S}^{\text{screw}}_{33}$	-0.3
$\hat{S}^{\text{edge}}_{13}$	0.0	$\hat{S}^{\text{screw}}_{13}$	0.0
$\hat{S}^{\text{edge}}_{23}$	-2.9	$\hat{S}^{\text{screw}}_{12}$	1.3
$\hat{S}^{\text{edge}}_{12}$	-	$\hat{S}^{\text{screw}}_{23}$	-

Table B.4: Slopes of core energy of edge and screw dislocations in Al with respect to external strains at zero strain, directly obtained from atomistic calculations using two different EAM potentials for Al. All values are in eV/Å.

Al99.eam.alloy [198]				Al-LEA.eam.alloy [199]			
Edge		Screw		Edge		Screw	
S^{edge}_{11}	0.0	S^{screw}_{11}	-0.9	S^{edge}_{11}	-4.5	S^{screw}_{11}	-7.7
S^{edge}_{22}	-3.0	S^{screw}_{22}	-1.6	S^{edge}_{22}	-4.4	S^{screw}_{22}	-3.9
S^{edge}_{33}	-1.8	S^{screw}_{33}	-2.0	S^{edge}_{33}	-2.1	S^{screw}_{33}	-0.6
S^{edge}_{13}	0.0	S^{screw}_{13}	0.0	S^{edge}_{13}	0.0	S^{screw}_{13}	0.0
S^{edge}_{23}	-1.5	S^{screw}_{12}	0.3	S^{edge}_{23}	-3.5	S^{screw}_{12}	6.2

---

[1] The values of $\hat{S}^{\text{screw}}_{12}$ and $\hat{S}^{\text{edge}}_{23}$ are obtained from the RS-OFDFT calculated core energy dependence on Escaig strains of screw dislocation (cf. Section 3.2.2) and edge dislocation [56, 57], respectively. The non-zero values of the slopes are due to the change in the Shockley partial separation distance in response to the Escaig strains. However, as the details of the partials are absent in the mesoscale model used for the case studies in Section 4.2, we do not include these contributions there.

APPENDIX C

Derivation of Nodal Core Forces for Dislocations Dissociated Into Partials

Here, we briefly discuss on extending the derivation of the nodal core forces for a network of perfect dislocations presented in Section 4.1.2 to the case where the perfect dislocation lines are dissociated into partials. Consideration of partials is crucial to correctly study various elementary mechanisms which govern plasticity and hardening in fcc materials, for e.g. , dislocation junction formation and cross-slip mechanisms (cf. [15, 135]). We consider the DDD framework developed by [15] which accounts for partials and stacking faults in fcc crystals, and briefly discuss incorporating the core-energetics information into such a framework. Their methodology considers the dissociated partials as independent segments, and introduce a new degree of freedom, $\gamma\mathbf{n}^{ij}$ to each partial segment $\mathbf{l}^{ij}$, where γ is the stacking fault energy per unit area, and $\mathbf{n}^{ij}$ is the unit normal to the slip plane on which the partials are dissociated. The force at any point on the segment corresponding to perturbations in the stacking fault energy is expressed as

$$f^{ij}_{\mathrm{sf},p} = \gamma\varepsilon_{pqk}\xi_q n^{ij}_k\,, \tag{C.1}$$

where the direction of $\mathbf{n}^{ij}$ is chosen such that the above force always points towards the other partial, or in other words it is attractive. The attractive force is balanced by the elastic repulsion between the partials and other external elastic forces, such as those resulting from Escaig stresses, producing the equilibrium stacking fault width. We refer to [15] for more details on topological considerations and conservation rules related to the consideration of partials. Focussing on the core energetics, similar to equation (B.4), we remove the non-singular elastic energy due to the Shockley partials and additionally the already accounted stacking fault energy effects from $E_{\mathrm{c}}^{\mathrm{edge/screw}}(\boldsymbol{\epsilon}^{\mathrm{ext}} = \mathbf{0})$ and $S_{\alpha\beta}^{\mathrm{edge/screw}}$, to obtain the non-elastic core energy and its slopes, denoted as $\check{E}_{\mathrm{cnel}}^{\mathrm{edge/screw}}(\boldsymbol{\epsilon}^{\mathrm{ext}} = \mathbf{0}; a)$ and $\check{S}_{\alpha\beta}^{\mathrm{edge/screw}}(a)$, respectively. Further, as the partials are treated as independent segments, it is convenient to assume the non-elastic core energy of each partial to be half of the full dislocation non-elastic core energy,

$$\check{E}_{\mathrm{cnel}}^{\mathrm{edge_p/screw_p}}(\boldsymbol{\epsilon}^{\mathrm{ext}}; a) = \frac{1}{2}\left(\check{E}_{\mathrm{cnel}}^{\mathrm{edge/screw}}(\boldsymbol{\epsilon}^{\mathrm{ext}} = \mathbf{0}; a) + \check{S}_{\alpha\beta}^{\mathrm{edge/screw}}(a)\epsilon_{\alpha\beta}^{\mathrm{ext}}\right) , \tag{C.2}$$

where $\check{E}_{\mathrm{cnel}}^{\mathrm{edge_p/screw_p}}(\boldsymbol{\epsilon}^{\mathrm{ext}}; a)$ is the non-elastic core energy of the edge or screw partial per unit length of dislocation line, and $\boldsymbol{\epsilon}^{\mathrm{ext}}$ is the external strain field experienced by the partial excluding the strain field contribution from the other partial in the pair. To exclude the other partial, the external strain field cutoff procedure developed for the perfect dislocation network in equation (4.20) can be modified as follows,

$$\boldsymbol{\epsilon}^{\mathrm{ext_{loc}}}(\mathbf{x}^{ij}(s_{ij})) = \sum_{kl\,\in\,U''_{ij}} \boldsymbol{\epsilon}^{kl_{\mathrm{loc}}}(\boldsymbol{\xi}^{kl}, \mathbf{b}^{kl}, \mathbf{x}^{ij}(s_{ij})) \, , \tag{C.3}$$

where the set U''_{ij} includes all distinct segments in the network excepting the ones which have one of their nodes as i or j and their respective Shockley partials. Rest of the analysis for derivation of the core forces follows along similar lines as the case of the perfect dislocation presented in Section 4.1.2.

BIBLIOGRAPHY

BIBLIOGRAPHY

[1] Linda Hung, Chen Huang, Ilgyou Shin, Gregory S. Ho, Vincent L. Lignres, and Emily A. Carter. Introducing PROFESS 2.0: a parallelized, fully linear scaling program for orbital-free density functional theory calculations. *Comput. Phys. Commun.*, 181(12):2208–2209, 2010.

[2] Yan Alexander Wang, Niranjan Govind, and Emily A. Carter. Orbital-free kinetic-energy density functionals with a density-dependent kernel. *Phys. Rev. B*, 60:16350–16358, Dec 1999.

[3] J. P. Perdew and Alex Zunger. Self-interaction correction to density-functional approximations for many-electron systems. *Phys. Rev. B*, 23:5048–5079, May 1981.

[4] L Goodwin, R J Needs, and V Heine. A pseudopotential total energy study of impurity-promoted intergranular embrittlement. *J. Phys.: Condens. Matter*, 2 (2):351, 1990.

[5] John P Hirth and Jens Lothe. *Theory of Dislocations*. John Wiley\ & Sons, 1982.

[6] A. S. Argon. *Strengthening Mechanisms in Crystal Plasticity*. Oxford University Press, Oxford, 2008.

[7] Robert E Reed-Hill and Reza Abbaschian. *Physical Metallurgy Principles*. Brooks/Cole Engineering Division Monterey, Calif, USA, 1973.

[8] Richard LeSar. Simulations of dislocation structure and response. *Annu. Rev. of Condens. Matter Phys.*, 5(1):375–407, 2014.

[9] Ladislas Kubin. *Dislocations, Mesoscale Simulations and Plastic Flow*. Oxford University Press, Oxford, 2013.

[10] Athanasios Arsenlis and David M. Parks. Modeling the evolution of crystallographic dislocation density in crystal plasticity. *J. Mech. Phys. Solids*, 50(9): 1979–2009, 2002.

[11] A Arsenlis, W Cai, M Tang, M Rhee, T Oppelstrup, G Hommes, T G Pierce, and V V Bulatov. Enabling strain hardening simulations with dislocation dynamics. *Model. Simul. Mater. Sci. Eng.*, 15(6):553, 2007.

[12] S. Aubry, M. Rhee, G. Hommes, V. V Bulatov, and A. Arsenlis. Dislocation dynamics in hexagonal close-packed crystals. *J. Mech. Phys. Solids*, 94:105–126, 2016.

[13] V. V. Bulatov, Wei Cai, Jeff Fier, Masato Hiratani, Gregg Hommes, Tim Pierce, Meijie Tang, Moono Rhee, Kim Yates, and Tom Arsenlis. Scalable line dynamics in ParaDiS. In *Proceedings of the 2004 ACM/IEEE Conference on Supercomputing*, SC '04, page 19, Washington, DC, USA, 2004. IEEE Computer Society. ISBN 0-7695-2153-3.

[14] Ladislas P. Kubin, G. Canova, M. Condat, Benoit Devincre, V. Pontikis, and Y. Bréchet. Dislocation microstructures and plastic flow: A 3D simulation. *Solid State Phenomen.*, 23–24:455–472, 1 1992.

[15] E. Martínez, J. Marian, A. Arsenlis, M. Victoria, and J. M. Perlado. Atomistically informed dislocation dynamics in fcc crystals. *J. Mech. Phys. Solids*, 56 (3):869–895, 2008.

[16] Lucia Nicola, Erik Van der Giessen, and Alan Needleman. Discrete dislocation analysis of size effects in thin films. *J. Appl. Phys.*, 93(10):5920–5928, 2003.

[17] Giacomo Po, Markus Lazar, Dariush Seif, and Nasr Ghoniem. Singularity-free dislocation dynamics with strain gradient elasticity. *J. Mech. Phys. Solids*, 68: 161–178, 2014.

[18] K. W. Schwarz. Simulation of dislocations on the mesoscopic scale. I. methods and examples. *J. Appl. Phys.*, 85(1):108–119, 1999.

[19] Hussein M. Zbib, Moono Rhee, and John P. Hirth. On plastic deformation and the dynamics of 3D dislocations. *Int. J. Mech. Sci.*, 40(2):113–127, 1998.

[20] I. J. Beyerlein and A. Hunter. Understanding dislocation mechanics at the mesoscale using phase field dislocation dynamics. *Philos. Trans. R. Soc. A*, 374 (2066):20150166, 2016.

[21] A. Hunter, R. F. Zhang, and I. J. Beyerlein. The core structure of dislocations and their relationship to the material γ-surface. *J. Appl. Phys.*, 115(13):134314, 2014.

[22] M. Koslowski, A. M. Cuitiño, and M. Ortiz. A phase-field theory of dislocation dynamics, strain hardening and hysteresis in ductile single crystals. *J. Mech. Phys. Solids*, 50(12):2597–2635, 2002.

[23] Dong Wook Lee, Hojin Kim, Alejandro Strachan, and Marisol Koslowski. Effect of core energy on mobility in a continuum dislocation model. *Phys. Rev. B*, 83: 104101, Mar 2011.

[24] Jaber Rezaei Mianroodi and Bob Svendsen. Atomistically determined phase-field modeling of dislocation dissociation, stacking fault formation, dislocation slip, and reactions in fcc systems. *J. Mech. Phys. Solids*, 77:109–122, 2015.

[25] Y. U. Wang, Y. M. Jin, A. M. Cuitiño, and A. G. Khachaturyan. Phase field microelasticity theory and modeling of multiple dislocation dynamics. *Appl. Phys. Lett.*, 78(16):2324–2326, 2001.

[26] Amit Acharya. A model of crystal plasticity based on the theory of continuously distributed dislocations. *J. Mech. Phys. Solids*, 49(4):761–784, 2001.

[27] A. K. Head, S. D. Howison, J. R. Ockendon, and S. P. Tighe. An equilibrium theory of dislocation continua. *SIAM Rev.*, 35(4):580–609, 1993.

[28] Ekkehart Kröner et al. Continuum theory of defects. *Phys. defects*, 35:217–315, 1981.

[29] T. Mura. Continuous distribution of moving dislocations. *Philos. Mag.*, 8(89): 843–857, 1963.

[30] A. Needleman and E. Van der Giessen. Discrete dislocation and continuum descriptions of plastic flow. *Mater. Sci. Eng.: A*, 309–310:1–13, 2001. Dislocations 2000: An International Conference on the Fundamentals of Plastic Deformation.

[31] Z. Wang, S. Rudraraju, and K. Garikipati. A three dimensional field formulation, and isogeometric solutions to point and line defects using Toupin's theory of gradient elasticity at finite strains. *J. Mech. Phys. Solids*, 94:336–361, 2016.

[32] M. Yu. Gutkin and E. C. Aifantis. Dislocations in the theory of gradient elasticity. *Scripta Mater.*, 40(5):559–566, 1999.

[33] Markus Lazar. The fundamentals of non-singular dislocations in the theory of gradient elasticity: Dislocation loops and straight dislocations. *Int. J. Solids Struct.*, 50(2):352–362, 2013.

[34] Markus Lazar. On gradient field theories: gradient magnetostatics and gradient elasticity. *Philos. Mag.*, 94(25):2840–2874, 2014.

[35] J. R. Willis. Second-order effects of dislocations in anisotropic crystals. *Int. J. Eng. Sci.*, 5(2):171–190, 1967.

[36] William A. Curtin, David L. Olmsted, and Louis G. Hector Jr. A predictive mechanism for dynamic strain ageing in aluminium–magnesium alloys. *Nat. mater.*, 5(11):875–880, 2006.

[37] J. Marian and A. Caro. Moving dislocations in disordered alloys: connecting continuum and discrete models with atomistic simulations. *Phys. Rev. B*, 74: 024113, Jul 2006.

[38] J R Morris, K M Ho, K Y Chen, G Rengarajan, and M H Yoo. Large-scale atomistic study of core structures and energetics of $< \mathrm{c+a} >\{11\bar{2}2\}$ dislocations in hexagonal close packed metals. *Model. Simul. Mater. Sci. Eng.*, 8(1):25, 2000.

[39] David L Olmsted, Louis G Hector Jr., W A Curtin, and R J Clifton. Atomistic simulations of dislocation mobility in Al, Ni and Al/Mg alloys. *Model. Simul. Mater. Sci. Eng.*, 13(3):371, 2005.

[40] David L. Olmsted, Louis G. Hector Jr., and W. A. Curtin. Molecular dynamics study of solute strengthening in Al/Mg alloys. *J. Mech. Phys. Solids*, 54(8): 1763–1788, 2006.

[41] S. G. Srinivasan, X. Z. Liao, M. I. Baskes, R. J. McCabe, Y. H. Zhao, and Y. T. Zhu. Compact and dissociated dislocations in aluminum: implications for deformation. *Phys. Rev. Lett.*, 94:125502, Mar 2005.

[42] Zhaoxuan Wu and W. A. Curtin. The origins of high hardening and low ductility in magnesium. *Nat.*, 526(7571):62–67, 2015.

[43] M. Ghazisaeidi, Louis G. Hector Jr., and W. A. Curtin. First-principles core structures of $< \mathrm{c} + \mathrm{a} >$ edge and screw dislocations in Mg. *Scripta Mater.*, 75: 42–45, 2014.

[44] Ilgyou Shin, Ashwin Ramasubramaniam, Chen Huang, Linda Hung, and Emily A. Carter. Orbital-free density functional theory simulations of dislocations in aluminum. *Philos. Mag.*, 89(34–36):3195–3213, 2009.

[45] Ilgyou Shin and Emily A Carter. Orbital-free density functional theory simulations of dislocations in magnesium. *Model. Simul. Mater. Sci. Eng.*, 20(1): 015006, 2012.

[46] Ilgyou Shin and Emily A. Carter. Possible origin of the discrepancy in Peierls stresses of fcc metals: first-principles simulations of dislocation mobility in aluminum. *Phys. Rev. B*, 88:064106, Aug 2013.

[47] C. Woodward, D. R. Trinkle, L. G. Hector, and D. L. Olmsted. Prediction of dislocation cores in aluminum from density functional theory. *Phys. Rev. Lett.*, 100:045507, Jan 2008.

[48] Christopher R. Weinberger, Garritt J. Tucker, and Stephen M. Foiles. Peierls potential of screw dislocations in bcc transition metals: predictions from density functional theory. *Phys. Rev. B*, 87:054114, Feb 2013.

[49] S. K. Yadav, R. Ramprasad, A. Misra, and X.-Y. Liu. Core structure and Peierls stress of edge and screw dislocations in TiN: a density functional theory study. *Acta Mater.*, 74:268–277, 2014.

[50] Dallas R. Trinkle and Christopher Woodward. The chemistry of deformation: how solutes soften pure metals. *Sci.*, 310(5754):1665–1667, 2005.

[51] Joseph A. Yasi, Louis G. Hector Jr., and Dallas R. Trinkle. First-principles data for solid-solution strengthening of magnesium: from geometry and chemistry to properties. *Acta Mater.*, 58(17):5704–5713, 2010.

[52] Sambit Das, Mrinal Iyer, and Vikram Gavini. Real-space formulation of orbital-free density functional theory using finite-element discretization: The case for Al, Mg, and Al-Mg intermetallics. *Phys. Rev. B*, 92:014104, Jul 2015.

[53] Vikram Gavini, Jaroslaw Knap, Kaushik Bhattacharya, and Michael Ortiz. Non-periodic finite-element formulation of orbital-free density functional theory. *J. Mech. Phys. Solids*, 55(4):669 – 696, 2007.

[54] Balachandran Radhakrishnan and Vikram Gavini. Effect of cell size on the energetics of vacancies in aluminum studied via orbital-free density functional theory. *Phys. Rev. B*, 82:094117, Sep 2010.

[55] Sambit Das and Vikram Gavini. Electronic structure study of screw dislocation core energetics in Aluminum and core energetics informed forces in a dislocation aggregate. *J. Mech. Phys. Solids*, 104:115–143, 2017.

[56] Mrinal Iyer, Balachandran Radhakrishnan, and Vikram Gavini. Electronic-structure study of an edge dislocation in Aluminum and the role of macroscopic deformations on its energetics. *J. Mech. Phys. Solids*, 76:260–275, 2015.

[57] Sambit Das, Mrinal Iyer, Balachandran Radhakrishnan, and Vikram Gavini. Corrigendum to "Electronic-structure study of an edge dislocation in Aluminum and the role of macroscopic deformations on its energetics" [Journal of the Mechanics and Physics of Solids 76 (2015) 260–275] . *J. Mech. Phys. Solids*, 95: 428–429, 2016.

[58] Yue Qi and Raja K. Mishra. *Ab initio* study of the effect of solute atoms on the stacking fault energy in aluminum. *Phys. Rev. B*, 75:224105, Jun 2007.

[59] T Tsuru and D. C. Chrzan. Effect of solute atoms on dislocation motion in Mg: an electronic structure perspective. *Sci. Rep.*, 5, 2015.

[60] Zhaoxuan Wu, Rasool Ahmad, Binglun Yin, Stefanie Sandlöbes, and W. A. Curtin. Mechanistic origin and prediction of enhanced ductility in magnesium alloys. *Sci.*, 359(6374):447–452, 2018.

[61] P. Motamarri, M. Nowak, K. Leiter, J. Knap, and V. Gavini. Higher-order adaptive finite-element methods for Kohn-Sham density functional theory. *J. Comput. Phys.*, 253:308–343, 2013.

[62] P. Motamarri and V. Gavini. Configurational forces in electronic structure calculations using Kohn-Sham density functional theory. *Phys. Rev. B.*, 97: 165132, 2018.

[63] Phani Motamarri, Sambit Das, Shiva Rudraraju, Krishnendu Ghosh, Denis Davydov, and Vikram Gavini. DFT-FE–a massively parallel adaptive finite-element code for large-scale density functional theory calculations. *accepted in Comput. Phys. Commun.*, 2019.

[64] S. Das, Motamarri P., Gavini V., B. Turcksin, Y. W. Li, and B. Leback. Fast, scalable and accurate finite-element based ab initio calculations using mixed precision computing: 46 pflops simulation of a metallic dislocation system. *accepted in Proceedings of the International Conference for High Performance Computing, Networking, Storage and Analysis*, 2019.

[65] R. M. Martin. *Electronic structure: Basic Theory and Practical Methods*. Cambridge University Press, Cambridge, 2008.

[66] P. Hohenberg and W. Kohn. Inhomogeneous electron gas. *Phys. Rev.*, 136: B864–B871, Nov 1964.

[67] W. Kohn and L. J. Sham. Self-consistent equations including exchange and correlation effects. *Phys. Rev.*, 140(4A):A1133, 1965.

[68] Stefan Goedecker. Linear scaling electronic structure methods. *Rev. Mod. Phys.*, 71:1085–1123, Jul 1999.

[69] D R Bowler and T Miyazaki. $\mathcal{O}(N)$ methods in electronic structure calculations. *Rep. Prog. Phys.*, 75(3):036503, 2012.

[70] Phani Motamarri and Vikram Gavini. Subquadratic-scaling subspace projection method for large-scale Kohn-Sham density functional theory calculations using spectral finite-element discretization. *Phys. Rev. B*, 90:115127, Jan 2014.

[71] R. G. Parr and W. Yang. *Density-Functional Theory of Atoms and Molecules*. Oxford University Press, Oxford, 1994.

[72] Lin-Wang Wang and Michael P. Teter. Kinetic-energy functional of the electron density. *Phys. Rev. B*, 45:13196–13220, Jun 1992.

[73] Enrico Smargiassi and Paul A. Madden. Orbital-free kinetic-energy functionals for first-principles molecular dynamics. *Phys. Rev. B*, 49:5220–5226, Feb 1994.

[74] Yan Alexander Wang, Niranjan Govind, and Emily A. Carter. Orbital-free kinetic-energy functionals for the nearly free electron gas. *Phys. Rev. B*, 58: 13465–13471, Nov 1998.

[75] Valentin V. Karasiev, Travis Sjostrom, and S. B. Trickey. Generalized-gradient-approximation noninteracting free-energy functionals for orbital-free density functional calculations. *Phys. Rev. B*, 86:115101, Sep 2012.

[76] Youqi Ke, Florian Libisch, Junchao Xia, Lin-Wang Wang, and Emily A. Carter. Angular-momentum-dependent orbital-free density functional theory. *Phys. Rev. Lett.*, 111:066402, Aug 2013.

[77] VV Karasiev, D Chakraborty, and SB Trickey. Many-electron approaches in physics, chemistry and mathematics, 2014.

[78] Youqi Ke, Florian Libisch, Junchao Xia, and Emily A. Carter. Angular momentum dependent orbital-free density functional theory: Formulation and implementation. *Phys. Rev. B*, 89:155112, Apr 2014.

[79] Flavien Lambert, Jean Clérouin, and Gilles Zérah. Very-high-temperature molecular dynamics. *Phys. Rev. E*, 73:016403, Jan 2006.

[80] F. Lambert, J. Clérouin, J.-F. Danel, L. Kazandjian, and G. Zérah. Direct verification of mixing rules in the hot and dense regime. *Phys. Rev. E*, 77: 026402, Feb 2008.

[81] D. A. Horner, F. Lambert, J. D. Kress, and L. A. Collins. Transport properties of lithium hydride from quantum molecular dynamics and orbital-free molecular dynamics. *Phys. Rev. B*, 80:024305, Jul 2009.

[82] L. Burakovsky, C. Ticknor, J. D. Kress, L. A. Collins, and F. Lambert. Transport properties of lithium hydride at extreme conditions from orbital-free molecular dynamics. *Phys. Rev. E*, 87:023104, Feb 2013.

[83] Daniel Sheppard, Joel D. Kress, Scott Crockett, Lee A. Collins, and Michael P. Desjarlais. Combining kohn-sham and orbital-free density-functional theory for hugoniot calculations to extreme pressures. *Phys. Rev. E*, 90:063314, Dec 2014.

[84] Gregory Ho, Mitchell T. Ong, Kyle J. Caspersen, and Emily A. Carter. Energetics and kinetics of vacancy diffusion and aggregation in shocked aluminium *via* orbital-free density functional theory. *Phys. Chem. Chem. Phys.*, 9:4951–4966, 2007.

[85] Qing Peng, Xu Zhang, Linda Hung, Emily A. Carter, and Gang Lu. Quantum simulation of materials at micron scales and beyond. *Phys. Rev. B*, 78:054118, Aug 2008.

[86] Mohan Chen, Junchao Xia, Chen Huang, Johannes M. Dieterich, Linda Hung, Ilgyou Shin, and Emily A. Carter. Introducing profess 3.0: An advanced program for orbital-free density functional theory molecular dynamics simulations. *Comput. Phys. Commun.*, 190:228–230, 2015.

[87] Vikram Gavini, Jaroslaw Knap, Kaushik Bhattacharya, and Michael Ortiz. Non-periodic finite-element formulation of orbital free density functional theory. *J. Mech. Phys. Solids*, 55:669–696, 2007.

[88] Phani Motamarri, Mrinal Iyer, Jaroslaw Knap, and Vikram Gavini. Higher-order adaptive finite-element methods for orbital-free density functional theory. *J. Comput. Phys.*, 231(20):6596–6621, 2012.

[89] C. J. Garćia-Cervera. An efficient real space method for orbital-free density-functional theory. *Commun. Comput. Phys.*, 2(2):334–357, 2007.

[90] Phanish Suryanarayana and Deepa Phanish. Augmented Lagrangian formulation of orbital-free density functional theory. *J. Comput. Phys.*, 275:524–538, 2014.

[91] Swarnava Ghosh and Phanish Suryanarayana. Higher-order finite-difference formulation of periodic orbital-free density functional theory. *J. Comput. Phys.*, 307:634–652, 2016.

[92] D. M. Ceperley and B. J. Alder. Ground state of the electron gas by a stochastic method. *Phys. Rev. Lett.*, 45:566–569, Aug 1980.

[93] D. C. Langreth and M. J. Mehl. Beyond the local-density approximation in calculations of ground-state electronic properties. *Phys. Rev. B*, 28:1809–1834, 1983.

[94] Chen Huang and Emily A. Carter. Transferable local pseudopotentials for magnesium, aluminum and silicon. *Phys. Chem. Chem. Phys.*, 10:7109–7120, 2008.

[95] Junchao Xia and Emily A. Carter. Density-decomposed orbital-free density functional theory for covalently bonded molecules and materials. *Phys. Rev. B*, 86:235109, Dec 2012.

[96] Chen Huang and Emily A. Carter. Toward an orbital-free density functional theory of transition metals based on an electron density decomposition. *Phys. Rev. B*, 85:045126, Jan 2012.

[97] M. Finnis. *Interatomic Forces in Condensed Matter.* Oxford University Press, Oxford, 2003.

[98] N. Choly and E. Kaxiras. Kinetic energy density functionals for non-periodic systems. *Solid State Comm.*, 121:281–286, 2002.

[99] Vikram Gavini, Kaushik Bhattacharya, and Michael Ortiz. Quasi-continuum orbital-free density-functional theory: a route to multi-million atom non-periodic DFT calculation. *J. Mech. Phys. Solids*, 55(4):697 – 718, 2007.

[100] S. C. Brenner and L. R. Scott. *The Mathematical Theory of Finite-element Methods.* Springer, New York, 2002.

[101] D. G. Anderson. Iterative procedures for nonlinear integral equations. *J. Assoc. Comput. Mach.*, 12(4):547–560, 1965.

[102] S. Balay, J. Brown, K. Buschelman, V. Eijkhout, W. D. Gropp, D. Kaushik, M. G. Knepley, L. C. McInnes, B. F. Smith, and H. Zhang. Petsc users manual. 2013.

[103] Y. Saad and M. Schultz. Gmres: A generalized minimal residual algorithm for solving nonsymmetric linear systems. *SIAM J. Sci. Stat. Comput.*, 7(3): 856–869, 1986.

[104] Xavier Gonze, J-M Beuken, R Caracas, F Detraux, M Fuchs, G-M Rignanese, Luc Sindic, Matthieu Verstraete, G Zerah, F Jollet, et al. First-principles computation of material properties: the ABINIT software project. *Comput. Mater. Sci.*, 25(3):478–492, 2002.

[105] N. Troullier and José Luís Martins. Efficient pseudopotentials for plane-wave calculations. *Phys. Rev. B*, 43:1993–2006, Jan 1991.

[106] Martin Fuchs and Matthias Scheffler. Ab initio pseudopotentials for electronic structure calculations of poly-atomic systems using density-functional theory. *Comput. Phys. Commun.*, 119(1):67 – 98, 1999.

[107] N. Chetty, M. Weinert, T. S. Rahman, and J. W. Davenport. Vacancies and impurities in aluminum and magnesium. *Phys. Rev. B*, 52:6313–6326, Sep 1995.

[108] M J Gillan. Calculation of the vacancy formation energy in aluminium. *J. Phys.: Condens. Matter*, 1(4):689–711, jan 1989.

[109] Mrinal Iyer and Vikram Gavini. A field theoretical approach to the quasi-continuum method. *J. Mech. Phys. Solids*, 59(8):1506 – 1535, 2011.

[110] S. Banerjee, N. Ghoniem, G. Lu, and N. Kioussis. Non-singular descriptions of dislocation cores: a hybrid *ab initio* continuum approach. *Philos. Mag.*, 87(27): 4131–4150, 2007.

[111] R Peierls. The size of a dislocation. *Proc. Phys. Soc.*, 52(1):34–37, 1940.

[112] Vikram Gavini, Kaushik Bhattacharya, and Michael Ortiz. Vacancy clustering and prismatic dislocation loop formation in aluminum. *Phys. Rev. B*, 76:180101, 2007.

[113] Balachandran Radhakrishnan and Vikram Gavini. Orbital-free density functional theory study of the energetics of vacancy clustering and prismatic dislocation loop nucleation in aluminium. *Phil. Mag.*, 96(23):2468–2487, 2016.

[114] V. Vítek, R. C. Perrin, and D. K. Bowen. The core structure of $\frac{1}{2}\langle 111\rangle$ screw dislocations in b.c.c. crystals. *Philos. Mag.*, 21(173):1049–1073, 1970.

[115] Vikram Gavini. Role of macroscopic deformations in energetics of vacancies in aluminum. *Phys. Rev. Lett.*, 101:205503, Nov 2008.

[116] Vikram Gavini. Role of the defect core in energetics of vacancies. *Proc. Roy. Soc. Lond A*, 465(2110):3239–3266, 2009.

[117] Mrinal Iyer, Vikram Gavini, and Tresa M. Pollock. Energetics and nucleation of point defects in aluminum under extreme tensile hydrostatic stresses. *Phys. Rev. B*, 89:014108, Jan 2014.

[118] L. Pizzagalli, J.-L. Demenet, and J. Rabier. Theoretical study of pressure effect on the dislocation core properties in semiconductors. *Phys. Rev. B*, 79:045203, Jan 2009.

[119] Ilgyou Shin and Emily A. Carter. Simulations of dislocation mobility in magnesium from first principles. *Int. J. Plast.*, 60:58 – 70, 2014.

[120] J A Yasi, T Nogaret, D R Trinkle, Y Qi, Louis G. Hector Jr., and W A Curtin. Basal and prism dislocation cores in magnesium: comparison of first-principles and embedded-atom-potential methods predictions. *Model. Simul. Mater. Sci. Eng.*, 17(5):055012, 2009.

[121] M P Dewald and W A Curtin. Multiscale modelling of dislocation/grain-boundary interactions: I. edge dislocations impinging on $\sum$11 (113) tilt boundary in Al. *Model. Simul. Mater. Sci. Eng.*, 15(1):S193, 2007.

[122] M Dewald and W A Curtin. Multiscale modeling of dislocation/grain-boundary interactions: III. 60° dislocations impinging on $\sum 3$, $\sum 9$ and $\sum 11$ tilt boundaries in Al. *Model. Simul. Mater. Sci. Eng.*, 19(5):055002, 2011.

[123] M de Koning, R. J Kurtz, V. V Bulatov, C. H Henager, R. G Hoagland, W Cai, and M Nomura. Modeling of dislocation-grain boundary interactions in FCC metals. *J. Nucl. Mater.*, 323(2–3):281–289, 2003. Proceedings of the Second IEA Fusion Materials Agreement Workshop on Modeling and Experimental Validation.

[124] C. S. Shin, M. C. Fivel, M. Verdier, and K. H. Oh. Dislocation-impenetrable precipitate interaction: a three-dimensional discrete dislocation dynamics analysis. *Philos. Mag.*, 83(31–34):3691–3704, 2003.

[125] S Soleymani Shishvan, S Mohammadi, and M Rahimian. A dislocation-dynamics-based derivation of the Frank-Read source characteristics for discrete dislocation plasticity. *Model. Simul. Mater. Sci. Eng.*, 16(7):075002, 2008.

[126] Wei Cai, Athanasios Arsenlis, Christopher R. Weinberger, and Vasily V. Bulatov. A non-singular continuum theory of dislocations. *J. Mech. Phys. Solids*, 54(3):561–587, 2006.

[127] R. de Wit. The self-energy of dislocation configurations made up of straight segments. *phys. stat. sol. (b)*, 20(2):575–580, 1967.

[128] L. M. Brown. The self-stress of dislocations and the shape of extended nodes. *Philos. Mag.*, 10(105):441–466, 1964.

[129] S. D. Gavazza and D. M. Barnett. The self-force on a planar dislocation loop in an anisotropic linear-elastic medium. *J. Mech. Phys. Solids*, 24(4):171–185, 1976.

[130] V. L. Indenbom and J Lothe. *Elastic Strain Fields and Dislocation Mobility.* North-Holland, Amsterdam, 1992.

[131] T. Mura. *Micromechanics of Defects in Solids.* Kluwer, Dordrecht, 1982.

[132] W. T. Read and W. Shockley. Dislocation models of crystal grain boundaries. *Phys. Rev.*, 78:275–289, May 1950.

[133] Wei Cai, Jie Deng, and Keonwook Kang. A short course on ddlab and paradis. 2005.

[134] F. C. Frank and W. T. Read. Multiplication processes for slow moving dislocations. *Phys. Rev.*, 79:722–723, Aug 1950.

[135] V. B. Shenoy, R. V. Kukta, and R. Phillips. Mesoscopic analysis of structure and strength of dislocation junctions in fcc metals. *Phys. Rev. Lett.*, 84:1491–1494, Feb 2000.

[136] Vasily V Bulatov, Luke L Hsiung, Meijie Tang, Athanasios Arsenlis, Maria C Bartelt, Wei Cai, Jeff N Florando, Masato Hiratani, Moon Rhee, Gregg Hommes, et al. Dislocation multi-junctions and strain hardening. *Nat.*, 440 (7088):1174, 2006.

[137] Paolo Giannozzi, Stefano Baroni, Nicola Bonini, Matteo Calandra, Roberto Car, Carlo Cavazzoni, Davide Ceresoli, Guido L Chiarotti, Matteo Cococcioni, Ismaila Dabo, Andrea Dal Corso, Stefano de Gironcoli, Stefano Fabris, Guido Fratesi, Ralph Gebauer, Uwe Gerstmann, Christos Gougoussis, Anton Kokalj, Michele Lazzeri, Layla Martin-Samos, Nicola Marzari, Francesco Mauri, Riccardo Mazzarello, Stefano Paolini, Alfredo Pasquarello, Lorenzo Paulatto, Carlo Sbraccia, Sandro Scandolo, Gabriele Sclauzero, Ari P Seitsonen, Alexander Smogunov, Paolo Umari, and Renata M Wentzcovitch. QUANTUM ESPRESSO: a modular and open-source software project for quantum simulations of materials. *J. Phys. Condens. Matter*, 21(39):395502, 2009.

[138] G. Kresse and J. Furthmüller. Efficient iterative schemes for ab initio total-energy calculations using a plane-wave basis set. *Phys. Rev. B*, 54(16):11169–11186, 1996.

[139] Andris Gulans, Stefan Kontur, Christian Meisenbichler, Dmitrii Nabok, Pasquale Pavone, Santiago Rigamonti, Stephan Sagmeister, Ute Werner, and Claudia Draxl. exciting: a full-potential all-electron package implementing density-functional theory and many-body perturbation theory. *J. Phys.: Condens. Matter*, 26(36):363202, aug 2014.

[140] W. J. Hehre, R. F. Stewart, and J. A. Pople. Self-consistent molecular-orbital methods. i. Use of Gaussian expansions of Slater-type atomic orbitals. *J. Chem. Phys.*, 51(6):2657–2664, 1969.

[141] F. Jensen. Polarization consistent basis sets. ii. estimating the Kohn–Sham basis set limit. *J. Chem. Phys.*, 116(17):7372–7379, 2002.

[142] Jrg Hutter, Marcella Iannuzzi, Florian Schiffmann, and Joost VandeVondele. cp2k: atomistic simulations of condensed matter systems. *Wiley Interdiscip. Rev.: Comput. Mol. Sci.*, 4, 2014.

[143] Volker Blum, Ralf Gehrke, Felix Hanke, Paula Havu, Ville Havu, Xinguo Ren, Karsten Reuter, and Matthias Scheffler. Ab initio molecular simulations with numeric atom-centered orbitals. *Comput. Phys. Commun.*, 180(11):2175–2196, 2009.

[144] M. Valiev, E.J. Bylaska, N. Govind, K. Kowalski, T.P. Straatsma, H.J.J. Van Dam, D. Wang, J. Nieplocha, E. Apra, T.L. Windus, and W.A. de Jong. Nwchem: A comprehensive and scalable open-source solution for large scale molecular simulations. *Comput. Phys. Commun.*, 181(9):1477–1489, 2010.

[145] Eiji Tsuchida and Masaru Tsukada. Electronic-structure calculations based on the finite-element method. *Phys. Rev. B*, 52:5573–5578, 1995.

[146] Eiji Tsuchida and Masaru Tsukada. Adaptive finite-element method for electronic-structure calculations. *Phys. Rev. B*, 54:7602–7605, Sep 1996.

[147] Eiji Tsuchida and Masaru Tsukada. Large-scale electronic-structure calculations based on the adaptive finite-element method. *J. Phys. Soc. Jpn.*, 67(11): 3844–3858, 1998.

[148] J. E. Pask, B. M. Klein, C. Y. Fong, and P. A. Sterne. Real-space local polynomial basis for solid-state electronic-structure calculations: A finite-element approach. *Phys. Rev. B*, 59:12352–12358, 1999.

[149] J E Pask and P A Sterne. Finite element methods in ab initio electronic structure calculations. *Modell. Simul. Mater. Sci. Eng.*, 13(3):R71, 2005.

[150] N. Sukumar and J. E. Pask. Classical and enriched finite element formulations for bloch-periodic boundary conditions. *Int. J. Numer. Methods Eng.*, 77(8): 1121–1138, 2009.

[151] P. Suryanarayana, V. Gavini, T. Blesgen, K. Bhattacharya, and M. Ortiz. Non-periodic finite-element formulation of Kohn–Sham density functional theory. *J. Mech. Phys. Solids*, 58:256–280, 2010.

[152] Huajie Chen, Lianhua He, and Aihui Zhou. Finite element approximations of nonlinear eigenvalue problems in quantum physics. *Comput. Methods in Appl. Mech. Eng.*, 200(21):1846–1865, 2011.

[153] Volker Schauer and Christian Linder. All-electron Kohn–Sham density functional theory on hierarchic finite element spaces. *J. Comput. Phys.*, 250:644–664, 2013.

[154] H. Chen, X. Dai, X. Gong, L. He, and A. Zhou. Adaptive finite element approximations for Kohn–Sham models. *Multiscale Model. Simul.*, 12(4):1828–1869, 2014.

[155] Denis Davydov, Toby D. Young, and Paul Steinmann. On the adaptive finite element analysis of the Kohn–Sham equations: methods, algorithms, and implementation. *Int. J. Numer. Methods Eng.*, 106(11):863–888, 2016.

[156] Bikash Kanungo and Vikram Gavini. Large-scale all-electron density functional theory calculations using an enriched finite-element basis. *Phys. Rev. B*, 95: 035112, Jan 2017.

[157] D. Davydov, T. Heister, M. Kronbichler, and P. Steinmann. Matrix-free locally adaptive finite element solution of density-functional theory with nonorthogonal orbitals and multigrid preconditioning. *Phys. Status Solidi B: Basic Solid State Physics*, 255(9), 2018. doi: 10.1002/pssb.201800069.

[158] Leeor Kronik, Adi Makmal, Murilo L. Tiago, M. M. G. Alemany, Manish Jain, Xiangyang Huang, Yousef Saad, and James R. Chelikowsky. PARSEC — the pseudopotential algorithm for real-space electronic structure calculations: recent advances and novel applications to nano-structures. *Phys. Status Solidi B*, 243(5):1063–1079, 2006.

[159] Vincent Michaud-Rioux, Lei Zhang, and Hong Guo. RESCU: A real space electronic structure method. *J. Comput. Phys.*, 307:593–613, 2016.

[160] Swarnava Ghosh and Phanish Suryanarayana. SPARC: Accurate and efficient finite-difference formulation and parallel implementation of density functional theory: Isolated clusters. *Comput. Phys. Commun.*, 212:189–204, 2017.

[161] Swarnava Ghosh and Phanish Suryanarayana. SPARC: Accurate and efficient finite-difference formulation and parallel implementation of density functional theory: Extended systems. *Comput. Phys. Commun.*, 216:109–125, 2017.

[162] Xavier Andrade, David Strubbe, Umberto De Giovannini, Ask Hjorth Larsen, Micael J. T. Oliveira, Joseba Alberdi-Rodriguez, Alejandro Varas, Iris Theophilou, Nicole Helbig, Matthieu J. Verstraete, Lorenzo Stella, Fernando Nogueira, Aln Aspuru-Guzik, Alberto Castro, Miguel A. L. Marques, and Angel Rubio. Real-space grids and the Octopus code as tools for the development of new simulation approaches for electronic systems. *Phys. Chem. Chem. Phys.*, 17:31371–31396, 2015.

[163] J Enkovaara, C Rostgaard, J J Mortensen, J Chen, M Dułak, L Ferrighi, J Gavnholt, C Glinsvad, V Haikola, H A Hansen, H H Kristoffersen, M Kuisma, A H

Larsen, L Lehtovaara, M Ljungberg, O Lopez-Acevedo, P G Moses, J Ojanen, T Olsen, V Petzold, N A Romero, J Stausholm-Møller, M Strange, G A Tritsaris, M Vanin, M Walter, B Hammer, H Hkkinen, G K H Madsen, R M Nieminen, J K Nørskov, M Puska, T T Rantala, J Schiøtz, K S Thygesen, and K W Jacobsen. Electronic structure calculations with GPAW: a real-space implementation of the projector augmented-wave method. *J. Phys. Condens. Matter*, 22(25):253202, jun 2010.

[164] Luigi Genovese, Alexey Neelov, Stefan Goedecker, Thierry Deutsch, Seyed Alireza Ghasemi, Alexander Willand, Damien Caliste, Oded Zilberberg, Mark Rayson, Anders Bergman, and Reinhold Schneider. Daubechies wavelets as a basis set for density functional pseudopotential calculations. *J. Chem. Phys.*, 129(1):014109, 2008.

[165] Chris-Kriton Skylaris, Peter D. Haynes, Arash A. Mostofi, and Mike C. Payne. Introducing ONETEP: Linear-scaling density functional simulations on parallel computers. *J. Chem. Phys.*, 122(8):084119, 2005.

[166] Wei Hu, Lin Lin, and Chao Yang. DGDFT: A massively parallel method for large scale density functional theory calculations. *J. Chem. Phys.*, 143(12): 124110, 2015.

[167] Phani Motamarri and Vikram Gavini. Tucker-tensor algorithm for large-scale Kohn-Sham density functional theory calculations. *Phys. Rev. B*, 93:035111, Jan 2017.

[168] Yunkai Zhou, Yousef Saad, Murilo L. Tiago, and James R. Chelikowsky. Self-consistent-field calculations using Chebyshev-filtered subspace iteration. *J. Comput. Phys.*, 219(1):172–184, 2006.

[169] R. M. Martin. *Electronic structure: basic theory and practical methods.* Cambridge university press, Cambridge, UK, 2004.

[170] S. Goedecker. Linear scaling electronic structure methods. *Rev. Mod. Phys.*, 71:1085–1123, 1999.

[171] G. E. Scuseria and V. N Staroverov. Progress in the development of exchange-correlation functionals, 2005.

[172] A. D. Becke. Density-functional exchange-energy approximation with correct asymptotic behavior. *Phys. Rev. A.*, 38:3098–3100, 1988.

[173] J. P. Perdew and Y. Wang. Accurate and simple analytic representation of the electron-gas correlation energy. *Phys. Rev. B.*, 45:13244–13249, 1992.

[174] J. P. Perdew, K. Burke, and M. Ernzerhof. Generalized Gradient Approximation made simple. *Phys. Rev. Lett.*, 77:3865–3868, 1996.

[175] L. Kleinman and D. M. Bylander. Efficacious form for model pseudopotentials. *Phy. Rev. Lett.*, 48(20):1425, 1982.

[176] N. Troullier and J. L. Martins. Efficient pseudopotentials for plane-wave calculations. *Phys. Rev. B*, 43:1993–2006, 1991.

[177] D. R. Hamann. Optimized norm-conserving Vanderbilt pseudopotentials. *Phys. Rev. B*, 88:239906, 1995.

[178] K. Lejaeghere et al. Reproducibility in density functional theory calculations of solids. *Sci.*, 351, 2016.

[179] Y. Zhou, Y. Saad, M. L. Tiago, and J. R. Chelikowsky. Parallel self-consistent-field calculations via Chebyshev-filtered subspace acceleration. *Phys. Rev. E*, 74(6):066704, 2006.

[180] C. G. Broyden. A class of methods for solving nonlinear simultaneous equations. *Math. Comput.*, pages 577–593, 1965.

[181] Martin Kronbichler and Katharina Kormann. A generic interface for parallel cell-based finite element operator application. *Comput. Fluids*, 63:135–147, 2012.

[182] G. Alzetta, D. Arndt, W. Bangerth, V. Boddu, B. Brands, D. Davydov, R. Gassmöller, T. Heister, L. Heltai, K. Kormann, M. Kronbichler, M. Maier, J.-P. Pelteret, B. Turcksin, and D. Wells. The `deal.II` Library, Version 9.0. *J. Numer. Math.*, 26(4):173–183, 2018.

[183] C. Bekas and A. Curioni. Very large scale wavefunction orthogonalization in density functional theory electronic structure calculations. *Comput. Phys. Commun.*, 181(6):1057–1068, 2010.

[184] L. S. Blackford, J. Choi, A. Cleary, E. D'Azevedo, J. Demmel, I. Dhillon, J. Dongarra, S. Hammarling, G. Henry, A. Petitet, K. Stanley, D. Walker, and R. C. Whaley. *ScaLAPACK Users' Guide.* SIAM, Philadelphia, PA, 1997. ISBN 0-89871-397-8 (paperback).

[185] Eiji Tsuchida and Yoong-Kee Choe. Iterative diagonalization of symmetric matrices in mixed precision and its application to electronic structure calculations. *Comput. Phys. Commun.*, 183(4):980–985, 2012.

[186] Amartya S. Banerjee, Lin Lin, Phanish Suryanarayana, Chao Yang, and John E. Pask. Two-level chebyshev filter based complementary subspace method: Pushing the envelope of large-scale electronic structure calculations. *J. Chem. Theory Comput.*, 14(6):2930–2946, 2018.

[187] Phani Motamarri, Vikram Gavini, Kaushik Bhattacharya, and Michael Ortiz. Spectrum-splitting approach for Fermi-operator expansion in all-electron Kohn-Sham DFT calculations. *Phys. Rev. B*, 95:035111, Jan 2017.

[188] Andreas Marek, Volker Blum, Rainer Johanni, Ville Havu, Bruno Lang, Thomas Auckenthaler, Alexander Heinecke, Hans-Joachim Bungartz, and Hermann Lederer. The ELPA library: scalable parallel eigenvalue solutions for electronic structure theory and computational science. *J. Phys.: Condens. Matter*, 26 (21):213201, 2014.

[189] Brandon Cook, Thorsten Kurth, Jack Deslippe, Pierre Carrier, Nick Hill, and Nathan Wichmann. Eigensolver performance comparison on Cray XC systems. *Concurr. Comp.-Pract. E.*, 0(0):e4997, 2018.

[190] P. Kus, A. Marek, S. S. Koecher, H.-H. Kowalski, Christian Carbogno, Ch. Scheurer, Karsten Reuter, Matthias Scheffler, and H. Lederer. Optimizations of the eigensolvers in the ELPA library. *arXiv:1811.01277*, 2018.

[191] Wolfgang Bangerth, Carsten Burstedde, Timo Heister, and Martin Kronbichler. Algorithms and data structures for massively parallel generic adaptive finite element codes. *ACM Trans. Math. Software*, 38(2):14:1–14:28, 2011.

[192] Martin Schlipf and Franois Gygi. Optimization algorithm for the generation of ONCV pseudopotentials. *Comput. Phys. Commun.*, 196:36–44, 2015.

[193] P Giannozzi, O Andreussi, T Brumme, O Bunau, M Buongiorno Nardelli, M Calandra, R Car, C Cavazzoni, D Ceresoli, M Cococcioni, N Colonna, I Carnimeo, A Dal Corso, S de Gironcoli, P Delugas, R A DiStasio Jr, A Ferretti, A Floris, G Fratesi, G Fugallo, R Gebauer, U Gerstmann, F Giustino, T Gorni, J Jia, M Kawamura, H-Y Ko, A Kokalj, E Kkbenli, M Lazzeri, M Marsili, N Marzari, F Mauri, N L Nguyen, H-V Nguyen, A Otero de-la Roza, L Paulatto, S Ponc, D Rocca, R Sabatini, B Santra, M Schlipf, A P Seitsonen, A Smogunov, I Timrov, T Thonhauser, P Umari, N Vast, X Wu, and S Baroni. Advanced capabilities for materials modelling with QUANTUM ESPRESSO. *J. Phys. Condens. Matter*, 29(46):465901, 2017.

[194] J. Magnus Rahm and Paul Erhart. Beyond magic numbers: Atomic scale equilibrium nanoparticle shapes for any size. *Nano Lett.*, 17(9):5775–5781, 2017.

[195] Xavier Andrade and Aln Aspuru-Guzik. Real-space density functional theory on graphical processing units: Computational approach and comparison to gaussian basis set methods. *Journal of Chemical Theory and Computation*, 9(10): 4360–4373, 2013.

[196] Luigi Genovese, Brice Videau, Matthieu Ospici, Thierry Deutsch, Stefan Goedecker, and Jean-Franois Mhaut. Daubechies wavelets for high performance electronic structure calculations: The bigdft project. *Comptes Rendus Mcanique*, 339(2):149 – 164, 2011. High Performance Computing.

[197] K. Ghosh, H. Ma, V. Gavini, and G. Galli. All-electron density functional calculations for electron and nuclear spin interactions in molecules and solids. *arXiv:1902.07377*, 2019.

[198] Y. Mishin, D. Farkas, M. J. Mehl, and D. A. Papaconstantopoulos. Interatomic potentials for monoatomic metals from experimental data and *ab initio* calculations. *Phys. Rev. B*, 59:3393–3407, Feb 1999.

[199] Xiang-Yang Liu, Furio Ercolessi, and James B Adams. Aluminium interatomic potential from density functional theory calculations with improved stacking fault energy. *Model. Simul. Mater. Sci. Eng.*, 12(4):665, 2004.